UNIVERSITY OF ICELAND

Ph.D. Dissertation

in Physics

Metal ion escape and gas rarefaction in high power impulse magnetron sputtering

Kateryna Barynova

May 2026

FACULTY OF PHYSICAL SCIENCES

Metal ion escape and gas rarefaction in high power impulse magnetron sputtering

Kateryna Barynova

Dissertation submitted in partial fulfillment of a
Philosophiae Doctor degree in Physics

Ph.D. Committee
Jón Tómas Guðmundsson (Chair)
Martin Rudolph
Daniel Lundin

Opponents
Tomáš Kozák
Julian Held

Faculty of Physical Sciences
School of Engineering and Natural Sciences
University of Iceland
Reykjavik, May 2026

Metal ion escape and gas rarefaction in high power impulse magnetron sputtering

(Metal ion escape and gas rarefaction in HiPIMS)

Dissertation submitted in partial fulfillment of a *Ph.D.* degree in Physics

Faculty of Physical Sciences
School of Engineering and Natural Sciences
University of Iceland
Dunhaga 5
IS-107 Reykjavik Reykjavik
Iceland

Telephone: 525-4000

Bibliographic information:
Kateryna Barynova, 2026, *Metal ion escape and gas rarefaction in high power impulse magnetron sputtering*, Ph.D. Dissertation, Faculty of Physical Sciences, University of Iceland, 166 pp.

Author ORCID: 0009-0009-0894-6160
ISBN: 978-9935-585-01-1

Printing: Háskólaprent, Fálkagata 2, 107 Reykjavik
Reykjavik, Iceland, May 2026

Abstract

High power impulse magnetron sputtering (HiPIMS) is an advanced ionized physical vapor deposition (IPVD) technique that uses almost the same hardware as dc magnetron sputtering (dcMS), but is more flexible in tuning film characteristics. Compared to conventional dc magnetron sputtered films, thin films produced by HiPIMS typically have enhanced properties, such as better crystallinity, higher mass density, and improved phase composition, primarily due to low-energy ion bombardment during the film growth process. However, the broader use of HiPIMS in industrial applications is constrained by the main disadvantage: often a significantly lower deposition rate. This drawback is mainly attributed to the back-attraction of the film-forming species after they have been ionized in the dense plasma near the cathode target.

The thesis focuses on addressing this primary limitation of HiPIMS deposition by investigating the physics governing the discharge, and the relationship between sputter yield and deposition rate. The central goal was to analyze and further develop the ionization region model (IRM) of HiPIMS discharges to optimize the deposition process. The research involved computational modeling, including studies on working gas rarefaction across multiple target materials, the detailed modeling of discharges with chromium, aluminum, and graphite targets in various gas mixtures (e.g., Ne/Ar), and the analysis of the results obtained from the simulations.

The main conclusion, supported by the data analysis of the IRM simulation results for various target materials under diverse discharge conditions, is that the sputter yield dictates the back-attraction probability of the sputtered species. The sputter yield is shown to be a key factor that significantly changes the discharge composition, electron temperature, degree of gas rarefaction, and, consequently, the possible limit on deposition rate and overall discharge characteristics. Furthermore, the sputter yield determines which process is mainly responsible for working gas rarefaction.

In conclusion, this work establishes that the target sputter yield is important for controlling and optimizing the HiPIMS discharge. The thesis serves as an introduction to the physical processes investigated, while the detailed results of the work are presented in the attached articles. The work also includes a supplementary experimental part focused on measurements of the ionized flux fraction (IFF) in the deposition flux. This experimental data served for constraining one of the parameters within the IRM, thereby improving the model's predictive power.

Ágrip

Háaflspúlsuð segulspæta (HiPIMS) er ræktunartækni sem byggir á háu hlutfalli jónaðra agna í agnaflæðinu sem myndar húðina, en notar nánast sama tækjabúnað og jafnstraumssegulspætun, en hefur meiri sveigjanleika hvað varðar það að stýra megi gæðum ræktaðrar húðar. Í samanburði við húðir ræktaðar með hefðbundinni dc segulspætu sýna húðir sem ræktaðar eru með HiPIMS yfirleitt bætta eðliseiginleika, svo sem betri kristallsbyggingu, hærri eðlismassa og bætta fasasamsetningu, aðallega vegna lágorku jónahríðar á vaxtarstiginu. Hins vegar er útbreiddari iðnaðarnotkun HiPIMS verulega takmörkuð vegna helsta ókosts þessarar tækni: verulega minni ræktunarhraða. Þessi lági ræktunarhraði er rakinn til þess að eftir jónun spættu atómanna í þéttu rafgasinu nærri bakskautsskotmarkinu, er stór hluti þeirra dreginn aftur að bakskautinu.

Megin markmið ritgerðarinnar er að leita leiða til að bregðast við þessari helstu takmörkun HiPIMS tækninnar með því að rannsaka eðlisfræðina sem lýsir afhleðslunni og tengslin milli afraksturs spætunar (e. sputter yield) og ræktunarhraða. Meginmarkmiðið var að greina og þróa áfram jónunarsvæðislíkanið (IRM) fyrir háflspúlsaðar segulspætur til þess að besta ræktunarferlið. Þetta fól í sér líkanagerð, þar á meðal rannsóknir á gasþynningu vinnugassins fyrir mörg mismunandi skotmörk, líkanagerð á afhleðslum með skotmörk úr króm, áli og grafíti í ýmsum gasblöndum (t.d. Ne/Ar), og greiningu á niðurstöðum úr þessum hermununum.

Meginniðurstaðan, sem studd er af gagnagreiningu á niðurstöðum úr IRM-hermunum fyrir ýmis skotmörk, við fjölbreytt afhleðsluskilyrði, er sú að afrakstur spætunar ræður líkunum á því að spættu agnirnar dragist aftur að skotmarkinu. Sýnt er fram á að afrakstur spætunar sé lykilþátturinn í að breyta samsetningu agna í afhleðslunni, rafeindahitastigi, hve mikið vinnugasið þynnist og þar með mögulegum takmörkunum á ræktunarhraða svo og heildar eiginleikum afhleðslunnar. Enn fremur ákvarðar afrakstur spætunar því hvaða ferli ber meginábyrgð á þynningu vinnugassins.

Þegar upp er staðið staðfestir þetta verk að afrakstur spætunar skotmarksins sé mikilvæg stýristærð þegar besta á háaflspúlsaða segulspætu. Ritgerðin þjónar sem inngangur að þeim eðlisfræðilegu ferlum sem rannsakaðir voru, en megin niðurstöður verksins eru kynntar í meðfylgjandi greinum. Í verkinu er einnig fjallað um tilraunir þar sem áhersla er lögð á að mæla hlutfall jónaðra agna í flæðinu (IFF) sem myndar húðina. Þessi tilraunagögn voru notuð til að afmarka eina af breytum IRM-líkansins, sem bætir forspárgildi líkansins.

Dedication
To my brother Marko

Table of Contents

List of Figures

List of Publications

List of scientific publications which are published or in the publication process and which are included in the thesis. Articles included in Publications chapter.

Paper I: **Kateryna Barynova**, Martin Rudolph, Swetha Suresh Babu, Joel Fischer, Daniel Lundin, Michael A. Raadu, Nils Brenning and Jon Tomas Gudmundsson, 2024, On working gas rarefaction in high power impulse magnetron sputtering. *Plasma Sources Science and Technology*, Vol. 33, Issue 6, pp. 065010. Accessed at https://iopscience.iop.org/article/10.1088/1361-6595/ad53fe.

The contribution of the Ph.D. candidate was to implement the revised mechanism of kick-out, based on the sputtered species flux; the addition of fast reflected argon atoms (Ar^H) to the kick-out term; the revision of the older IRM model for the various target materials, including modeling aluminum discharge from scratch, as it was implemented in Maple software (which was the original version of the IRM) and not MATLAB; the simulation; the writing of data analysis scripts; data analysis; visualization; the participation in the discussions, and writing.

Paper II: **Kateryna Barynova**, Nils Brenning, Swetha Suresh Babu, Joel Fischer, Daniel Lundin, Michael A Raadu, Jon Tomas Gudmundsson and Martin Rudolph, 2025, Self-regulating electron temperature in high-power impulse magnetron sputtering discharges and its effect on the metal ion escape. *Plasma Sources Science and Technology*, Vol. 34, Issue 6, pp. 06LT01. Accessed at https://iopscience.iop.org/article/10.1088/1361-6595/adde82.

The contribution of the Ph.D. candidate included implementation of the chromium target and the chromium discharge chemistry into the IRM, unification of the approaches with different targets such as regarding sputter yield treatment and secondary electron emission, running the simulations, data analysis of the simulations results, visualization.

Paper III: **Kateryna Barynova**, Tetsuhide Shimizu, Rommel Paulo B. Viloan, Michal Zanáška, Joel Fischer, Martin Rudolph, Daniel Lundin and Jon Tomas Gudmundsson, 2025, High power impulse magnetron sputtering from a chromium target. *Plasma Sources Science and Technology*, Vol. 35, Issue 2, pp. 025028. Accessed at https://iopscience.iop.org/article/10.1088/1361-6595/ae42e5.

The contributions of the Ph.D. candidate included implementing the chromium discharge chemistry, modeling the discharge, such as calculating and implementing sputter yield, secondary electron emission, effective ionization cost, reactions in the IR, kick-out term, data analysis, visualization, and interpretation of the simulation results, participation in the discussions, and writing.

Paper IV: Swetha Suresh Babu, Joel Fischer, **Kateryna Barynova**, Martin Rudolph, Daniel Lundin and Jon Tomas Gudmundsson, 2024, High power impulse magnetron sputtering of a zirconium target. *Journal of Vacuum Science and Technology A*, Vol. 42, Issue 4, pp. 043077. Accessed at `https://doi.org/10.1116/6.0003647`.

The contribution of the Ph.D. candidate included part of visualization and data analysis scripts, in particular regarding the kick-out of the sputtered species, as well as participation in the discussions.

List of relevant scientific publications, which are not included in the thesis.

Paper V: Jon Tomas Gudmundsson, **Kateryna Barynova**, Nils Brenning, Joel Fischer, Daniel Lundin, Michael A. Raadu and Martin Rudolph, 2025, On metal ion escape in high-power impulse magnetron sputtering. *68^{th} Annual Technical Conference Proceedings*, Nashville, TN, USA, May 19–22, pp. 0014. Accessed at `https://doi.org/10.14332/svc25.proc.0014`.

The contributions of the Ph.D. candidate included the visualization, interpretation of the results, running the simulations, and participation in the discussion.

Paper VI: Nastaran Behravan, Dmytro Solonenko, Alireza Farhadizadeh, Tatiana Pitonakova, **Kateryna Barynova**, Tamara Terzic, Robert Boyd, Magnus Odén, Marco Deluca, Mohssen Moridi and Daniel Lundin, 2026, Controlling metal ion acceleration via gas rarefaction for enhanced epitaxial AlN growth on silicon. *Acta Materialia*, submitted April 2026.

The contributions of the Ph.D. candidate included part of the visualization, participation in the experiments, and running the simulations for some cases.

Conference Presentations

List of presentations at scientific conferences on the topics covered in the thesis:

Conference I: **Kateryna Barynova**, Martin Rudolph, Swetha Suresh Babu, Joel Fischer, Daniel Lundin, Michael A Raadu, Nils Brenning and Jon Tomas Gudmundsson, 2024, On working gas rarefaction in high power impulse magnetron sputtering, 51st IEEE International Conference on Plasma Science (ICOPS), June 15-20, 2024, Beijing, China, oral presentation

Conference I: **Kateryna Barynova**, Martin Rudolph, Swetha Suresh Babu, Joel Fischer, Daniel Lundin, Michael A Raadu, Nils Brenning and Jon Tomas Gudmundsson, 2024, On working gas rarefaction in high power impulse magnetron sputtering, 17th International Symposium on Sputtering and Plasma Processes (ISSP), July 2-5, 2024, Kyoto, Japan, oral presentation

Conference III: **Kateryna Barynova**, Martin Rudolph, Swetha Suresh Babu, Joel Fischer, Daniel Lundin, Michael A Raadu, Nils Brenning and Jon Tomas Gudmundsson, 2024, On working gas rarefaction in high power impulse magnetron sputtering, HiPIMS Today 2024, March 11-13, 2024, virtual poster

Conference IV: **Kateryna Barynova**, Nils Brenning, Swetha Suresh Babu, Joel Fischer, Daniel Lundin, Michael A Raadu, Jon Tomas Gudmundsson and Martin Rudolph, 2025, On the connection between back-attraction probability and sputter yield in HiPIMS, HiPIMS Today 2025, March 17-19, 2025, virtual invited speaker

Conference V: **Kateryna Barynova**, Nils Brenning, Swetha Suresh Babu, Joel Fischer, Daniel Lundin, Michael A Raadu, Jon Tomas Gudmundsson and Martin Rudolph, 2025, Self-regulating electron temperature in high power impulse magnetron sputtering discharges and its effect on the metal ion escape, AVS 71 International Symposium and Exhibition, September 21-26, 2025, oral presentation

Abbreviations

ac	alternating current
CVD	chemical vapor deposition
dc	direct current
DLC	diamond-like carbon
DR	diffusion region
DSMC	direct simulation Monte Carlo
EEDF	electron energy distribution function
HiPIMS	high power impulse magnetron sputtering
IC	integrated circuit
IEDF	ion energy distribution function
IFF	ionized flux fraction
IPVD	ionized physical vapor deposition
IR	ionization region
IRM	ionization region model
MCC	Monte Carlo collision
MS	magnetron sputtering
MPPMS	modulated pulse power magnetron sputtering
ODE	ordinary differential equation
PECVD	plasma-enhanced chemical vapor deposition
PVD	physical vapor deposition
QCM	quartz crystal microbalance
rf	radio frequency
SZD	structure zone diagram

Symbols

$\mathbf{B}$	magnetic field
d	distance
D	diffusion constant
e	elementary charge
$\mathbf{E}$	electric field
E^*	normalized energy flux
$\mathscr{E}_\mathrm{c}$	collisional energy loss per ion–electron pair created
$\mathscr{E}_\mathrm{max}$	cutoff energy
$\mathscr{E}_\mathrm{sb}$	surface binding energy
$\mathscr{E}_\mathrm{t}$	kinetic energy
$\mathscr{E}_\mathrm{th}$	threshold energy
f	fraction of total discharge voltage drop across the ionization region
f_p	pulse frequency
F_flux	ionized flux fraction
I_D	discharge current
I_g	working gas ion current
I_prim	primary current
I_SS	self-sputter current
$\mathbf{J}$	current density
$\mathbf{J}_\mathrm{e}$	electron current density
k_B	Boltzmann constant
m	probability of electron's ionization in the sheath
n	density of species
r	electron recapture probability
t^*	net thickness
T	temperature
T_e	electron temperature
T_i	ion temperature

T^*	generalized temperature
u_B	Bohm velocity
$\bar{v}$	mean speed
V_D	discharge voltage
$\mathcal{V}_{IR}$	volume of the ionization region
V_{IR}	voltage across ionization region
V_{SH}	voltage across sheath
V_{Th}	Thornton discharge voltage
Y_{SS}	self-sputter yield
Y_g	sputter yield of the target by working gas ions
α_g	ionization probability of the working gas atoms
α_{prim}	ionization probability of the working gas atoms, ionized for the first time
α_t	ionization probability of the sputtered target atoms
β_g	working gas ion back-attraction probability
β_t	target ion back-attraction probability
γ_{SE}	secondary electron emission yield
$\gamma_{SE,eff}$	effective secondary electron emission yield
$\gamma_{Ar^+,eff}$	effective secondary electron emission yield for Ar^+-ions bombarding the target
$\gamma_{M^{2+},eff}$	effective secondary electron emission yield for doubly ionized metal ions bombarding the target
Γ_a	flux of species *a*
Γ_{sput}	flux of sputtered species
δ	duty cycle
ε_e	fraction of the secondary electrons that cause ionization before they are lost
ε_0	vacuum permittivity
Θ	incident angle
λ	mean free path
λ_{De}	Debye lenght

Λ	energy transfer factor
μ_e	mobility of the electrons
ν_m	momentum transfer frequency
ξ_{pulse}	probability of the ions, neutralized at the target to return to the discharge during the pulse
ξ_{ti}	transport parameter for ions
ξ_{tn}	transport parameter for neutrals
τ_c	the electron's effective collision time
σ	cross section
χ	degree of ionization of plasma
ω_{ge}	electron (angular) gyro frequency
Al	aluminum atom in ground state
$\mathbf{Al}^{+}$	singly ionized aluminum
$\mathbf{Al}^{2+}$	doubly ionized aluminum
Ar	argon atom in ground state
$\mathbf{Ar}^{+}$	singly ionized argon
$\mathbf{Ar}^{m}$	argon in metastable state
$\mathbf{Ar}^{2+}$	doubly ionized argon
$\mathbf{Ar}^{W}$	"warm" argon atom in ground state
$\mathbf{Ar}^{H}$	"hot" argon atom in ground state
Cr	chromium atom in ground state
$\mathbf{Cr}^{+}$	singly ionized chromium
$\mathbf{Cr}^{2+}$	doubly ionized chromium
$\mathbf{e}_c$	primary or "cold" electron
$\mathbf{e}_h$	secondary or "hot" electron

Acknowledgements

First and foremost, I wish to express my gratitude to my supervisor, prof. Jón Tómas Guðmundsson, for his guidance, support, and the time he dedicated to this project. I am extremely grateful for the support of my doctoral committee, dr. Martin Rudolph and prof. Daniel Lundin, without whose contributions to this project, it have been nearly impossible to complete. I would like to thank the members of our weekly IRM meetings for their discussions and comments. In particular, I am grateful to dr. Michael A. Raadu, prof. Nils Brenning, and dr. Joel Fischer, as well as to prof. Tiberiu M. Minea, dr. Swetha Suresh Babu, and Vigo Tegara. I am grateful to the University of Iceland Research Fund for Doctoral Students, the University of Iceland Research Fund (Grant no. 93940), and the Icelandic Research Fund (Grants no. 196141 and 2511073) for funding the project, and the University of Iceland for providing the necessary facilities, and for ensuring heat during the cold winters. I would like to thank the Plasma and Coatings Division at Linköping University for hosting me and helping me gain experimental experience with the things I am modeling. There I would like to once again express my gratitude to prof. Daniel Lundin and dr. Joel Fischer, as well as to Nastaran, Tatiana, and Rommel. I am grateful to my former supervisors dr. Sarah Antier, dr. Nicolas Leroy, dr. Bertrand Cordier, dr. Damien Turpin, dr. Oleg Bezshyyko, and dr. Andrii Simon, and dr. Oleksandr Baransky. I would also like to thank my family and friends, whose support helped me stay sane: Robert, Nadia, Andrii, Marko, Daria, Yuliia, Elli, Ursula, and Astrid.

CHAPTER 1

INTRODUCTION

Magnetron sputtering (MS) is a thin film deposition technique that has a number of advantages, compared to other *physical vapor deposition* (PVD) methods, as it allows the control of the microstructure and characteristics of the deposited film or coating. Sputtering is based on momentum exchange between energetic species and the atoms constituting the cathode target. In magnetron sputtering the ions are accelerated toward a solid target, which is the source of the film-forming material. The ions are typically ions of a heavy inert gas, and as they bombard the cathode target, its atoms are released. These sputtered atoms propagate through the discharge chamber, some of which deposit on a substrate, and a thin film or coating is formed. Magnets behind the target trap electrons in the target vicinity and prevent escape of electrons to the chamber walls. This allows for the discharges to be operated at lower pressure and lower discharge voltage. The widespread use of magnetron sputtering is seen from the diversity of its applications, from microelectronic circuit manufacturing, forming protective layers on cutting tools, to deposition of optical films on architectural glass, among others. In PVD virtually any material can be deposited and material combinations and components can be synthesized using either multiple targets or by addition of a reactive gas. ***Chapter 2*** of the thesis gives a general introduction to PVD methods with a focus on magnetron sputtering.

Chapter 3 gives an introduction to *high power impulse magnetron sputtering* (HiPIMS), which is a magnetron sputtering technique that provides ionized flux of the film forming species. Magnetron sputtering discharges are typically operated by applying dc voltage to a cathode target. The application of high power pulses instead gives increased electron density and ionization of the sputtered species. This allows for better control over the deposited film characteristics. Compared with dc magnetron sputtered films, the HiPIMS-deposited films exhibit better crystallinity, higher mass density, and overall improved film properties, which is achieved through low-energy ion bombardment throughout the deposition process. This allows for the adjustment of reactivity, kinetics, microstructure, phase composition, grain size, orientation, density, and internal stress within the deposited materials. However, often the deposition rate is significantly lower in HiPIMS deposition due to high *back-attraction probability* of the sputtered species after they have been ionized. This is the main factor as to why HiPIMS has not gained wide range industrial use.

The project's goal was to analyze and further develop the *ionization region model* (IRM) of HiPIMS discharges to better understand and optimize the process. IRM is a semi-empirical time-dependent, volume averaged plasma chemistry model of a HiPIMS discharge focused on the *ionization region* (IR). ***Chapter 4*** gives a description of the model and HiPIMS modeling in general.

This thesis addresses the main disadvantage of HiPIMS by focusing on the relation between the *sputter yield* and the *deposition rate*. The work included studying working gas rarefaction in front of the target for multiple target materials, modeling a discharge with a chromium target, updating the model for a discharge with an aluminum target, modeling a discharge with graphite target operated in Ne/Ar gas mixture, and experimentally measuring the *ionized flux fraction* (IFF) in discharges with aluminum target. In addition, all discharge systems previously studied were recalculated for this work, as this was required because the IRM has been updated over the years. Furthermore, after bringing previous studies together, it became possible to examine the dependence of the back-attraction probability on the sputter yield of the target material. This allows us to get a better understanding of how the deposition rate can be improved without losing the high ionized flux fraction of the deposition flux. The main finding confirms that the sputter yield of the target material is a significant factor in determining the discharge physics, based on the data analysis of IRM simulations across seven different target materials under various discharge conditions.

The central part of the thesis is a compilation of published papers that detail the results found during the course of work. The summary of the articles is presented in ***Chapter 5***. The primary conclusion of the thesis is presented in ***Chapter 6***. In summary, the sputter yield of the target, considering both the sputter yield by the ions of the working gas and the self-sputter yield, plays an important role in dictating the HiPIMS discharge properties. The sputter yield significantly influences the discharge composition, electron temperature, gas rarefaction, deposition rate, and overall discharge characteristics. The published papers are presented in ***Chapter 7***.

CHAPTER 2

FUNDAMENTALS OF SPUTTER DEPOSITION

2.1 Plasma material processing

Plasma processing technology is irreplaceable for most major modern manufacturing industries as plasma discharges play an important role in the treatment of surfaces in ways that are not possible by the other methods. This can be attributed to the nature of a plasma discharge. The term *plasma* was introduced by Irving Langmuir in 1928, by which he meant to describe a quasi-neutral collection of ions and electrons that may or may not contain a background neutral gas and that are capable of responding to electric and magnetic fields (Tonks, 1967). This composition allows plasma to interact with materials in unique and controlled ways (Roth, 1995, p. 33). The flexibility of plasma processing can be seen from a wide range of its methods and applications. Some examples include: anisotropic etching in fabrication of microelectronic chips; plasma deposition of silicon nitride for surface passivation and insulation; surface oxidation used in fabrication of silicon-based microelectronic circuits; surface treatment for improved film adhesion to polymer surfaces; nitriding, which is used to harden the surface of steel; plasma-enhanced chemical vapor deposition and thermal plasma chemical vapor deposition of diamond thin films; spray deposition of ceramic or metal alloy coatings used for protection against wear or corrosion in aircraft and automotive engines; spray deposition of clearance control coatings; melting and refining of alloys; manufacture of optical fibers used in communications; synthesis of ultrapure powders used as ceramic precursors; spray deposition and thermal plasma chemical vapor deposition of high-temperature superconductors and refractory materials; welding and cutting; and plasma sputter deposition of magnetic films for memory devices (National Research Council, 1991).

There are several plasma-based material processing methods, such as:

- etching – reactive ion etching, plasma enhanced etching (Donnelly and Kornblit, 2013);
- deposition – physical vapor deposition (PVD) (Gudmundsson et al., 2022)/sputter deposition, plasma-enhanced chemical vapor deposition (CVD), thermal plasma CVD

(Snyders et al., 2023);

- cleaning (Thanu et al., 2019);
- sterilization (Moisan et al., 2002);
- conversion (Rudolph et al., 2023);
- activation (Suni et al., 2002) and (Pocius, 2012, Chapter 7);
- polymerization (Chen et al., 2011);
- ashing (Takagi et al., 2001);
- implantation (Thomae, 1998).

Plasma material processing is irreplaceable in the production of very large scale integrated circuits (ICs) in microelectronics. It is estimated that 40 – 45 % of all process steps in microelectronic fabrication use plasmas (Graves et al., 2024). The other industries that are highly dependent on plasma technology are aerospace, automotive, steel, biomedical, and waste management sectors. Furthermore, plasma processing technology has been implemented in new industry areas, particularly for the growth of diamond and superconducting films (Lieberman and Lichtenberg, 2005, p. 630).

An advantage of plasma processing, particularly for electrically driven low-pressure discharges, is its non-equilibrium nature. The electrons are generally not in thermal equilibrium with the ions nor the neutrals. In modern integrated circuit manufacturing, film and mask deposition, mask patterning, implantation or other modifications, etching, and mask removal are repeated multiple times during the production. Due to the temperature sensitivity of the process, in many cases the use of high-temperature deposition processes is ruled out. Fortunately, plasma processing can provide film deposition at low substrate temperatures (see Section 2.3). Furthermore, thin films can be deposited with improved properties, non-equilibrium chemical compositions, and crystal morphologies that cannot be achieved under equilibrium deposition conditions at any temperature (Lieberman and Lichtenberg, 2005, p. 619). Anisotropy is important in integrated circuit production and other manufacturing industries and is easily achieved with plasma processing, for example, to deposit material in narrow vials with good sidewall and bottom coverage. Material selectivity is another important parameter, and it is not as easily achieved with plasma processing as with CVD.

In essence, plasma material processing provides a powerful tool for engineering materials, advancing the development of technologies, and improving the performance of existing processes.

2.2 Physical vapor deposition

The term *physical vapor deposition* (PVD) covers a variety of techniques that are used to form a thin film or coating on a substrate by depositing target material released into the gas phase. This involves physical release/ejection of atoms or molecules, and then their nucleation/deposition on a substrate. Released species can remain neutral, be ionized in the chamber volume, or react chemically with the feedstock gas. The species can be removed from the solid target surface by physical means such as laser or electron beam, sputtering due to ion bombardment, thermal evaporation or sublimation. This "vapor" then reaches the substrate and forms a layer of the target material. It should be emphasized that in most cases there is no thermal equilibrium between the target and the surrounding space, so the use of the word "vapor" is purely historical, since now PVD covers much wider range of methods than in the past, when the main process was thermal evaporation (Gudmundsson et al., 2022). Note that PVD methods such as sputtering in particular give particle fluxes that have energetic particles that travel in a preferred direction.

Today, PVD processes include but are not limited to a number of evaporation and sputter deposition techniques:

- thermal evaporation (Glang, 1970);
- electron beam evaporation (Graper, 1970);
- sputter deposition (Wright, 1877a; Maissel, 1970; Rossnagel, 1990);
- magnetron sputter deposition (Gudmundsson, 2020; Waits, 1978a);
- ion beam sputtering (Harper, 1978; Rossnagel and Cuomo, 1988);
- cathodic/anodic arc deposition (Anders, 2008a; Meassick et al., 1992);
- ion plating (Mattox, 1998);
- pulsed laser deposition (Ogugua et al., 2020);
- molecular beam epitaxy (Bean, 1993);
- thermal laser epitaxy (Braun and Mannhart, 2019);
- close space sublimation (Birkett et al., 2018)

There are as well hybrid processes that combine PVD and chemical vapor deposition (CVD) methods, which are not mentioned. The classification of PVD can be complicated since various techniques can have many names and there is an uncertainty of classification. However, they can be described by parameters such as the thermal equilibrity of the process, the energy of the ejected species, and the state of the ejected species (atomic, molecular, and ionized).

When choosing a PVD method (or a combination of methods) for a specific application, there is a lot to consider for the optimal result: growth rate, energy distribution, and ionized flux fraction of the film-forming species, since these parameters control the microstructure of the

deposited film (see Section 2.3 and Section 2.4). The thesis focuses on magnetron sputtering deposition technique called high power impulse magnetron sputtering (HiPIMS) (the details will be discussed in Chapter 3), and not on the properties of the deposited film; however, it is crucial to discuss the impact of the parameters of film-forming species on film growth to clarify the benefits of HiPIMS as a technique.

2.3 Energy of the film-forming species

One way to classify PVD is by thermal balance, into equilibrium and non-equilibrium deposition processes (Anders, 2026). In equilibrium processes, the target and the surrounding space are in thermal equilibrium. Methods of deposition which fall into this category are thermal evaporation and electron beam evaporation. The crucial factor is that the energy of the film-forming species they provide is typically significantly below 1 eV, while *non-equilibrium sputter techniques* provide energetic neutrals with kinetic energies of a few eV, and pulsed laser deposition or arc deposition can produce species with energies above 100 eV. Thus, the different PVD techniques provide film-forming species that cover a wide kinetic energy range (Gudmundsson et al., 2022).

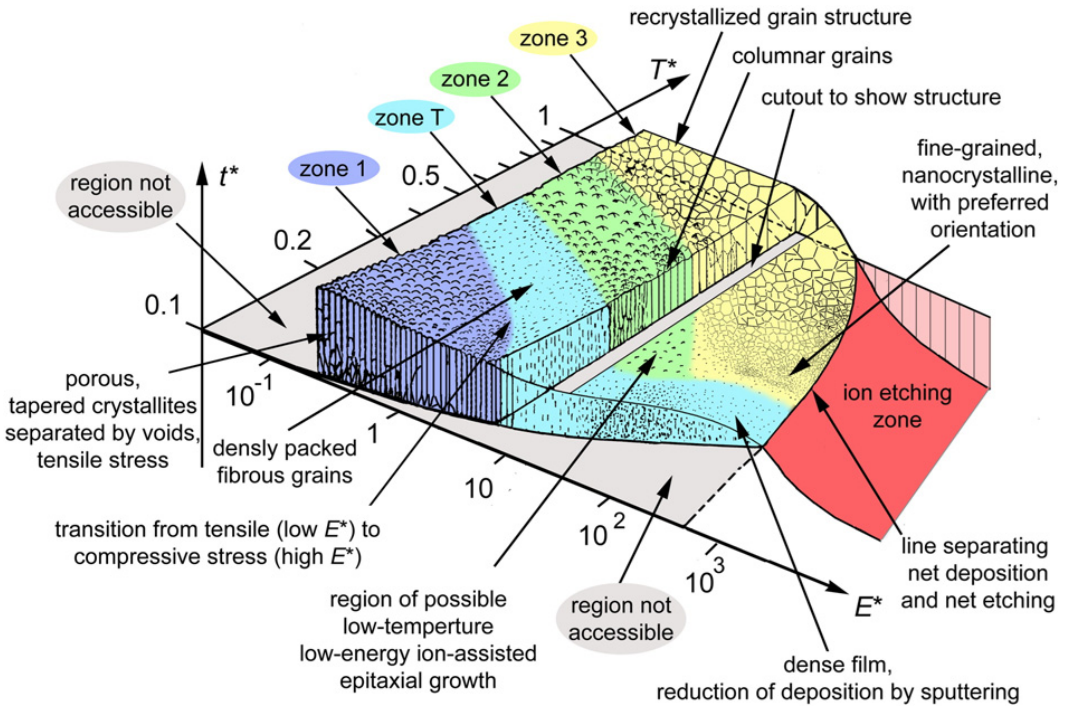

Figure 2.3.1. Structure zone diagram (SZD) for energetic thin film deposition. The axes are the generalized temperature T^*, the normalized energy flux E^*, and the net thickness t^*. The divisions between areas are continuous and for illustrative purposes only, and the actual values on axes depend on the material and other conditions. Reprinted from Anders (2010b), Copyright (2010), with permission from Elsevier.

The microstructure of the deposited polycrystalline films is affected by both the substrate (or film) temperature and the kinetic energy of the film-forming species. This relationship forms a structure zone diagram (SZD) (see Figure 2.3.1), that accounts for the generalized temperature T^*, the normalized energy flux E^* of the film-forming species, and the net thickness t^* (Anders, 2010b). SZD serves as a practical method for demonstrating the morphology of relatively thick epitaxially grown films (>100 nm) as a function of deposition parameters and illustrating how they influence the structure of the film. Generally, higher energy results in films characterized by larger grains and fewer defects, which also impact the alignment or orientation of the growing crystallites. The diagram shows that the substrate temperature can be partially compensated for by the energy of the incoming ions, since comparable film structures, defined by the various color deposition zones in Figure 2.3.1, are achieved at a lower generalized temperature T^* when the normalized energy flux E^* is higher. On the microscopic scale, this can be attributed to the increased mobility of adatoms, as more energetic species take part in the film growth process at higher E^*, and the mobility of adatoms is determined not only by the thermal energy but also by bombardment with energetic particles. From a technological perspective, this provides a benefit as the substrate can be kept at a much lower temperature while the PVD process is in progress (Gudmundsson et al., 2022).

The reason for the observed SZD is that the high kinetic energy leads to the displacement of film atoms and creation of defects, followed by re-nucleation, while the release of potential energy and the subsequent thermal spike result in atomic-scale heating and defect annihilation due to increase in adatom mobility. So, the ratio of potential energy to kinetic energy of an incoming particle, along with the magnitude of the kinetic energy, will influence the development of preferred orientation and intrinsic stress in the film (Anders, 2010b).

There is a maximum intrinsic stress for kinetic energies ranging from a few tens to a few hundreds of eV; the actual value depends on the material and other factors (Bilek and McKenzie, 2006). At higher substrate temperatures, the grains become larger as the increase of adatom mobility outweighs the rise in defects caused by ion bombardment and the rates of re-nucleation. When the kinetic energy of the ions increases even more, for instance, by applying a bias to the substrate, the sputtering yield increases as well, resulting in a decrease in the deposition rate due to the simultaneous etching (or sputtering) and deposition processes taking place. Film growth stops when the average yield reaches unity, typically occurring for most elements between 400 and 1400 eV. As the energy increases even further, the etching process takes over (Anders, 2010b).

2.4 Ionized physical vapor deposition

The other characteristic of the film-forming species is the charge. In thermal evaporation the film is formed by the predominantly neutral species. In contrast, techniques such as arc deposition, magnetron sputtering, and pulsed laser deposition are able to generate a significant

ionized fraction in the flux of the film-forming species (this is referred to as the *ionized flux fraction*, IFF) (Helmersson et al., 2006).

Even partially ionized flux of sputtered material allows for direct control over the particle momentum, direction, and flux using electromagnets (Cuomo et al., 1989), creating possibilities for improved film properties and substrate-coating interface engineering (Anders, 2010b,a; Ehiasarian et al., 2007, 2008). In numerous applications, achieving a high level of ionization in the flux of sputtered species is beneficial because the ion flux reaching the substrate significantly affects the quality of the resulting film (Rossnagel and Cuomo, 1988).

The point of operation in an extended SZD that represents the film parameters such as growth rate (negative in a case of etching), temperature and kinetic energy flux, mentioned in Section 2.3, depends on the degree of ionization of the film-forming species, since the average kinetic energy of these species is often defined by the ionized fraction in the deposition flux due to the acceleration in the sheath (see Section 2.8) above the substrate. Ionized sputtered flux may be used to bring regulated ion bombardment of the growing film, introducing an additional control parameter over the deposition process. IFF of a species is defined as:

$$F_{\text{flux}} = \frac{\Gamma_{\text{i}}}{\Gamma_{\text{i}} + \Gamma_{\text{n}}} \tag{2.1}$$

where Γ_{i} is the ion deposition flux, and Γ_{n} is the neutral deposition flux. IFF should be distinguished from the ionization probability of the sputtered atom (α_{t}), introduced in the HiPIMS pathway model by Christie (2005) (see Section 4.2) and the ionized density fraction (or dergee of ionization):

$$\chi = \frac{n_{\text{i}}}{n_{\text{i}} + n_{\text{n}}} \tag{2.2}$$

where n_{i} is the ion density and n_{n} is the neutral gas density. This is discussed further by Butler et al. (2018).

Additionally, the energy of ions that form a film on the substrate can be influenced by applying a bias voltage to the substrate to accelerate these ions. In case of highly ionized flux, there is also the possibility to separate in both time and energy the ions of the working gas and the ions of the film-forming species by applying a synchronized substrate bias in pulsed operation (on pulsed deposition see Section 3.1). There are a number of proposals on how to utilize this technique in HiPIMS (Vavassori et al., 2023; Hubička et al., 2020; Greczynski et al., 2017). The advantage of using synchronized bias is that it reduces the incorporation of the working gas species into the growing film, which might be unwanted since it leads to increased intrinsic stress (Farahani et al., 2025). The challenge is that the bias voltage can drop during the HiPIMS pulse due to the gradual discharge of the internal capacitance of the bias power supply and also due to the voltage drop over the output impedance of the power supply, which is a feature that has to be accounted for (Hubička et al., 2020).

Another important application of the highly ionized fluxes is the possibility of coating high aspect ratio structures, required in IC manufacturing. The motion of neutral atoms is difficult to direct, but ions can be controlled by an electric field, and the ions that traverse the sheath are accelerated towards the substrate and are naturally collimated. Because of this, ions can

penetrate to the base of deep, narrow trenches or vias, whereas neutral flux is more likely to accumulate on the upper sections of sidewalls, resulting in lower film coverage at the trench bottom and potentially lead to void formation. This leads to the observed enhanced coverage by ion flux, including bottom and lower sidewall (Hopwood, 2000b).

Due to the advantages that ionization gives, the term *ionized physical vapor deposition* (IPVD) is used to refer to the deposition techniques which provide a high degree of ionization in the deposition flux, meaning that the flux to a substrate consists of more ions than neutrals $\Gamma_i > \Gamma_n$ (Hopwood, 2000b). In such methods usually a very high plasma density is required. Initially, IPVD techniques were primarily developed to deposit metal layers and diffusion barriers into high aspect ratio trenches or vias for ICs (Hopwood, 1998). However, in recent years, these techniques have been applied to numerous new areas of applications.

In IPVD processes that use magnetron sputtering (see Section 2.7), a secondary discharge located between the cathode target and the substrate can be utilized to generate even denser plasma, leading to high degree of ionization. Secondary discharge can be in the form of inductively coupled plasma assisted magnetron sputtering (ICP-MS) (Yamashita, 1989; Rossnagel and Hopwood, 1993) or microwave amplified magnetron sputtering source (Yoshida, 1992). The ICP-MS discharge is currently widely used in the semiconductor industry (Rossnagel, 2008).

Another way to achieve high ionization fraction in the deposition flux in magnetron sputtering is by delivering a high power unipolar pulse with a low frequency and a low duty cycle to the cathode, where low duty cycle is required to not overheat the target (see Section 3.1).

2.4.1 Quartz crystal microbalance

Since it was evident that the high degree of ionization of film-forming species in magnetron sputtering has a positive impact on the film quality (increased hardness, durability, better control over film growth, etc.), the problem of finding a technique to measure it became important. The first report of an attempt to measure the ionized flux fraction of sputtered species was by Yamashita (1989). They used a retarding potential method to measure the fraction of ionization in sputtered atoms. Knowing that the high energy limit of kinetic energy of positive ions was 25 eV, by using the positive potential of 30 V applied to the control mesh grid and the substrate, most of the ions can be repelled. The author compared the thickness of the deposited film with and without repelling ions using optical absorbance, which gave insight into the fraction of ions in the film-forming material.

IFF in the deposition flux can be measured using the quartz crystal microbalance (QCM), also called an ion meter, which provides the data on the amount of deposited mass by changing its resonance frequency. The first to use this method was demonstrated by Sauerbrey (1959). They showed that the change in the resonance frequency (Δf) is linearly related to the change in mass (Δm):

$$\Delta f = -\frac{2f_0^2}{A\sqrt{\rho_q \mu_q}}\Delta m \tag{2.3}$$

This equation is called Sauerbrey equation, where f_0 is the resonant frequency of the fundamental mode (Hz), Δf is the normalized frequency change (Hz), Δm is the mass change (g), A is the piezoelectrically active crystal area (area between electrodes, cm^2), ρ_q is the density of the quartz crystal ($\rho_q = 2.648\ g/cm^3$), and μ_q is the shear modulus of quartz for AT-cut crystal $\left(\mu_q = 2.947 \times 10^{11}\ g\ cm^{-1}s^{-2}\right)$. The equation is valid when the mass deposited is much smaller than the mass of the crystal itself, the deposited layer is evenly distributed and rigidly attached. The technique was investigated further by Rossnagel and Hopwood (1993). Their configuration enabled rapid and spatially resolved measurement of the IFF on the substrate.

The ion meter can be operated in two different modes:

- measuring only the neutral particle flux. A positive bias ($\sim +40$ V) has to be applied to QCM to prevent any ions from being deposited on the sensor. This gives the mass deposition rate (proportional to the flux) of neutral particles only, M_{neutral}.
- measuring both ion and neutral flux. QCM is connected to ground, and it doesn't discriminate between the types of particles arriving at the sensor, and the total mass deposition rate, M_{total}, is measured.

For each series of varying pulse length/peak current density/voltage/frequency, the total mass deposition rate, M_{total}, including both deposited neutrals and ions, and the mass deposition rate by neutrals alone, M_{neutral}, can be obtained with the QCM. The ionized fraction of the metal flux is obtained using the formula (Hajihoseini et al., 2019)

$$F_{\text{flux}} = \frac{M_{\text{total}} - M_{\text{neutral}}}{M_{\text{neutral}}} = 1 - \frac{\text{dep. rate bias}}{\text{dep. rate ground}} \tag{2.4}$$

assuming that the adhesion of ions and neutrals is the same, this equation is identical to Eq. (2.1). The uncertainty of the method is approximated to be 15% according to the estimation of Kubart et al. (2014).

There are other methods of determining the ionized fraction of the sputtered material, for example optical emission spectroscopy, which gives the fraction of ionization rather than the IFF. The gridded QCM (g-QCM, QCM head measuring the mass deposition rate and a grid retarding field system) measures IFF but gives somewhat different values then gridless QCM (instead of the electron repelling grid a magnetic field is employed to prevent electrons from reaching the crystal top electrode) (Kubart et al., 2014). The difference in the two methods is explored further by Butler et al. (2018).

In the ionization region model (IRM, see Chapter 4), to account for the difference between IFF at the substrate position and within the IR the relative ion to neutral transport parameter $\xi_{\text{ti}}/\xi_{\text{tn}}$ has to be used. The transport parameter relates the deposition flux fractions of the target ions (subscript ti) and neutrals (subscript tn) on a substrate. A value of $\xi_{\text{ti}}/\xi_{\text{tn}} < 1$ indicates a larger spread of metal ions compared to metal neutrals, which is explained by larger scattering cross sections of ions compared to neutrals, and by ions being subjected to electric fields (the details can be found in Rudolph et al. (2021)). Experimentally, these parameters have been determined for HiPIMS of a titanium target in argon to be roughly $\xi_{\text{ti}}/\xi_{\text{tn}} \approx 0.8$ for a

substrate located 3 cm from the target surface and $\xi_{ti}/\xi_{tn} \approx 0.5$ for a substrate located 7 cm from the target surface (Hajihoseini et al., 2022).

2.5 Sputter deposition

At its core, *sputter deposition* is a PVD method utilized to create a thin film or coating (thickness 1 nm – 10 μm) on a substrate for various applications, based on sputtering of a solid target, which is the source of the film-forming material. In sputter deposition a plasma discharge is generated by applying a high negative voltage to a cathode target inside a vacuum chamber filled with working gas at pressures of $\sim$ 1 Pa (Lieberman and Lichtenberg, 2005, p. 539), causing its ionization. The working gas ions are accelerated toward the negatively charged cathode target, resulting in the ejection of target atoms by the bombarding ions. The ejected atoms then propagate through the chamber and deposit onto a substrate, forming a thin film. Examples of sputter deposition are diode sputtering (Vossen and Cuomo, 1978) (see Section 2.6) and later magnetron sputtering (Chapin, 1974; Waits, 1978a) (see Section 2.7). A primitive schematic of the sputtering process is illustrated in Figure 2.5.1.

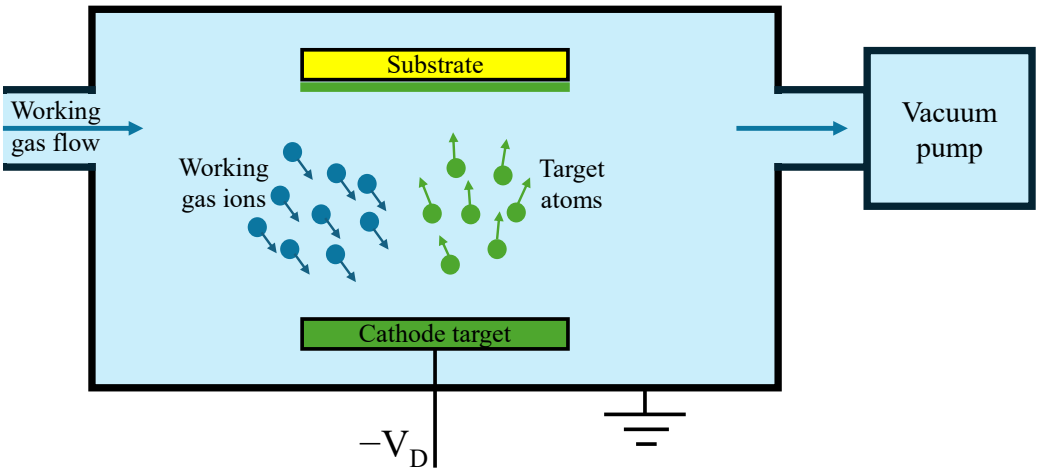

Figure 2.5.1. A simple schematic of a sputter deposition process. Working gas enters the chamber. When a discharge voltage is applied, part of the working gas becomes ionized, and the resulting ions are attracted toward the cathode target, sputtering the target, that emits target atoms. These atoms then travel across the chamber and deposit onto the substrate, forming a thin film.

In sputter deposition, a glow discharge in the working gas frequently serves as the primary source of ions, as it provides a cost-effective source for the first sputtering ions (Gudmundsson et al., 2022). The preferred working gas is a heavy inert gas to enhance the sputtering process with heavy ions. Argon is used the most often because it is relatively inexpensive.

A sputtering discharge is typically utilized in configurations where it occurs between two electrodes, with the cathode and anode placed several centimeters apart. A dc, rf, or some

other periodic voltage waveform is applied between the electrodes. The discharge process sustains itself when the discharge voltage V_D remains above a specific minimum threshold (see Section 2.11).

Arthur W. Wright is widely acknowledged as the founder of vacuum coating technology due to his research on sputtering (Wright, 1877b; Mattox, 2001). Although prior to Wright, several scientists had identified and documented the sputtering phenomenon (Grove, 1852; Plücker, 1858), it seems that no one had explored its potential for thin film deposition applications (Mattox, 2001). Wright stood out as the first researcher to construct equipment for film deposition and to conduct a systematic analysis of various metal films deposited in a vacuum, studying their optical characteristics.

So, sputter deposition has been utilized for the creation of thin films for almost 150 years. During the first five decades cathode sputtering was primarily used to produce reflective coatings on mirrors (Fruth, 1932). With improvements in vacuum technology sputter deposition gave way to thermal evaporation deposition, which became the dominant film deposition method for several decades. However, in the early 1960s, interest in sputter deposition renewed as a method for thin film production. Industry recognized that this technique can be used to deposit a broader range of materials, including alloys, dielectrics, ceramics, compared to evaporation techniques (Baptista et al., 2018).

In summary, in plasma-based sputtering deposition, a plasma discharge is often used as the source of ions for the sputtering process; alternatively, the sputter process is driven by ions originating from an ion source. In both cases, the ions are accelerated in the direction of a solid target, which serves as the source of the material to be deposited on a substrate.

2.6 Diode sputtering

A typical method for producing a plasma involves placing two metal electrodes: a cathode and an anode inside a sealed chamber filled with working gas. To generate a plasma discharge, an energy source is required, for example, a dc power supply. The general schematic of the sputtering chamber is shown in Figure 2.5.1. If the potential applied between the electrodes, where the grounded walls serve as the anode and the negatively biased target is the cathode in this setup, is above the breakdown voltage of the medium (see the Thornton equation, Eq. (2.15)), the discharge is self-sustained ((Chapman, 1980, Chapter 4) and (Gudmundsson, 2020)).

Let us first explore the dc glow discharge. It is formed between the cathode and the anode when a dc voltage is applied as shown schematically in Figure 2.6.1. The largest continuous region between the electrodes is occupied by a bright emission, called a negative glow, which arises from the optical de-excitation produced after the excitation process. Next to the cathode lies a relatively dark region, referred to as Aston dark space. It comes from the sheath that

forms in front of the cathode because the electron density is low. A comparable sheath also forms near the anode, but it is significantly thinner. The positive column is the region in the discharge situated between the negative glow and the anode glow, closer to the anode. Alternating dark and bright regions may form in the positive column as a result of electrons gaining sufficient energy to ionize and excite the gas molecules, which creates a luminous region and depletes the energy of the electrons. They then accelerate while passing through a dark region until they gain enough energy to once more excite and ionize the gas, forming the next striation, and this process repeats. When the electric field is uniform in this region, the striations are clearly visible and are evenly spaced. It is observed that, as the two electrodes are moved closer to each other, the cathode dark space and the negative glow remain unchanged, while the positive column size decreases. This continues until first the positive column and then the Faraday dark space are effectively gone, so that only the negative glow and the dark regions next to each electrode remain (Chapman, 1980, Chapter 4).

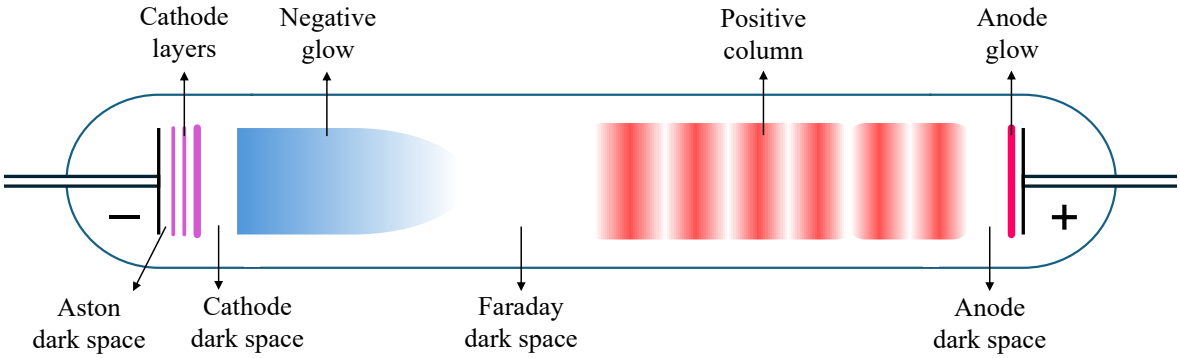

Figure 2.6.1. Schematic illustration of a dc glow discharge showing its various structural regions with the each of them labeled.

In a dc glow discharge, nearly the full applied voltage is droped across the cathode sheath, so the energy of the ions that bombard the cathode is roughly equal to the applied voltage (Chapman, 1980, Chapter 4). The ions generated in the discharge are accelerated through the cathode dark space, the cathode layers, and the Aston dark space toward the cathode, as these regions form the cathode sheath (Gudmundsson and Lundin, 2020). When ions bombard the electrode, they generate secondary electrons (see Section 4.10), which are then accelerated away from the negatively biased cathode and acquire enough energy to excite and ionize the atoms of the working gas. The dc discharge is sustained by this *secondary electron emission*. The dc glow discharge is the simplest source of ions for a sputtering process. In most cases, when the dc discharge is applied as a sputtering source, the cathode is held at a negative bias of 2 – 5 kV, and is electrically insulated from ground, while the grounded chamber serves as the anode.

When a cathode target is bombarded by high-energy ions, atoms of the target material are sputtered. In dc sputtering, the plasma is typically only weakly ionized, with an ionization fraction on the order of 10^{-4}, so the discharge behavior is mainly governed by collisions with neutral atoms. Some of the high-energy secondary electrons can traverse the plasma and are lost either to the substrate or the chamber walls, which reduces the rate of ionization needed

to sustain the discharge. The bombardment by the secondary electrons leads to heating of the substrate. Therefore, the pressure of the working gas must be sufficiently high to ensure that the secondary electrons are not lost to the anode or grounded surfaces before ionizing atoms of the working gas (Buyle et al., 2003). The pressure also needs to allow for the transport of sputtered atoms to the substrate, so dc glow discharge sputtering is only practical within a relatively narrow pressure window of about 2 – 4 Pa (Gudmundsson, 2020).

The dc diode sputtering system can be used only for depositing electrically conductive materials and is therefore primarily suited for sputtering metals. Although it is a relatively simple technique, the dc diode sputter discharge is no longer used in industry, since film deposition rates are too low and the power needed is too high (Gudmundsson, 2020).

2.7 Magnetron sputtering

One of the ways to enhance the sputtering process is to use magnetron assemblies to trap electrons in a static magnetic field near the target surface (on electron motion see Section 2.9). This method was first introduced by Frans M. Penning in 1930s, who invented the Penning trap and the basic magnetron principle (Penning, 1936). *Magnetron sputtering* was firstly described by Penning and Moubis (1940), further developed in the 1960s (Kay, 1963; Gill and Kay, 1965), and took off with the invention of the planar magnetron assembly in the 1970s (Chapin, 1974; Waits, 1978a). The addition of a magnetic trap leads to the formation of an *ionization region* (IR) in the close vicinity of the cathode target – extended pre-sheath where the rate of ionization is the highest, since electron impact ionization is the leading source of ions in such a setup (Gudmundsson, 2020) (see Section 4.6). This results in a higher sputter rate of the negatively biased target by ions. The presence of a magnetic field also has an influence on the electron power absorption in these discharges, which are referred to as ohmic or partially *ohmic discharges* (Anders, 2024) (see Section 2.11). Some of the atoms and ions of the target material escape from the IR into the diffusion region, where they can be deposited onto the substrate, forming a thin film or coating. Films formed in such a manner have excellent uniformity and smoothness over large areas, which is irreplaceable in industrial production.

Figure 2.7.1 shows a schematic representation of a circular planar magnetron setup, illustrating both the cathode target and the magnets mounted below the surface of the target. The magnetic field lines curve above the target surface from a central magnet to an external magnet ring, trapping the electrons.

The magnetron sputtering deposition technique is widely used for the deposition of metallic and compound layers. Over the years, the mainly utilized setups have been driven by either a direct current (dc) or a radio frequency (rf) current or voltage source. Typical operating parameters include the cathode potentials between -300 and -1000 V (Gudmundsson and Lundin, 2020), resulting in electron densities near the substrate of 10^{15} to 10^{17} m^{-3} (Manova

et al., 2010; Helmersson et al., 2006). The plasma density is limited by the thermal load on the target, due to bombardment by ions. By adding magnetic confinement, the working gas pressure could be reduced from ∼4 Pa to ∼1 Pa (with typical working gas pressures 0.1 – 2 Pa), and the discharge voltage lowered significantly ($\sim 300 - 700$ V) compared to what a diode sputter tool requires (∼4 kV) (Gudmundsson et al., 2022).

The magnetron sputtering discharge can be utilized in numerous applications due to the variety of configurations and setups, such as different cathode target dimensions and cathode voltage or discharge current waveforms (Gudmundsson, 2020). The dimensions of the anode in a magnetron sputtering discharge can be large because the chamber walls sometimes act as the anode. Nonetheless, due to deposition on these walls, they typically aren't a good path for current return. In most cases, the anode role is given to a grounded shield surrounding the magnetron target (Gudmundsson, 2020).

Today, magnetron sputtering is widely used in the industrial sector. The main areas for its implementation include:

- hard coatings – often nitrides such as TiN, ZrN, TiCN, TiAlN, CrN, etc: deposition of wear-resistant films as protective coatings on mechanical components and cutting tools (García González et al., 2013; Constantin et al., 2011);
- microelectronics – Al and Cu, and their alloys, Ta, Ti, TiN, TaN, WTi, SiN, SiO_2, etc: deposition of conducting, semiconducting, and dielectric films: deposition of metal or metal compounds as layers for diffusion barriers, adhesion or seed layers, primary conductors, etc. (Rossnagel, 1999; Cai et al., 2015; Song et al., 2025; Kim et al., 2022);
- anti-reflective and reflective coatings – Cu, Al, Cu+Zn, SiO_2, TiO_2, SiN, TiN, etc: to minimize reflection and improve optical transparency, as well as coatings with high reflectivity for mirrors (Changyom et al., 2023; Valluzzi et al., 2018);
- data storage devices – Al_2O_3, Pt-NCs, IGZO, SiO_2, HfO_2, TiN, etc: fabrication of magnetic thin films for hard drive disks (Naqi et al., 2021);
- decorative coatings – ITO, TiO_2, SiO_2, Ta_2O_5, etc: new aesthetic features, color range, and textures (de Arruda et al., 2024);
- solar cells – Si and C composition, SiO_2, Si_2N_3, etc: production of thin-film photovoltaic layers for solar cells (Joung et al., 2012);
- fuel cells – $NiCo_2O_4$, etc: application of protective coatings and catalyst layers (Hammadi and Naji, 2018; Sun et al., 2025).

Over the years, research and improvements in magnetron sputtering technology have progressed, and in modern systems advanced plasma control can be achieved, improving film uniformity and the ability to customize the material properties. Real-time monitoring tools, such as quartz crystal microbalance (QCM) (see Section 2.4.1) and optical emission spectroscopy, enhance process control and help to maintain uniform film quality. By integrating magnetron sputtering with other deposition methods, it is possible to create complex multilay-

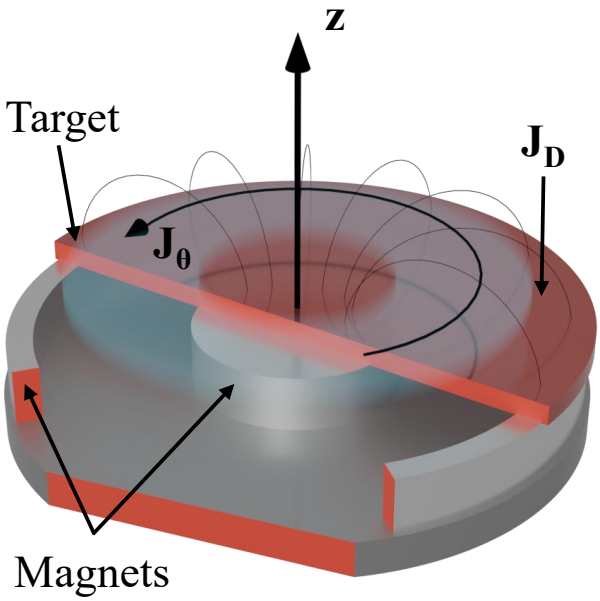

Figure 2.7.1. A schematic view of the cathode target and the magnetron assembly. The target and the magnets are marked with arrows, the glow above the target represents the ionization region. The azimuthal current density $\mathbf{J}_\theta$ *and the axial current density to the target* $\mathbf{J}_\mathrm{D}$ *are shown. The arches above the target surface show the magnetic field lines.*

ered structures with a wider range of properties. The process is environmentally friendly, and efforts are made to further reduce the environmental footprint of sputtering techniques, such as using more sustainable sputtering gasses and creating more energy-efficient power supplies (Merlo and Léonard, 2021).

With magnetron sputtering, the film properties such as the crystalline phase, microstructure, stress, morphology, electrical resistivity, mechanical, and optical properties can be tuned by adjusting the applied power and working gas pressure, while, for example, in thermal evaporation deposition there is no control over the energy distribution of the evaporated species, the resulting film properties, and depositing alloys is challenging (Sarakinos et al., 2010; Samuelsson et al., 2012).

2.7.1 Magnetron configurations

Thornton and Penfold (1978) along with other early researchers of the magnetron sputtering technique utilized cylindrical magnetron configurations with an axial magnetic field. These were either two concentric cylindrical tubes, with the inner cylinder being the cathode target, or an inverted magnetron, with the outer cylinder being the cathode target. Today, it is *planar* magnetron sputtering systems that are commonly used for the deposition of thin films in both laboratory (circular targets) and industrial (rectangular targets) applications. Although for depositing coatings on large areas of architectural glass and display panels, large cylindrical

targets are often used (Gudmundsson and Lundin, 2020). During sputtering, the target rotates and the magnet system is stationary, leading to more uniform erosion on the target surface (see Section 2.9). This is an important technique for coating large glass surfaces used in the architecture and automotive industries, as well as for manufacturing flat panel displays and photovoltaic solar cells (Blondeel et al., 2009).

The electrons are confined close to the cathode target surface by a relatively weak magnetic field **B** (magnetized, see Section 2.9), while the trajectories of the ions are not directly affected (not magnetized, see Section 2.10). Different magnetron sputtering configurations typically use permanent magnets with magnetic induction in the range $\sim$10 – 100 mTesla at the target surface (Hajihoseini, 2020; Krüger et al., 2018).

If the inner and outer magnets have the same magnetic field strength, magnetic field lines are confined around the cathode, making it a balanced magnetron, while in an unbalanced magnetron assembly one magnet is stronger than the other leading to partially open magnetic field lines towards the chamber walls (unbalanced type 1) or substrate holder (unbalanced type 2). Window and Savvides (1986) were first to formally recognize and classify unbalanced magnetron assemblies. The closer the null point is to the target surface, the more easily the electrons can escape, and the more unbalanced the magnetron assembly is. Unbalanced design of type 2 can produce high ion bombardment of the substrate, which is sometimes beneficial. The experimentally measured data used in this thesis is also mostly obtained from type 2 unbalanced magnetron assembly.

2.7.2 Direct current magnetron sputtering

Direct current magnetron sputtering (dcMS) is the most popular and the most simple method of operating the magnetron, where the cathode target is kept at a constant negative voltage. The dc power supply can be operated as a power, current, or voltage source, depending on the regulation method desired (Gudmundsson, 2020).

The typical voltage required for the dcMS process is usually in the range of several hundred volts ($\sim$ -300 – -700 V), based on the target material and the experimental setup. The power density at the target surface is typically $\sim$10 W/cm^2 and the resulting discharge current densities are in the range 4 — 60 mA/cm^2 (Waits, 1978b). Planar dcMS sources are commonly operated using argon as a working gas in the pressure range 0.2 – 4 Pa. The process generates mostly neutral sputtered atoms whose trajectory and energy cannot be easily controlled, and rather low pressures are used to minimize scattering of the sputtered target atoms (Hajihoseini, 2020). Deposition rates in dcMS operation can be up to 10 nm s^{-1} (Gudmundsson et al., 2022). As much as 80% of the power supplied gets converted to heat, requiring efficient cooling systems to prevent the target from melting (Vossen and Cuomo, 1978). In a dcMS system, the primary ionized species are typically those of the working gas, though due to Penning ionization the ions of the target material are detected as well ($\sim$ 2 – 3 %) (Christou and Barber, 2000). Most of the particles that are sputtered have energies around several eV, but the energy distribution function extends up to a few tens of eV (Kadlec et al., 1997).

Although dcMS is an effective coating method for depositing thin metallic films from electrically conducting targets, it faces issues such as low target utilization, and target poisoning during reactive sputtering, which leads to process instabilities, charging of dielectric targets, and lower deposition rates. To address some of these issues, alternative methods like rf magnetron sputtering (Nowicki, 1977), additional ionization with rf coils or microwaves, or enhanced magnetic confinement using a multi-polar magnetic configuration are used. An alternative technique for enhancing the ionization fraction in the deposition flux is the application of high power pulses to the target (Schiller et al., 1993; Helmersson et al., 2006; Alami et al., 2009) (see Section 3.1). The choice of applied target voltage waveform will vary depending on the application. The waveform selection aims to prevent instabilities like arcing, enhance the ionization flux fraction of the sputtered species, enable sputtering from dual targets or sputtering from insulating targets.

2.8 Plasma sheaths

Plasmas are quasi-neutral on scales larger than the Debye length (Lieberman and Lichtenberg, 2005, p. 38):

$$\lambda_{\mathrm{De}} = \left(\frac{\varepsilon_0 T_{\mathrm{e}}}{e n_0} \right)^{1/2} \tag{2.5}$$

where ε_0 is the vacuum permittivity, T_{e} is the electron temperature, and $n_0 = n_{\mathrm{e}} = n_{\mathrm{i}}$ is the plasma density, and e is the elementary charge.

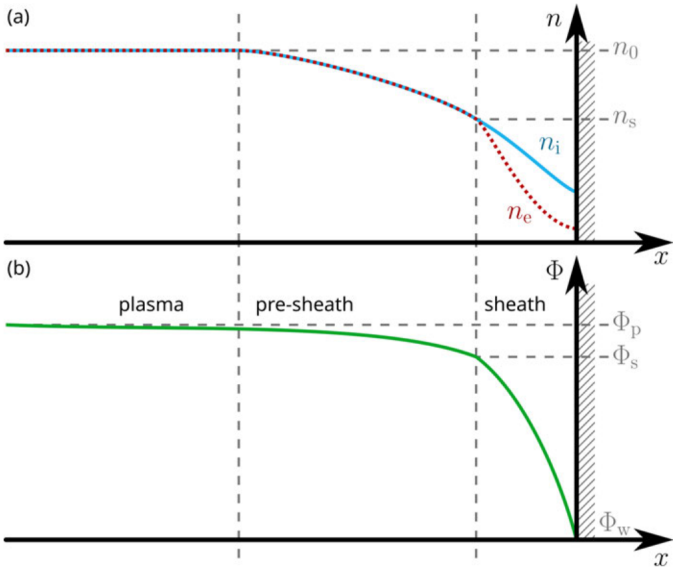

Figure 2.8.1. Qualitative behavior of sheath and pre-sheath in contact with a wall. (a) shows the ion n_{i} and electron n_{e} densities, and (b) shows the plasma potential. Reprinted from Fischer (2025), Copyright (2025).

Quasi-neutrality can only break within the sheath region that forms between the plasma and an adjacent boundary, for example, the chamber walls. This occurs because electrons are much more mobile than ions, so they escape from the plasma more quickly, leaving it with a net positive charge. In practice, the sheath thickness is typically observed to be around $5\lambda_{\mathrm{De}}$ (Chen and Chang, 2003, p. 5). Within the sheath, the ion density exceeds the electron density, i.e., $n_{\mathrm{i}} > n_{\mathrm{e}}$. The wall maintains a potential that is negative with respect to the plasma, creating a Coulomb barrier that repels electrons. This condition is required because electrons, without being repelled by this "sheath drop", would leave the plasma, causing it to become even more positively charged. In addition, a transition region, or pre-sheath (also see Section 4.6), must form between the quasi-neutral plasma and the non-neutral sheath to preserve continuity of the ion flux, resulting in an ion speed at the plasma–sheath boundary referred to as the Bohm velocity u_{B} (Lieberman and Lichtenberg, 2005, p. 169):

$$u_{\mathrm{B}} = \left(\frac{e\,\mathrm{T_e}}{M} \right)^{1/2} \tag{2.6}$$

An illustration of the ion and electron densities as well as the electric potential is shown in Figure 2.8.1.

2.9 Electron motion

The basic equation of motion for an electron is the Lorenz equation:

$$\frac{d\mathbf{v}_{\mathrm{e}}}{dt} = \frac{e}{m_{\mathrm{e}}} \left(\mathbf{E} + \mathbf{v}_{\mathrm{e}} \times \mathbf{B} \right) \tag{2.7}$$

where e is the elementary charge, m_{e} is the mass of electron.

An electron in the discharge has a complex trajectory as a result of the magnetic field. Initially, electrons travel in *gyromotion* paths around a magnetic field line, simultaneously oscillating back and forth along the line (occurring on a time scale of ∼MHz).

Over extended time intervals (∼kHz), electrons experience several other drifts, including the drift $\mathbf{E} \times \mathbf{B}$ from the applied target voltage. As a result, electrons move with a $\mathbf{E} \times \mathbf{B}$ drift $\mathbf{J}_{\theta}$ along a torus (for planar magnetron) in the azimuthal direction, which is known as a Hall drift (Bradley et al., 2001; Machura et al., 2014):

$$\mathbf{v}_{\mathbf{E}\times\mathbf{B}} = \frac{\mathbf{E} \times \mathbf{B}}{B^2} \tag{2.8}$$

as illustrated in Figure 2.7.1. The drift in the HiPIMS discharges $\mathbf{E} \times \mathbf{B}$ is slightly faster than in the dcMS (Vašina et al., 2008).

The B field is not uniform, so there is also a ∇B drift and the drift due to the curvature of the magnetic field lines. These drift movements are oriented in the same azimuthal direction,

leading to an eventual electron motion around the target's center with speeds ranging from 10^4 to 10^5 m/s (Bradley et al., 2001; Rauch and Anders, 2013; Dubois et al., 2022). The net result of this motion in the planar magnetron is a complicated path of the electron involving the gyration with changing radius around the magnetic field lines while bouncing off the target and moving along the torus of the glowing IR, schematically illustrated in Figure 2.9.1. Among the drifts, $\mathbf{E} \times \mathbf{B}$ is the dominant one.

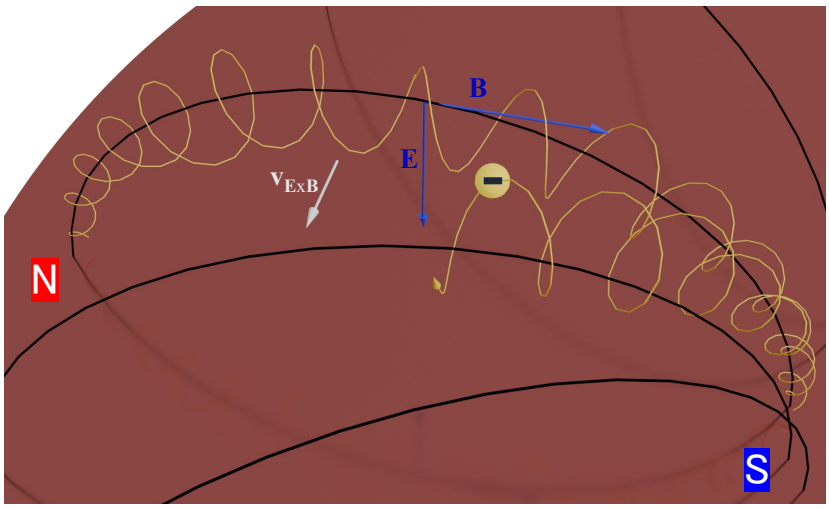

Figure 2.9.1. A schematic illustration of motion of the electron in magnetic trap above the cathode target surface. The path of electron (in yellow) is a net result of gyromotion along the magnetic field lines (in black) with changing radius, bouncing motion due to gradient of magnetic field **B** *and sheath presence, and* $\mathbf{E} \times \mathbf{B}$ *drift along the racetrack. The inner magnet has* ***S****, and outer magnet has* ***N*** *polarities.*

Apart from azimuthal drift, plasma diffuses outwards from the target toward the substrate. In a homogeneous plasma, the magnetic field lines are equipotentials, but during the dynamic and non-uniform HiPIMS pulses, this is not necessarily the case, especially with high-energy secondary electrons that have been accelerated across the sheath. Due to the increase in the plasma density, such as in the HiPIMS operation regime, the plasma electrons increase their capacity to escape from the magnetic trap, a phenomenon called de-confinement. Another mechanism that seems to play an important role is likely the Coulomb interaction between electrons and ions, proposed by Vašina et al. (2008). The observed cross-**B** diffusion in plasmas exceeds the rate predicted by classical transport (Rossnagel and Kaufman, 1987), and it is commonly characterized using the semi-empirical Bohm diffusion formula (Bohm et al., 1949):

$$D_{\mathrm{B}} = \frac{1}{16} \frac{k_{\mathrm{B}} T_{\mathrm{e}}}{eB} \tag{2.9}$$

However, the electron cross-**B** transport in a HiPIMS discharge is significantly faster than what is classically predicted, and it even exceeds the rate of Bohm diffusion (Lundin et al., 2011; Brenning et al., 2009). Brenning et al. (2009) found that the diffusion coefficient is approximately five times larger than the value predicted by Eq. (2.9). The anomalous transport can be attributed to plasma instabilities (Lundin et al., 2008) as well as spokes (Brenning et al., 2013; Anders et al., 2012).

Although only the electrons are *magnetized*, both electrons and ions remain confined, since any electron distribution defined by the magnetic field lines generates negative space charge that lead to the confinement of ions as well. The ionization rate is enhanced by the higher electron density because of electron confinement by a magnetic field, allowing the discharge voltage to be reduced compared to that in a diode sputtering. For the same reason the mean free path for ionization can be longer and the working gas pressure can be decreased, increasing the deposition rate substantially, compared to non-magnetized dc diode sputtering (Waits, 1978b; Chapin, 1974) (see Section 2.6). The observable result of a magnetic confinement of electrons is the race track on the cathode target from the sputter erosion. For a planar circular magnetron sputtering target the race track has a circular groove-like erosion pattern. The target cannot be fully utilized because of this and needs to be replaced in time, leading to target utilization in the range of 20 – 40 % (Iseki, 2009). This problem has been largely fixed by using rotating magnet assemblies, which significantly increase target utilization and enhance the uniformity of the deposited film thickness. A completely flat erosion magnetron cathode has been developed for planar magnetron sputtering using a rotating asymmetrical yoke magnet with target utilization of up to 77% (Iseki, 2010).

2.10 Ion motion

The ions of the working gas bombard the cathode target, sputtering the target atoms, and releasing secondary electrons (unlike singly ionized metal target atoms). For the case with zero **E** field, as in the pulse afterglow after the power is switched off (see Section 3.3), the ions can be treated as diffused through the gas in the deposition chamber (Lundin et al., 2020). The diffusion law, called the Fick law, relates the flux Γ to the density gradient:

$$\Gamma = -D\nabla n \tag{2.10}$$

where n is the density of the surrounding gas and D is the diffusion constant:

$$D = \frac{\pi}{8}\lambda^2 \nu_{\mathrm{m}} \tag{2.11}$$

where $\lambda = \bar{\mathrm{v}}/\nu_{\mathrm{m}} = (8kT/\pi m)^{1/2}/\nu_{\mathrm{m}}$ is the mean free path, $\bar{\mathrm{v}}$ is the mean speed, and ν_{m} is the momentum transfer frequency.

The sputtering of target atoms originates from collision cascades of ions that impinge on a target (see Figure 2.10.1) and eject atoms from it into the ionization region or bulk plasma with substantial energies (Stuart et al., 1969) that follow the Thompson energy distribution (Thompson, 1968, 1987; Sigmund, 1969), sometimes referred to as the Sigmund-Thompson distribution function when written in the following form:

$$\frac{d\Gamma_{\mathrm{sput}}}{d\mathscr{E}_{\mathrm{t}}} \propto \frac{\mathscr{E}_{\mathrm{t}}}{(\mathscr{E}_{\mathrm{t}} + \mathscr{E}_{\mathrm{sb}})^{3-2m}} \tag{2.12}$$

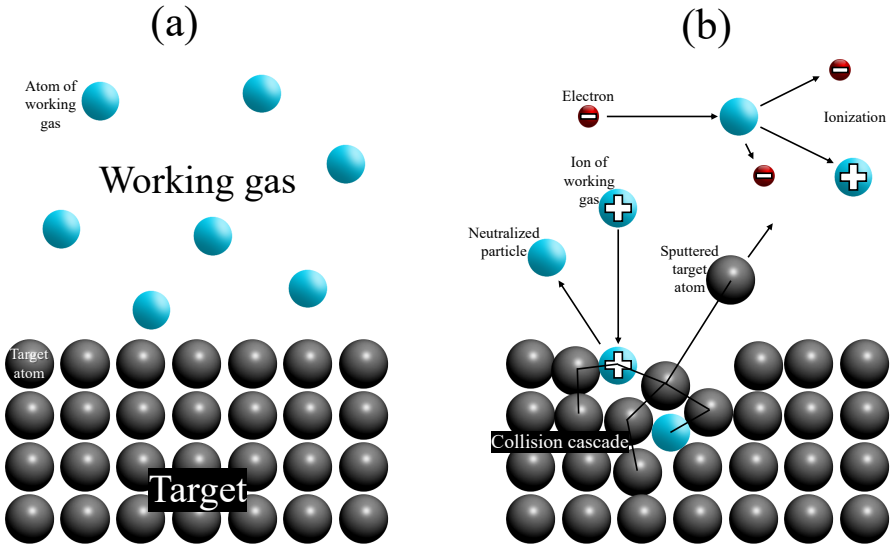

Figure 2.10.1. Sputtering on the atomic level. (a) The target surface and the working gas above with no voltage applied to the target. (b) The target surface when the voltage is on: the discharge in the working gas creates ions and free electrons, the ions are accelerated in the cathode sheath and have enough energy to emit secondary electrons (not shown) and sputter target atoms (if enough discharge voltage is applied) creating collision cascade in the target; electrons trapped by the magnetic field ionize both atoms of the working gas as well as sputtered target species.

where Γ_{sput} is the flux of the sputtered target atoms, $\mathscr{E}_{\text{t}}$ is the kinetic energy of the target species, $\mathscr{E}_{\text{sb}}$ is the surface binding energy of the target material, and m is a parameter from the interaction potential $V(r) \propto d^{-m}$ (Hofer, 1991). The energy distribution as described by this equation has a peak at roughly $\frac{1}{2}\mathscr{E}_{\text{sb}}$, which then gradually decreases toward higher energies according to $\propto \mathscr{E}_{\text{t}}^{-2}$. The Sigmund–Thompson energy distribution function slightly overestimates the probability of sputter ejection of energetic atoms. Stepanova and Dew (2004), introduced a modified distribution function, where a cutoff energy $\mathscr{E}_{\text{max}}$ was added to better reflect the experimentally measured energy spectra (Stepanova and Dew, 2001):

$$\frac{d\Gamma_{\text{sput}}}{d\mathscr{E}_{\text{t}}} = \frac{\mathscr{E}_{\text{t}}}{(\mathscr{E}_{\text{t}} + \mathscr{E}_{\text{sb}})^{3-2m}} \left[1 - \left(\frac{\mathscr{E}_{\text{t}} + \mathscr{E}_{\text{sb}}}{\mathscr{E}_{\text{max}} + \mathscr{E}_{\text{t}}}\right)^{n}\right] \tag{2.13}$$

Typical values of the constants are $n = 1$, $m = 0.2$ (Stepanova and Dew, 2004), and $\mathscr{E}_{\text{max}} = 20$ eV (Lundin et al., 2013). Since $\mathscr{E}_{\text{sb}}$ is typically in the range 3–6 eV, most sputtered atoms are emitted with energy in the range 1.5 -– 3 eV (Gudmundsson et al., 2022).

The angular distribution of the sputtered species is proportional to $\cos\theta$ (Thompson, 1981):

$$\frac{d\Gamma_{\text{sput}}}{d\theta} \propto \cos\theta \tag{2.14}$$

where θ is the incident angle.

The scattered primary incident particle and the recoiled target atom may undergo further collisions, and collision cascades can develop (see Figure 2.10.1). For discharge voltages

typically applied, the incident species has sufficient energy to break bonds and change the position of atoms within the target. The target species that are close to the surface can leave the target: when the target species gain enough energy to overcome the surface binding energy $\mathscr{E}_{\mathrm{sb}}$ they can be sputtered. This process may occur due to a single collision (direct sputtering) or as a result of multiple collisions (collision cascade) (see Section 4.9). The primary species that bombard the target can either leave the target (scattered species) or they can become implanted in the target. As the sputter process progresses the implanted primary particles can be sputtered or they can diffuse out of the target (Gudmundsson et al., 2022).

The ion energy distribution function (IEDF) of the HiPIMS discharge exhibits high-energy tails, with measured energies sometimes exceeding 100 eV (Bohlmark et al., 2006; Hecimovic et al., 2008). These ions can be beneficial for the process, yet the mechanism by which they accelerate remains not fully understood. Lundin et al. (2008) propose that the energization of the ions is linked to the anomalous resistivity effect, which enhances electron transport across the magnetic field lines. Experimental data supported this hypothesis, as a mass spectrometer showed a significantly more distinct high-energy tail in the IEDF in the predicted azimuthal direction (Lundin et al., 2020). Another mechanism proposed to contribute to the production of high-energy ions in the plasma is the occurrence of plasma instabilities. These include non-stationary double-layer potential structures linked to rotating spokes (see Section 4.1), which accelerate ions within the ionization region close to the target surface away from the target (Palmucci et al., 2013; Panjan et al., 2014).

2.11 Ohmic heating

The discussion of the energization mechanism in magnetron sputtering discharges by the energy gained from the electron impact ionization requires the introduction of the Thornton equation. In its original form (Thornton, 1978), it gives the minimum discharge voltage to sustain a discharge by secondary electrons as:

$$V_{\mathrm{D}} \geqslant V_{\mathrm{Th}} = \frac{\mathscr{E}_{\mathrm{c}}}{\gamma_{\mathrm{SE,eff}} e} \tag{2.15}$$

where $\mathscr{E}_{\mathrm{c}}$ is the average collisional energy loss per ion– electron pair created (see Section 4.8), and $\gamma_{\mathrm{SE,eff}}$ is the effective secondary electron emission yield per ion hitting the target (see Section 4.10).

However, in experimental setups, magnetron sputtering discharges can operate at even lower voltages, which means that there are additional means of sustaining the discharge. Improvements to the Thornton equation have been incorporated to include more energization aspects, such as ionization in the sheath region and the depletion of electrons before the ionization. The effective $\gamma_{\mathrm{SE,eff}}$ differs from the secondary electron emission yield γ_{SE} due to ionization in the sheath with a probability m, and recapture of the secondary electron at the target with a

probability r. The new formula, as given by Depla et al. (2009) is:

$$V_{\mathrm{D}} = \frac{\mathscr{E}_{\mathrm{c}}}{\varepsilon_{\mathrm{e}}\beta_{\mathrm{t}}m(1-r)\gamma_{\mathrm{SE}}} \tag{2.16}$$

where β_{t} is the ion back-attraction probability and ε_{e} is the fraction of the secondary electrons that cause ionization before they are lost from the system. However, in Eq. (2.16), the basic assumption remains that the sheath energization of electrons is the main energy source.

Plasma chemical model calculations that include the energy balance (Brenning et al., 2012) have demonstrated that there is a motivation to re-evaluate the classical description of electron energization. The reason is that electric fields extend into the plasma and add the possibility of direct *ohmic heating*. It was demonstrated by Brenning et al. (2012) that in magnetron sputtering discharges, especially in HiPIMS, this can be much more energy efficient compared to sheath energization. One significant finding is that the percentage of ohmic heating increases with increasing applied power. This trend was attributed to a higher degree of self-sputtering with higher discharge power. The consequence of ohmic heating is that magnetron sputtering discharges can burn far below the proposed lower voltage limit V_{Th} than the Thornton equation (Eq. (2.15)) would suggest (Huo et al., 2013).

Subsequent probe measurements on both dcMS (Mishra et al., 2010) and HiPIMS (Mishra et al., 2011) systems have shown that as much as 20% of the discharge voltage V_{D} applied can be dropped within the plasma outside the cathode sheath. This region is commonly referred to as the extended pre-sheath, or the IR (on the IR in the IRM see Section 4.6). The voltage applied or the discharge voltage can be written as:

$$V_{\mathrm{D}} = V_{\mathrm{SH}} + V_{\mathrm{IR}} \tag{2.17}$$

where V_{SH} is the voltage drop across the sheath and V_{IR} is the voltage drop across the IR, or the pre-sheath (see Figure 2.11.1).

Except at the IR center (distance from the center of the generating arc to the axis of revolution of the torus, $(r_{\mathrm{c1}} + r_{\mathrm{c1}})/2$, see Section 4.6), seen as a projection of the racetrack center, the magnetic field lines are inclined relative to the target surface. Consequently, the majority of electrons generated from secondary emission ("hot" electrons, $\mathrm{e_h}$) are able to cross the cathode sheath, despite being constrained by the magnetic field lines. As they cross the sheath, they acquire the energy corresponding to V_{SH}. Since the mean free path of a secondary electron is much longer than the thickness of the cathode sheath (collisionless sheath), the energy distribution of "hot" electrons is non-Maxwellian as it depends mostly on the voltage across the sheath V_{SH}.

Ohmic heating can be understood as the average energy gain of the electron in the created ion-electron pairs, that is moving across a potential V_{IR}, which is a fraction f of the discharge potential V_{D} (Brenning et al., 2016):

$$V_{\mathrm{IR}} = fV_{\mathrm{D}} \tag{2.18}$$

while experiencing the complicated bouncing motion described in Section 2.9.

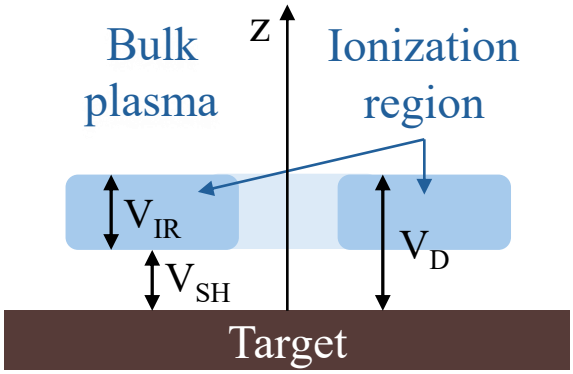

Figure 2.11.1. The ionization region, side view. The applied discharge voltage V_D drops across the sheath V_{SH} and the pre-sheath (ionization region) V_{IR}, so that $V_D = V_{SH} + V_{IR}$.

Ohmic heating can also be described as the electron energization due to $\mathbf{J}_e \cdot \mathbf{E} > 0$ in the plasma outside the sheath, where $\mathbf{J}_e$ is the electron current density and $\mathbf{E}$ is electric field (Brenning et al., 2016). The potential across the sheath varies between the center of the racetrack and the edge of the racetrack because the electric equipotential surfaces are parallel to the magnetic field lines and arc in the same way (Depla et al., 2009). In such configuration with a planar magnetron assembly, ohmic heating is related to the movement of electrons across the magnetic field lines. This process is significantly slower compared to crossing the sheath due to the sheath potential, and is constrained by the electrons' cross-**B** mobility:

$$\mu_{e,perp} = \frac{\mu_e}{1 + \omega_{ge}^2 \tau_c^2} \tag{2.19}$$

where $\mu_e = e\tau_c/m_e$ is the mobility of the electrons in the absence of a magnetic field, $\omega_{ge} = eB/m_e$ is the electron (angular) gyro frequency and τ_c is the effective collision time of the electron, including anomalous transport.

To conclude, in contrast to non-magnetized dc diode sputtering discharges, mainly sustained by ion-induced secondary electron emission that are accelerated within the cathode sheath (Gudmundsson, 2020), the presence of a magnetic field introduces a potential drop V_{IR} across the IR. This potential allows for ohmic heating of the electrons in the IR (Brenning et al., 2016). In dcMS discharges, ohmic heating represents a notable portion of the electron power absorption. It is also considered the primary mechanism for electron power absorption in HiPIMS discharges (Huo et al., 2013; Brenning et al., 2016; Huo et al., 2017). For discharges with a higher fraction of ohmic heating over total electron heating, which includes ohmic heating and sheath acceleration, the same discharge current can be maintained at a lower discharge voltage, as the discharge becomes more energy efficient because sheath heating is associated with a large ion current to the target. The ion current due to the electric field in the IR is much lower (Rudolph et al., 2022; Gudmundsson et al., 2022).

2.12 Plasma chemistry

A magnetron sputtering discharge consists of electrons, ions, neutral atoms, molecules, and photons. There are many interactions between all of these species, but some of them are more significant than others. At low pressure, the number of collisions is low, and the energy transfer between species is inefficient. While at high pressure, more collisions occur between the different plasma species, resulting in more uniform energy distribution of the species.

The primary parameter that describes an interaction between particles is the cross section σ of a reaction or collision, which depends, among other factors, on the relative velocity of the particles involved. The probability of interaction between species can be described using the mean free path λ, which is the average distance traveled by a particle between collisions:

$$\lambda = \frac{1}{n\sigma} \tag{2.20}$$

where n is the density of the species, and σ is the cross section of the collision.

Collisions can be elastic or inelastic, and particles may change their energy, momentum, become ionized/excited, or recombine. To describe the kinetic energy transfer in elastic collisions, the transfer parameter $\Lambda = 4M_1M_2/(M_1+M_2)^2$ can be used (where M_1 and M_2 stands for masses of particles colliding). From it we can see that the kinetic energy transfer between electrons and heavy species is negligible. In inelastic collisions the kinetic energy is not conserved and such reactions include ionization, excitation, and charge transfer. In molecular gas, other significant processes can take place, such as vibrational and rotational excitation, dissociation, dissociative recombination, and attachment and detachment when negative ions are present.

In a magnetron sputtering discharge, the plasma consists of atoms and ions of the working gas, as well as atoms ejected from the target and their ions, together with free electrons. Atoms (as well as ions) originating from both components – the working gas and the sputtered target material – may be in excited states, some of which are metastable.

As an example, the list of reactions considered in the IRM for HiPIMS discharges with a chromium target is given in Table 2.12.1. The rate coefficients for argon reactions are taken from Rudolph et al. (2021), and for chromium reactions from Barynova et al. (2026). The rate coefficients for electron impact ionization are determined by integrating over a cross section assuming a Maxwellian electron energy distribution function (EEDF). For the primary electron population they are fitted for T_e ranging from 1 to 7 eV, while for the secondary electron population, the fit is in range 200 – 1000 eV (for more on electron populations and EEDF, see Section 4.7.2). For electron impact ionization of the chromium atom, the cross sections recommended by Lennon et al. (1988) (< 15 eV) and Nelson (1976) (> 15 eV) are used. The cross sections for electron impact ionization of the Cr^+ ion to produce the doubly ionized Cr^{2+} was measured by Man et al. (1987), while the cross sections for electron impact ionization of the neutral chromium atom to form the doubly ionized Cr^{2+} was measured by Nelson (1976). The rate coefficients for the charge exchange process between Ar^+ and Cr, and

for Penning ionization are taken from Bogaerts et al. (2007). The rate coefficients for electron impact excitation into the 4s levels of the argon atom are determined using cross sections from the IST-Lisbon collection on LXCat (www.lxcat.net/ist-lisbon). The ionization rate coefficients for electron impact from the metastable states are derived from the cross sections measured by Dixon et al. (1973). The rate coefficients for electron impact de-excitation of the metastable levels are determined using the principle of detailed balancing (see Section 2.12.1). It should be noted that the recombination cross section is not included, as it is a three-body collision, and the likelihood of it is negligible in the ionization region (as opposed to on the target and wall surfaces, which the IRM does not address) (Lieberman and Lichtenberg, 2005, p. 298).

Table 2.12.1. The reactions and rate coefficients used in the IRM for discharges with Cr target. The rate coefficients are calculated assuming a Maxwellian electron energy distribution function and fit in the range $T_e = 1-7$ eV for primary electrons and 200 – 1000 eV for secondary electrons.

Reaction	Threshold [eV]	Rate coefficient [m^3/s]
$e + Ar(3p^6) \longrightarrow Ar^+ + e + e$	15.76	$2.34\times10^{-14}\ T_e^{0.59}\exp(-17.44/T_e)$ $8\times10^{-14}\ T_e^{0.16}\exp(-27.53/T_e)$
$e + Ar(3p^6) \longrightarrow Ar(4s[3/2]_2) + e$	11.548	$1.617\times10^{-14}T_e^{-0.8238}\exp(-14.1256/T_e)$ $1.1397\times10^{-22}T_e^2 - 1.8975\times10^{-19}T_e + 8.7910\times10^{-17}$
$e + Ar(3p^6) \longrightarrow Ar(4s'[1/2]_0) + e$	11.723	$2.86\times10^{-15}T_e^{-0.8572}\exp(-14.6219/T_e)$ $1.8045\times10^{-23}T_e^2 - 2.9825\times10^{-20}T_e + 1.357\times10^{-17}$
$e + Ar(4s[3/2]_2) \longrightarrow Ar(3p^6) + e$		$3.23\times10^{-15}T_e^{-0.8238}\exp(-2.578/T_e)$ $(1.1397\times10^{-22}T_e^2 - 1.8975\times10^{-19}T_e + 8.7910\times10^{-17})/5$
$e + Ar(4s'[1/2]_0) \longrightarrow Ar(3p^6) + e$		$2.86\times10^{-15}T_e^{-0.8572}\exp(-2.8989/T_e)$ $1.8045\times10^{-23}T_e^2 - 2.9825\times10^{-20}T_e + 1.357\times10^{-17}$
$e + Ar(4s'[1/2]_0) \longrightarrow Ar^+ + 2e$	4.21	$1.14356\times10^{-13}T_e^{0.2548}\exp(-4.4005/T_e)$ $1.5213\times10^{-19}T_e^2 - 2.9599\times10^{-16}T_e + 1.8155\times10^{-13}$
$e + Ar(4s[3/2]_2) \longrightarrow Ar^+ + 2e$	4.21	$1.14356\times10^{-13}T_e^{0.2548}\exp(-4.4005/T_e)$ $1.5213\times10^{-19}T_e^2 - 2.9599\times10^{-16}T_e + 1.8155\times10^{-13}$
$e + Ar^+ \longrightarrow Ar^{2+} + 2e$	27.63	$8.6365\times10^{-15}T_e^{0.6746}\exp(-24.3019/T_e)$ $5.22\times10^{-14} - 4.943\times10^{-17}T_e$
$e + Ar \longrightarrow Ar^{2+} + 3e$		- $6.169\times10^{-15} - 1.6316\times10^{-17}T_e$
$e + Cr \rightarrow Cr^+ + e$	6.7666	$8.95\times10^{-14}T_e^{0.4682}\exp(-7.0786/T_e)$ $4.0586\times10^{-13} - 2.6729\times10^{-16}\times T_e$
$e + Cr^+ \rightarrow Cr^{2+} + 2e$	16.4857	$9.2132\times10^{-15}T_e^{0.5702}\exp(-14.3882/T_e)$ $9.2457\times10^{-14} - 5.7450\times10^{-17}\times T_e$
$e + Cr \rightarrow Cr^{2+} + 3e$	23.25	$2.9309\times10^{-16}T_e^{1.2029}\exp(-20.8886/T_e)$ $5.6848\times10^{-14} - 3.6485\times10^{-17}\times T_e$
$Ar^+ + Cr \rightarrow Ar + Cr^+$		6.2×10^{-16}
$Ar(4s'[1/2]_0) + Cr \rightarrow Ar + Cr^+ + e$		2.38×10^{-16}
$Ar(4s[3/2]_2) + Cr \rightarrow Ar + Cr^+ + e$		2.38×10^{-16}

2.12.1 Detailed balancing

According to the principle of detailed balancing, which expresses the time-reversible nature of the equations of motion for a collision, the cross sections and rate constants for both forward (endothermic with threshold energy $\mathscr{E}_{\text{th}}$ and cross section $\sigma(\text{v})$) and reverse ($\sigma'(\text{v}')$) reactions are related (Lieberman and Lichtenberg, 2005, p. 265). An example of such reactions can be the excitation of ground state argon $\text{Ar}(3\text{p}^6)$ to the metastable state $\text{Ar}(4\text{s}[3/2]_2)$ in the electron impact:

$$\text{A} + \text{B} \longrightarrow \text{C} + \text{D} \tag{2.21}$$

$$\text{e} + \text{Ar}(3\text{p}^6) \longrightarrow \text{e} + \text{Ar}(4\text{s}[3/2]_2) \tag{2.22}$$

and the reverse reaction of the electron impact de-excitation of the metastable state:

$$\text{C} + \text{D} \longrightarrow \text{A} + \text{B} \tag{2.23}$$

$$\text{e} + \text{Ar}(4\text{s}[3/2]_2) \longrightarrow \text{e} + \text{Ar}(3\text{p}^6) \tag{2.24}$$

Then $\sigma(\text{v})$ and $\sigma'(\text{v}')$ are connected by:

$$m^2 g_{\text{A}} g_{\text{B}} \text{v}^2 \sigma(v) = m'^2 g_{\text{C}} g_{\text{D}} \text{v}'^2 \sigma'\left(\text{v}'\right) \tag{2.25}$$

where g stands for degeneracy of the energy level of a species: 2 for free electron, 1 for $\text{Ar}(3\text{p}^6)$ and $\text{Ar}(4\text{s}[3/2]_2)$. The variables m and m' are the reduced masses for left and right parts of the forward reaction (Eq. (2.22)), in this case $m = m' \approx m_{\text{Ar}}$ can be assumed. In general form, m and m' connected by:

$$\frac{1}{2} m \text{v}^2 = \frac{1}{2} m' \text{v}'^2 + e\mathscr{E}_{\text{th}} \tag{2.26}$$

After integration over a Maxwellian velocity distribution, the ratio of rate coefficients for forward ($K(T)$) and reverse ($K'(T)$) reactions can be expressed as:

$$\frac{K(T)}{K'(T)} = \left(\frac{m'}{m}\right)^{3/2} \frac{g_{\text{C}} g_{\text{D}}}{g_{\text{A}} g_{\text{B}}} \text{e}^{-\mathscr{E}_{\text{th}}/T} \tag{2.27}$$

The statistical weights in the above equation are determined for thermal equilibrium, the ratio of statistical weights is the same for a system that is not in thermal equilibrium. The only assumption required is that the velocity distribution is Maxwellian (Lieberman and Lichtenberg, 2005, p. 267).

CHAPTER 3

HIGH POWER IMPULSE MAGNETRON SPUTTERING

3.1 Pulsed power deposition

To increase the energy and fraction of ions in the flux of film-forming species (the advantages of which are mentioned in Sections 2.3 and 2.4) higher power can be applied to the cathode target (Anders, 2010b; Helmersson et al., 2006). Unfortunately, this leads to heating of the target to a point where the cooling rate becomes insufficient, since rather than increasing the ionization rate, most of the power dissipates into heating the target. This could lead to a target melting and potentially disrupting the setup or demagnetization of the static magnets that are responsible for the electron trap, if the temperature rises close to the Curie point. A solution to this is to apply the high power in pulses with a low duty cycle, keeping the average power similar to dcMS (0.05 kW/cm^2 is a typical upper limit for target damage) (Hála et al., 2012).

Different waveforms of the cathode target voltage can be used based on the specific application. Pulsing the voltage may also increase the ionized fraction of the sputtered species, and allow sputtering from two targets and insulating materials (Gudmundsson, 2020). The goal of the different pulsing schemes is usually to achieve better control over the process and therefore the properties of the deposited films.

There are several periodic waveforms that are applied in magnetron sputtering techniques, such as:

- sinusoidal (radio frequency):
  - rf generator (Nowicki, 1977);
- unipolar pulsed:
  - square voltage pulse generators: high power pulsed magnetron sputtering (HPPMS), including high power impulse magnetron sputtering (HiPIMS), and deep oscillation magnetron sputtering (DOMS) (Kouznetsov et al., 1999; Hubička et al., 2020; Ferreira et al., 2014);

  - custom-shaped voltage generators producing longer pulses of lower amplitude: modulated pulse power magnetron sputtering (MPPMS) (Hála et al., 2012);

- symmetric bipolar or mid-frequency ac pulsed (Este and Westwood, 1988; Scherer et al., 1992):

- asymmetric bipolar pulsed (Sellers, 1998).

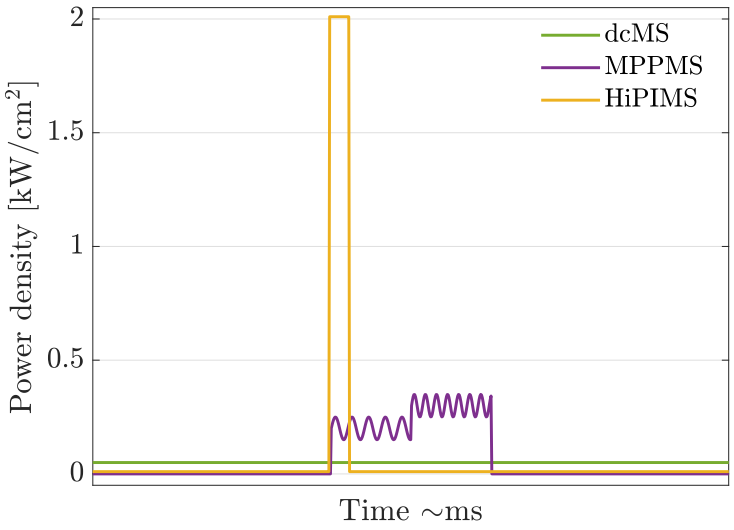

Figure 3.1.1. Schematic representation of the power delivery for dcMS, MPPMS and HiPIMS when operated at the same average power. After Hála et al. (2012)

The pulsed magnetron sputtering method benefits from using the same equipment as traditional magnetron sputtering, with the exception of the power supply. There are a few variations of the HPPMS technique. In *high power impulse magnetron sputtering* (HiPIMS) a pulse of very high amplitude, an impulse, is applied to the cathode and a long pause exists between the pulses, with the duty cycle ∼1 %. In order to distinguish this technique from other pulsed magnetron processes Anders (2011) defines HiPIMS as pulsed magnetron sputtering where the peak power exceeds the time-averaged power by two orders of magnitude.

Alternative methods involve adjusting the pulse so that during its early phase, which lasts up to a few hundred microseconds, the power level is moderate. This phase is then followed by a high power pulse lasting from several hundred microseconds up to a millisecond. The resulting pulse is referred to as a macro-pulse. The macro-pulse can be up to 3 ms long, and the repetition frequencies are in the lower end of HiPIMS operation. The macro-pulse is composed of a train of shorter micro-pulses that appear with frequencies in the range of several tens of kHz. This technique is termed modulated pulse power magnetron sputtering (MPPMS) (Musson and Elsayed-Ali, 2024). The duration of "on" and "off" periods of micro-pulses, which usually extend to several tens of microseconds, along with their frequency, can be modified within the macro-pulse. By using this method, the micro-pulse frequency, along with the "on" and "off" durations, target voltage, and discharge current waveforms can

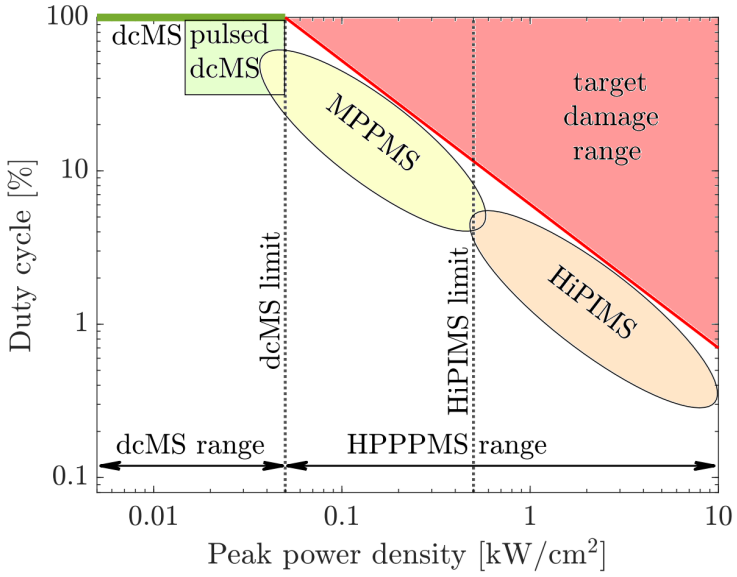

Figure 3.1.2. Schematic representation of the peak power density at the target versus the duty cycle. For dc operation 0.05 kW/cm^2 is a typical upper limit to prevent the target damage. Pulsed discharges operated below this limit are referred to as pulsed dcMS. All discharge operation above the dcMS limit is referred to as HPPMS. In this range, the higher peak power must be compensated for by a lower duty cycle. After Gudmundsson et al. (2012)

be customized. The result is a rather complex step-like shape of the target voltage and the discharge current waveform (see Figure 3.1.1) (Liebig et al., 2011).

The peak power density varies between dcMS and different pulsing schemes, although the average power during one pulse cycle may be the same, as shown in Figure 3.1.1, assuming that the time interval shown in the figure corresponds to the repetition rate of the pulses. All MS discharge operations that exceed the dcMS power limit threshold are termed high power pulse magnetron sputtering (HPPMS), where the increased peak power requires compensation by reducing the duty cycle (see Figure 3.1.2) (Gudmundsson et al., 2012).

3.2 Operating parameters

High power impulse magnetron sputtering (HiPIMS) is characterized by a very high power density at the target during each pulse, usually exceeding the power densities used in dcMS by about two orders of magnitude.

Because the sputtered atoms can be ionized within the ionization region, the ions of the sputtered species can also contribute to sputtering of the target. This is referred to as the self-sputtering in the HiPIMS discharge.

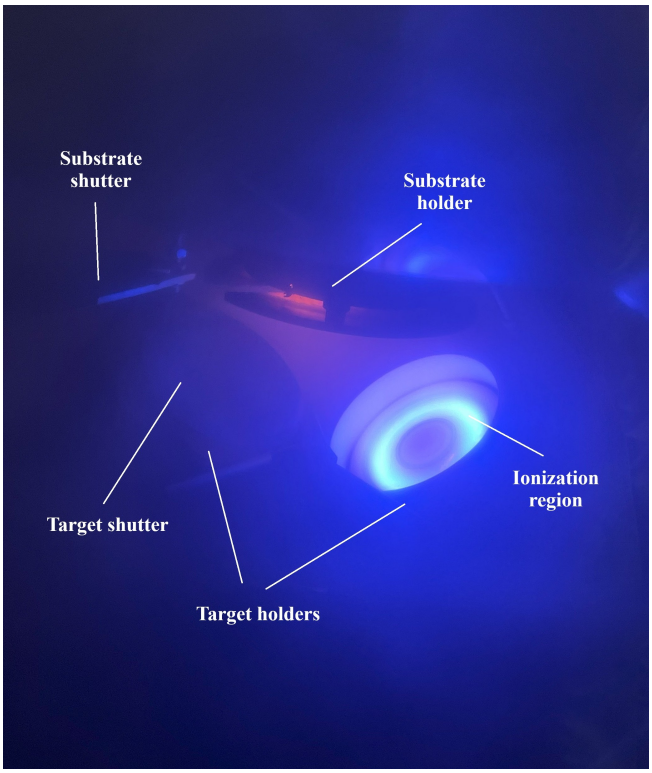

Figure 3.2.1. Photo of the HiPIMS discharge with aluminum target and two empty target holders. The substrate is on the upped part of the picture and is visibly heated.

HiPIMS operates with a cathode voltage in the range of -400 — -2000 V and current densities of up to 3 – 4 A/cm^2. The peak power density is greater than 0.5 kW cm^{-2} and can reach 10 kW cm^{-2}. As was mentioned above, employing a magnetron sputtering discharge in this manner would overheat the cathode target if the duty cycle was long, and therefore in HiPIMS operation the duty cycle is short, where δ is defined as (Anders, 2010a):

$$\delta = t_{on}/(t_{on} + t_{off}) = t_p f_p \tag{3.1}$$

Here t_p denotes the duration of the pulse and f_p is the HiPIMS pulse frequency. The repetition frequency is in the range of 50 – 5000 Hz, and the duty cycle δ is in the range of 0.5% – 5%. The power is therefore supplied to the plasma in short pulses lasting between 10 μs and 1 ms (Sarakinos et al., 2010).

The high applied power leads to large electron densities, up to $\sim 10^{19}$ m^{-3}, which corresponds to mean free path for electron impact ionization of a sputtered metal atoms of the order of 1 cm (Gudmundsson, 2010), leading to a substantial degree of IFF of the sputtered particles (reported up to $\sim$ 70 -– 90%) (Fischer et al., 2023). Even after the pulse is turned off, the plasma density stays relatively high at 10^{17} -– 10^{18} m^{-3} for hundreds of μs (Gudmundsson et al., 2002; Bohlmark et al., 2005). Indeed, a considerable plasma density of approximately 10^{17} m^{-3} is detected at significant distances from the target surface for duration of up to a few milliseconds (Gudmundsson et al., 2012). The possible discharge parameters in HiPIMS have a wider range than in conventional dc and rf sputtering discharges. Furthermore, the ability

to use the pulsing scheme offers increased flexibility by incorporating additional control parameters like pulse width, duty cycle, and pulse frequency (Gudmundsson et al., 2012).

The response of the discharge current to the cathode voltage change is highly non-linear. The empirical relation shows a power-law dependence between the discharge current and voltage (Thornton, 1978):

$$I_{\mathrm{D}} = kV_{\mathrm{D}}^{n} \tag{3.2}$$

where n depends on the working gas and its pressure, target material and magnetic field. Typically n is in the range of 5 to 15 for dcMS (Rossnagel and Kaufman, 1988; Waits, 1978b), but can be lower for HiPIMS operation. Possible reasons for the lower power value of V_{D} in the HiPIMS discharge are:

- change in the secondary electron emission mechanism (Anders, 2008b; Huo et al., 2013);
- sheath thickness (Anders, 2004);
- loss of magnetic confinement (Waits, 1978b);
- gas rarefaction near the target (Anders, 2004).

At low discharge currents, the value of n in HiPIMS operation is comparable to the coefficient in dcMS discharges (Ehiasarian et al., 2002; Alami et al., 2006). A high value of n shows that for the discharge a significant increase in discharge current comes with a relatively small increase in target voltage. This is because the discharge is characterized by a relatively low level of ionization, allowing for the generation of additional charge carriers as required. The value of the exponent drops as the discharge enters the HPPMS regime and then increases again at higher voltages (Alami et al., 2006). The constant k in Eq. (3.2) depends on the target material, the sputter yield, the type and pressure of the working gas, the magnetic field configuration, the secondary emission yield of electrons, and the discharge geometry (Gudmundsson, 2020).

3.3 Pulse phases

Pulsed power systems may include pre-ionization by supplying a conventional dcMS or rf discharge (Poolcharuansin et al., 2010). In a HiPIMS discharge operated without pre-ionization, the time delay between the onset of the discharge voltage and the discharge current can be significant at low operating pressures. In certain situations, if the delay exceeds the pulse duration, the plasma may fail to ignite (Hubička et al., 2020). This delay depends on the working gas pressure (Gudmundsson et al., 2002), the gas composition (Hala et al., 2010), the target material (Hecimovic and Ehiasarian, 2011), the applied voltage (Yushkov and Anders, 2010), and in case of reactive sputtering it also depends on the partial pressure of the reactive gas (Hajihoseini and Gudmundsson, 2017).

The discharge current waveforms $I_D(t)$ in HiPIMS pulses can exhibit significant variations with target material, pulse length, and applied power (Anders et al., 2007), and whether operated in metal mode or poisoned mode in reactive sputtering (see Section 3.5) (Magnus et al., 2012; Gudmundsson, 2016). As the discharge current increases, magnetron sputtering discharges are often characterized as transitioning from *working gas sputtering*, to working gas-sustained self-sputtering, and ultimately, at the highest currents, reaching either self-sustained *self-sputtering* or self-sputter runaway (Anders, 2008b; Lundin et al., 2020).

A typical HiPIMS discharge current waveform can be divided into five phases, following Lundin et al. (2020):

- Phase 1 — *ignition* — roughly the first 10 μs of the discharge pulse, during which the discharge chamber contains almost no plasma. The discharge is expected to first appear as a localized glow discharge on the target surface, near the anode ring, where the vacuum electric field reaches its maximum strength.
- Phase 2 — *current rise* — the initial rise in current that typically follows the bulk plasma breakdown. Secondary electrons ("hot" electrons, e_h) together with electrons generated in the ionization region close to the target ("cold" electrons, e_c) are accelerated along the magnetic field lines into the bulk plasma, where they start ionizing the neutral working gas, producing a strong axial ion current.
- Phase 3 — *current decay/transition* — the bulk plasma density increases sufficiently above the target race track and becomes high enough that this path has the least resistance for the electron current to traverse the magnetic field lines, leading to a more extended axial current. Around the time of the current peak, the density of the working gas atoms decreases significantly, a phenomenon known as working gas rarefaction (see Section 4.13).
- Phase 4 — *plateau/runaway* — at this stage, the discharge may follow different current paths. A dense plasma torus is consequently sustained above the target racetrack in an approximately steady state (depending on the evolution of the current), resulting in substantial ionization in this volume. Electrons are now carried across the magnetic field lines, traveling all the way from the target surface, through the plasma volume, until they arrive at the first grounded magnetic field line that intersects the grounded anode ring. The axial current transport now accounts for the majority of the total current.
- Phase 5 — *afterglow* — once the HiPIMS pulse is turned off, the current rapidly drops. During the afterglow, the electron density first drops rapidly (up to 30 μs), and then transitions to a much slower decay rate (around 3500 μs). The effective electron temperature T_{eff} rapidly decreases to about 0.2 eV and remains at this level for several milliseconds. In addition, both the density and temperature of the metastable working gas atoms drop quickly as the sputtered flux vanishes and plasma species are lost through recombination and diffusion toward the chamber walls.

All five of the identified phases are observed only in sufficiently long pulses (approximately

200 μs), a pulse length that has been shown not to be the optimal waveform for thin film deposition with HiPIMS discharges. Nowadays, triangular current waveforms are generally regarded as the most effective for achieving the highest IFF and require the lowest power (Brenning et al., 2021).

3.4 Influence of the target material

Several research groups have examined how the target material affects the spatial and temporal development of plasma parameters. One of the first reports, which compares plasma parameters for discharges using different target materials, is by Vetushka and Ehiasarian (2008), where discharges in argon with chromium and titanium targets were analyzed. They found that at an argon working gas pressure of 0.28 Pa, the electron density for a discharge with Cr target is approximately twice as high as for a discharge with Ti target ($\approx 8 \times 10^{17}$ m^{-3} vs $\approx 4 \times 10^{17}$ m^{-3}) at the same distance from the target, which was 10 cm. Additionally, the electron density began to increase simultaneously with the discharge current for the discharge with Cr target, while there was a delay of approximately 25 μs when the Ti target was used. The maximum plasma density was reached simultaneously, approximately 16 μs after the end of the pulse (duration 70 μs) for both targets. The authors associated this with a higher sputter yield (see Section 4.9) of Cr and a higher cathode voltage on the Cr target in comparison to the discharge with Ti target. This suggests a greater degree of argon gas rarefaction near the target (see Section 4.13) along with secondary electrons having higher kinetic energy as a result of increased cathode voltage for the Cr target (Gudmundsson and Lundin, 2020).

Despite differences in process conditions (such as pressure, target size, and target material), the HiPIMS pulse configuration, and the precise position of the density measurement (Čada et al., 2020), the electron density correlates quite well with the peak current density. For typical peak current densities of about 1 A/cm^2, the plasma density in the vicinity of the cathode target is expected to be in the range of $1 -- 3 \times 10^{18}$ m^{-3}. However, in the argon discharge with niobium and tungsten targets the plasma density is higher, giving an electron density closer to 10^{19} m^{-3} for the same peak discharge current density (Lockwood Estrin et al., 2017). For these two discharge systems, a triple probe was positioned much closer to the target surface (10 – 15 mm) than in the other discharges, which were studied using Langmuir probes. The probe position is likely responsible for the higher electron density values. There is also a slight increase in the electron density as the pressure is raised from 0.5 Pa to 2.0 Pa. However, further increasing the pressure above 2.0 Pa does not lead to a higher electron density (Hubička et al., 2020; Vetushka and Ehiasarian, 2008; Pajdarová et al., 2009; Lundin et al., 2015; Lockwood Estrin et al., 2017).

3.5 Reactive sputtering

Sputter deposition can be applied to deposit compound films either by sputtering a compound target or by sputtering an elemental target in a mixture of the inert working gas and the reactive gas (e.g. O_2, N_2, CH_4). The latter process is termed *reactive sputter deposition* or reactive sputtering (Strijckmans et al., 2018), and it is attractive because a variety of compounds can be prepared from a low-cost metal target by adding an appropriate reactive gas to the noble working gas. Consequently, reactive sputter deposition is a topic of significant industrial and technological relevance, as the majority of commercially important thin films and coatings are compounds (Kelly, 2011). The most common compounds deposited by reactive sputtering are oxides and nitrides (see Section 2.7). Such coatings are typically deposited by reactive magnetron sputtering using asymmetric bipolar mid-frequency, rf or unipolar pulsed (HiPIMS) waveforms.

With the introduction of a reactive gas, a chemical reaction in the gas phase is unlikely as the reactive gas pressure and the density of the sputtered atoms are generally so low during sputtering that three-body collisions are rare, but chemical reactions occur on both the target and substrate surfaces as well as on the chamber walls, in addition to sputtering and deposition, leading to a much more complicated picture in comparison with non-reactive sputtering. The most significant is that a compound can form on the target surface, and the sputter yield changes.

Although reactive HiPIMS has been successfully applied to grow various high-quality compound films, there are a number of issues that require better understanding, including the low deposition rate and the variations in the hysteresis effect. Due to recent findings that the sputter yield plays a significant role in discharge properties (Brenning et al., 2020, 2021; Barynova et al., 2025), the development of a model for the degree of poisoning of the target is important since it directly affects the sputter yield (Berg and Nyberg, 2005). In reactive sputtering the low deposition rate in the HiPIMS discharge is particularly problematic for oxide deposition because when the target is oxidized, the sputter yield typically drops significantly (Schelfhout et al., 2020). The cause of hysteresis is poisoning, or compound formation, on the target. One of the first measurements and explanations of hysteresis and a model to describe it qualitatively came as early as the mid 1970s (Goranchev et al., 1976). Later, more quantitative models were developed to describe the poisoning of the target as well as the drop in the deposition rates at a certain threshold pressure, which was the consequence. The initial model to describe the S-shape of the hysteresis comes from Steenbeck et al. (1982). A further developed version was published by Berg et al. (1986, 1987) and Berg and Nyberg (2005), which describes the process in simple analytical terms. They added the steady state equations that describe the hysteresis as a function of the gas flow, meaning, using practical parameters. The Berg model simplifies the sputtering process to obtain a simpler balance equation. A number of improvements to the original model were proposed, such as a mix of reactive gases, alloy target, implantation of reactive gas, gettering as well as the development of temporary and spatially resolved models. Note that all mentioned models cover the reactive dc sputter deposition, not pulsed, and require the steady state.

Strijckmans et al. (2018) published a more advanced model of the reactive sputtering process. The reasoning is that the original Berg model, while able to describe the basic mechanisms, lacks accuracy due to a number of approximations made. It also allows to model the pulsed operation, however it is still not able to model the HiPIMS discharge due to the reliability on the secondary electrons to sustain the discharge which is not always the case, as in HiPIMS operation ohmic heating can be vary important as well (see Section 2.11).

Furthermore, several unexpected results have been observed experimentally in reactive HiPIMS (Gudmundsson, 2016), most of which have not been completely explained. An important finding is that reactive HiPIMS exhibits narrower hysteresis curves or no hysteresis at all under some conditions (Wallin and Helmersson, 2008). The reduced or eliminated hysteresis has been explained by the increase in ion flux to the target, in particular metal ion flux (Kadlec and Čapek, 2017; Čapek and Kadlec, 2017).

More recently the reactive Ar/N_2 discharge with a titanium target has been implemented into the IRM code (Fischer, 2025). This later model of the Ar/N_2 discharge included a number of improvements regarding the target surface, such as correcting the sputter yield with the compound fraction (Berg and Nyberg, 2005; Depla et al., 2008) and calculating the binding energy for each component of the compound, based on the Pauling formalism for calculating bond energies (Pauling, 1960) as suggested by Malherbe et al. (1986) for oxides and which has been implemented more recently for nitrides (Depla et al., 2008; Rudolph et al., 2018). It also includes improved treatment of working gas rarefaction that had been developed earlier (Barynova et al., 2024).

The current work does not include modeling of reactive sputtering, but part of the experimental work included the deposition of AlN thin films using HiPIMS.

3.6 Advantages and disadvantages of HiPIMS

HiPIMS provides high fraction of ions in the deposition flux, and combined with the sheath near the substrate and/or substrate biasing, leads to a good coverage even for a high aspect ratio trenches, providing better conformal coating, which means much more similar growth rates parallel and perpendicular to the target surface which is not the case in dcMS (Bobzin et al., 2009). As mentioned earlier, HiPIMS can operate with the same configuration as dcMS, only requiring the pulse generator, which simplifies its implementation in industrial setups where dcMS is already in use (Hubička et al., 2020).

Glow discharges, especially those in magnetron sputtering discharges, tend to exhibit "arcing". The arc is an undesirable form of a discharge, with high current and low voltage, that creates cathode spots on the target, which leads to a release of tiny droplets when deposited onto the substrate that degrade the quality of the coatings. The probability of forming an arc was shown to be greatly reduced by operating the pulsed sputtering process in the mid-frequency

range (20 – 70 kHz) (Schiller et al., 1993). But with higher current density, like in HiPIMS operation, the issue is more pronounced. Modern HiPIMS power supplies come with methods for detection and suppression of arcs. Despite the presence of arc suppression, the brief duration of an arc before it is suppressed can negatively affect the quality of the coating. It would be advantageous to set up a process in which arcing is unlikely. One strategy is to use short pulses, each lasting less than 50 μs, a method that proved effective for mid-frequency sputtering because arc spots usually develop with some delay in the presence of plasma (Anders, 2011).

In addition to its application in PVD, HiPIMS can serve as a powerful tool for substrate etching and interface engineering (Ehiasarian et al., 2003, 2004; Reinhard et al., 2007; Münz et al., 1992). Films deposited after the substrate is pretreated with HiPIMS have been shown to exhibit good adhesion and performance in mechanical tests, and have been successfully deposited on industrial scale machines with improved adhesion and corrosion resistance.

One of the main disadvantages of HiPIMS is the lower deposition rate compared to dcMS. There are a number of reasons for that, while the main ones can be summarized as follows (Anders, 2010a):

- sputtered ions back-attraction to the target;
- less-than-linear increase in the sputtering yield with increasing ion energy;
- greater film mass density and self-sputtering on the substrate;
- power losses in the switch module;

The back-attraction in HiPIMS discharges can be explained by a high degree of ionization of the sputtered species, which become ionized near the target, and, as a result, can be pulled back by the electric field towards the biased target. This is known as the return effect, explained by Christie (2005), which reduces the deposition rate compared to the traditional deposition with dcMS operation at the same average power.

In HiPIMS the objectives are to have a significant ionized flux fraction of the sputtered target species and to ensure high deposition rate. However, in HiPIMS operation a high ionized flux fraction always comes at the cost of a low deposition rate. This makes the HiPIMS compromise necessary when optimizing the deposition process (Brenning et al., 2020). Since the implementation of HiPIMS technology there have been a lot of attempts to overcome the issue with a low film deposition rate. Several discoveries have been made, such as the dependence of a deposition rate on pulse length (Konstantinidis et al., 2006), suggesting a benefit in shortening pulse length (Rudolph et al., 2020; Shimizu et al., 2021); on target material (Lundin and Sarakinos, 2012); on magnetic field strength, and the benefit of weaker magnetic field strength (Hajihoseini et al., 2019; Mishra et al., 2010). There is a proposal to optimize the HiPIMS discharge operation by mixing two different power levels (Brenning et al., 2021), where the pulse scheme makes it possible to partially separate the production of ions and neutrals, which constitute the film-forming flux to the substrate. The negative back-attraction effect can be reduced by introducing a positive voltage pulse to the target

immediately, following the high power negative sputter pulse, as proposed by Nakano et al. (2013). This increases the plasma potential, accelerating ions from the ionization region toward the substrate where the film or coating is formed (Keraudy et al., 2019). The positive pulse typically ranges from a few tens to several hundred volts, and this technique is known as bipolar HiPIMS (Scherer et al., 1992; Gudmundsson et al., 2022).

CHAPTER 4

IONIZATION REGION MODEL

In this chapter different aspects of modeling the HiPIMS discharge are discussed with focus on the IRM.

4.1 Introduction to modeling magnetron sputtering discharge

Plasma processing has a large set of applications in both scientific and industrial research, and its use in industrial fabrication is extensive, and therefore good understanding of its properties and behavior is necessary. One way to achieve this is by modeling the plasma discharge.

Due to a significant demand for magnetron sputter deposition in industry, there is a motivation to model the complete magnetron deposition process to avoid the experimental trial and error in process development. If successful, this can lead to a significant cost reduction since for a typical coating machine, one of the main expenses is the installation cost. In addition, there is the possibility to optimize the parameters of the deposition process of an existing plasma processing system (Hurlbatt et al., 2017).

This work focuses on modeling the plasma chemistry of the discharge itself. The behavior of the magnetron sputtering discharge depends on the magnetic field, the working gas pressure, the plasma surface interaction, and the electrical power input. In addition, the basic physics that describes the motion of charged particles in a region subjected to electric and magnetic fields is needed. This, combined with the necessary cross sections for particle interactions, sputter yields, and electron yields, is in principle sufficient to describe the magnetron sputtering discharge. The complication is that a comprehensive model must include the computation of the electric field using the spatial distribution of the charged plasma species along with the externally applied voltage. Moreover, a comprehensive model must consider the interaction between charged particle motion and the electromagnetic field, while also computing the electromagnetic field itself. To further complicate the modeling, even in the planar magnetron

sputtering discharge configuration, the magnetic field has a complex geometry requiring a multi-dimensional approach (Gudmundsson, 2020). Such systems are nonlinear and challenging to analyze. Additionally, inter-particle collisions, which are also electromagnetic in nature, occur on a much shorter time and space scales compared to the applied fields because of the particles' average motion (Lieberman and Lichtenberg, 2005, p. 418).

The presence of a magnetic field that confines the electrons gives the opportunity to divide the volume into the ionization region (IR) and the the diffusion region (DR) (or bulk plasma region). Thanks to this, the model can focus on one region taking input from the model of another region, and not rely on simulating the full magnetron sputtering discharge chamber. This current work focuses on modeling the IR. The particle-target interaction, required to model the magnetron sputtering discharge, are taken into account as the sputter yield and secondary electron emission. The deposition and thin film growth as well as particle transport are not considered apart from accounting for the transport parameters when comparing the measured IFF with the modeled one (Rudolph et al., 2021) (see Section 2.4.1). Despite the fact that with this approach, the model relies on the results of other models or empirical data, models or simulations that focus on isolated aspects of the deposition process are practical because a fully self-consistent simulation has a high computational cost (Kozák and Lazar, 2018).

When choosing the right approach for modeling, the properties of the particular discharge have to be taken into account, such as (non)thermal equilibrium, electron density, dominant transport mechanism, magnetic field, dominant reactions, surface interaction, time and space scale, gas flow/diffusion, instabilities, etc. Modeling magnetron sputtering discharges can be categorized into analytical and numerical models. Numerical models can be additionally categorized into either fluid or kinetic models. Kinetic models, derived from the numerical solutions of the Boltzmann equation or direct simulation Monte Carlo (DSMC), lack self-consistency, and need a Poisson equation solution, leading to the development of either hybrid models or Particle-In-Cell – Monte Carlo collision (PIC–MCC) simulations. Different approaches in modeling can be summarized as (Bogaerts et al., 2008):

- Analytical models
- Fluid models
- Boltzmann equation models
- Direct simulation Monte Carlo (DSMC)
- Particle-In-Cell – Monte Carlo collision (PIC–MCC) simulations
- Pathways models
- Hybrid models
- Global models

For weakly ionized plasmas, the ionized density fraction is low $\chi \ll 1$ (see Eq. (2.2)), and the electron density n_e is equal to the ion density n_i due to quasi-neutrality. With such a degree of

ionization, ion and electron collisions with neutral gas atoms are important and ionization of neutrals by electrons sustains the plasma discharge. The mean electron temperature is usually lower than the ionization energy of the working gas, but the reaction still occurs due to the electron energy distribution. The electrons exhibit a distribution on energy often with a high energy tail. The tail of the distribution might be below or above the Maxwellian distribution due to electron heating and collisions with neutrals. Non-Maxwellian distributions can only be described with kinetic theory of discharges (Lieberman and Lichtenberg, 2005, p. 187).

In practice, plasmas are almost always non-uniform and time-varying. A charged particle in a plasma interacts simultaneously with numerous nearby particles, leading to observed shared collective behavior. When energy is added, a positive feedback mechanism can amplify the density variation until it develops into large-scale macroscopic structures or patterns – an instability. The instability is identified by strong variations in the local plasma parameters, including particle density, particle temperature, plasma potential, and pressure (Lundin et al., 2020). In dcMS common instabilities include electron drift waves disturbed by the density gradient and electric field (Martines et al., 2001). In magnetron sputtering discharges there also exist "ionization zones", or "spokes" (Hecimovic and von Keudell, 2018). Spokes propagate along the race track, and appear either diffuse or triangular in images from fast intensified CCD cameras, indicating nonuniform light emission caused by higher ionization rates (Ehiasarian et al., 2008). Another common instability in HiPIMS discharges is the oscillation of the plasma in a direction normal to the target surface, which has been termed the "breathing instability" (Yang et al., 2016; Hecimovic and von Keudell, 2018).

Modeling the plasma discharge can help to better understand the process and to improve and optimize the plasma-based technologies. Accurate modeling requires significant computational resources and different approaches are adopted depending on the application, while plasma instabilities additionally complicate the picture.

4.2 Material pathway model

The first HiPIMS model was a target material pathway model that was developed by Christie (2005), using the representation of a signal flow graph. The key model parameters are the sputtered metal ionization efficiency and the magnetron extraction efficiency. The model diagram may be viewed as a signal flow graph, with parameters interpreted as gains. This view makes the application of Mason's gain formula to solve the signal flow graph by inspection straightforward (Mason, 1953). The model can account for the observed lower HiPIMS deposition rates compared to dcMS rates at the same average power. It also explains the relatively low percentages of ionized metal species reaching the substrate, which are sometimes below 10%, despite the plasma appearing to be highly metallic. This modeling technique has proven to be useful for understanding the HiPIMS discharge. However, this model does not track the electrons, so their properties are unknown (Rudolph et al., 2021),

and due to the steady-state assumption, the model can only be applied to discharges with a long discharge current plateau or with respect to averaged discharge characteristics (Minea et al., 2020).

The model was later developed further by Vlček et al. (2007), where a parameter was introduced to account for the increased ionization that occurs in the bulk plasma between the target and the substrate, a result of the efficient magnetic confinement of electrons. It determines the degree of additional ionization of sputtered atoms in a gap, from where the created ions are not directed back to the cathode target because of the flatter electric potential profile. Furthermore, the explanation of the losses of target material neutrals and ions during transfer to the substrate was made more straightforward by introducing the relative ion-to-atom transport factor.

The material pathway model became a predecessor to the IRM, as its modeling approach has proven to be important for understanding a few issues, mentioned earlier, related to the operation of the HiPIMS discharge. The pathway model introduced such HiPIMS discharge modeling parameters as the probability of ionization of a sputtered atom α_t, the ion back-attraction probability β_t, and the transport parameters for neutrals ξ_{tn} and ions ξ_{ti} (Christie, 2005; Hajihoseini et al., 2022), which are used in the IRM.

4.3 Global models

In modeling and in plasma discharge modeling, in particular, one is required to choose which considerations are critical to a process and which can be neglected. Instead of calculating precise spatial variations of species in a plasma discharge, the emphasis can be on conservation of charge and energy laws in a defined volume. Models that use this approach are referred to as global models and are typically zero-dimensional, although some also incorporate a time dimension. Global models can be a good way to understand some aspects of discharge processes without additional computational complexity, since many reactions and species already require a significant amount of computational power, and ignoring the spatial variation makes it a lot less expensive in terms of computation. Apart from the low computational cost, global models are a good approach to the initial survey of plasma parameters in the particular system before starting more complex modeling.

Global models are based on two types of equations: *particle balance equations*, written for each species involved, and *power balance equations*, generally focused on electrons but extendable to other species. Solving this set of equations requires additional data about the system of interest, such as physical properties, power coupling method, and a set of species involved along with reactions.

Plasma chemistry is another strength of global models. Global models can be particularly useful for modeling complex chemistry. Particle balance equations are stated for each species

in the plasma, and to solve them, the data on the reactions between them is needed. When the set of reactions becomes complex, especially in discharges with a reactive gas, the outcome of the model is often not intuitive, which makes it useful to first consult with global models before taking on more computationally demanding approaches, such as particle-in-cell Monte Carlo collision (PIC–MCC) simulations, to identify the main reactions in the plasma (Hurlbatt et al., 2017). Consequently, global models are widely employed in studying chemistry and identifying key reactions in low-temperature plasmas as they allow for complex chemical reaction schemes, with a large number of species and reactions (Hurlbatt et al., 2017). However, even in a global model, the selection of plasma species and the corresponding reactions can present a challenge.

There is a long list of existing global model platforms for low temperature plasma discharges in particular. This includes software like GlobalKin (Munro and Tennyson, 2008), ZDPlasKin (Pancheshnyi et al., 2008), PLASIMO's Global Model (van Dijk et al., 2009), LisbOn KInetics LoKI-B+C (Tejero-del-Caz et al., 2014), etc. However, none of the models above can be used to model a HiPIMS discharge.

A time-dependent global model for argon plasmas was formulated by Ashida et al. (1995). This model examines the dynamics of an argon discharge subjected to time-modulated power in high-density inductively coupled plasma reactors. The changes with time in both electron temperature and plasma density are determined by solving the equations of particle and energy balance. The model only takes argon into account and does not consider a sputtering target, but it's approach served as one of the foundations for developing IRM. Based on the time-dependent global model of the argon discharge developed by Ashida et al. (1995), a volume averaged model of the HiPIMS discharge that covered the entire plasma chamber, included sputtering from the target, and was expanded to include metal species as described by Hopwood (2000a), was developed by Gudmundsson (2008).

Note that global models cannot describe instabilities nor nonlinear potential structures (shocks) that can appear in the plasma (see Section 2.9), since they are highly spatially nonuniform. For example, spokes form within the IR, where plasma density is high. Their presence is thought to significantly impact the movement of species across magnetic field lines and is considered the primary cause of the observed strong anomalous cross-field transport of charged species in HiPIMS (Lundin et al., 2008). A thorough comprehension of these phenomena requires data of local electric and magnetic fields. Spatially resolved measurements of the plasma potential are necessary for determining the local electric fields, as well as calculating drift velocities. Accuracy of global models is limited due to simplifying assumptions made about the spatial configuration of the discharge as well as the simplified model of plasma species transport (Kozák and Lazar, 2018).

4.4 Historic development of IRM

The *ionization region model* (IRM) is a semi-empirical time-dependent, volume averaged plasma chemistry model of a HiPIMS discharge focused on the ionization region (IR; see Section 4.6 and Section 2.8) (Raadu et al., 2011), while the surrounding plasma is supposed to be treated using the bulk plasma model (BPM) (Brenning et al., 2008). The IRM is based on the global model developed by Ashida et al. (1995) that was extended to describe the HiPIMS discharge process by Gudmundsson (2008), which eventually became a model covering only the IR (Raadu et al., 2011).

The HiPIMS discharge for the sputtering of a metallic target in an inert gas has been extensively studied with the IRM over the past decade for a number of target materials including graphite (Eliasson et al., 2021), aluminum (Huo et al., 2012), titanium (Rudolph et al., 2021), tungsten (Suresh Babu et al., 2022, 2023), chromium (Barynova et al., 2026) and zirconium (Suresh Babu et al., 2024). Due to the use of the IRM, the basic operation of the HiPIMS discharge is relatively well understood. The IRM has been applied to study the reduction in deposition rate (Brenning et al., 2012), the electron power absorption mechanism (Huo et al., 2013), the electron energy distribution function with the help of a Boltzmann solver (Rudolph et al., 2021), the onset of self-sputtering (Huo et al., 2014), the working gas rarefaction and refill process (Raadu et al., 2011; Huo et al., 2012; Barynova et al., 2024). In fact, the most recent findings indicate that the sputter yield of the target is the defining parameter for the discharge operation, in particular the determination of the back-attraction probability and therefore the deposition rate (Barynova et al., 2024, 2025).

4.5 Overview of the ionization region model

The initial global model of the HiPIMS discharge was developed to model only the dense plasma region that forms due to the magnetic confinement of the electrons next to the cathode target – the ionization region (IR; see Section 4.6). This therefore became termed the *ionization region model* (IRM). The IRM allows for the calculation of the temporal evolution of neutral and charged species, as well as the electron temperature in HiPIMS discharges. The model is confined to the IR, characterized as an annular cylinder where the outer and the inner radii represent the race-track area. As it is a global model, the geometrical effects are indirectly accounted for through the loss and gain rates at the boundaries of this annular cylinder, both to the target and to the bulk plasma. A set of ordinary differential equations (ODE) determines the temporal evolution, providing the first derivatives with respect to time for both the electron energy and the particle densities of all heavy particles. The electron density is determined by the assumption of quasi-neutrality in the plasma.

To ensure accuracy, the model must align with the experimental data input. Initially, this involves adapting the model to an existing discharge, considering factors such as geometry,

working gas and its pressure, sputter yields, target species, and a reaction set for these species. After that, the model is adjusted using a number of free parameters, allowing it to fit the empirical discharge current and voltage data, denoted as $I_D(t)$ and $V_D(t)$, respectively. The free parameters are the back-attraction probability of ions to the target, β_t, and the fraction of the total discharge voltage drop across the ionization region, $f = V_{IR}/V_D$. Another parameter is the ionized fraction of the deposition flux (ionized flux fraction, IFF) (Huo et al., 2017), which is used as a fitting constraint. The secondary electron recapture probability r has to be mentioned as it was treated in IRM as a free parameter, but now for HiPIMS discharges with metal target it is used as one of the fixed parameters, with a value $r = 0.7$ (see Section 4.10).

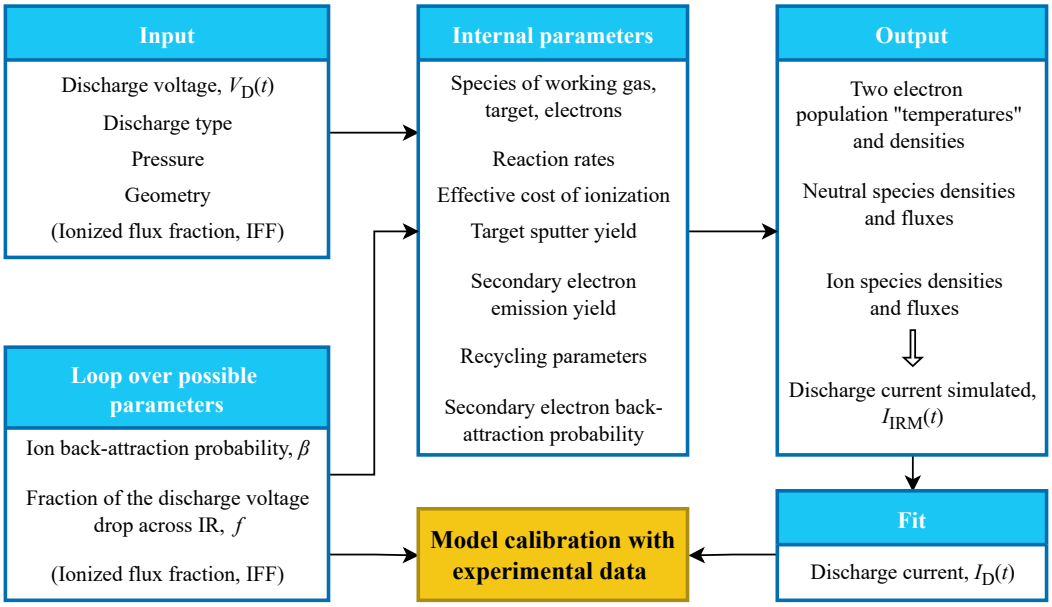

Figure 4.5.1. Block diagram showing the ionization region model pipeline.

4.6 Ionization region in IRM

The IRM relies on the observation that in the magnetron sputtering discharge a dense, brightly glowing torus-shaped plasma floats and extends a few centimeters from the cathode target (see Figure 3.2.1), which is situated within a bulk of lower density plasma (Raadu et al., 2011). In the IRM the IR is modeled as an annular cylinder with outer radius r_{c2}, inner radius r_{c1} and length $L = z_2 - z_1$ (see Figure 4.6.1).

The presence of a magnetic field near the target makes it possible for the potential drop to exist in the region of dense plasma in the vicinity of the cathode target outside the cathode sheath. It is called the ionization region (IR) (Brenning et al., 2008; Raadu et al., 2011). The definition is based on experimental observations, such as by Bradley et al. (2001), and

PIC–MCC simulations (Bultinck and Bogaerts, 2009), and was explored experimentally by Antunes et al. (2023) using optical emission measurements. The voltage drop occurs across both the cathode sheath and a pre-sheath (IR), as shown in Figure 2.8.1 (also see Section 2.8).

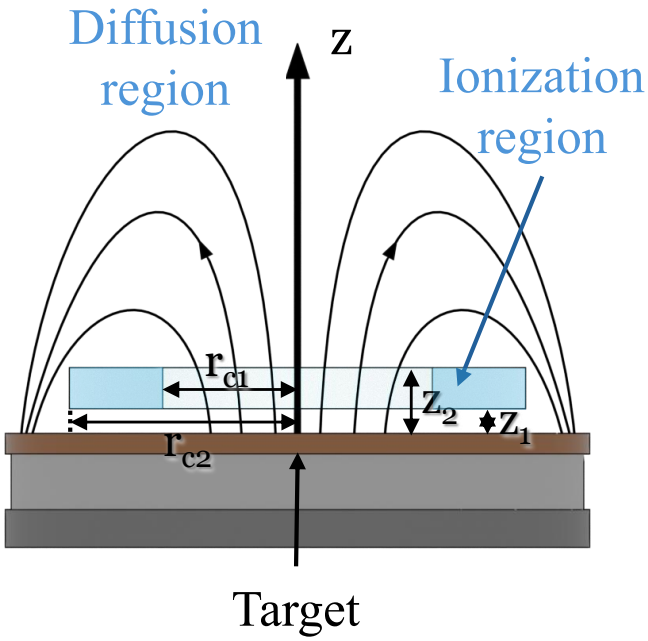

Figure 4.6.1. The ionization region (IR), where most of the ionization occurs, side view. The IR is approximated in the ionization region model (IRM) as an annular cylinder with outer radius r_{c2}, inner radius r_{c1} and length $L = z_2 - z_1$.

Although understanding the IR is crucial for HiPIMS discharge modeling, its spatial extend remains poorly characterized. Recent experiments by Dubois et al. (2022) using Thomson scattering measurements indicate that both the electron temperature and electron density decrease exponentially as the distance from the target surface increases. Another study by Kanitz et al. (2016), used a laser absorption spectroscopy setup to determine the spatial and temporal dynamics in HiPIMS discharges. They showed that the spatial distribution of the metastable argon atoms is confined below the magnetic null point. Furthermore, it is observed that the light emission from Ar^+ ions follows the magnetic field lines.

Antunes et al. (2023) studied the extension of the IR in a HiPIMS discharge as the magnetic field strength and configuration were varied. For this, they took images within the second half of a discharge pulse using a fast camera and a band pass filter to collect the emission of the transition from one of the excited levels of the argon atom to a metastable state. The authors assumed the edge of the IR to be where the light intensity had fallen to less than half of its maximum intensity. They show that the shape of the IR closely follows those of the magnetic field lines which are determined by the location of the permanent magnets at the back of the cathode. The axial extent of the IR ($z_2 - z_1$) depends inversely on the strength of the magnetic field, as expected for gyrating electrons. It was found to vary from 10 to 17 mm. The width of the IR ($r_{c2} - r_{c1}$), and the cross sectional area, show similar behavior with increasing magnetic field strength B, i.e. a linear decrease for $B < 18.1$ mT, and constant

values in the range 18.1 mT $\leq B \leq$ 23.8 mT.

4.7 Particle and power balance

Since the IRM is a global model, it assumes the volume-averaged values over the IR. This allows for the calculation of the temporal evolution of species and the electron temperature. Geometrical effects are indirectly accounted for through loss and gain rates at the IR boundaries. Therefore, the outcomes of the IRM should be considered more as qualitative trends rather than providing precise quantitative values.

The IRM consists of a set of ordinary differential equations (ODEs) on rate and balance inside the IR (Huo, 2013):

- Density evolution equations of the process gas species;
- Density evolution equations of the sputtered target species;
- Density evolution of the electrons assuming quasi-neutrality;
- Power balance equation for the electron temperature.

In order to consider electrons that escape trapping, an effective secondary electron emission coefficient, $\gamma_{\mathrm{SE,eff}}$, is introduced. This coefficient accounts for both the probability of electrons returning to the target and the loss of secondary electrons due to inefficient electron trapping (see Section 4.10).

In the IRM the resulting system of $N_{\mathrm{spe}} + 1$ ODEs describing the particle and power balance (N_{spe} being the number of species considered) are solved in MATLAB using `ode15s` method.

```
[t,y] = ode15s(odefun, tspan, y0, options),
```

where `odefun` are the functions to solve, `tspan = [t0, tf]`, integrates the system of differential equations $y' = f(t,y)$ from `t0` to `tf` with initial conditions `y0`, and `options` is an optional structure, which, for example, specifies a relative error tolerance or turns on the display of solver statistics. Each row in the solution array `y` corresponds to a value returned in the column vector `t`. In the IRM the time $t \mathrel{\widehat{=}}$ `t` is an independent variable, and the constraint comes from empirical data on I_{D} and U_{D} waveforms.

4.7.1 Particle balance equations

Within the IRM, the considered species include electrons, ground state argon atoms $\mathrm{Ar}(3\mathrm{p}^6)$, "hot" ground state argon atoms Ar^{H}, "warm" ground state argon atoms Ar^{W}, metastable argon atoms Ar^{m}, argon ions Ar^{+}, doubly ionized argon ions Ar^{2+}, metal neutrals M, singly ionized metal ions M^{+}, and doubly ionized metal ions M^{2+}. The hot argon atoms correspond to the

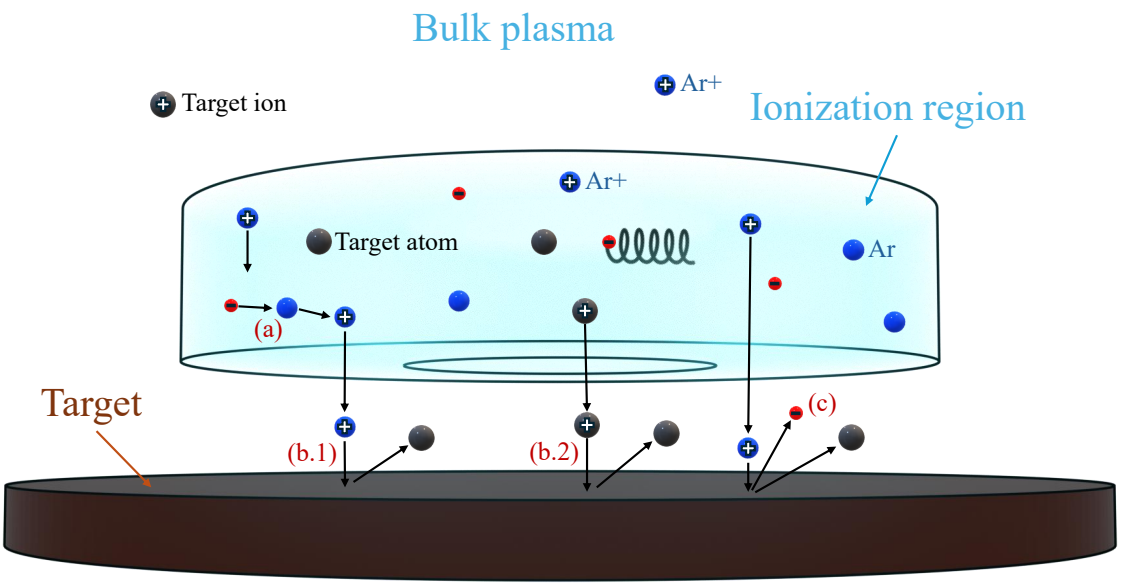

Figure 4.7.1. A schematic view of some of the processes occurring on the target surface and in the ionization region, including (a) ionization by the electron impact; (b.1) sputtering of a target atom by working gas ion defined by the working gas sputtering yield Y_g; (b.2) self-sputtering of the target material defined by the self-sputtering yield Y_{SS}; (c) "hot" electron emission defined by the secondary electron emission yield γ_{SE}

reflected or sputtered back from the target neutralized argon ions, and the warm argon atoms correspond to the diffused back from the target neutralized argon ions, mentioned in Section 2.10.

In general, the particle balance equation for species X is expressed in the form (Huo et al., 2017):

$$\frac{dn^{(X)}}{dt} = \sum_i R^{(X)}_{\text{Generation},i} - \sum_j R^{(X)}_{\text{Loss},j^*} \tag{4.1}$$

The terms $R_{\text{Generation},i}$ and $R_{\text{Loss},j}$ represent the reaction rates of generation and loss processes concerning species X in the IR. The list of processes depends on the species X, and can be broken down by the charge of the species, since the behavior in the plasma is mostly guided by it. The reaction rate R_j for any reaction j within the volume is determined by multiplying the reactant densities by the reaction's rate coefficient k_j:

$$R_j = k_j \times \prod_i n_{\text{reactant},i} \quad \left(\text{m}^{-3}\,\text{s}^{-1}\right) \tag{4.2}$$

where, $n_{\text{reactant},i}$ denotes the density of the i-th reactant.

Eq. (4.1) also represents additional generation and loss processes, such as sputtering $R_{\text{n,sputt}}$, neutral flux diffusion $R_{\text{n,diff}}$, gas refill $R_{\text{g,refill}}$, gas kick-out $R_{\text{g,kick-out}}$, ion loss from the IR or to surfaces $R_{\text{i,loss}}$, and the return of recombined gas ions $R_{\text{g,return}}$ from the target. A detailed

description of how these processes are treated is provided elsewhere (Huo et al., 2017), with the exception of $R_{\text{g,kick-out}}$, which is discussed in Section 4.13.2.

4.7.2 Power balance equations

The majority of the energy in a HiPIMS discharge is absorbed by electrons leading to observed high electron temperature $T_e \gg T_i$. The power balance equates the power absorbed by the plasma electrons with power lost from events like elastic collisions, inelastic collisions, de-excitation processes, and Penning ionization. Before diving into power balance, the "cold" and "hot" electron populations and their heating mechanisms need to be discussed.

Let us consider the electron energy distribution function (EEDF). Electrons typically do not achieve thermal equilibrium with ion species and frequently lack thermal equilibrium even among themselves. Experimental observations have shown that the bulk (<10 eV) EEDF in magnetron sputtering discharge can be either Maxwellian-like or bi-Maxwellian-like. The specifics depends on the gas pressure and the specific spatial location within the HiPIMS discharge (Gudmundsson et al., 2002; Pajdarová et al., 2009; Rudolph et al., 2021). It was also observed, using Langmuir probe measurements, that the EEDF was Maxwellian during the peak in electron density, followed by a Druyvesteyn-like EEDF with slightly higher average electron energy, but further measurements in the same system show that EEDF was in fact closer to Maxwellian during the whole pulse (Gudmundsson et al., 2009). Based on the Langmuir probe characterization by Poolcharuansin and Bradley (2010), the authors claim that during the early stages of the pulse (< 4 μs), electrons can be classified into three distinct groups. These groups are identified as "super-thermal", "hot", and "cold" electrons, with effective electron temperatures ranging 70 — 100 eV, 5 — 7 eV, and 0.8 -– 1 eV, respectively. It is suggested that the presence of super-thermal electrons is explained by the initial condition of the sheath, which is either very thin or absent, influenced by the remaining plasma during off-time.

In the growing axial electric field of the developing sheath, the remnant off-time plasma electrons are accelerated. As the sheath edge progresses, these electrons can reflect off the leading edge of the sheath. Consequently, beam-like electrons form with very high effective electron temperature during the initial microseconds following the onset of the voltage. The first few tens of microseconds into the pulse, the effective electron temperature is typically relatively high with values between 2 and 6 eV, which later decrease to a range of 0.3 to 1 eV. After the pulse has been off for a minimum of 300 μs at 0.3 Pa, the temperature stabilizes around 0.4 eV and 0.8 eV for chromium (Cr) and titanium (Ti) targets, respectively (Vetushka and Ehiasarian, 2008). In the study by Gudmundsson et al. (2009), again using a Langmuir probe, comparable results were observed, showing that the effective electron temperature decreases to a steady value of approximately 0.7 eV at 0.4 Pa and 0.3 – 0.4 eV at 2.7 Pa until the pulse is over. Furthermore, secondary electrons, created by ion bombardment of the cathode target, are even more energetic (> 100 eV), since they are accelerated across the cathode sheath and their EEDF is generally not Maxwellian (Rudolph et al., 2021).

It is apparent that the experimental measurements of electron temperature show a similar temporal trend within the pulse as described by Gudmundsson et al. (2009). At the same time the absolute value of the electron temperature is reported to be lower in experimental measurements (Held et al., 2020; Gudmundsson et al., 2009) than predicted by the IRM. One must ask question why IRM overestimates the electron temperature. An explanation proposed by Suresh Babu et al. (2023) is that apart from the overestimation of the electron temperature, the IRM underestimates the electron density. Being a global model IRM gives the average value in the defined IR while in experiments the value in a certain volume ($\sim$10 mm^3, in case of Langmuir probe) is measured, and the average over the IR can be lower. This would explain the overestimation of the temperature since power has to be distributed over the lower number of electrons. The other way to look at the problem is accepting that IRM underestimates the ionization rate and the reason for that is non-uniformity of the plasma in the IR volume. One phenomenon that contributes to non-uniformity in ionization is known as spokes that arise in magnetron sputtering discharges, and their nature is highly debated and global model such as IRM cannot help in this matter (see Section 4.1).

In the IRM two distinct electron populations are assumed: "cold" or primary electrons e_c and "hot" or secondary electrons e_h. The reason for this choice is explained in details in Huo et al. (2017). The use of two distinct electron populations gives two primary benefits. First, it provides a more precise ionization costs based on electron energy. For example, metal ionization degree, degree of self-sputtering, and bulk electron temperature tend to decrease, while gas rarefaction and plasma density tend to increase if two electron populations are assumed, as compared to the first version of the IRM where only one electron population is assumed (Raadu et al., 2011). These trends are explained by the reduced energy required for ionization due to the presence of "hot" electrons introduced earlier. Secondly, this allows the quantification of two electron heating mechanisms: secondary electron acceleration through the sheath and ohmic heating in the IR. The power transferred to the electrons is expressed by:

$$P_e = P_{SH} + P_{Ohm} \tag{4.3}$$

where P_e gets divided into sheath energization P_{SH} and ohmic heating P_{Ohm}. This is done by breaking down the discharge voltage into two components: the potential drop over the sheath and the potential drop in the ionization region as shown in Eq. (2.17). In each segment, electrons get a part of the total electric power, $I_D V_{SH}$ and $I_D V_{IR}$ respectively, determined by the share of the current they transport (see Figure 2.11.1).

The power transfer to the "hot" electrons that travel through the sheath is derived from the ion currents to the target as calculated by the model (Huo et al., 2017).

$$P_{SH} = I_{e,SH} V_{SH} = \left(I_{Ar+} \gamma_{Ar+,eff} + \frac{1}{2} I_{M^2+} \gamma_{M^2+,eff} \right) V_{SH} \tag{4.4}$$

where $\gamma_{Ar+,eff} = \gamma_{Ar+} m \varepsilon_e (1-r)$ is the effective secondary electron emission yield for Ar^+-ions bombarding the target and $\gamma_{M^{2+},\,eff} = \gamma_{M^{2+}} m \varepsilon_e (1-r)$ is the effective secondary electron emission yield for doubly ionized metal ions bombarding the target, and ε_e represents the fraction of the electron energy that is used for ionization before being lost from the discharge

process. The values in parentheses on the right indicate the amount of secondary electrons emitted by argon ions and doubly ionized metal ions from the target.

In the ionization region the electrons are heated by ohmic heating:

$$P_{\mathrm{Ohm}} = I_{\mathrm{e,IR}} V_{\mathrm{IR}} = \left\langle \frac{I_{\mathrm{e}}}{I_{\mathrm{D}}} \right\rangle I_{\mathrm{D}} V_{\mathrm{IR}} \tag{4.5}$$

where $\langle I_{\mathrm{e}}/I_{\mathrm{D}} \rangle$ is the volume average of the fraction of the discharge current in the IR that is carried by electrons, taken to be $\approx 1/2$. The electron current is small at the cathode sheath edge, while at the boundary to the diffusion region the electrons carry almost the entire discharge current. The electron current over the ionization region is therefore on average $I_{\mathrm{D}}/2$ (Huo et al., 2013). V_{IR} is the fraction of the discharge voltage that drops across the IR: $V_{\mathrm{IR}} = f V_{\mathrm{D}}$.

These two electron heating mechanisms transfer the energy to distinct populations of the electrons, which define the EEDF. The electron populations vary in their ionization rate coefficients and effective ionization costs, and are considered as distinct "hot" and "cold" components, allowing to treat them separately.

4.8 Effective ionization cost

In the case of low pressure, low temperature, partially ionized plasma discharges, the power is mainly absorbed by electrons that transfer it to other species through collisions. The rate of cooling of electrons can be described as the sum of the losses due to different elastic and inelastic collisions with neutral species. Dividing it by the rate of ionization by electron impact yields the effective ionization cost or energy loss per electron-ion pair created $\mathscr{E}_{\mathrm{c}}^{(X)}$ (Lieberman and Gottscho, 1994). So, for every ionization reaction that creates a pair of ion and electron there is energy that the electron consumes, not only on ionization but also on elastic and inelastic collisions as well. The *effective ionization cost* $\mathscr{E}_{\mathrm{c}}^{(X)}$ can be expressed as:

$$\mathscr{E}_{\mathrm{c}}^{(X)} = \mathscr{E}_{\mathrm{iz}}^{(X)} + \sum_i \mathscr{E}_{\mathrm{ex},i}^{(X)} \frac{k_{\mathrm{ex},i}^{(X)}}{k_{\mathrm{iz}}^{(X)}} + \frac{k_{\mathrm{el}}^{(X)}}{k_{\mathrm{iz}}^{(X)}} \frac{3 m_{\mathrm{e}}}{M^{(X)}} T_{\mathrm{e}} \tag{4.6}$$

where $\mathscr{E}_{\mathrm{iz}}^{(\mathrm{X})}$ is the ionization energy of species X; $\mathscr{E}_{\mathrm{ex},i}^{(\mathrm{X})}$ is the excitation energy; $k_{\mathrm{iz}}^{(X)}$ is the rate coefficient of ionization of species X; $k_{\mathrm{ex},i}^{(X)}$ is the rate coefficient of the i^{th} excitation process of species X; $k_{\mathrm{el}}^{(\mathrm{X})}$ is the elastic scattering rate coefficient of species X; m_{e} is the electron mass; and $m^{(X)}$ is the mass of species X. The terms on the right hand side of Eq. (4.6) therefore represent the electron energy loss due to ionization, excitation and elastic scattering on neutral atoms.

The exact value of $\mathscr{E}_{\mathrm{c}}$ depends on the material, the reaction rate and the energy of the electron and are pre-calculated in the IRM. Where the rates of elastic collisions, excitation and

ionization reactions are summed up and used to calculate the consequential effective cost of ionization, taking energy thresholds into account. Reaction cross sections highly depend on the energy of the incoming electron, so the energy distribution of the electrons needs to be taken into account.

In IRM the two electron populations (primary and secondary) are used and the effective ionization cost is pre-calculated for all the energy ranges:

- "cold" electrons with energies from 1 to 7 eV, resolution 0.001 eV;
- "hot" electrons with energies from 200 to 1000 eV, resolution 0.1 eV.

For the primary electron population the dependence of $\mathscr{E}_c$ on T_e can be fitted in a form of an exponent of a polynom. For the secondary electron population using a constant or linear fit proves adequate as the elastic cross sections become negligible (see Section 4.7.2).

For singly ionized metals the effective double ionization cost is used as the second ionization energy that corresponds to the threshold energy for the ionization: $M^+ \longrightarrow M^{2+}$.

4.9 Sputter yield

Sputtering refers to the process where atoms are ejected from a solid or liquid surface as a result of bombarding by energetic particles, typically ions. The fundamental sputtering parameter is the *sputtering yield* $Y_{g/SS}$ for incident working gas (g) and target ions (self-sputtering, SS):

$$Y_{g/SS} = \frac{\text{number of ejected target particles}}{\text{number of incident ions (g or SS)}} \tag{4.7}$$

and is defined as the average number of atoms displaced from a target surface per incident ion, and the sputtering yield depends on the incident ion energy, $\mathscr{E}_i$, the incidence angle, θ, the masses of the incoming ion and the the target species, M_i and M_t, and the surface binding energy, $\mathscr{E}_{sb}$ of the target material (Bundesmann and Neumann, 2018). The maximum transferable energy in a collision has to be larger than the surface binding energy in order to sputter the atom. The minimum ion energy required for sputtering to take place is known as the threshold energy for sputtering $\mathscr{E}_{th}$ and is given by Yamamura and Tawara (1996) in a form:

$$\begin{aligned} \frac{\mathscr{E}_{th}}{\mathscr{E}_{sb}} &= \frac{6.7}{\Lambda}, && M_i \geqslant M_t, \\ &= \frac{1+5.7\,(M_i/M_t)}{\Lambda}, && M_i \leqslant M_t, \end{aligned} \tag{4.8}$$

where Λ is an energy transfer factor $4M_iM_t/\left(M_i+M_t\right)^2$.

Depending on the energy and type of the incoming ion bombarding the target with defined surface properties, the number of sputtered atoms will be different. The voltage applied to

the cathode target almost entirely drops across the target sheath (Lieberman and Lichtenberg, 2005, p. 170). It means that the ions will be accelerated towards it gaining the kinetic energy $\Delta\mathscr{E}_{\text{kin}}$:

$$\Delta\mathscr{E}_{\text{kin}} \approx Qe\Delta V_{\text{SH}} \approx QeV_{\text{D}} \tag{4.9}$$

where Q is the number of electrons removed from the ion. In the IRM the energy of an ion is solely defined by V_{D} and the average number of such released atoms is used.

Several empirical models exist that describe the sputter yield and the angular distribution in relation to the ion bombardment energy and the various ion-target material pairings (Sigmund, 1969; Dembowski et al., 1986; Yamamura and Tawara, 1996; Eckstein, 2007). The sputter yield for a specific ion bombarding a particular target can also be derived as a function of incident particle energy using computational codes such as TRIM (Transport of Ions in Matter) (Biersack and Haggmark, 1980), with upgraded versions such as SRIM (Stopping and Range of Ions in Matter) (Ziegler et al., 2008, 2010), TRIDYN (Möller and Eckstein, 1984; Möller et al., 1988) and Kalypso (Karolewski, 2005). The latter codes are TRIM simulations that includes dynamical composition changes. These packages are based on numerical simulations, which means a substantial computational load. This is particularly true to the dynamical codes. Therefore, determining the characteristics such as the sputter yield, as well as the angular and energy distributions of the sputtered particles, using analytical expressions is beneficial. These expressions may be entirely empirical or based on a simplified theoretical model (Bogaerts et al., 2008).

When a particle hits the cathode surface, some atoms, known as primary knock-on atoms, can absorb a significant amount of energy from the incoming ion as a result of the collision. These, in turn, can collide with other atoms, transferring momentum. Tracking these mechanisms and calculating their combined effect is important (Sarakinos and Martinu, 2020). Depending on the energy of the incident particles and the collisional cross section between the incident particles and the atoms of the target, the identification of the regime can simplify the modeling for a particular case (Bundesmann and Neumann, 2018; Behrisch and Eckstein, 2007):

- Single knock-on regime for light ions and low energy heavier ions. The recoil atoms resulting from collisions between the incident particles and target atoms acquire enough energy to sputter off the target; however, they do not have enough energy to initiate a collision cascade.
- Linear cascade regime. Recoil atoms from the incident ion and target atom collisions receive enough energy to generate recoil cascades. However, the density of recoil atoms is low, knock-on collisions with atoms of the target at rest dominate, and collisions between moving atoms are rare.
- Spike regime. The density of recoil atoms is high enough and the majority of atoms in a certain volume is set in motion.

The typical sputter processes, where ion energies are $\lesssim 1$ keV, falls into the single knock-on regime, and in particular magnetron sputtering falls into the lower energy part of the linear cascade process.

The sputter yield used in the IRM for ions bombarding the target was in some cases taken from Anders (2010a) where it was based on the calculations by the TRIM code, and fitted assuming a dependence on the form:

$$Y_{\mathrm{g/SS}} = a_k \mathscr{E}_k^{b_k} \tag{4.10}$$

where a_k and b_k are fitting parameters that are given for a particular combination of bombarding ion and target materials.

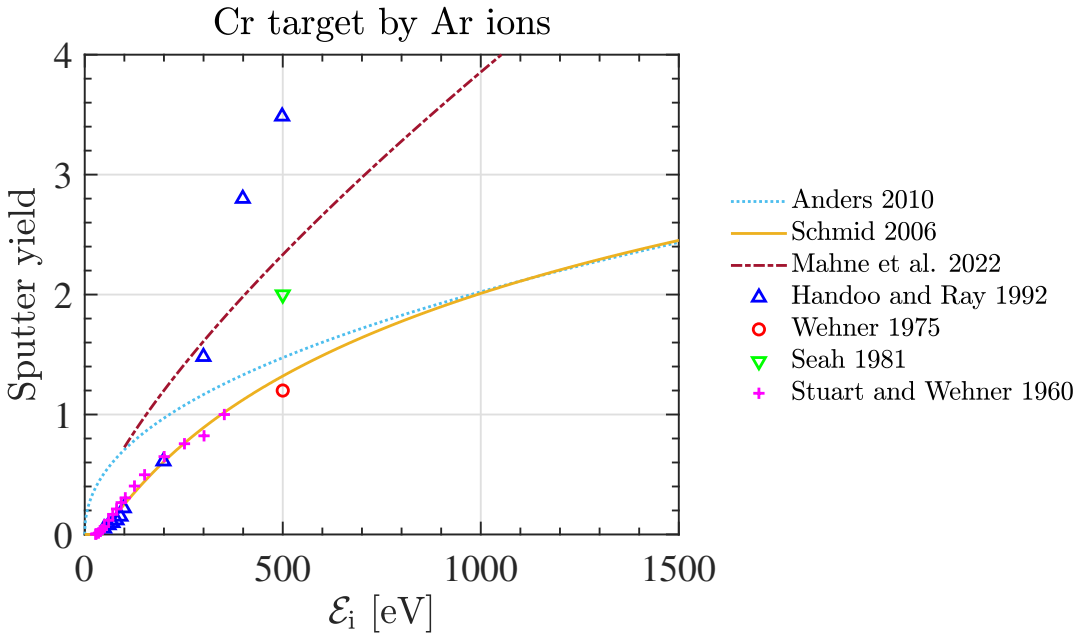

Figure 4.9.1. Sputtering yield of chromium by argon ions. Theoretical fits are taken from Anders (2010a), Schmid (2006) and Mahne et al. (2022). Experimental data points are from Handoo and Ray (1992), Wehner (1975), Seah (1981), and Stuart and Wehner (1960).

In the latest version of the IRM, the sputter yield is now determined using the IAP/TU Wien Sputter Yield Calculator (Schmid, 2006). The reason for switching to the Wien Sputter Yield Calculator in determining the sputter yield is that it is in better agreement with the experimental data (see Figure 4.9.1 and Figure 4.9.2). The IAP/TU Wien Sputter Yield Calculator is based on analytical expression for sputter yields at normal incidence, developed by Matsunami et al. (1984), which are further based on equations by Yamamura et al. (1983).

Matsunami et al. use the formula

$$Y(\mathscr{E}) = 0.42 \frac{\alpha^* Q K s_\mathrm{n}(\varepsilon)}{U_\mathrm{s}\left[1 + 0.35 U_\mathrm{s} s_\mathrm{e}(\varepsilon)\right]} \left[1 - (\mathscr{E}_\mathrm{th}/\mathscr{E})^{1/2}\right]^{2.8} \tag{4.11}$$

to determine the sputter yield, $Y(\mathscr{E})$, where $Y(\mathscr{E})$ is the yield of sputtering by incident ions at an energy of $\mathscr{E}$; α^*, Q and $\mathscr{E}_\mathrm{th}$ are empirical parameters; U_s is the sublimation energy in eV; $s_\mathrm{n}(\varepsilon)$ and $s_\mathrm{e}(\varepsilon)$ are Lindhard's elastic and inelastic stopping functions, respectively. These functions are expressed in terms of the reduced energy ε and can be found in Matsunami et al. (1983).

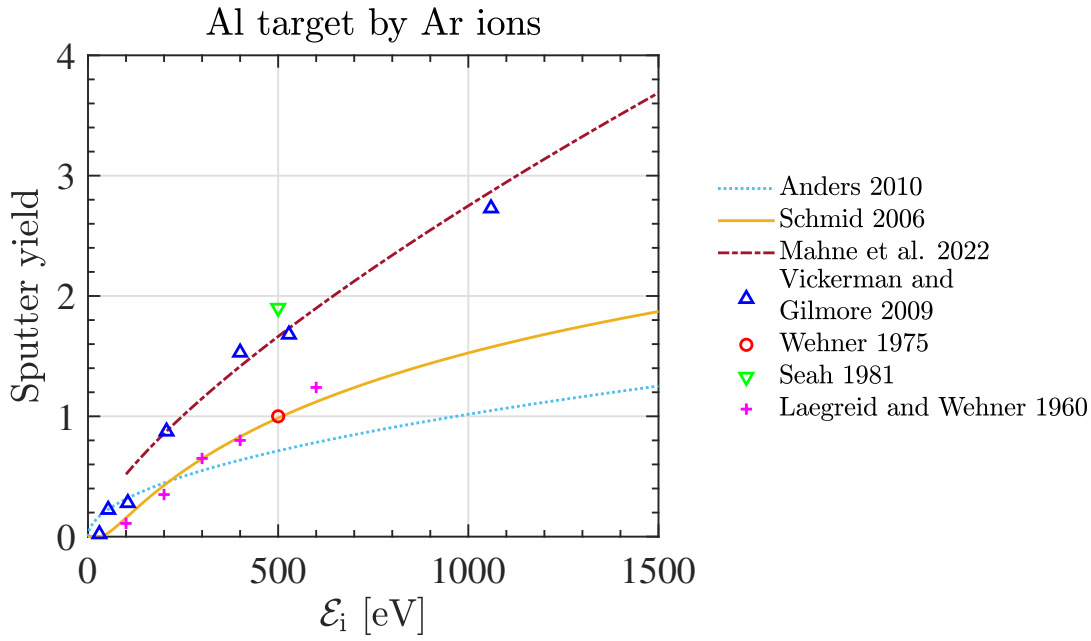

Figure 4.9.2. Sputtering yield of aluminum by argon ions. Theoretical fits are taken from Anders (2010a), Schmid (2006), Mahne et al. (2022). Experimental data points are from Vickerman and Gilmore (2009), Wehner (1975), Seah (1981), and Laegreid and Wehner (1961).

Although there is some ambiguity in the literature if the sputter yield is temperature dependent – if the rate enhancement effects are due to enhanced sputtering or onset of sublimation/evaporation (Anders, 2010a), in the IRM this is not taken into account.

Note that in HiPIMS operation self-sputtering can play a significant role. Furthermore, self-sputtering and the self-sputter yield are responsible for the working gas-free sputtering in the HiPIMS discharges. In the HiPIMS processes, the discharge includes ionized sputtered material, and the amount of it depends on various factors such as pulse power density, material of the target and pressure of the working gas. This indicates that a portion, frequently a noteworthy portion, of the ions participating in the sputtering process consists of ions of the target material (see Section 4.11 and 4.12). This suggests that a significant portion of the ions of the sputtered species may be drawn back to the target, rather than being deposited onto the substrate to create a film or coating. Self-sputtering and the associated self-sputter yield can substantially influence the HiPIMS operation, significantly affecting the film deposition rate, particularly for metal targets. Therefore, under specific circumstances, HiPIMS processes can also operate through self-sputtering (see Section 3.2). This is notably the case for materials with a high self-sputter yield. Furthermore, it was shown that the magnetron sputtering discharge is capable of self-sustaining with a Cu target and can escalate to high discharge current through self-sputter runaway (Andersson and Anders, 2008). However, despite a significant self-sputter component, the pulsed nature of the discharge makes it difficult to operate without working gas at all (see Section 4.11).

4.10 Secondary electron emission

Ions that bombard the target not only sputter its atoms but also produce *secondary electrons*, which in the IRM are referred to as "hot" electrons after they have been accelerated across the cathode sheath. The release of secondary electrons is due to ions or neutral particles striking a target surface, and it has a significant role in discharge physics: in dcMS this is an important mechanism in sustaining the discharge, while in HiPIMS they also play some role. Secondary electrons are accelerated in the sheath away from the target and are trapped in the magnetic field from the magnet assembly where they join the primary (or "cold") electrons. The difference is that secondary electrons gain energy from the electric field of the sheath and can transfer it to the species in the IR. Depending on the discharge, secondary electron impact ionization can be the dominant process of generating ions.

The secondary electron emission yield γ_{SE} is defined as the average number of secondary electrons emitted per incident species. The sputter targets are maintained at high negative potentials, causing the secondary electrons to be accelerated away from the target surface with an initial energy equal to the target potential, leading to ionization of the gas in front of the cathode target. The created ions then bombard the cathode target and subsequently release more secondary electrons.

Generally, secondary electron emission due to ion bombardment depends on the surface material, its condition, the type of bombarding ion, and the energy of the ion, both kinetic and potential (Winter et al., 1991). Electrons are excited or ejected from the target or the projectile ion as a result of Coulomb interactions that are grouped in two categories: potential and kinetic, depending on the source of the electron excitation energy. Such excitations occur mostly in binary collisions at the surface or very shallow depths $\sim$10 nm (Sigmund and Schinner, 2020). The excited electrons can either be ejected directly into the vacuum or undergo a series of collisions within the target solid (process known as electron transport) on their way to the surface. The collisions are either elastic scattering with atomic nuclei, which cause significant deflections of the trajectories, or energy loss collisions by scattering with other electrons, depending on the availability of electronic states (Baragiola and Riccardi, 2008).

In an initial approximation, the secondary electron emission yield does not depend on the velocity of the bombarding particle when their energy is low. When a bombarding particle transfers sufficient kinetic energy to an electron in the target, the kinetic emission starts to contribute to the total yield. It occurs when a bombarding particle transfers sufficient kinetic energy to an electron in the target, at a threshold energy of around a few hundred eV. This becomes the predominant effect at even higher energies (Hannesdottir and Gudmundsson, 2016). In the typical HiPIMS discharge ion kinetic energies are 10 – 30 eV/amu, which is below the limit where this type of secondary electron emission becomes dominant $\approx$ 300 eV/amu. Clean metals, that is, metals free of oxidation, gas adsorption, and other contamination generally have a lower kinetic emission yield than contaminated metals (Phelps et al., 1999). So the emission of the secondary electrons is determined by the potential

energies of the ions arriving at the target surface in case of HiPIMS.

The model for potential electron emission resulting from the interaction of slow ionized or excited particles with surfaces is due to Hagstrum (1954), who developed a semi-empirical theory based on his experimental results and previous considerations (Hasselkamp, 1992). It is believed that the potential emission is due to processes involved in resonance, Auger and quasi-resonant transitions (Hasselkamp, 1992).

Based on this, the secondary electron emission yield used in the IRM is sometimes calculated according to Baragiola and Riccardi (2008). They give the secondary electron emission yield for clean target in the form:

$$\gamma_{\mathrm{SE}} = 0.032\left(0.78\mathscr{E}_{\mathrm{pot}} - 2\phi\right) \tag{4.12}$$

where $\mathscr{E}_{\mathrm{pot}}$ is the potential well, the ionization energy in this case, and ϕ is the work function of the target surface.

The potential electron emission is only possible when $0.78\mathscr{E}_{\mathrm{pot}} > 2\phi$. Which is not satisfied for the first ionization energies for any metal target. It means only doubly ionized metal ions produce secondary electrons. In earlier versions of the IRM this secondary electron emission from doubly ionized ions was neglected but in updated version this emission was included in a form:

$$\gamma_{\mathrm{SE}} = 0.032\left(0.78\mathscr{E}_{1\to 2} - 2\phi\right) \tag{4.13}$$

where $\mathscr{E}_{1\to 2}$ is the second ionization energy. Data on first and second ionization energy is taken from Kramida et al. (2024).

For the case where the target being bombarded by the argon ions, there is more data available (Phelps and Petrović, 1999), where the research combined the experimental data and modeling.

The next energy dependent formula combines kinetic and potential electron emission for the argon ions is used in IRM (from (Phelps and Petrović, 1999), see Phelps et al. (1999) as well):

$$\gamma_{\mathrm{SE}}^{\mathrm{Ar}}(E \leq 500\mathrm{eV}) \approx 0.07 \tag{4.14}$$

$$\gamma_{\mathrm{SE}}^{\mathrm{Ar}}(\mathscr{E} > 500\mathrm{eV}) \approx \frac{10^{-5}\mathscr{E}(\mathscr{E}-500)^{1.2}}{1+(\mathscr{E}/70000)^{0.7}} \tag{4.15}$$

where Phelps and Petrović (1999) combined the experimental data and modeling to develop the fit. As we see it is energy dependent for argon ions with energies above 500 eV.

In IRM the secondary electron emission yield by argon ions is considered to be independent on the target material as suggested by Phelps and Petrović (1999). While it is an assumption, the lack of experimental data makes it impractical to assume otherwise. The electron emission yield is highly sensitive to a degree of poisoning of the target, and in a case of reactive sputtering, the more careful consideration needs to be taken.

A magnetic field near the cathode surface can significantly affect the emission of secondary electrons. After emission, the movement of secondary electrons is dictated by the motion equation, leading to complicated trajectory above the cathode (see Section 2.9). Despite

the strong repulsive electric field, a portion of the secondary electrons can still make their way back to the cathode, where they are either reflected or recaptured, which reduces the secondary electron emission yield. Thus, it is necessary to separate the standard γ_{SE}, which is dependent on the material, and the effective secondary electron emission yield $\gamma_{SE,eff}$ as observed in the discharge (Gudmundsson and Lundin, 2020). The recapture probability in HiPIMS discharges has been examined by Huo et al. (2013) and Gudmundsson et al. (2016), who report values ranging from $r = 0.50$ to 0.86. In the current work, the median value of $r \approx 0.7$ is used. Typically, the recapture is expected to be influenced by the system's geometry, the magnetic field, target erosion, and operational parameters like the working gas pressure (Buyle et al., 2003).

4.11 Gas and self-sputter recycling

In HiPIMS the discharge current waveforms show significant variations with the target material, pulse length, applied power (Anders et al., 2007), and if operated in metal or poisoned mode (Gudmundsson, 2016). As the discharge current increases, magnetron sputtering discharges are typically described as going through different regimes: they first operate in a regime dominated by working gas sputtering, then transition to gas-sustained self-sputtering, and at the highest currents they enter either a fully self-sustained self-sputtering mode or a self-sputter runaway regime (Anders, 2008b; Huo et al., 2014).

To describe the current evolution the generalized recycling model (Gudmundsson, 2016) can be used. The idea of the model is to focus on the ion current at the target surface, where the electron fraction of the discharge current is insignificant due to an effective secondary electron emission yield typically below 0.1. The ions that hit the target are separated into three groups depending on their history: primary ions of the working gas, which are ionized for the first time, recycled ions of the process gas, and ions of the sputtered species. Following the discussion in Brenning et al. (2017), the left feedback loop in Figure 4.11.1 represents the recycling of the working gas. The primary current I_{prim} is defined by those atoms and molecules of the process gas (index g), which are ionized for the first time, with a probability α_{prim} , and then go to the target. I_{prim} acts as a seed for the whole discharge current. The ions in I_{prim} are neutralized at the target and a fraction ξ_{pulse} return to the discharge during the pulse. Embedded Ar atoms are most likely to leave the target when it is bombarded by ions (Huo et al., 2014). This corresponds to a value $\xi_{\mathrm{pulse}} = 1$, which is used in the IRM. The returning gas atoms are subsequently ionized with a probability α_{g}, and drawn back to the target with a probability β_g. The remaining fraction ($1 - \beta_{\mathrm{g}}$) goes to the surrounding volume.

The right feedback loop in Figure 4.11.1 describes the self-sputter recycling. Each ion in I_{g} sputters target atoms with a sputter yield Y_{g}, which are subsequently ionized with a probability α_{t} and drawn back to the target with a probability β_{t}. This is the start of a self-sputter recycling process. The self-sputtering parameter is defined as (Hosokawa et al., 1980; Anders et al.,

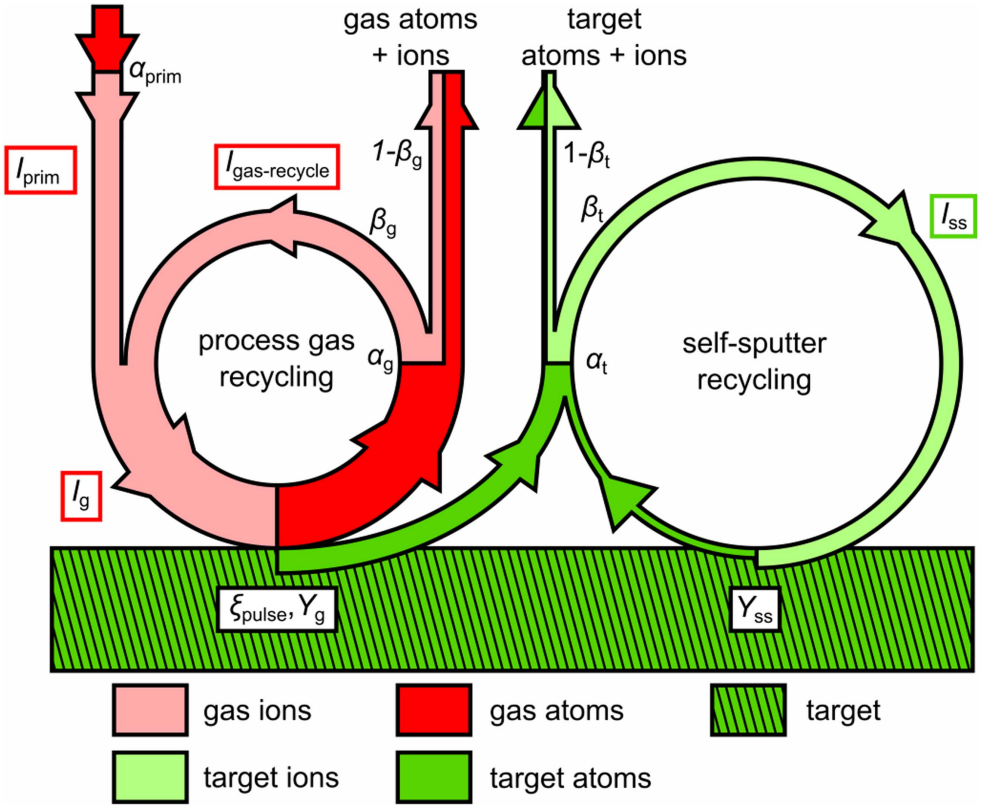

Figure 4.11.1. A schematic illustration of the combined processes of the working gas and the self-sputter recycling. I_{prim} is the primary current, I_g is the working gas ion current, $I_{gas-recycle}$ is the current carried by recycled working gas ions, I_{SS} is the target ion current, Y_g is the sputter yield of the target by the working gas ions, Y_{SS} is the self-sputter yield, α_{prim}, α_g and α_t are the ionization probability of the working gas atoms, ionized for the first time, the returning working gas atom and the sputtered target atom, respectively, β_g and β_t, are the back-attraction probability of the working gas and sputtered target ions to the target, respectively, and ξ_{pulse} is the fraction of the neutralized ions that return to the discharge during the pulse. Reprinted from Brenning et al. (2017), with permission of IOP Publishing.

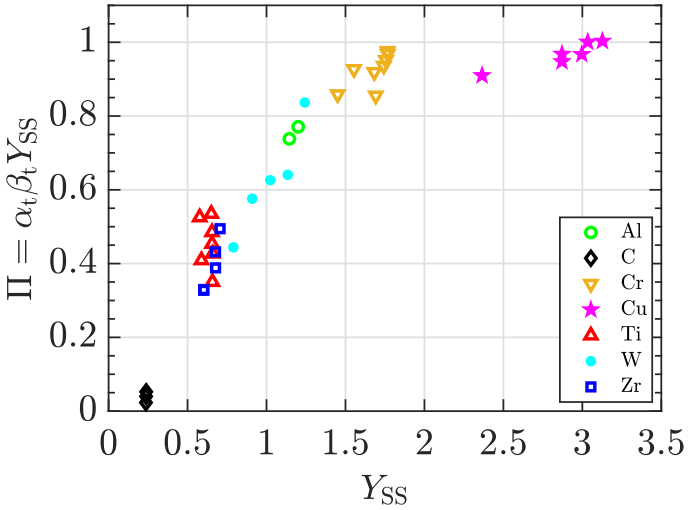

Figure 4.11.2. The self-sputter parameter, $\Pi = \alpha_t \beta_t Y_{SS}$, versus the self-sputter yield, Y_{SS} for a number of experimental discharges simulated by the IRM, listed in Table 1 of the attached Article II.

2007):

$$\Pi = \alpha_t \beta_t Y_{SS} \tag{4.16}$$

where Y_{SS} is the self-sputter yield. If $\Pi > 1$ there is a runaway, which means that the release of atoms by sputtering amplifies until it reaches the arc regime or the power limit of the power supply and is suppressed. If the ionization and loss processes balance each other, a new steady state is reached with a high current. In this case $\Pi = 1$, which means that the discharge can purely run on self-sputtering without working gas species. Anders (2008b) attributed the self-sputtering runaway to the production and influence of doubly and higher charged ions. Later this conclusion became questionable since there are not that many multiply charged ions in HiPIMS discharge due to high threshold energy, and the runaway cannot be purely attributed to it (Huo et al., 2013).

The study by Brenning et al. (2017) found a gradual trend: targets with high sputter yields produce discharges driven primarily by self-sputter recycling, while targets with low self-sputter yields result in discharges governed by working gas recycling or by a mixture of gas and self-sputter recycling. When targets have a high sputter yield, the discharge sputters large quantities of target atoms that are easily ionized. This leads to efficient self-sputter recycling, which makes it possible to sustain high discharge currents. In contrast, in discharges using target materials with a low self-sputter yield, ions sputter only small amounts of target atoms and instead depend on ionizing the working gas, a process that requires electrons with higher energy. Even in such cases the current can reach high values through the gas recycling when the working gas is substantially ionized. This gradual transition in the self-sputter parameter, which approaches unity for discharges with chromium and copper targets. This can be seen in Figure 4.11.2, that shows the self-sputter parameter for experimental discharges studied with the IRM and discussed further in Article II in Chapter 7.

The effect of the self-sputter yield on the behavior of HiPIMS discharges is different from the low-current dcMS regime, where the proportion of sheath energization is governed primarily by the secondary electron emission coefficient of the process gas ions (Brenning et al., 2017).

The IRM does not distinguish between α_g and α_t, as well between β_g and β_t, assuming the ionization probability and the back-attraction probability do not depend on the atom being of the target or of the working gas.

4.12 Internal discharge parameters

In thin film deposition, the main parameters that the industry is concerned about are the deposition rate and the ionized flux fraction (IFF) of the species that form the film. For HiPIMS operation the influence of the external control parameters -— such as working gas pressure, pulse waveform, and magnetic field strength – on both the deposition rate and the IFF is commonly studied in terms of two internal discharge parameters: the ionization probability of the sputtered atoms, α_t, and the probability that ions of the sputtered species are back-attracted to the target, β_t. When modeling a discharge, these two internal discharge parameters give a quantitative measure of both the quality and the efficiency of the deposition process. So, understanding how α_t and β_t vary in response to changes in external parameters is a key to optimization of HiPIMS discharges. The complication with using these parameters in HiPIMS is that the pathway model that introduced them requires the steady state, which is not always possible in HiPIMS (Vlček and Burcalová, 2010).

Experimentally, using a QCM (see Section 2.4.1), it is possible to measure the deposition rate, IFF, and calculate the probability $\alpha_t\beta_t$ of ionized sputtered species being back-attracted to the cathode target (Bradley et al., 2015). However, the study by Brenning et al. (2021) shows that minor changes in $\alpha_t\beta_t$ can hide significant and opposing individual variations in α_t and β_t, so these two parameters should be examined independently. Later it was demonstrated by Hajihoseini et al. (2019) that both α_t and β_t could be determined by the QCM measurements. However, to do this properly, the ratio of transport parameters had to be known. The transport parameters ξ_{ti} and ξ_{tn} for ions and neutrals, respectively, relate the fluxes out of the diffusion region and the fluxes onto the ion meter, and, in general, are not equal (Britun et al., 2015) (see Section 2.4.1). The variation in the transport parameters with distance from the target surface was later studied by Hajihoseini et al. (2022) for a discharge with titanium target and the relative ion-to-neutral transport factor, ξ_{ti}/ξ_{tn}, is determined to be in the range from 0.4 to 1.1, depending on the distance and magnet configuration. In some of the early works the transport parameter ratio used in the IRM was based on the work of Britun et al. (2015), and is assumed to be twice higher at the distance of the substrate, where the QCM is located, for neutrals than the transport parameter for ions, $\xi_{tn} = 2\xi_{ti}$.

To lock the IRM and confine the two free parameters f and $\beta_{t,pulse}$, the ionized flux fraction (and the experimentally measured discharge current waveform) is necessary (Butler et al.,

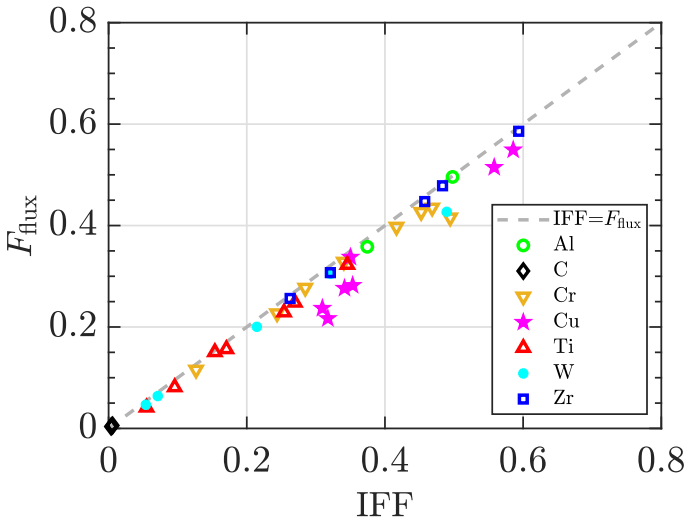

Figure 4.12.1. Comparison of the ionized flux fraction calculated using the internal discharge parameters determined by IRM (F_{flux}) with the ones measured using QCM or fitted in the IRM (IFF). The transport parameters for neutrals ξ_{tn} and ions ξ_{ti} are assumed to be $\xi_{\text{tn}} = 2\xi_{\text{ti}}$. The data points here and on the next figures in this section are taken from modeled HiPIMS discharges using a graphite (Eliasson et al., 2021), a zirconium (Suresh Babu et al., 2024), a titanium (Rudolph et al., 2021, 2020), a tungsten (Suresh Babu et al., 2022), an aluminum (Raadu et al., 2011), a chromium (Barynova et al., 2026), and a copper (Gudmundsson et al., 2022) target. The experimental operating parameters for the modeled discharges are listed in Table 1 of the attached Article II.

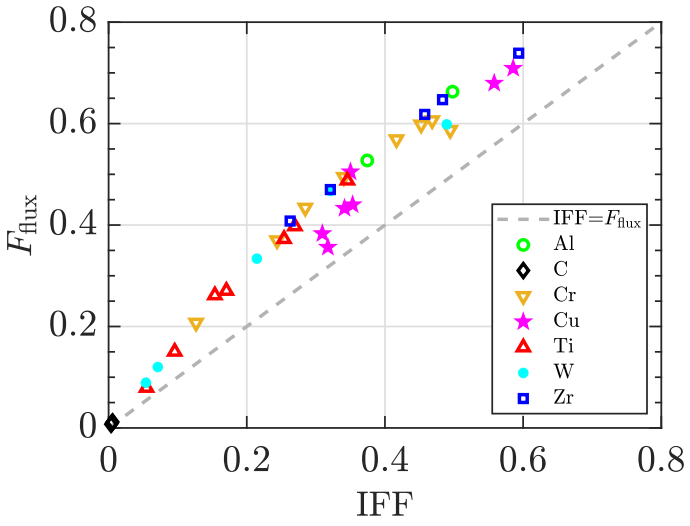

Figure 4.12.2. The ionized flux fraction F_{flux} calculated using the internal discharge parameters determined by the IRM α_t and β_t, assuming that transport parameters for neutrals ξ_{tn} and ions ξ_{ti} are equal, versus the IFF measured using QCM or fitted in the IRM.

2018). The ionized flux fraction, F_{flux}, onto a substrate is related to the time-integrated total number of metal atoms and metal ions reaching the ion meter over the discharge pulse, T, can be written as:

$$F_{\text{flux}} = \frac{\int_T \tilde{\Gamma}_{\text{ti}}(t)\mathrm{d}t}{\int_T \left(\tilde{\Gamma}_{\text{tn}}(t) + \tilde{\Gamma}_{\text{ti}}(t)\right)\mathrm{d}t} \tag{4.17}$$

where $\tilde{\Gamma}_{\text{ti}}$ is the target ion species flux onto the ion meter, and $\tilde{\Gamma}_{\text{tn}}$ is the target neutral species flux onto the ion meter. Then F_{flux} onto a substrate is related to the time-integrated total number of metal atoms and metal ions leaving the IR for the diffusion region (DR) over the discharge pulse as:

$$\begin{aligned} F_{\text{flux}} &= \frac{\xi_{\text{ti}} \int_T \Gamma_{\text{ti}}^{\text{DR}} dt}{\xi_{\text{tn}} \int_T \Gamma_{\text{tn}}^{\text{DR}} dt + \xi_{\text{ti}} \int_T \Gamma_{\text{ti}}^{\text{DR}} dt} = \frac{\int_T \Gamma_{\text{ti}}^{\text{DR}} dt}{\frac{\xi_{\text{tn}}}{\xi_{\text{ti}}} \int_T \Gamma_{\text{tn}}^{\text{DR}} dt + \int_T \Gamma_{\text{ti}}^{\text{DR}} dt} \\ &= \left(1 + \left(\frac{\xi_{\text{tn}}}{\xi_{\text{ti}}}\right) \frac{\int_T \Gamma_{\text{tn}}^{\text{DR}}(t)\mathrm{d}t}{\int_T \Gamma_{\text{ti}}^{\text{DR}}(t)\mathrm{d}t}\right)^{-1} = \frac{1}{1 + \frac{\xi_{\text{tn}}}{\xi_{\text{ti}}} \frac{1-\alpha_{\text{t}}}{\alpha_{\text{t}}(1-\beta_{\text{t}})}} \end{aligned} \tag{4.18}$$

where $\Gamma_{\text{tn}}^{\text{DR}}$ is the total flux of target neutrals and $\Gamma_{\text{ti}}^{\text{DR}}$ is the total flux of target ions into the diffusion region, and T is the pulse period (Christie, 2005; Butler et al., 2018; Hajihoseini et al., 2022; Rudolph et al., 2021).

For the case $\xi_{\text{tn}} = 2\xi_{\text{ti}}$ this becomes

$$F_{\text{flux}}(\xi_{\text{tn}} = 2\xi_{\text{ti}}) = \frac{\alpha_{\text{t}}(1-\beta_{\text{t}})}{2 - \alpha_{\text{t}}(1+\beta_{\text{t}})} \tag{4.19}$$

Figure 4.12.1 shows the comparison of the ionized flux fraction calculated using the internal discharge parameters determined by the IRM (F_{flux}) with the one measured using QCM or fitted in the IRM (IFF). The transport parameters for neutrals ξ_{tn} and ions ξ_{ti} are assumed to be $\xi_{\text{tn}} = 2\xi_{\text{ti}}$. We see there is in general a good agreement between the calculated and measured values.

Often the case $\xi_{\text{tn}} = \xi_{\text{ti}}$ is used, then F_{flux} becomes

$$F_{\text{flux}}(\xi_{\text{tn}} = \xi_{\text{ti}}) = \frac{\alpha_t\,(1-\beta_t)}{1 - \alpha_t \beta_t} \tag{4.20}$$

See Figure 4.12.2 for the comparison of the ionized flux fraction F_{flux} calculated using the internal discharge parameters α_{t} and β_{t}, assuming that the transport parameters for neutrals ξ_{tn} and ions ξ_{ti} are the same, and the IFF measured using QCM or fitted in the IRM. We see that in this case there is a significant discrepancy between the calculated and measured values.

The deposition rate and its variation with the internal discharge parameters are also of interest. The sputter rate-normalized deposition rate F_{sput} is

$$F_{\text{sput}} = \frac{\xi_{\text{tn}} \int_T \Gamma_{\text{tn}}^{\text{DR}} dt + \xi_{\text{ti}} \int_T \Gamma_{\text{ti}}^{\text{DR}} dt}{\xi_{\text{tn}} \int_T \Gamma_{\text{sput}} dt} \tag{4.21}$$

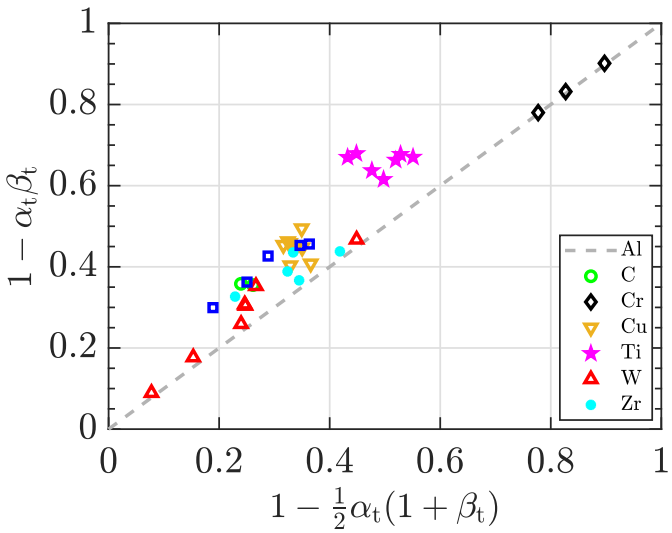

Figure 4.12.3. The comparison of the sputter rate-normalized deposition rate F_{sput} assuming that the transport parameters for neutrals ξ_{tn} and ions ξ_{ti} are: (x-axis) $\xi_{tn} = 2\xi_{ti}$, giving $F_{sput} = 1 - \frac{1}{2}\alpha_t(1+\beta_t)$; (y-axis) $\xi_{tn} = \xi_{ti}$, giving $F_{sput} = 1 - \alpha_t\beta_t$, when F_{sput} is described using the internal discharge parameters.

where Γ_{sput} is the flux of sputtered atoms. F_{sput} can also be written in terms of the internal discharge parameters (Rudolph et al., 2021):

$$F_{sput} = (1-\alpha_t) + \left(\frac{\xi_{ti}}{\xi_{tn}}\right)\alpha_t\,(1-\beta_t) \tag{4.22}$$

In the case $\xi_{tn} = 2\xi_{ti}$ it can be simplified to:

$$F_{sput}(\xi_{tn} = 2\xi_{ti}) = 1 - \frac{1}{2}\alpha_t(1+\beta_t) \tag{4.23}$$

For a case more often considered in the literature, $\xi_{tn} = \xi_{ti}$ it is simply

$$F_{sput}(\xi_{tn} = \xi_{ti}) = 1 - \alpha_t\beta_t \tag{4.24}$$

The values of F_{sput} from Eq. (4.23) and Eq. (4.24) are compared in Figure 4.12.3. Here, the difference between the two values of the transport parameter ratio, ξ_{ti}/ξ_{tn}, is less pronounced.

As can be seen, to increase the deposition rate two different parameters can therefore be influenced: decrease the probability of ionization of the sputtered atoms α_t, and/or decrease the ion back-attraction probability β_t.

A parameter that the IRM can give an insight on, is the fraction of the ion current carried by Ar^+ ions, ζ, and it can be estimated using the formula from Hosokawa et al. (1980):

$$\zeta = \frac{I_{Ar^+}}{I_{Ar^+} + I_{Cr^+}} = \frac{1-\alpha_t\beta_t Y_{SS}}{1+\alpha_t\beta_t\left(Y_g - Y_{SS}\right)} \tag{4.25}$$

where Y_{SS} is the self-sputter yield, and Y_g is the sputter yield of the target by the working gas ions. Figure 4.12.4 shows the fraction of Ar^+ ions versus self-sputter yield. The figure

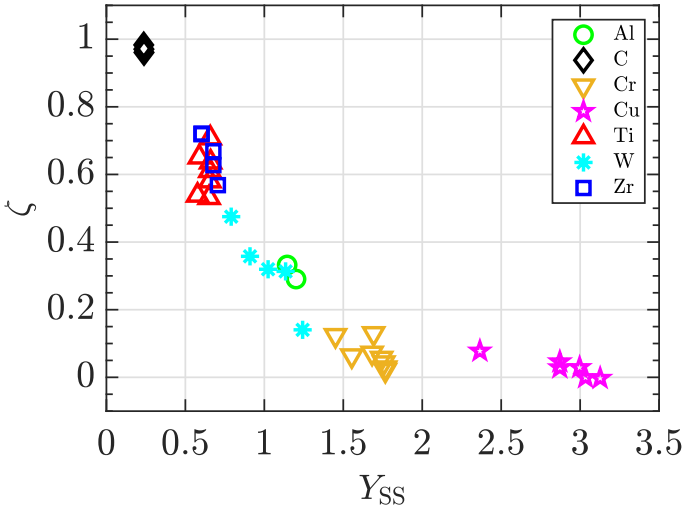

Figure 4.12.4. The fraction of the argon ion current in the total discharge current calculated from the internal discharge parameters α_t and β_t versus the self-sputter yield Y_{SS}.

shows how the role of Ar^+ ions in the sputter process decreases with increasing self-sputter yield, calculated using the Eq. (4.25). The fraction of Ar^+ ions in the total ion current at the target surface is almost 100 % for a discharge with graphite target and falls to almost zero for a discharge with copper target. This also indicates that a HiPIMS discharge with graphite target is operated on working gas recycling and a discharge with a copper target operates on self-sputter recycling, while discharges with titanium, tungsten, and zirconium targets operate on a mixture of the two operating modes (see Section 4.11).

The probability of back-attraction, directly connected to the ion escape probability as $1 - \beta_t$, has been evaluated for several HiPIMS discharges using different elemental targets (see Figure 4.12.5). It is observed that the probability of ion escape increases and that the discharge becomes increasingly metal rich with increasing self-sputter yield of the target material. This is important, because for a given ionized flux fraction, the deposition rate is higher when the back-attraction probability is lower. Furthermore, the self-sputter parameter $\alpha_t \beta_t Y_{SS}$ increases with increased self-sputter yield and approaches sustained self-sputtering for chromium and copper targets, both of which have high sputter yield (see Figure 4.11.2). One could ask why the discharge currents in discharges with strong metal recycling ($Y_{SS} > 1$) are not strongly amplified from these recycling loops. Oks and Anders (2009) have pointed out the importance of the electron cooling by metal atoms for stabilizing current fluctuations. In the current project, with the IRM it was shown that the systematically lower electron temperatures observed in discharges with high sputter yield materials prevent an uncontrolled amplification of the discharge current (Barynova et al., 2025).

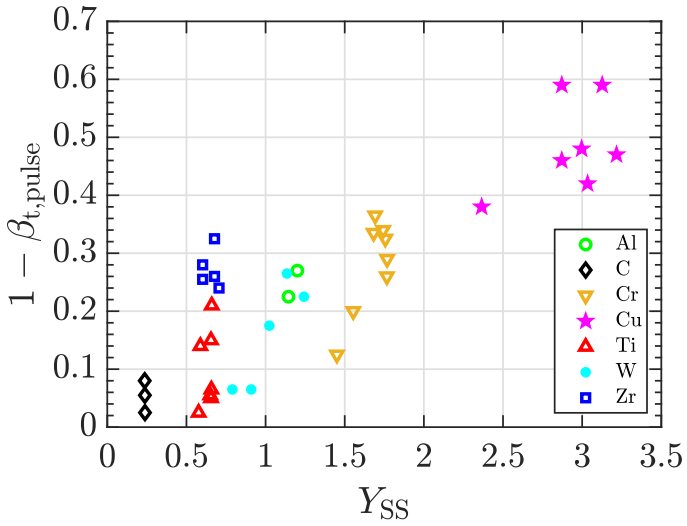

Figure 4.12.5. The ion escape probability of the target ion from the ionization region toward the diffusion region, $1-\beta_t$*, versus the self-sputter yield of the target material,* Y_{SS}*.*

4.13 Working gas rarefaction

4.13.1 Historic overview of rarefaction

The sputter process releases atoms of the film-forming species from the target, and the sputtered species enter the discharge volume with considerable energy, which, as a first approximation, can be described by the Thompson distribution (Thompson, 1968; Hofer, 1991; Gnaser, 2007). The interaction between the energetic sputtered particles and the working gas atoms not only influences the momentum of the sputtered species, but also the discharge properties as it leads to a reduction in the working gas density, and an increase in the working gas temperature in front of the cathode target. The pressure drop was first identified in a dc magnetron sputtering (dcMS) discharge, in the cylindrical configuration, by Hoffman (1985), who referred to the observed phenomena as 'sputtering wind', as he argued this to be a pressure variation resulting from collisions between the sputtered particles and the working gas atoms. This phenomena was further explored experimentally in planar dcMS discharges by Rossnagel *et al.* (Rossnagel, 1988a; Rossnagel and Kaufman, 1988; Rossnagel, 1988b) and Drüsedau (2002), who observed a pressure drop just in front of the cathode target and referred to it as working gas rarefaction or gas heating. Rossnagel *et al.* (Rossnagel, 1988a; Rossnagel and Kaufman, 1988) found the working gas rarefaction to depend on the discharge current, sputter yield, sputtered species type (velocity and collision cross section) and the mass of the sputtered species and the working gas atoms. They further argued that the reduction in working gas density drives up the plasma impedance.

These studies were followed by a development of analytical models to describe the working gas rarefaction process (Rossnagel, 1988a; Drüsedau, 2002; Palmero et al., 2005, 2006). The occurrence of rarefaction has also been observed using the direct simulation Monte Carlo

(DSMC) method (Kobayashi, 2001; Kadlec, 2007; Kersch et al., 1994) and particle-in-cell Monte Carlo simulations (Serikov et al., 1999; Kolev and Bogaerts, 2008) of dc magnetron sputtering discharges. In fact, it has been suggested that working gas rarefaction improves both the deposition rate and the coverage in sub-micron sized holes (Kobayashi, 2001). Working gas rarefaction has been observed experimentally in HiPIMS operation (Alami et al., 2006). Kozák and Lazar (2018) performed a 3D DSMC simulation of a rarefaction process for several consecutive pulses in HiPIMS operation in a sufficiently large volume with realistic working gas flow for a few targets and compared it to the results of the volume averaged models, and found that global models underestimate working gas rarefaction.

4.13.2 Kick-out mechanism

Within the IRM, the reduction of gas density due to the sputter wind is modeled as an argon kick-out mechanism, resulting from interactions with fast sputtered particles (Raadu et al., 2011; Huo et al., 2017). Where "kick-out" is a momentum transfer followed by a removal from the IR. In Barynova et al. (2024) we modify the model to also include Ar^H ("hot" ground state argon) species that originate from the target and have a considerable energy ~ 2 eV. Species of Ar^W ("warm" ground state argon), which also originate from the target, are not considered to contribute to the kick-out, since their energy of 0.1 eV is insufficient to substantially influence gas rarefaction by kicking-out argon species. "Hot" argon atoms are formed when argon ions recombine at the target surface and leave it with energies comparable to sputtered atoms ($\sim 1/2\,\mathscr{E}_{sb}$ right after the impact, see Section 2.5). In contrast, "warm" argon atoms originate from argon ions that are implanted a few atomic layers beneath the target surface and subsequently diffuse back out, carrying only thermal energy.

In this study revisions have been made to the kick-out term in the IRM code based on previous works (Raadu et al., 2011; Huo et al., 2012, 2017). In deriving a kick-out term, X refers to the species causing the kick, while Y represents the species being kicked out. Here, X is represented by {M, Ar^H}, with M being target atoms, and Y includes {Ar^C, Ar(4s[3/2]$_2$), Ar(4s'[1/2]$_0$)}. Within the model, when species X collides with species Y, species Y is promptly removed from the IR, provided two conditions are satisfied:

- At a working gas temperature of 500 K, the momentum of species X is bigger than the average momentum of "cold" Ar species (species Y). Considering the mass of the lightest target atom, carbon, as $M = 12M_p$, where M_p is the proton mass, and setting the ejection energy $\mathscr{E}_{ejection}$ to $\frac{1}{2}\mathscr{E}_{sb} = 3.7$ eV (Eliasson et al., 2021), results in a momentum of 10^{-22} kg m/s. This is greater than the average momentum of argon at $T_g = 500$ K, which is approximately 10^{-23} kg m/s. Thus, the first condition is satisfied.

- In HiPIMS, the pulse duration exceeds the typical loss time of species Y from the IR post-collision. For instance, a collision at the IR's midpoint with height $h = 2$ cm and velocity $v = 1000$ m/s results in species Y being lost within $t = h/2v = 10$ μs. The HiPIMS pulses analyzed are 3 to 20 times longer, validating the assumption. Although this assumption may slightly underestimate argon density, it remains valid for

the discharges studied here.

Moreover, for argon projectiles Ar^H colliding with Ar^C, we disregard the impact of direct collisions, which would just swap velocity vectors without altering the argon density in the IR. Angled collisions, in contrast, lead to both particles exiting the IR.

For each species X, there exists a probability of colliding with those of species Y. This probability is represented by Poisson

$$F_{\text{coll,X}\to\text{Y}} = 1 - \exp\left(-\frac{L}{\lambda_{\text{X}\to\text{Y}}}\right) \tag{4.26}$$

where L is the height of the IR, and $\lambda_{\text{X}\to\text{Y}}$ is the mean free path of a species X in a background gas composed of species Y is given by:

$$\lambda_{\text{X}\to\text{Y}} = \frac{1}{\sigma_{\text{X}\to\text{Y}} n_{\text{Y}}}. \tag{4.27}$$

where the cross sections $\sigma_{\text{X}\to\text{Y}}$ are the momentum transfer cross sections, as discussed above for each pair of X and Y, and n_{Y} is the density of species Y.

$F_{\text{coll,X}\to\text{Y}}$ could be interpreted as the momentum fraction transferred from the sputtered species to the ejected species Y. Then the sputter flux Γ_{sputter} (m^{-2} s^{-1}) is related to the kick-out flux Γ_{kickout} leaving the IR as follows:

$$R_{\text{kickout,X}\to\text{Y}} = F_{\text{coll,X}\to\text{Y}} \Gamma_{\text{sputter,X}} \frac{S_{\text{RT}}}{\mathscr{V}_{\text{IR}}} = \Gamma_{\text{kickout}} \frac{S_{\text{DR}}}{\mathscr{V}_{\text{IR}}}, \tag{4.28}$$

where $\mathscr{V}_{\text{IR}}$ is the volume of the IR, S_{RT} is the surface area of the IR facing the racetrack, and S_{DR} is the surface area of the IR facing the diffusion region (Raadu et al., 2011). The sputtered flux is

$$\Gamma_{\text{sputter,X}} = \sum_i \Gamma_i^{\text{RT}} Y_i(\mathscr{E}_i) \tag{4.29}$$

where $Y_i(\mathscr{E}_i)$ is the sputter yield for an ion species i bombarding the target. In such a way, the kick-out rate directly depends on the sputter rate. Eq. (4.28) actually corresponds to six equations, each depicting a pair (X,Y) of species X that's kicking out and species Y being kicked out. It is assumed in this model that at most one collision occurs between a sputtered species and a gas species. Given the long mean free path of sputtered species in the IR compared to the IR's typical height, this assumption is reasonable.

4.13.3 Rarefaction with IRM

Figure 4.13.1 illustrates a summary of the gas rarefaction model within the IRM, showing the various pathways that argon atoms can follow during the processes associated with working gas rarefaction. This study focused on the behavior of argon atoms within the IR, specifically how they enter and exit the IR. Green arrows represent neutral atoms, orange arrows – "hot" and "warm" argon atoms (Ar^H and Ar^W) and blue arrows – ions. Arrows represent the processes considered for rarefaction and are featured in the time-resolved plots in the related

article (Barynova et al., 2024). Argon ions that bombard the target return to the IR as "hot" argon atoms (Ar^H, reflected from the target) or "warm" (Ar^W, diffused back from the target) argon atoms, each with probability 50%. Argon atoms can be kicked out into the diffusion region (DR) by "hot" argon atoms Ar^H and by sputtered metal neutrals (not shown in Figure 4.13.1 as it only features argon). "Cold" Ar^C atoms can be refilled from the DR through the diffusion. It is shown that diffused Ar^W and Ar^H can be ionized and back-attracted again. This cycle can reoccur several times, acting as a recycling loop for the working gas (Brenning et al., 2017). Eventually, these heated argon atoms escape from the IR. To not overestimate the contribution of ionization to the overall rarefaction, in the following only the first ionization of the argon species are counted (hatched horizontal arrow). This can then be compared to the kick-out of argon neutrals by sputtered species and "hot" argon atoms (vertical hatched arrow). These are the two principal processes that lead to working gas rarefaction.

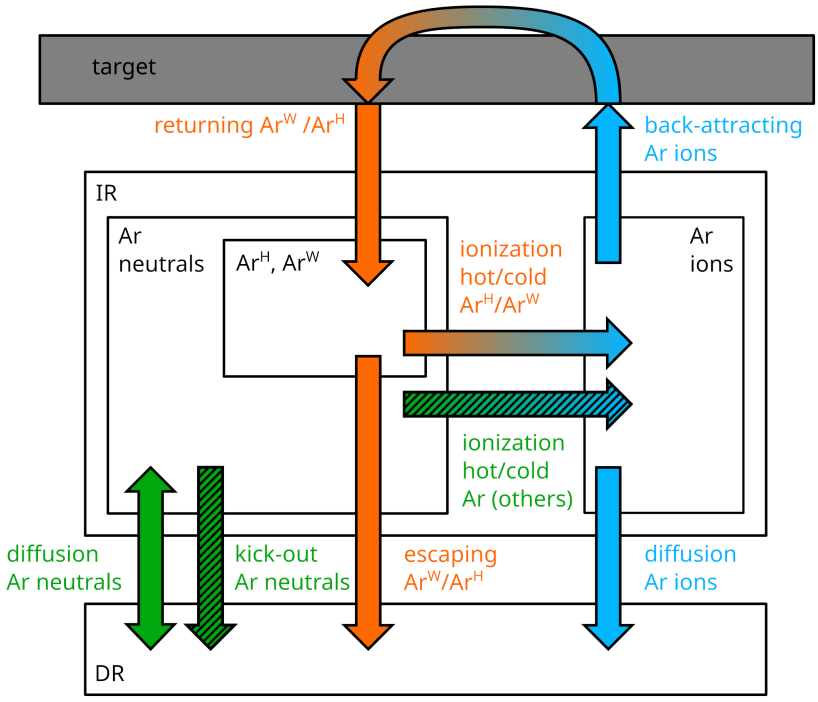

Figure 4.13.1. Scheme of the processes involved in working gas rarefaction. The green arrows denote the neutrals, orange the "hot" (Ar^H) and "warm" (Ar^W) argon atoms, and blue arrows denote the ions. Reprinted from Barynova et al. (2024) ©IOP Publishing. All rights reserved.

The ionization probability increases smoothly with increased discharge current at first (Rudolph et al., 2022). However, at high discharge current density this increase is slower due to working gas rarefaction. This leaves the back-attraction probability as the parameter of interest. Which is important, because this is the parameter that essentially determines the deposition rate for a given discharge peak current density. To achieve this goal the two target materials were added to the studied discharge systems: zirconium (Suresh Babu et al., 2024) and chromium (Barynova et al., 2026). Furthermore, all the previously studied discharge systems were re-evaluated for this study, and re-calculated using the revised approach for the kick-out term. This was required as the IRM has been updated over the years.

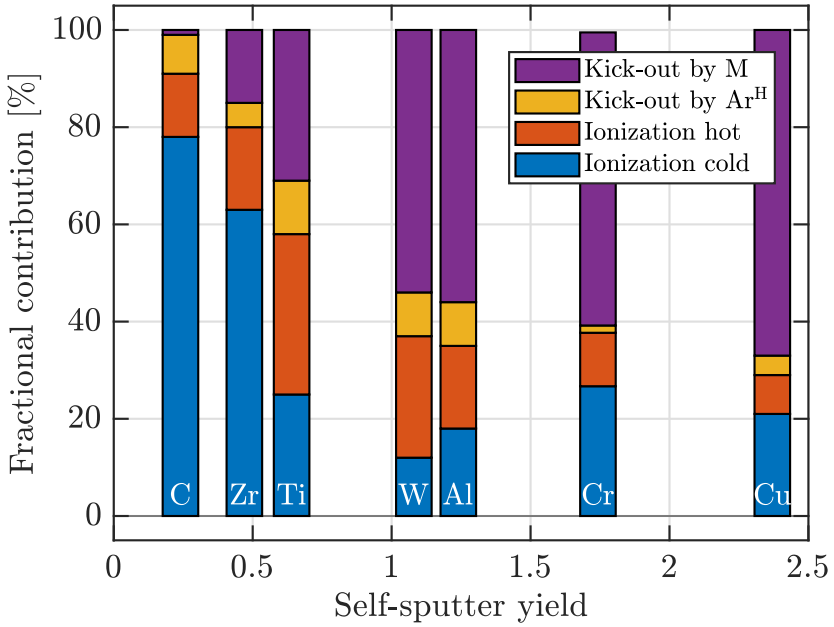

Figure 4.13.2. The fractional contribution of the various processes to working gas rarefaction within the ionization region versus self-sputter yield.

Since the article on the IRM study of rarefaction in HiPIMS discharges (Barynova et al., 2024) was published in June 2024 we have updated the final figure showing the fractional contributions from different rarefaction processes versus the self-sputter yield by adding data for a discharge with a chromium target. This updated version of the figure is featured as Figure 4.13.2. The HiPIMS discharge with the chromium target fills the previous gap in the self-sputter yield and follows the general trend.

The IRM doesn't consider heating in the gas rarefaction process. As well IRM neglects the angular distribution of sputtered atoms, assumes their energy to be $\frac{1}{2}\mathscr{E}_{\mathrm{sb}}$, and relies on the volumetric rate coefficients for collision reactions, it cannot account for the dependence on the incidence angle and the spacial distribution of the species inside the IR. The other uncertainty that IRM brings is how the probability of collision (for the kick-out term) is defined by Eq. (4.26) assuming the average particle's path length through the IR is simply equal to the height of the IR.

The spatial extend of the working gas rarefaction in dcMS and HiPIMS is much larger then the size of the IR according to experimental data (Alami et al., 2006; Palmucci et al., 2013; Greczynski et al., 2017). This means that the IRM overestimates the return of Ar atoms into the IR by the diffusion and underestimates the time needed to return to equilibrium after the pulse is turned off. Kozák and Lazar (2018) also conclude that volume averaged description of the sputtering wind effect on gas rarefaction is insufficient to capture the interaction of sputtered atoms with the process gas in front of the target under various conditions without tuning the parameters for each individual case.

4.14 Ar/Ne mixture as the working gas

The high discharge voltage in HiPIMS leads to a high fraction of ionized sputtered metal species, which has been experimentally observed for various metallic targets. For these targets the deposited films exhibit higher mass density and improved crystallinity overall. While for a graphite target the measured ionized flux fraction has been found to be significantly lower or below 5 % (DeKoven et al., 2003). Furthermore, Sarakinos et al. (2012) have reported that C^+ ions constitute only about 1 % of the total ionic contribution in the substrate region.

This is of significance when depositing amorphous carbon films, as bombardment of the substrate by energetic ions during deposition is known to increase the sp^3 content in the deposited films, which enhances the film properties. It is established that the mechanical properties and the film mass density of the amorphous carbon films depend on the sp^3/sp^2 bonding ratio (Robertson, 1994). It is referred to as diamond-like carbon (DLC) when the amorphous carbon film contains a significant fraction of tetrahedrally bonded carbon sp^3 (Robertson, 2002), and when the sp^3 content is larger than 60 % it is called tetrahedral amorphous carbon (ta-C) (Casiraghi et al., 2007). Amorphous carbon films with high sp^3 content are mechanically very hard, resistant to scratching, have high dielectric constants, and exhibit excellent optical transparency. These are highly desired properties for a wide range of applications (Lettington, 1998; Casiraghi et al., 2007), in particular for films that are utilized as protective and wear resistance coatings (Erdemir and Donnet, 2006; Donnet and Erdemir, 2008; Hauert et al., 2013).

Despite the limited ionized carbon flux fraction, the deposition of DLC films by HiPIMS (DeKoven et al., 2003; Aijaz et al., 2012; Sarakinos et al., 2012), bipolar HiPIMS (García et al., 2020), and deep oscillation magnetron sputtering (DOMS) (Lin et al., 2014) has been explored. These studies using HPPMS generally report on deposited films that exhibit improved DLC properties compared to dcMS deposited DLC films.

One approach that has been suggested in order to increase the ionization of carbon and to increase the ionized carbon flux fraction is to use working gas atoms with high ionization potential. This includes using neon as the working gas instead of argon or a mixture of the two (Aijaz et al., 2012; Aijaz and Kubart, 2017; Ferreira et al., 2021; Cardoso et al., 2021; Vahidi et al., 2021; Oliveira et al., 2024). Neon has ionization potential of 21.56 V, which is higher than the ionization potential of argon 15.76 V. Adding neon to the discharge is therefore expected to increase the average electron energy. This was indeed demonstrated by (Petrov et al., 1990), who observed higher electron temperature and higher ion energy for C^+ ions when operating with neon compared to using argon as the working gas, as they sputtered graphite target in a dcMS discharge. Furthermore, in HiPIMS operation it has been shown experimentally, that the electron temperature increases with increased neon content in the Ar/Ne mixture (Aijaz et al., 2012). More recently, Schmidt et al. (2013) measured comparable ion fluxes for Ne^+ and C^+ ions in a HiPIMS discharge with a graphite target when operated in neon atmosphere. They found increased peak discharge current with increased ionization potential which implies elevated average electron energy. Furthermore, they observed that the

relative, but not the total C^+ ion flux, is largest when the graphite target is sputtered in pure Ar as the working gas, followed by Ne and Kr. Also they found the deposition rates to be higher when the graphite is sputtered in Kr and Ar atmosphere, while in the Ne atmosphere the deposition rates are lower. Aijaz et al. (2012) determined the ion energy distribution function (IEDF) in a HiPIMS discharge in Ar/Ne mixture with graphite target. A low energy peak around 1 eV is determined to correspond to thermalized carbon ions in addition to a high-energy peak that shifts up to about 10 – 12 eV with increasing Ne content in the Ne/Ar gas atmosphere. They also determined the electron energy distribution function (EEDF) and find it to consists of two electron populations, a low-energy and a high-energy populations.

The addition of neon to the discharge has been claimed to lead to a substantial increase in carbon ionization in HiPIMS operation and lead to enhanced film properties. Vahidi et al. (2021) report smoother DLC film surfaces, lower sliding coefficient of friction, better wettability, higher surface free energy, and higher hardness when depositing with Ar/Ne mixture compared to using pure argon as the working gas. In fact while depositing with deep oscillation magnetron sputtering the sp^3 content in the top section of films deposited in Ar/Ne mixture discharge is found to be close to 40 % and remain constant across the film thickness while for films deposited in pure argon discharge, the sp^3 content decreases from approximately 30 % to 18 % towards the surface (Oliveira et al., 2024). However, Vitelaru et al. (2018), despite reporting improved DLC film properties as a result of adding neon to the HiPIMS discharge, argue that when the discharge is operated with significant working gas recycling, and therefore adding neon to the working gas mixture, does not influence the carbon ionization much.

The IRM for a HiPIMS discharge with graphite target and Ne or Ne/Ar mixture as the working gas was developed. The assumed species in the IRM for the discharge in neon as a working gas are the ground state neon atom and the metastable levels, Ne^+ and Ne^{2+} ions, and "warm" and "hot" neon atoms, in addition to the species discussed in Section 4.7.1.

CHAPTER 5

SUMMARY OF ARTICLES

5.1 Article I. On working gas rarefaction in HiPIMS

The study focused on analyzing different contributions to the working gas rarefaction for a number of different target materials (Barynova et al., 2024). The interaction between the atoms and ions of the sputtered material and the working gas leads to a decreased density of the working gas as the sputtered particles kick-out argon species from the IR as they move through it. In the literature, this phenomenon is referred to as sputter wind, causing the working gas rarefaction. Furthermore, the density of the working gas can also be reduced by other processes, like the ionization of the working gas atoms and their subsequent attraction towards the cathode target. At the same time, processes exist that refill the working gas near the target, including diffusion from the bulk plasma and the return of recombined working gas atoms from the target. The discharge conditions and plasma chemistry are altered by the rarefaction of working gas in front of the cathode target, which consequently affects the deposition rate.

The IRM was applied to determine the degree of working gas rarefaction and the relative contribution of various processes to working gas rarefaction in HiPIMS discharges with different target materials. The study showed that the predominant contribution to the working gas rarefaction of the various processes varies between the different target materials. For targets with low sputter yields, electron impact ionization is the dominant process. Such as in the case of a graphite target with argon as the working gas at 1 Pa, electron impact ionization (by both primary and secondary electrons) is the dominant contributor to working gas rarefaction, with more than 90% contribution, while the contribution of sputter wind kick-out is small $< 10\%$. While for high sputter yield target materials, such as tungsten or copper targets, the kick-out of argon atoms by metal atoms is the dominant contributor, with over 60% contribution. For discharges with metal targets, the kick-out of argon atoms is mainly due to metal atoms sputtered from the target, and the kick-out by "hot" argon atoms that return from the target has a smaller contribution. The main finding is that the sputter

yield is the primary factor dictating which process is the most important when it comes to working gas rarefaction. The rarefaction of the working gas is more significant for the lower pressures, and the kick-out mechanism is much more important at higher working gas pressures. Furthermore, we note that in most cases there is a significant fraction of "hot" and "warm" argon atoms within the IR. This value is highest or 67 % when operating with the graphite target, and this fraction is smaller for the copper target (16 %) and the tungsten target (26 %).

The summary plot of the fractional contribution of the various processes to working gas rarefaction within the ionization region versus self-sputter yield is featured in Figure 4.13.2, updated with data for chromium target at 0.3 Pa.

5.2 Article II. Self-regulating electron temperature in high-power impulse magnetron sputtering discharges and its effect on the metal ion escape

The work that resulted in the second article (Barynova et al., 2025) focused on the analysis of IRM simulations of HiPIMS discharges with different target materials. The study is based on the results of modeling and simulating HiPIMS discharges, using the IRM, with 7 different target materials and 35 discharges in total with argon as a working gas. According to the IRM simulations, the electron temperatures stabilize at the end of a HiPIMS pulse ($T > 30$ μs) due to the balance reached between the electron heating and electron collision cooling processes. The cause of this is a self-regulating system, where the rate coefficients for ionization by primary electrons monotonically increase with increasing electron temperature, leading to a situation in which increased electron temperature boosts electron collisional cooling, and a decreased electron temperature slows down this cooling.

In addition, the IRM results show that the electron temperature in a steady state is inversely related to the sputter yield of the target material. The effect can be explained by the atomic composition in the IR. At low sputter yield the IR is mostly composed of argon, while at high sputter yield the IR is rich with sputtered metal. The self-regulating mechanism sustains a lower electron temperature in metal-rich discharges because the metal ionization rate coefficients are higher than those for argon at lower electron temperatures and the collisional cooling rate is proportional to it, sustaining the effective cooling. This affects the escape of metal ions in a HiPIMS discharge, as the ionization mean free path for sputtered atoms directly depends on the electron temperature. An ion created at a greater distance from the target has to overcome a smaller potential barrier, making it easier for the metal ion to reach the substrate. By using the IRM, we demonstrate that this can be the case. Figure 4.12.5 illustrates the target ion escape probability $1 - \beta_t$ for the discharges studied as a function of the self-sputter yield Y_{SS}. The general trend is evident, showing an increase in $1 - \beta_t$ as the

self-sputter yield increases.

In summary, discharges using target materials with high self-sputter yield, such as chromium or copper, exhibit a lower electron temperature, and are abundant in metal atoms that are easier to ionize. At these low electron temperatures, collisional cooling effectively counters electron heating. This lower temperature extends the mean free path for the ionization of metal atoms ejected from the target, leading to ionization occurring farther from the cathode, where the remaining potential hill to climb, in order for a metal ion to escape to the bulk plasma, is lower. As a result, metal ions can escape more readily towards the substrate, minimizing the loss in deposition rate. In contrast, discharges with target materials that have a low self-sputter yield, such as carbon or titanium, are dominated by argon within the IR. Here, collisional cooling is effective only at high electron temperatures due to argon's high ionization potential. In these cases, sputtered metal atoms ionize closer to the target, where they encounter strong back-attracting fields, leading to an increased loss in deposition rate.

5.3 Article III. High power impulse magnetron sputtering from a chromium target

HiPIMS discharges with chromium target and argon as a working gas were studied both experimentally and using the IRM model (Barynova et al., 2026). The experimental results indicate that, at a specific pulse length, the deposition rate declines while the ionized flux fraction rises as the discharge current density is increased within the range of 0.4 to 1.0 A/cm^2. The fraction of ionization in the chromium flux measured at the substrate position varies from 10 to 50%, the maximum for the highest peak discharge current density and the minimal pulse duration. The highest deposition rate is achieved with a pulse duration of 50 μs, and it decreases by reducing the pulse duration up to 25 μs or by extending it up to 200 μs.

The IRM provides insight into how species densities and the composition of discharge current change during the pulse. In addition, it provides modeled parameters on the voltage drop over the IR, the probability of ionization, and the probability of back-attraction of the sputtered target species. The modeling results show that the singly charged chromium ion is the dominant ion within the ionization region, and the discharge operates mainly in self-sputter recycling mode. We find that the back-attraction probability of the sputtered species decreases with decreasing pulse length and with increasing peak discharge current density. The probability of ionization for sputtered species rises with a higher peak discharge current. Initially, it also increases with longer pulse lengths, then reaches a maximum (50 μs), and then decreases as the pulse length continues to increase. Ohmic heating significantly contributes between 75% and 93% to the overall electron heating, and its influence grows with longer pulse durations and higher peak discharge current densities. Moreover, the kick-out of argon atoms from the IR due to sputtered chromium atoms was determined as the primary

factor in the rarefaction of the working gas, which is consistent with what has been modeled earlier (Barynova et al., 2024) for high sputter yield target materials, followed by electron impact ionization by the primary electrons.

5.4 Article IV. High power impulse magnetron sputtering of a zirconium target

This work (Suresh Babu et al., 2024) deals with HiPIMS discharges with a zirconium target, analyzing both experimental and results from IRM model. The ionized flux fraction measured varies between 25% and 59%, increasing as the peak discharge current density rises from 0.5 to 2 A/cm^2 at a working gas pressure of 1 Pa. Simultaneously, the measured deposition rate normalized by the sputter rate (meaning the back-attraction probability of the sputtered atoms) declines in line with the HiPIMS compromise.

With an empirical discharge current and voltage waveform, the IRM uses the measured ionized flux fraction to lock the model. The IRM was used to provide temporal variations of different species and calculate the average electron energy within the IR. Argon and zirconium ions both significantly contribute to the discharge current at the target surface, meaning, that the discharge operates on a combination of working gas and self-sputter recycling.

Additionally, the IRM determines the internal discharge parameters, including the ionization probability and the probability of back-attraction for sputtered species. The probability of ionization is found to be in the range of 73% to 91%, and the probability of back-attraction is in the range of 67% to 77%. In the discharges studied, significant rarefaction of the working gas is observed, in the range of 45 to 85%, higher for low pressure and higher peak discharge current density. Electron impact ionization is the primary factor in working gas rarefaction, accounting for more than 80% of the effect, and the kick-out by zirconium and argon atoms from the target has a much smaller impact. The significant role of electron impact ionization in the rarefaction of working gas is comparable to that in other materials with low sputter yield in agreement with Barynova et al. (2024).

CHAPTER 6

CONCLUSIONS

The ionization region model (IRM) was applied to determine the temporal variation of the species densities in high power impulse magnetron sputtering (HiPIMS) discharges, with different target materials, and for various operating conditions. The sputter yield is shown to be a key parameter that significantly changes the discharge composition, electron temperature, and, consequently, the possible limit on deposition rate and more or less determines the overall discharge characteristics. Analyzing the IRM simulation results, focusing on working gas rarefaction, it is observed that the primary parameter governing which rarefaction mechanism dominates in the discharge is the self-sputter yield (Barynova et al., 2024). Similarly, the importance of the self-sputter yield is found in the study of the impact of the target material on the self-regulating electron temperature in HiPIMS discharges (Barynova et al., 2025). Furthermore, the back-attraction probability is found to decrease with increasing sputter yield of the target material. The deposition rate scales with $1 - \alpha_t \beta_t$, which is found to increase with increasing sputter yield. Therefore, for a given ionization probability, it is beneficial to lower the back-attraction probability. Similarly, the lower the back-attraction probability, the smaller the decrease in deposition rate with increased ionization probability or increased current density. Previous studies highlight that a high sputter yield is responsible for the discharge current runaway and it determines the mode of gas recycling, thereby enabling gas-less sputtering. A preliminary study indicates that the sputter yield may also determine the fraction of ohmic heating in the overall power transfer to the electrons, and that this fraction increases as the sputter yield rises. Because it correlates with both the back-attraction probability of the ions and the ionization probability of the sputtered atoms, it makes it possible to connect the internal discharge parameters with the fraction of the current transported by the ions of the sputtered material. It is therefore clear from both the IRM simulations and earlier investigations that the sputter yield plays a decisive role in various aspects of HiPIMS discharge physics.

The main conclusion is that the sputter yield governs the effectiveness of the HiPIMS discharge. The IRM shows that the deposition rate increases with increasing sputter yield, and that the HiPIMS compromise is most advantageous for targets with high sputter yields. This indicates that, in practical use, the sputter yield should be considered one of the key criteria when selecting a material for a given application. The observed link between sputter yield and

electron temperature implies that using weaker magnets can help lower the probability of target ion back-attraction. Weaker magnets increase the mean free path of the sputtered particles before they are ionized, which compensates for the effect of the higher electron temperature.

CHAPTER 7

PUBLICATIONS

Article I

On working gas rarefaction in high power impulse magnetron sputtering

Kateryna Barynova, Martin Rudolph, Swetha Suresh Babu, Joel Fischer, Daniel Lundin, Michael A Raadu, Nils Brenning and Jon Tomas Gudmundsson

*Plasma Sources Science and Technology*33(6) (2024) 065010

OPEN ACCESS
IOP Publishing
Plasma Sources Science and Technology
Plasma Sources Sci. Technol. **33** (2024) 065010 (17pp)
https://doi.org/10.1088/1361-6595/ad53fe

On working gas rarefaction in high power impulse magnetron sputtering

Kateryna Barynova[1], Martin Rudolph[2], Swetha Suresh Babu[1], Joel Fischer[3], Daniel Lundin[3], Michael A Raadu[4], Nils Brenning[3,4] and Jon Tomas Gudmundsson[1,4,*]

[1] Science Institute, University of Iceland, Dunhaga 3, IS-107 Reykjavik, Iceland
[2] Leibniz Institute of Surface Engineering (IOM), Permoserstraße 15, 04318 Leipzig, Germany
[3] Plasma and Coatings Physics Division, IFM-Materials Physics, Linköping University, SE-581 83 Linköping, Sweden
[4] Division of Space and Plasma Physics, School of Electrical Engineering and Computer Science, KTH Royal Institute of Technology, SE-10044 Stockholm, Sweden

E-mail: tumi@hi.is

Received 19 February 2024, revised 26 April 2024
Accepted for publication 4 June 2024
Published 18 June 2024

Abstract

The ionization region model (IRM) is applied to explore working gas rarefaction in high power impulse magnetron sputtering discharges operated with graphite, aluminum, copper, titanium, zirconium, and tungsten targets. For all cases the working gas rarefaction is found to be significant, the degree of working gas rarefaction reaches values of up to 83%. The various contributions to working gas rarefaction, including electron impact ionization, kick-out by the sputtered species or hot argon atoms, and diffusion, are evaluated and compared for the different target materials, and over a range of discharge current densities. The relative importance of the various processes varies between different target materials. In the case of a graphite target with argon as the working gas at 1 Pa, electron impact ionization (by both primary and secondary electrons) is the dominating contributor to working gas rarefaction, with over 90% contribution, while the contribution of sputter wind kick-out is small $<10\%$. In the case of copper and tungsten targets, the kick-out dominates, with up to $\sim 60\%$ contribution at 1 Pa. For metallic targets the kick-out is mainly due to metal atoms sputtered from the target, while for the graphite target the small kick-out contribution is mainly due to kick-out by hot argon atoms and to a smaller extent by carbon atoms. The main factors determining the relative contribution of the kick-out by the sputtered species to working gas rarefaction appear to be the sputter yield and the working gas pressure.

Keywords: magnetron sputtering, high power impulse magnetron sputtering (HiPIMS), sputter yield, sputtering

* Author to whom any correspondence should be addressed.

1. Introduction

Magnetron sputtering [1–3] is a versatile and widely applied physical vapor deposition technique [4], in which the film-forming material is sputtered from a cathode target by ion bombardment. A discharge is formed in a working gas, preferentially constituting heavy noble atoms, most often argon. The ions for the sputter process are accelerated from a dense plasma region created near the target and confined there by a static magnetic field, that traps the electrons. Often, the discharge is driven by a dc voltage or current, in particular when depositing metallic films. In that case the sputtered species are mainly neutral atoms, and the ions available in the discharge are the ions of the working gas [3].

A variation of the magnetron sputtering technique is high power impulse magnetron sputtering (HiPIMS), where the discharge is driven by high power pulses delivered at a low repetition frequency, and with low duty cycle [5–7]. As a result of the HiPIMS process, the discharge is composed of atoms and ions of both the working gas and target material. Pulsing the discharge at high peak power results in a high peak discharge current density, increased electron density [3, 8], increased ionization of the sputtered species [9], and higher ionization fraction in the flux of film-forming species to the substrate [6, 10, 11], which ultimately leads to denser deposited films [12], that exhibit better crystallinity [13], and overall improved film properties [14, 15].

The sputter process releases atoms of the film-forming species from the target, and the sputtered species enter the discharge volume with considerable energy, which, as a first approximation, can be described by the Thompson distribution [16–18]. The most probable energy of the Thompson distribution corresponds to roughly half the cohesive energy of the solid target [17, 18]. The interaction between the energetic sputtered particles and the working gas atoms not only influences the momentum of the sputtered species, but also the discharge properties as it leads to a reduction in the working gas density, and increase in the working gas temperature, in front of the cathode target. The pressure drop was first identified in a dc magnetron sputtering (dcMS) discharge, in the cylindrical configuration, by Hoffman [19], who referred to the observed phenomena as 'sputtering wind', as he argued this to be a pressure variation resulting from collisions between the sputtered particles and the working gas atoms. This phenomena was further explored experimentally in a planar dcMS discharge by Rossnagel [20–22] and Drüsedau [23], who observed a pressure drop just in front of the cathode target and referred to it as working gas rarefaction or gas heating. Rossnagel [20, 21] found the working gas rarefaction to depend on the discharge current, sputter yield, sputtered species type (velocity and collision cross section) and the mass of the sputtered species and the working gas atoms. They further argued that the reduction in working gas density drives up the plasma impedance. Therefore, the discharge requires a higher discharge voltage to operate at the same discharge current, as the resulting current density is determined by the reduced concentration of the working gas species in the target vicinity. These studies were followed by a development of analytical models to describe the working gas rarefaction process [20, 23–26]. The occurrence of rarefaction has also been observed using the direct simulation Monte Carlo (DSMC) method [27] and particle-in-cell Monte Carlo simulations [28, 29] of dc magnetron sputtering discharges. In fact, it has been suggested that working gas rarefaction improves both the deposition rate and the coverage in sub-micron sized holes [27].

The HiPIMS discharge is operated at much higher peak discharge current densities than the dcMS discharge, and therefore, working gas rarefaction could be expected to be even more significant. However, as the duty cycle in HiPIMS operation is short, the gas refill during the off-times could result in lower working gas rarefaction on average. A brief discussion on how the rarefaction influences the discharge current waveform in HiPIMS operation was given by Lundin [30], where it was observed that several mechanisms lead to working gas rarefaction—not only sputter wind. Experimentally, using optical emission spectroscopy (OES) [31–36], measuring time-resolved ion saturation currents by a probe array [37], and mass spectrometry [38, 39], it has been demonstrated that working gas rarefaction occurs and can indeed be rather significant in HiPIMS discharges, and be even more pronounced for longer pulses [38]. Alami *et al* [31] observed almost an order of magnitude drop in the Ar^0 emission intensity when operating with a chromium target, 50 μs long pulses, an average current density of 2.8 A cm^{-2} and a working gas pressure of 0.8 Pa. Palmucci *et al* [33] also observed a strong gas rarefaction, which significantly reduces the sputtered species energy dissipation during a certain time interval at the end of a 20 μs long pulse, when operating with a titanium target. They referred to this phenomena as 'rarefaction window'. Incidentally, recent studies seem to indicate that working gas rarefaction may be a desired property of the discharge process in the case of HiPIMS operation and have some benefits for the deposition process [40, 41]. Using mass spectrometry, Greczynski *et al* [39] observed that the time- and energy integrated metal-ion-to-gas-ion ratio increases when the peak discharge current density is increased during HiPIMS operation. This, they claim to be due to working gas rarefaction. Also, they find this effect to become even stronger with increasing atom mass of the sputtered species. Vitelaru *et al* [42] applied time-resolved tunable diode-laser absorption spectroscopy measurements on the argon metastable (Ar^m) level $3s^23p^5(^2P^\circ_{3/2})4s$ excited by 801.478 nm photons, in the dense plasma region in front of the titanium cathode target in a HiPIMS discharge. From the Doppler profile they determined the temporal evolution of the working gas temperature and the metastable argon Ar^m density during the pulse as well as during the plasma afterglow. They showed that the metastable argon Ar^m density sharply increases at the beginning of the discharge pulse, followed by a severe Ar^m density depletion, along with increasing working gas temperature around the peak in the discharge current. The working gas temperature was found to increase during the pulse and more so with increased discharge current. This is in agreement with the increased sputtering of metal particles resulting in more

metal-argon collisions, and thus increased momentum transfer to the neutral working gas atoms, and increased density of hot working gas neutrals, due to recombination of Ar^+ ions.

Working gas rarefaction in HiPIMS operation has also been explored through modeling. Kadlec [43] studied the behavior of the neutral argon working gas atoms during a HiPIMS pulse by the three-dimensional DSMC method, assuming a titanium target. When the discharge current density reached the 2.2 A cm^{-2} range very strong gas rarefaction was observed. The volume density of sputtered metal exceeded the working gas density several times and the working gas atoms moved rapidly away from the target as a shock wave a few microseconds into the pulse. Note that in the DSMC simulations the ionization of the working gas is neglected. In a more recent study Kozák and Lazar [44] investigated working gas rarefaction in HiPIMS operation using a three-dimensional DSMC simulation and compared the findings to results from volume-averaged models. The DSMC results indicate that the working gas rarefaction is only slightly more pronounced for target atoms with higher mass and that the rarefied region extends much further from the target than the extent of the ionization region (IR), that is typically defined for volume-averaged modeling. They found that volume-averaged models provide good approximation for the temporal evolution of the target material density in front of the target compared to the DSMC simulation. However, they found the volume-averaged models underestimate the magnitude of the rarefaction during the pulse-on time, and predict faster return to equilibrium during the pulse-off time compared to the DSMC simulation. This is because the size of the IR assumed in volume-averaged modeling of the HiPIMS discharge is small and in reality the region where the working gas density is significantly reduced extends somewhat farther from the target surface than the extent of the high plasma density region that is maintained by the magnetic confinement. More recently the DSMC model has been updated to simulate the dynamics of both atoms and ions in an HiPIMS discharge [45].

The ionization region model (IRM) is a semi-empirical time-dependent volume-averaged plasma chemical model of the IR of the HiPIMS discharge. It provides the temporal evolution of the densities of ions, neutrals and electrons with known discharge current and voltage waveforms [46]. The IRM has been applied to model HiPIMS discharges in argon with aluminum [46–48], titanium [46, 49–51], copper [52], tungsten [53, 54], graphite [55], and zirconium [56] targets. From the IRM studies, using various target materials, it has been observed that there is indeed a significant working gas rarefaction. The IRM results have furthermore verified that several rarefaction mechanisms are involved [47]. When operating a HiPIMS discharge with an aluminum target it has been shown that electron impact ionization has the largest contribution to working gas rarefaction [47], while when operating with a tungsten target the sputter wind appears to have the largest contribution [53].

Here, using the IRM, we explore the relative contributions of the various mechanisms that contribute to the working gas rarefaction in HiPIMS discharges with a few different target materials, in the order of increasing atomic mass, graphite, aluminum, copper, titanium, zirconium, and tungsten. This we do by reevaluating the IRM results for discharges studied in the past, while focusing on the rarefaction processes. In section 2 we give an introduction to the IRM and the various terms that contribute to working gas rarefaction. There we also introduce an updated kick-out term into the IRM. The temporal evolution of the gain and loss processes of argon atoms within the IR, as well as diffusion of argon atoms in and out of the IR, for the six target materials, spanning a wide range in atomic mass and sputter yield, is evaluated in section 3. The results are discussed in section 4, where we determine the main contributor for working gas rarefaction and how they depend on the target material and which parameter determines which contributor is the most important. The main findings are summarized in section 5.

2. The IRM

The IRM is a global plasma chemistry model of the IR of a pulsed magnetron sputtering discharge. The IR is taken to be an annular cylinder with outer radius r_2, and inner radius r_1 sitting above the race track of width $w_{RT} = r_2 - r_1$, and height $L = z_2 - z_1$, extending from z_1 to z_2 axially away from the target surface [46, 57]. The loss and gain rates across the boundaries of this annular cylinder to the target on one side, and the bulk plasma on the other side, account for the geometry of the IR [57]. To determine the electron density the quasi-neutrality condition is applied. The model gives the temporal variation of the various species, electrons, ions, and neutrals, that constitute the discharge for a given discharge setup and experimentally determined discharge voltage and current waveforms. The IRM is therefore a tool that allows us to explore, among other processes, the mechanisms responsible for working gas rarefaction.

The plasma chemistry is introduced through two sets of rate coefficients that are calculated using an assumed electron energy distribution function (EEDF), one set for cold, or primary electrons, and another set for the secondary electrons, emitted from the target due to ion bombardment. This assumption has been tested against a kinetic Boltzmann solver and a good agreement has been achieved [58]. The cold electrons are created through the ionization processes within the IR volume and are referred to as primary electrons in the discussion below. The majority of the electrons are primary electrons and belong to the cold Maxwellian electron population which therefore dictates the electron density and the effective electron temperature. The rate coefficients are calculated assuming Maxwellian EEDFs and fit in the range $T_e = 1 - 7$ eV for the primary electrons, and in the range 200 – 1000 eV for secondary electrons. The reaction set and the rate coefficients involving argon in the IRM are described in our earlier works on HiPIMS discharges with titanium target [49, 59], with a few modifications of the rate coefficients involving the metastable argon atom [58] and addition of Ar^{2+} to the reaction set [55]. The reaction set and the parameters that describe the

plasma surface interactions, such as sputter yields, and secondary electron emission, involving the various target materials are given in respective publications, for graphite [55], aluminum [46], copper [52], titanium [59], zirconium [56], and tungsten [53] targets.

2.1. The model implementation

To further explore working gas rarefaction we look at the processes that are involved in the gain and loss of argon atoms within the IR. There are a number of processes that contribute to working gas rarefaction in the magnetron sputtering discharge. Below we discuss these processes and how they are implemented in the IRM, following the discussion given by Huo *et al* [46], which also provides a more detailed discussion of the IRM in general. We also discuss a number of modifications to the IRM made for this current study.

The film-forming species are sputtered out of the cathode target by ion bombardment. The rate at which the sputtered species enter the discharge is given by

$$R_{\mathrm{n,sputt}} = \frac{\sum_i \Gamma_i^{\mathrm{RT}} S_{\mathrm{RT}} Y_i(\mathcal{E}_i)}{\mathcal{V}_{\mathrm{IR}}} \tag{1}$$

where n stands for neutral atom sputtered off the target and i stands for the ion species involved in the process, Γ_i^{RT} is the flux of ion species i towards the target in [ions/m^2 s], S_{RT} is the area of the sputtered region (racetrack area), $Y_i(\mathcal{E}_i)$ is the energy-dependent sputter yield for ion species i bombarding the target, and $\mathcal{V}_{\mathrm{IR}}$ is the total volume of the IR. The sum is taken over all the positive ion species in the discharge, and each ion species i has its energy-dependent sputter yield. The sputter yields for most of the various targets are taken from fits suggested by Anders [60], but for titanium the sputter yields are taken from fits provided by Tomas Kubart at Uppsala University [59]. For a zirconium target the sputter yield was estimated using the TU Wien Sputter Yield Calculator [61], which is based on the empirical equations for sputter yields at normal incidence developed by Matsunami *et al* [62]. The sputter yields depend on the ion energy $\mathcal{E}_i(t)$ which we take to be the energy equivalent of the discharge voltage $V_{\mathrm{D}}(t)$.

In addition to cold argon neutrals in ground state Ar$^{\mathrm{C}}$ with density $n_{\mathrm{Ar}}^{\mathrm{C}}$, and metastable argon (the densities of both Ar(4s[3/2]$_2$) and Ar(4s'[1/2]$_0$)), the model considers two additional populations of argon atoms originating from argon ions that bombard the target and then return to the discharge volume as neutrals. These are warm argon atoms with density $n_{\mathrm{Ar}}^{\mathrm{W}}$ and hot argon atoms with density $n_{\mathrm{Ar}}^{\mathrm{H}}$. The hot argon population originates from argon species that are reflected from the target [63, 64]. They are assumed to have an average energy of 2 eV [47]. The warm population Ar$^{\mathrm{W}}$ is due to argon ions that penetrate the target surface, and then slowly diffuse back as atoms. Their energy is taken to be the thermal energy of the surface, with about 0.1 eV (∼1000 K) as an upper bound [65]. We assume that a fraction ξ_{H} of the recombined Ar$^+$ ions return as hot neutrals Ar$^{\mathrm{H}}$ during the pulse, and a fraction $(1-\xi_{\mathrm{H}})$ return as warm neutrals Ar$^{\mathrm{W}}$ during the pulse. We further assume that all target-implanted argon atoms leave the target during the pulse [47, 66]. Of importance for the working gas rarefaction are the hot argon atoms, as they have a considerable momentum. They are incorporated in the IRM as a generation term for hot argon neutrals Ar$^{\mathrm{H}}$

$$R_{\mathrm{Ar^H,return}} = \xi_{\mathrm{H}} \left(\Gamma_{\mathrm{Ar^+}}^{\mathrm{RT}} + \Gamma_{\mathrm{Ar^{2+}}}^{\mathrm{RT}}\right) \frac{S_{\mathrm{RT}}}{\mathcal{V}_{\mathrm{IR}}} \tag{2}$$

where $\Gamma_{\mathrm{Ar^+}}^{\mathrm{RT}}$ is the flux of Ar$^+$ ions and $\Gamma_{\mathrm{Ar^{2+}}}^{\mathrm{RT}}$ is the flux of Ar^{2+} ions towards the target racetrack. For the generation of warm neutrals ξ_{H} in equation (2) is replaced by $(1-\xi_{\mathrm{H}})$. Coming from the target, the hot argon neutrals Ar$^{\mathrm{H}}$ and the warm argon neutrals Ar$^{\mathrm{W}}$ have a directed flux away from the target, giving a loss out of the IR at random velocity defined by

$$v_{\mathrm{ran}} = \sqrt{\frac{2eT_{\mathrm{n}}}{\pi m_{\mathrm{n}}}} \tag{3}$$

where T_{n} is the temperature and m_{n} is the mass of the neutral species and thus the loss rate is

$$R_{\mathrm{Ar^Z,loss}} = v_{\mathrm{ran}} n_{\mathrm{Ar^Z}} \frac{S_{\mathrm{DR}}}{\mathcal{V}_{\mathrm{IR}}} \tag{4}$$

where the superscript Z stands for hot (H) and warm (W) argon atoms. For this current study we assume $\xi_{\mathrm{H}} = 0.5$ i.e. 50% are Ar$^{\mathrm{W}}$, with $T_{\mathrm{Ar}}^{\mathrm{W}} = 0.1$ eV, and 50% are Ar$^{\mathrm{H}}$ with $T_{\mathrm{Ar}}^{\mathrm{H}} = 2$ eV for all the target materials studied. This choice is arbitrary and has been motivated in earlier studies [47, 66]. However, ξ_{H} will possibly vary with the mass of the target element, and for heavier target elements the fraction of Ar$^{\mathrm{W}}$ is expected to be higher (see Rudolph *et al* [64]), which we neglect in this current study.

Neutral atoms created through volume reactions within the IR along with atoms sputtered or released from the target are lost as they diffuse out of the IR, described by a loss term

$$R_{\mathrm{n,diff}} = \Gamma_{\mathrm{n,diff}} \frac{S_{\mathrm{DR}}}{\mathcal{V}_{\mathrm{IR}}}, \tag{5}$$

where $\Gamma_{\mathrm{n,diff}}$ is the flux of neutral atoms or molecules through the border of the IR with the diffusion region (DR), S_{DR} is the surface area of the IR facing the DR, and $S_{\mathrm{DR}}/\mathcal{V}_{\mathrm{IR}}$ is the distance through the IR, which represents the typical length that species with a directed flow from the target travel when diffusing out of the IR. The atom flux is

$$\Gamma_{\mathrm{n,diff}} = \Gamma_{\mathrm{n,0}} \exp\left(\frac{-L}{\lambda_{\mathrm{n,Ar}}}\right), \tag{6}$$

where $\lambda_{\mathrm{n,Ar}} = 1/(\sigma_{\mathrm{m}} n_{\mathrm{Ar}})$ is the mean free path for target atoms colliding with argon atoms and σ_{m} is the momentum transfer cross section for collisions between atoms. For the cold working gas atoms $\Gamma_{\mathrm{n,0}}$ is the random atom flux governed by the thermal energy. For the species coming off the target, the sputtered species and warm and hot argon atoms, the flux $\Gamma_{\mathrm{n,0}}$ is governed by the velocity of the particle coming off the target, directed away from the target surface. For the sputtered species the flux is dictated by the cohesive energy of the target.

The cross section σ_{m} for collisions of sputtered metal atoms and argon atoms is based on the momentum-exchange

Table 1. Selected atomic data for the various target atoms. The values for the cohesive energy $\mathcal{E}_{\text{cohesive}}$ are taken from Kittel [69] and the atomic radius is from Clementi *et al* [68].

Atom	$\mathcal{E}_{\text{iz}}[eV]$	$\mathcal{E}_{\text{cohesive}}[eV]$	Atomic mass [amu]	Atomic radius [pm]	σ_{m} [10^{-19} m^2]	Y_{SS}	$V_{\text{D}}[V]$
C	11.26	7.37	12.0	67	1.2	0.24	611
Al	6.0	3.39	27.0	118	2.6	1.19	730
Ti	6.8	4.85	47.9	176	4.1	0.64	625
Cu	7.73	3.49	63.5	145	3.4	2.37	575
Ar	15.76		39.95	71	1.2–1.5		
Zr	6.63	6.25	91.2	206	4.9	0.47	550
Mo	7.09	6.82	95.9	190	4.2	0.51	450
W	7.98	8.90	183.8	193	4.0	1.14	800

cross section calculated for the Ar–Ar interaction by Phelps *et al* [67]. As pointed out by Rossnagel [22], it has to be noted that the momentum transfer cross section for the sputtered atoms, with energy of few eVs, is up to a factor 10 larger than the momentum transfer cross section for the energetic reflected neutrals with energy of few hundred eVs (see also Phelps *et al* [67]). To get a more reasonable value for the momentum-exchange between the sputtered species and the argon atoms we approximate this to be a billiard-ball collision, and assume that the momentum-exchange cross section scales as $\pi(a_1 + a_2)^2$, where a_1 is the atomic radius of the sputtered species and a_2 is the atomic radius of the argon atom. The velocity of the particle coming off the target is assumed to be the most probable velocity from the Thompson distribution [16, 17] or $\frac{1}{2}\mathcal{E}_{\text{cohesive}}$. The Ar–Ar cross section is determined at the most probable energy for each metal atom using the fit given in Phelps *et al* [67]. This value is then multiplied by the ratio $((a_1 + a_2)/(a_2 + a_2))^2$ to get the momentum exchange cross section for each argon-metal atom pair. The values used to calculate the cross sections and the calculated momentum transfer cross sections are given in table 1. The values for the atomic radius are taken from the work of Clementi *et al* [68] and the values for the cohesive energy are from the textbook by Kittel [69]. This is a revision from our earlier works where we assumed the metal–Ar momentum transfer cross section to be 2×10^{-19} m^2 as a typical cross section for all neutral-neutral collisions [46, 47, 57].

For this study the working gas temperature (cold argon atoms) is assumed to be 500 K. At a gas temperature of 500 K and using the cross sections in table 1 the mean free path for the sputtered atoms is roughly 8–30 mm at 1 Pa and 2–8 mm at 4 Pa. Due to the energy transfer from the sputter process and heat conduction from the cathode target the effective gas temperature is high. We will see later (section 3) that late in the pulse a significant fraction of the argon atoms within the IR are warm and hot atoms. Therefore, the effective working gas temperature can be significantly higher, and argon gas a temperature above 1200 K has been measured for a 200 μs long pulse [42].

In the IRM, gas rarefaction by the effect of the sputter wind [19] is implemented as an argon kick-out term due to collisions with fast sputtered particles [46, 57]. Here, we slightly modify the model from our previous studies to also include the hot argon atoms Ar$^{\text{H}}$ species that originate from the target with a considerable energy. The warm argon species Ar$^{\text{W}}$ on the other hand, also originating from the target, are still neglected in the model, as their energy of 0.1 eV is too low to have a significant impact on gas rarefaction by kicking out argon species. Also, we neglect kick-out by the metal ions.

For this current study we significantly revise the kick-out term in the IRM code from our earlier studies [46, 47, 57]. For the derivation of a kick-out term, we denote the kicking-out species by an X, and those that are kicked-out by a Y. Here, X = {M, Ar$^{\text{H}}$}, where M stands for the target atoms, and Y = {Ar$^{\text{C}}$, Ar(4s[3/2]$_2$), Ar(4s'[1/2]$_0$)}. In the model, we assume that a collision of a species X with a species Y leads to the instantaneous loss of species Y from the IR. This is acceptable if two conditions are met: (i) The momentum of species X is always higher than the average momentum of the cold Ar species (species Y) at an assumed working gas temperature of 500 K. The lightest target atom studied here, carbon, has the mass $M = 12M_{\text{p}}$, where M_{p} is the proton mass, and an ejection energy $\mathcal{E}_{\text{ejection}} = \frac{1}{2}\mathcal{E}_{\text{cohesive}} = 3.7$ eV [55]. This yields a momentum of 10^{-22} kg m s^{-1} which is higher than the momentum of an average argon species at $T_{\text{g}} = 500$ K which is $\sim 10^{-23}$ kg m s^{-1}. We therefore consider the first condition to be fulfilled. (ii) The length of a HiPIMS pulse is longer than the typical loss time of species Y out of the IR after the collision. For example, a collision in the middle of the IR with a typical height $h = 2$ cm and a post-collision velocity of $v = 1000$ m s^{-1}, results in a loss of species Y within $t = h/2v = 10\,\mu$s. The pulse lengths of the HiPIMS discharges investigated in this study are longer by a factor of 4 to 20, which is why the assumed instantaneous loss is an acceptable assumption. We neglect that this assumption underestimates the momentary argon density. This approximation of instant loss of species from the IR is therefore acceptable for the discharges studied in this work. Furthermore, for collisions between Ar$^{\text{H}}$ and Ar$^{\text{C}}$, we neglect the effect that head-on collisions would simply result in the exhange of velocity vectors with no net change in the argon density in the IR. Collisions under an angle result in both particles to be lost out of the IR. As collisions under an angle are much more probable compared to head-on collisions, also this is an acceptable assumption.

For each species X, we assume that there is a certain probability for these particles to collide with particles of the species Y. This is given by

$$F_{\mathrm{coll,X\to Y}} = 1 - \exp\left(-L/\lambda_{\mathrm{X\to Y}}\right), \tag{7}$$

where L is the height of the IR and the mean free path $\lambda_{\mathrm{X\to Y}}$ of a species X in a background gas composed of species Y is given by

$$\lambda_{\mathrm{X\to Y}} = \frac{1}{\sigma_{\mathrm{X\to Y}} n_{\mathrm{Y}}}. \tag{8}$$

where the cross sections $\sigma_{\mathrm{X\to Y}}$ are the momentum transfer cross sections, as discussed above for each pair of X and Y, and n_{Y} is the density of species Y.

Note that $F_{\mathrm{coll,X\to Y}}$ is the fraction of the momentum carried by the sputtered species that is transferred to the kicked-out species Y. We can therefore link the sputter flux $\Gamma_{\mathrm{sputter}}$ (in $\mathrm{m^{-2}\,s^{-1}}$) to the kick-out flux $\Gamma_{\mathrm{kickout}}$ out of the IR by

$$R_{\mathrm{kickout,\,X\to Y}} = F_{\mathrm{coll,X\to Y}}\Gamma_{\mathrm{sputter,X}}\frac{S_{\mathrm{RT}}}{\mathcal{V}_{\mathrm{IR}}} = \Gamma_{\mathrm{kickout}}\frac{S_{\mathrm{DR}}}{\mathcal{V}_{\mathrm{IR}}}, \tag{9}$$

where S_{RT} is the surface area of the IR facing the racetrack, and S_{DR} is the surface area of the IR facing the DR [57]. The sputtered flux is

$$\Gamma_{\mathrm{sputter,X}} = \sum_i \Gamma_i^{\mathrm{RT}} Y_i\left(\mathcal{E}_i\right) \tag{10}$$

where $Y_i(\mathcal{E}_i)$ is the sputter yield for an ion species i bombarding the target. Note that equation (9) represents 6 equations, representing each pair (X,Y) of kicking-out species X and species Y that are kicked-out. Note that this model assumes that there is at most one collision between a sputtered species and a gas species. Based on the long mean free path of sputtered species in the IR compared to the typical height of the IR (see above), this is acceptable assumption.

A second loss mechanism is the ionization of the argon atoms followed by attraction to the target. The argon atoms within the IR are lost through electron impact ionization

$$\mathrm{e + Ar \longrightarrow Ar^+ + 2e}$$

where the argon atom can be in the ground state or in an excited state. This includes cold, warm and hot argon atoms. The electrons that drive the reaction can be from either the cold (primary) or hot (secondary) population. In addition charge exchange

$$\mathrm{Ar^+ + M \longrightarrow Ar + M^+}$$

contributes to adding argon atoms to the IR, however the contribution is expected to be very small. Due to the electric fields within the IR, most of these gas ions are drawn toward the target and are lost from the IR.

As discussed above, gas rarefaction lowers the density of the working gas (the neutral argon atoms) within the IR below the density value in the surrounding gas reservoir, $n_{\mathrm{g,0}}$ [19, 20, 29, 30]. This leads to back-diffusion (gain) that is modeled by the term

$$R_{\mathrm{g,refill}} = \frac{1}{2} v_{\mathrm{g,ran}} \frac{\left(n_{\mathrm{g,0}} - n_{\mathrm{g}}\right) S_{\mathrm{DR}}}{\mathcal{V}_{\mathrm{IR}}} \tag{11}$$

where the subscript g stands for the atoms of the working gas and $v_{\mathrm{g,ran}}$ is their random thermal velocity as defined by equation (3). The argon gas diffusional refill term is determined by the gas temperature and the gas density difference $(n_{\mathrm{Ar,0}} - n_{\mathrm{Ar}})$ between the IR and the surrounding volume. By definition, only atoms moving towards the boundary are involved so that the densities are taken to be one half of the volume densities.

2.2. The degree of working gas rarefaction

The working gas rarefaction is either presented as a percentage of the total neutral argon density at the start of the pulse $n_{\mathrm{Ar}}(t)/n_{\mathrm{Ar,0}}$ or as a degree of working gas rarefaction

$$\text{degree of working gas rarefaction} = 1 - \frac{n_{\mathrm{Ar}}(t)}{n_{\mathrm{Ar,0}}}, \tag{12}$$

where $n_{\mathrm{Ar,0}}$ is the total argon density at the start of the pulse and $n_{\mathrm{Ar}}(t)$ is the temporal variation of the total argon density. As discussed in section 2.1 there are several factors that contribute to working gas rarefaction, including electron impact ionization of argon atoms and kick-out of argon atoms by the sputter wind, which is then balanced by diffusion (refill) of cold argon atoms from the bulk plasma, returning hot and warm argon atoms from the target, and charge-exchange collisions [47]. When we compare the relative contribution of each of the processes to working gas rarefaction they are all determined by integrating the contribution of each term throughout the entire pulse and the afterglow.

3. Results

3.1. Overview

As mentioned in section 1 the IRM has been applied to study HiPIMS discharges using a number of different target materials including graphite [55], aluminum [46, 47], copper [52], titanium [51], and tungsten [53]. For all the target materials the IRM calculations have shown that the cold (or primary) argon ground state density (denoted $\mathrm{Ar^C(3p^6)}$) decreases steadily to a minimum close to the peak in the discharge current and then it increases again. The question that we will answer with this work is: What processes contribute to working gas rarefaction in the HiPIMS discharge? Is the sputter wind important? In the following, we will re-analyze some of these discharges in terms of working gas rarefaction.

In the following we explore how much each of the four terms described in section 2.1 contributes to working gas rarefaction for a few target materials, from low atom mass (graphite) to high atom mass (tungsten). For this we model discharges with targets of various materials and of varying sizes. For the various target sizes the dimensions of the IR for the IRM calculations are listed in table 2. Note that in some cases we use different dimensions for the size of the IR in this current study than in the original study of that particular target material. However, all the dimensions are within ±1 mm from the earlier assumed dimensions. The size of the IR is chosen rather

Table 2. The dimensions of the ionization region used in the model calculations for the different targets and target sizes.

Target	Target diameter [mm]	z_1 [mm]	z_2 [mm]	r_1 [mm]	r_2 [mm]
C	50	2	13	6	20
Al, Zr	50	2	20	6	20
Cu	50	2	28	6	20
W	75	2	22	8	28
Ti	100	2	25	11	39

arbitrary. Also, it has been observed experimentally that the size of the IR varies with the magnetic field strength among other operating parameters [70]. In fact the absolute value of the degree of rarefaction scales with the size of the IR. Electron impact ionization scales with $1/\mathcal{V}_{\rm IR}$, while kick-out scales as $1/L$, and therefore the absolute values mentioned in the text for the degree of working gas rarefaction are just rough estimates. Also keep in mind that as mentioned in section 1 that the size of the IR is small compared to the actual extent of the working gas rarefaction in the discharge [44], which also influences the absolute value of the degree of working gas rarefaction. Working gas rarefaction is therefore expected to be less pronounced when modeling with volume average models compared to DSMC simulations. Furthermore, Kozák and Lazar [44] point out that volume-averaged models do not take into account the spatial distribution of the neutral Ar and M densities, and therefore the velocity and angular distribution of the sputtered atoms [71, 72], and secondary M–Ar and Ar–Ar collisions are neglected. The latter is justified by a mean free path of a few tens of mm as discussed in section 2.1 and given the extension of the IR it means that only a single collision occurs.

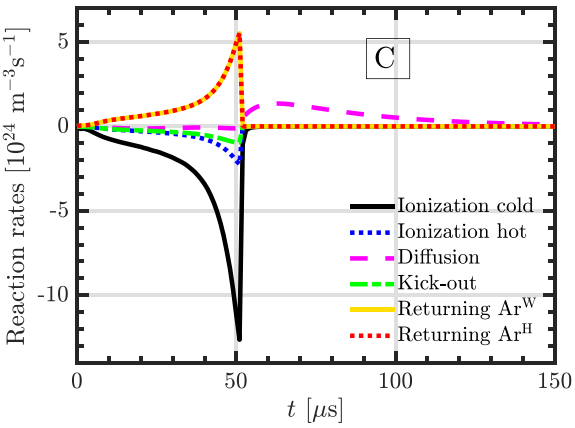

Figure 1. The reaction rates for the argon atom loss and argon atom gain within the ionization region for a discharge with 50 mm diameter graphite target operated at working gas pressure of 1 Pa, with a peak discharge current $I_{\rm D,peak}$ of 20 A ($J_{\rm D,peak} = 1\ \mathrm{A\,cm^{-2}}$) and 50 μs long pulse.

3.2. Graphite target

In a recent study we applied the IRM to analyze HiPIMS discharges with a 50 mm diameter graphite target and argon working gas at a pressure of 1 Pa [55]. It was observed that the discharge operates on working gas recycling and most of the discharge current at the cathode target surface is composed of Ar^+ ions, which constitute over 90% of the discharge current, while the contribution of the C^+ ions is always small (<5%). The ion back-attraction probability during the pulse $\beta_{\rm t}$ is high (>83%), and the ionized flux fraction is low, or in the range 2%–4%. The maximum in the degree of working gas rarefaction derived from the IRM is 45%, 51%, and 55%, for peak discharge current densities of 1, 2, and 3 $\mathrm{A\,cm^{-2}}$, respectively. These values are determined from the maximum drop in the total argon atom density within the IR, calculated using equation (12), by adding the densities of all the neutral argon atom species densities within the IR. Earlier we reported a maximum in the degree of cold argon atom rarefaction of 66%, 74%, and 81% for discharge current densities of 1, 2, and 3 $\mathrm{A\,cm^{-2}}$, respectively [55]. The difference in the degree of working gas rarefaction values, reported here, compared to the earlier published values, is mainly due to warm and hot argon atoms that enter the IR during the pulse, which have influence on the rarefaction, and were not taken into account when the degree of working gas rarefaction was evaluated in the earlier study. Note, that the various values we report here for the discharge with graphite target have changed slightly as we discovered a few minor errors in the calculations published earlier [55], that have now been corrected, in addition to the modifications of the kick-out term discussed in section 2.1. Also, note that this does not affect the key results of that study concerning the reasons for low carbon ionization in HiPIMS. Furthermore, we have adjusted the size of the IR.

Here, we analyze the contributions of the various processes to rarefaction for a HiPIMS discharge with a graphite target in more detail. Figure 1 shows the temporal evolution of the reaction rates for the loss and gain of argon atoms within the IR for the $J_{\rm D,peak} = 1\ \mathrm{A\,cm^{-2}}$ and 50 μs long pulse case explored earlier by Eliasson *et al* [55]. The main contributor to the loss of argon atoms is electron impact ionization of the argon atoms by primary electrons (referred to as ionization cold), and the second most important loss process is electron impact ionization by secondary electrons (referred to as ionization hot) has much smaller contribution. This is the case even though both argon ions and carbon ions contribute to the creation of secondary electrons as they bombard the cathode target. Warm and hot argon atoms released from the target enter the IR and constitute the main contribution to the gain of argon atoms within the IR. The reaction gain rates for the warm and hot

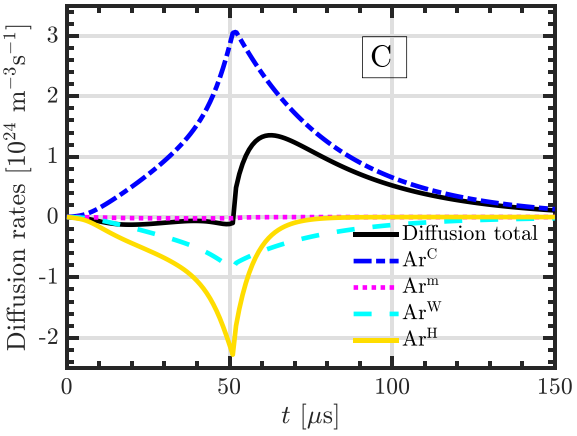

Figure 2. The reaction rates for the cold argon atom diffusion and warm and hot argon atom escaping from the ionization region for a discharge with 50 mm diameter graphite target operated at working gas pressure of 1 Pa, with a peak discharge current $I_{D,peak}$ of 20 A ($J_{D,peak} = 1\ A\,cm^{-2}$) and 50 μs long pulse.

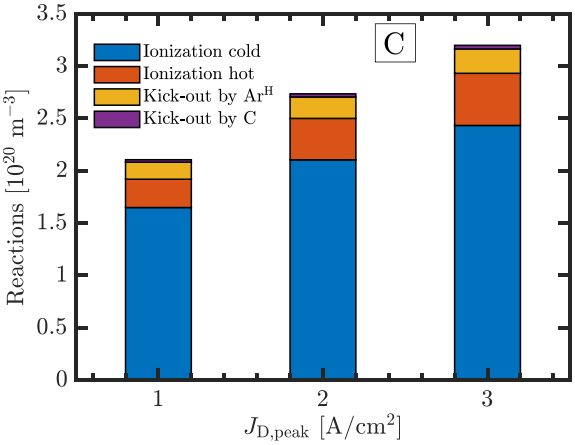

Figure 3. The contribution of the various processes to working gas rarefaction within the ionization region for a discharge with 50 mm diameter graphite target versus the peak discharge current density for argon at 1 Pa, pulse length of 50 μs and average discharge power $\langle P_D \rangle$ of 80 W.

argon atoms in figure 1 are assumed to be the same and overlap, due to the assumption that equal number of argon atoms leaves the target during one pulse [47]. We see in figure 1 that when operating with a graphite target the contributions of kick-out is small and charge-exchange is negligible (not shown). We note that diffusion contributes to a net loss of argon atoms during the pulse, but to a flow into the IR after the pulse is off.

We explore the diffusion terms more closely in figure 2. The main contribution to the diffusion is the refill of cold argon atoms into the IR, while the warm and hot argon atoms escape out of the IR, and the hot argon atoms are lost faster than the warm atoms. The total diffusion (the dashed pink line in figure 1), i.e. the sum of the diffusion terms for Ar^C, Ar^m, Ar^W, and Ar^H, is also shown in figure 2. During the pulse-on time the escape of warm and hot argon atoms out of the IR is larger than the refill by cold argon atoms, this is the reason why the total diffusion term appears negative during the pulse. This reverses after the pulse is off. Almost a fifth of the warm and hot argon atoms that are released from the target escape out of the IR without being ionized. For $J_{D,peak} = 1\ A\,cm^{-2}$, at the peak in the degree of working gas rarefaction cold argon atoms in ground state account for 42%, metastable argon atoms 0.5%, warm argon atoms 37%, and hot argon atoms 21% of the argon atoms within the IR. So a substantial portion of the argon atoms within the IR, during the pulse, consists of warm and hot atoms.

Figure 3 shows the contribution of each of the terms to the working gas rarefaction versus the peak discharge current density for discharges with graphite target. We see that electron impact ionization by primary and secondary electrons has over 90% contribution and its role increases with increased peak discharge current density, and is the dominating process. Electron impact ionization by hot secondary electrons has about ~10% overall contribution. Kick-out by the sputtered species, the sputter wind, has small (<10%) contribution on working gas rarefaction when operating with graphite target at a working gas pressure of 1 Pa, and 87% is due to kick-out by hot argon atoms and 13% is due to sputtered carbon atoms. The discharge current density does not have much influence on the relative contribution of the various terms. From the above discussion we see that the composition of the argon atoms within the IR changes during the pulse.

3.3. *Aluminum target*

The early development of the IRM [57] was based around HiPIMS discharges with an aluminum target, that were studied experimentally by Anders *et al* [73], and included studies of the discharge composition at the target surface [46], working gas rarefaction [47], and electron heating mechanisms [46, 66]. When the discharge enters the HiPIMS operating regime the Al^+ ions dominate the discharge current at the target surface, while the contribution of Ar^+ ions is low [46] and the discharge operates in the self-sputter regime to reach the high discharge currents [74]. When operating with aluminum target, electron impact ionization of argon atoms was determined to be the biggest contributor to working gas rarefaction, when the degree of working gas rarefaction was determined to be about 50%, for $J_{D,peak} \approx 0.6\ A\,cm^{-2}$ and $t_{pulse} = 400\ \mu s$ at $p_g = 1.8$ Pa [47].

Here, we analyze a few discharges that were explored experimentally by Lundin *et al* [10], who measured the electron density and the ionized flux fraction as the working gas pressure, pulse length, and discharge current density was varied. The aluminum target was 50 mm in diameter and the working gas pressure was 0.5 and 2.0 Pa. At average current density $J_{D,average} \approx 1.4\ A\,cm^{-2}$ the measured ionized flux fraction was 50% at 0.5 Pa and at $J_{D,average} \approx 1.2\ A\,cm^{-2}$ the ionized flux fraction was 38% at 2 Pa for a 100 μs long pulse. Here, we further explore these discharges with the help of the IRM. For the IRM calculations the rate coefficients for

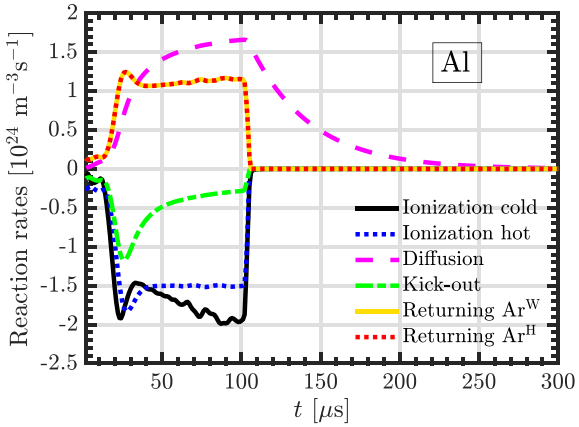

Figure 4. The reaction rates for the argon atom loss and argon atom gain within the ionization region for a discharge with 50 mm aluminum target operated at working gas pressure of 0.5 Pa, with a discharge voltage of $V_D =$ 730 V giving average discharge current $I_{D,average}$ of 27 A ($J_{D,average} = 1.4\,A\,cm^{-2}$) for 100 μs long pulse.

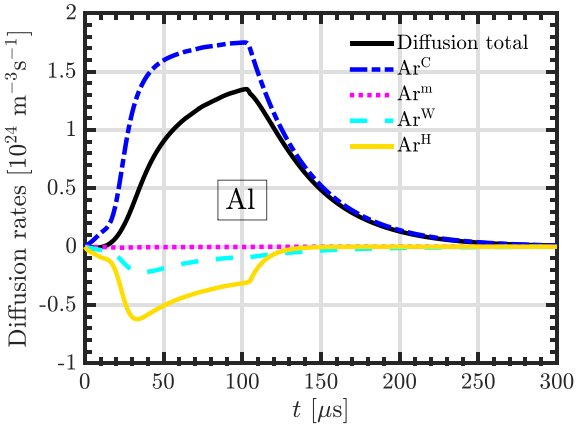

Figure 5. The reaction rates for the cold argon atom diffusion and warm and hot argon atom escaping the ionization region for a discharge with 50 mm aluminum target operated at working gas pressure of 0.5 Pa, with a discharge voltage of $V_D = 730$ V giving average discharge current $I_{D,average}$ of 27 A ($J_{D,average} = 1.4\,A\,cm^{-2}$) for 100 μs long pulse.

reactions involving aluminum atoms and ions are the same as given by Huo *et al* [46]. When applying the IRM we use the measured ionized flux fraction to lock the model as proposed by Butler *et al* [75]. The maximum degree of working gas rarefaction derived from the IRM calculations is 83% at 0.5 Pa and 57% at 2 Pa close to the end of the pulse. The working gas rarefaction is much more significant for the lower pressure. The back-attraction probability of the ionized aluminum is 70% at 0.5 Pa and 75% at 2.0 Pa.

The reaction rates for the argon atom loss and argon atom gain within the IR for a discharge with a 50 mm aluminum target operated at a working gas pressure of 0.5 Pa are shown in figure 4. We see that the loss of argon atoms is mainly due to electron impact ionization of the argon atom, while kick-out also has 14% contribution. Electron impact ionization by the primary electrons has 46% contribution, and the secondary electrons 40% contribution, to the loss of argon atoms from the IR. The diffusion processes (figure 5) are dominated by refill of cold argon atoms, while the warm and hot argon atoms escape out of the IR. At 2 Pa (figure 6) kick-out has similar contribution to the loss of argon atoms from the IR as does electron impact ionization. Electron impact ionization by the primary electrons and secondary electrons have each similar contributions.

The contribution of kick-out increases significantly (from 14% to 53%) with increasing working gas pressure from 0.5 to 2 Pa. At 0.5 Pa the kick-out is 83% due to aluminum atoms and 17% due to hot argon atoms, while at 2 Pa 86% is due to aluminum atoms and 14% due to hot argon atoms. As before, argon atoms enter the IR as returning warm and hot atoms from the target and by diffusion of cold argon atoms. Huo *et al* [47] pointed out that the long mean free path is the reason why rarefaction by electron impact ionization losses dominate over the sputter wind in the discharge. Therefore, for higher working gas pressures the sputter wind contribution would become

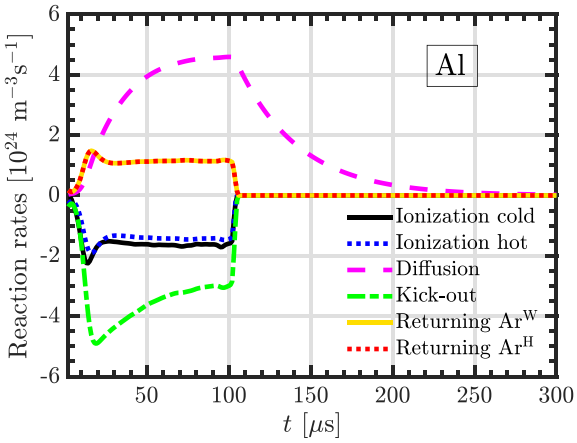

Figure 6. The reaction rates for the argon atom loss and argon atom gain within the ionization region for a discharge with 50 mm aluminum target operated at working gas pressure of 2.0 Pa, with a discharge voltage of $V_D = 540$ V giving average discharge current $I_{D,average}$ of 23 A ($J_{D,average} = 1.2\,A\,cm^{-2}$) for 100 μs long pulse.

more significant, which is indeed what is observed here. At the peak in the degree of working gas rarefaction (for 0.5 Pa) cold argon atoms in the ground state are 44%, metastable argon atoms 0.5%, warm argon atoms 31%, and hot argon atoms 25% of the argon atoms within the IR. Again, more than half the argon atoms within the IR are warm and hot atoms.

3.4. Copper target

In a recent study the IRM was applied to study a few historical HiPIMS discharges operated with a copper target [52].

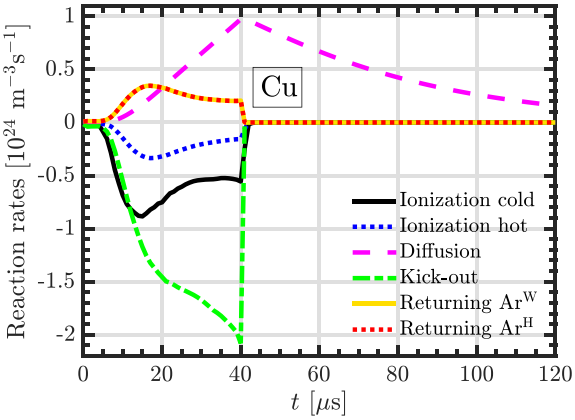

Figure 7. The reaction rates for the argon atom loss and argon atom gain within the ionization region for a discharge with 50 mm diameter copper target operated at working gas pressure of 0.5 Pa, with a peak discharge current density of $J_{\mathrm{D,peak}} = 1.0\,\mathrm{A\,cm^{-2}}$ for 40 μs long pulse.

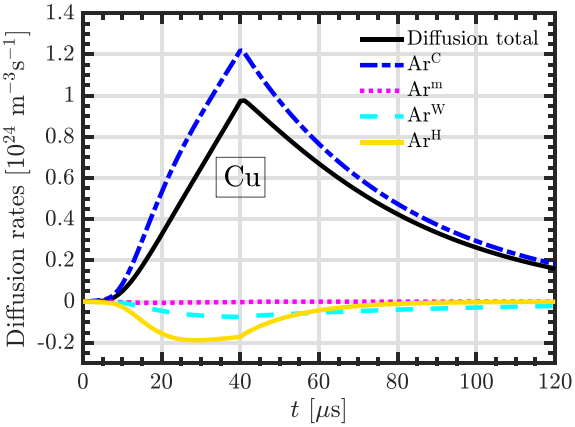

Figure 8. The reaction rates for the cold argon atom diffusion and warm and hot argon atom escaping the ionization region for a discharge with 50 mm diameter copper target operated at working gas pressure of 0.5 Pa, with a peak discharge current density of $J_{\mathrm{D,peak}} = 1.0\,\mathrm{A\,cm^{-2}}$ for 40 μs long pulse.

It was observed that Cu^+ ions dominate the total ion current at the target surface. This indicates that the discharge is dominated by self-sputter recycling in order to reach the high discharge currents [74]. For peak discharge current densities in the range 0.9–1.3 $\mathrm{A\,cm^{-2}}$ the back-attraction probability was found to be in the range 44%–50%, while the ionization probability was in the range 61%–69%, and the ionized flux fraction was in the range 32%–40% [52]. The model results showed that copper ions dominate the ion flux out of the IR, with about ∼77%–88% contribution, in agreement with experimental observations [32]. Recall that for a HiPIMS discharge with copper target, the ionized flux fraction was early on determined experimentally to be as high 70% [76] and more recently an ionized flux fraction up to 80% has been measured experimentally [77]. Gas compression and rarefaction have been observed in a HiPIMS discharge with a copper target by measuring time-resolved ion saturation currents from probe array [37]. It was observed as an onset of the sputter flux that causes a transient densification of the working gas, followed by rarefaction.

Here, we explore reaction rates for the gain and loss of argon atoms within the IR for a discharge created with a 50 mm diameter copper target operated at a working gas pressure of 0.5 Pa, with a peak discharge current density of $J_{\mathrm{D,peak}} = 1.0\,\mathrm{A\,cm^{-2}}$ and 40 μs long pulse. The discharge current and voltage waveforms were recorded by Cemin *et al* [78] and explored in an earlier work as Case I [52]. The degree of working gas rarefaction was determined to reach 60% toward the end of the pulse.

The reaction rates for the loss and gain of argon atoms within the IR are shown in figure 7. The main contributor to the loss of argon atoms is kick-out by the sputtered copper atoms while kick-out by the hot argon atoms has rather small contribution. Electron impact ionization of the argon atoms by primary and secondary electrons have smaller contributions. Warm and hot argon atoms released from the target and diffusion adds argon atoms to the IR. The diffusion terms are explored more closely in figure 8. The main contribution to the diffusion is the refill of cold argon atoms into the IR, while the warm and hot argon atoms escape out of the IR. The hot argon atoms are lost faster than the warm atoms as to be expected. At the peak in the degree of working gas rarefaction, the cold argon atoms in ground state constitute 75%, metastable argon atoms 0.5%, warm argon atoms 16%, and hot argon atoms 8%, of the argon atoms within the IR.

3.5. *Titanium target*

For a HiPIMS discharge with a titanium target the IRM results have shown that the ion composition at the target surface is composed of both argon and titanium ions in roughly equal numbers, and roughly a third of the titanium ions are the doubly ionized Ti^{2+}, depending on the peak discharge current [46]. In this case, as the self-sputter yield is somewhat below unity, a combination of self-sputter recycling and working gas-recycling is necessary to maintain the high discharge currents.

Here, we model discharges that were explored experimentally by Hajihoseini *et al* [11]. As the magnet configuration was varied, the deposition rate and the ionized flux fraction was determined, while maintaining fixed averaged power by varying the repetition frequency as either the discharge current or discharge voltage was kept fixed. The titanium target was 100 mm in diameter, the working gas pressure 1 Pa, and the average power 300 W. These discharges have been analyzed extensively in order to gain understanding on how the magnetic field strength and topology influence the discharge parameters and operation, including the ionization probability [9], the deposition rate and ionized flux fraction [11, 79, 80], the size of the IR [70], and transport parameters for both ions and neutrals [72], as well as modeling by the IRM [51] and DSMC simulations [45] to determine the ionization and the target ion back-attraction probabilities. The IRM studies

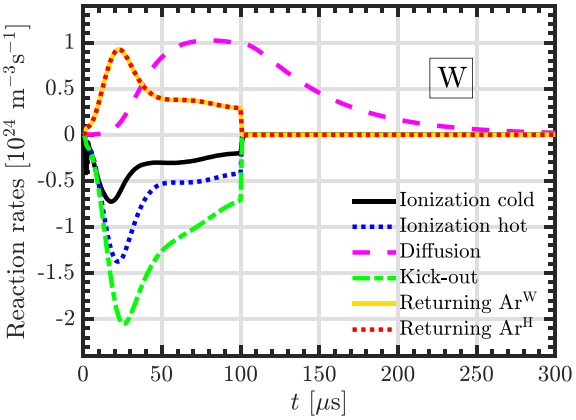

Figure 9. The reaction rates for the argon atom loss and argon atom gain within the ionization region for a discharge with 100 mm diameter Ti target operated at working gas pressure of 1 Pa, with a discharge voltage $V_D = 625$ V giving peak discharge current $I_{D,peak}$ of 80 A ($J_{D,peak} = 1.0\,A\,cm^{-2}$) and 100 μs long pulse.

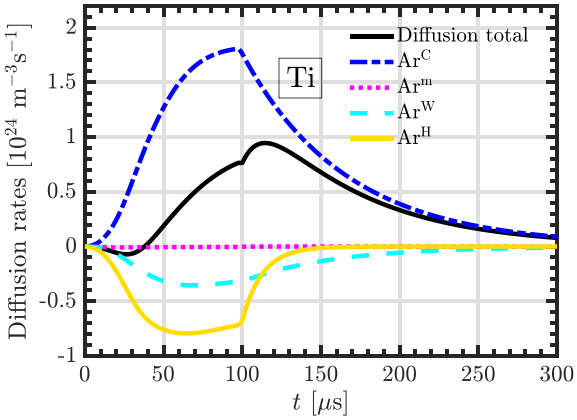

Figure 10. The reaction rates for the cold argon atom diffusion and warm and hot argon atom escaping the ionization region for a discharge with 100 mm diameter Ti target operated at working gas pressure of 1 Pa, with a discharge voltage $V_D = 625$ V giving peak discharge current $I_{D,peak}$ of 80 A ($J_{D,peak} = 1.0\,A\,cm^{-2}$) and 100 μs long pulse.

showed that the back-attraction probability is high > 0.8 [51]. Here, we explore the various contributions to rarefaction in the discharge operated with the strongest magnetic field, referred to as C0E0 by Hajihoseini *et al* [11]. The peak discharge current density was $J_{D,peak} = 1.0\,A\,cm^{-2}$ and the argon working gas pressure $p_g = 1$ Pa. The IRM calculations give a peak in the degree of working gas rarefaction of 77%. For comparison for this particular discharge the DSMC simulations give the maximum in the degree of working gas rarefaction of 53% shortly after the end of the pulse [45]. The various contributions to rarefaction are shown in figure 9. The loss of argon atoms is due to a combination of electron impact ionization by primary electrons and ionization by hot electrons, as well as kick-out, all with similar contributions. Charge-exchange has negligible contribution as before (not shown). The kick-out is split up in 74% contribution due to titanium atoms and 26% due to hot argon atoms. The large fraction of Ar^+ and Ti^{2+} ions at the target surface lead to a high contribution of secondary electrons in the ionization process. Hot and cold argon atoms as well as diffusion of argon atoms into the IR add to the argon atom density within the IR. The contribution of diffusion is explored further in figure 10, and it is seen that diffusion of cold argon atoms into the IR is the most important factor. At maximum degree of working gas rarefaction the cold ground state argon atoms constitute 42%, metastable argon atoms 0.3%, warm argon atoms 36%, and hot argon atoms 22% of the argon atoms within the IR.

3.6. Zirconium target

We apply the IRM to a discharge operated with a 50 mm diameter zirconium disk. The discharge voltage V_D was kept at 550 V, the pulse was kept at constant length of 50 μs and the argon working gas pressure was kept at 1 Pa [56]. The ionized flux fraction and the normalized deposition rate was measured as the peak discharge current density was varied in the range 0.5 – 2.0 $A\,cm^{-2}$. We use the ionized flux fraction measured at 30 mm (45%) to lock the model. We apply the IRM to study a discharge operated with peak current density of $J_{D,peak} = 1\,A\,cm^{-2}$. The back-attraction probability is determined by the IRM to be 73% and the peak in the degree of working gas rarefaction was determined to be 70%. We also note that aproximately 2/3 of the discharge current at the target surface is carried by Ar^+ ions [56]. This discharge therefore operates on combination of working gas recycling and self-sputter recycling to reach the high discharge currents [74].

The reaction rates for loss and gain of argon atoms within the IR are shown in figure 11. Electron impact ionization by primary electrons contributes 67% to the total rarefaction, while secondary electron ionization contributes 18% to the loss of argon atoms and kick-out contributes 15%. The kick-out is 74% due to zirconium atoms sputtered from the targets and 26% due to hot argon atoms. The diffusion term is analyzed further in figure 12 and shows a refill by cold argon atoms and loss due to diffusion of warm and hot argon atoms out of the IR. At the peak in the degree of working gas rarefaction cold argon atoms in the ground state constitute 50%, metastable argon atoms 0.4%, warm argon atoms 32%, and hot argon atoms 18% of the argon atoms within the IR.

3.7. Tungsten target

Earlier, we applied the IRM to study a HiPIMS discharge with 75 mm diameter tungsten target as the discharge voltage was varied [53]. The peak discharge current and the peak discharge current density $J_{D,peak}$ increases in the range 0.33 – 0.73 $A\,cm^{-2}$, with increased discharge voltage in the range 500 – 800 V. The details of the experiment, experimental setup, and method can be found elsewhere [36]. The model results show that when operating with a tungsten target an initial peak appears in the discharge current, which is due to argon ions

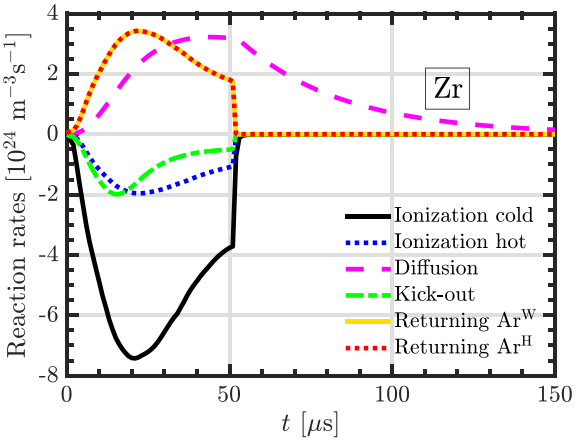

Figure 11. The reaction rates for the argon atom loss and argon atom gain within the ionization region for a discharge with 50 mm diameter Zr target operated at working gas pressure of 1 Pa, with a discharge voltage $V_D = 550$ V giving peak discharge current density of $J_{D,peak} = 1.0\,A\,cm^{-2}$ and 50 μs long pulse.

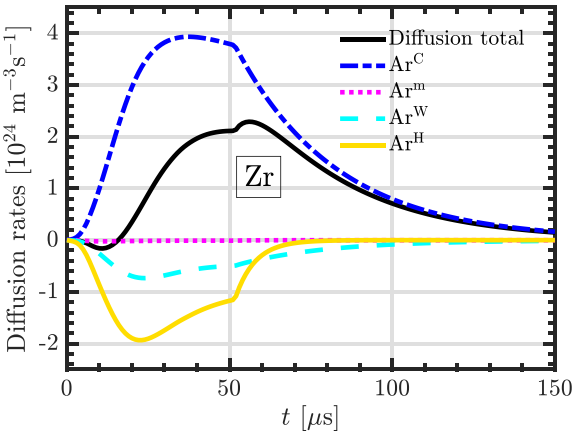

Figure 12. The reaction rates for the cold argon atom diffusion and warm and hot argon atom escaping the ionization region for a discharge with 50 mm diameter Zr target operated at working gas pressure of 1 Pa, with a discharge voltage $V_D = 550$ V giving peak discharge current density of $J_{D,peak} = 1.0\,A\,cm^{-2}$ and 50 μs long pulse.

bombarding the cathode target [53]. After this initial peak W^+ ions become the dominating ions and remain as such to the end of the pulse, and the role of W^+ ions increases with increased discharge voltage [53]. However, there is always a rather significant contribution from the Ar^+ ions, which contribute to the creation of secondary electrons. For the sputtered tungsten the back-attraction probability β_t decreases from 91% to 68% with increasing discharge voltage. With increased discharge voltage, the degree of working gas rarefaction increases from 34% at 500 V ($J_{D,peak} = 0.33\,A\,cm^{-2}$) to 64% at 800 V ($J_{D,peak} = 0.73\,A\,cm^{-2}$), when all the neutral argon species are included in the calculation. These are somewhat lower values

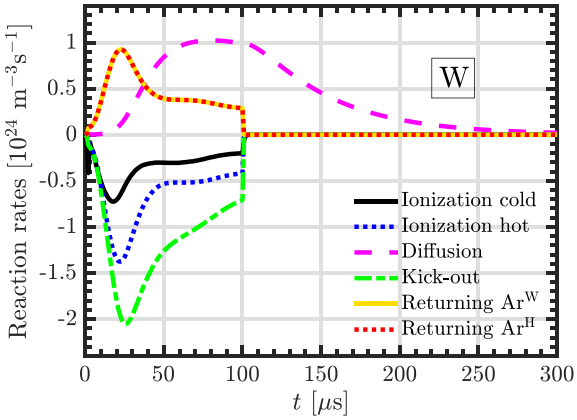

Figure 13. The reaction rates for the argon atom loss and argon atom gain within the ionization region for a discharge with 75 mm tungsten target operated at working gas pressure of 1 Pa, with a discharge voltage of $V_D = 600$ V giving peak discharge current $I_{D,peak}$ of 24 A ($J_{D,peak} = 0.54\,A\,cm^{-2}$) for 100 μs long pulse.

than we reported in the earlier work [53] as there the degree of rarefaction was calculated assuming only cold argon atoms in the ground state when reporting the degree of working gas rarefaction.

Figure 13 shows the reaction rates for the loss and gain of argon atoms within the IR for the 600 V ($J_{D,peak} = 0.54\,A\,cm^{-2}$) case explored earlier by Suresh Babu *et al* [53]. The degree of working gas rarefaction peaked at 46% when all the argon atoms are taken into account. We see that the main contributor to the loss of argon atoms from the IR is kick-out of the argon atoms by tungsten atoms sputtered from the target. The second most important loss process is electron impact ionization by secondary electrons followed by electron impact ionization by the primary electrons. Charge exchange has negligible contribution (not shown). Diffusional refill of argon atoms is the main contributor to adding argon to the IR, while warm and hot argon atoms released from the target also have a contribution to add argon atoms to the IR. The reaction rates for the warm and hot argon atoms are the same and overlap, due to the assumption that an equal number of argon atoms leaves the target during one pulse [47]. The diffusion of argon atoms is explored further in figure 14, where it is seen that the main contribution to the diffusion is the refill of cold argon atoms into the IR, while the warm and hot argon atoms escape out of the IR, and as expected that the hot argon atoms are lost faster than the warm atoms. The total diffusion is also shown in figure 14. At the peak in the degree of working gas rarefaction cold argon atoms in the ground state constitute 78%, warm argon atoms 17%, and hot argon atoms 5% of the argon atoms within the IR.

Figure 15 shows the contribution of each of the terms to the working gas rarefaction versus the peak current density. We see that kick-out has 49%–56% contribution to working gas rarefaction and is the dominating process, and its relative contribution increases with increased discharge current density.

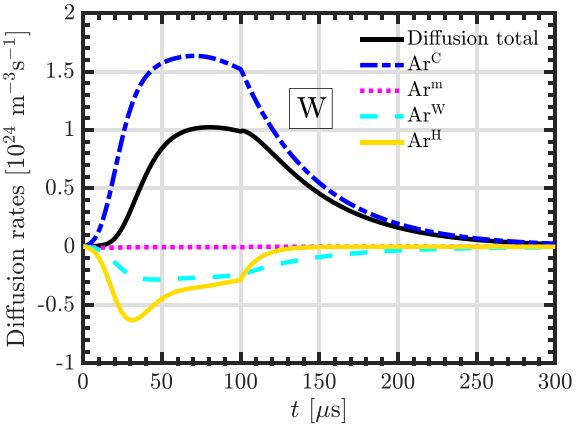

Figure 14. The reaction rates for the argon atom diffusion and hot and warm argon atoms escaping out of the ionization region for a discharge with 75 mm tungsten target operated at working gas pressure of 1 Pa, with a discharge voltage of $V_D = 600$ V giving peak discharge current $I_{D,peak}$ of 24 A ($J_{D,peak} = 0.54$ A cm^{-2}) for 100 μs long pulse.

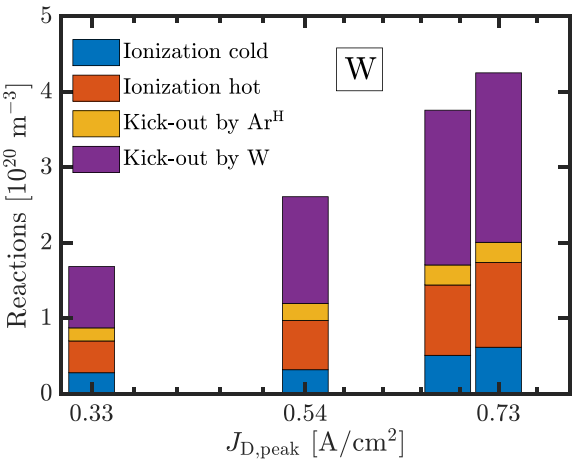

Figure 15. The contribution of the various processes to working gas rarefaction within the ionization region for a discharge with 75 mm tungsten target versus the discharge current density for argon working gas pressure of 1 Pa and pulse length of 100 μs.

The kick-out is mostly due to tungsten atoms sputtered out of the target. The second most important process is electron impact ionization by secondary electrons, which has about 30% contribution, and its role also increases with increased discharge current density. The contributions of electron impact ionization by primary electrons is always smaller.

4. Discussion

We have applied the IRM to determine the various contributions to working gas rarefaction in HiPIMS discharges with a number of different cathode targets, spanning a wide range

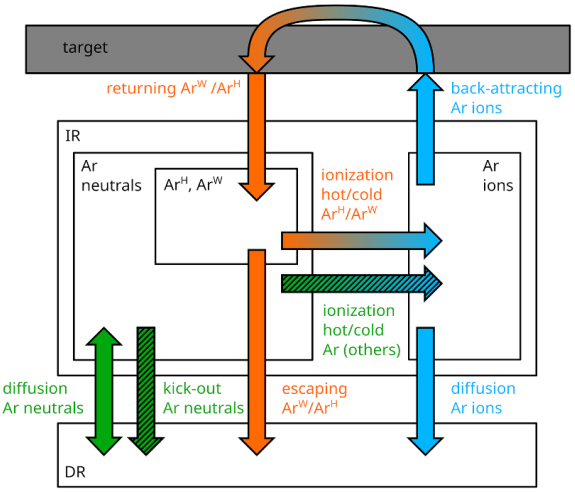

Figure 16. A schematic showing the processes involved in working gas rarefaction. The green arrows denote the neutrals, orange the hot (Ar^H) and warm (Ar^W) argon atoms, and blue arrows denote the ions. Metal sputtering and its influence on working gas rarefaction is omitted in this sketch for clarity.

in atomic mass and sputter yield. We have observed that the working gas rarefaction is driven by electron impact ionization by both primary and hot electrons as well as by kick-out by fast neutrals coming from the target. We observed charge-exchange to have a negligible contribution to working gas rarefaction for all the target materials.

Figure 16 shows the different pathways for argon atoms within the IR and how they enter and are lost from the IR. The green arrows denote the neutrals, orange the hot and warm argon atoms (Ar^H and Ar^W), and blue arrows denote the ions. The argon ions that bombard the target return to the IR as hot (Ar^H) and warm (Ar^W) argon atoms. The argon atoms can be kicked out into the DR by hot argon atoms Ar^H and by sputtered metal neutrals M (not shown in figure 16) and cold argon neutrals can be re-filled from the DR. We see that diffused Ar^W and Ar^H can be ionized and back-attracted again. This loop can proceed several times and appears as a working gas recycling loop [74]. Eventually, these particles escape from the IR. To not overestimate the contribution of ionization to the overall rarefaction, in the following we count only the first ionization of the argon species (hatched horizontal arrow). This can then be compared to the kick-out of argon neutrals by sputtered species and hot argon atoms (vertical hatched arrow). These are the two principal processes that lead to working gas rarefaction.

Figure 17 shows the various contributions to rarefaction, versus the atomic mass of the target material for discharges operated at discharge current densities close to 1 A cm^{-2} and working gas pressures close to 1 Pa. The results show that the processes that are responsible for working gas rarefaction and their relative contributions vary greatly depending on the target material. The relative contribution is determined by integrating the reaction rate for each process throughout the entire

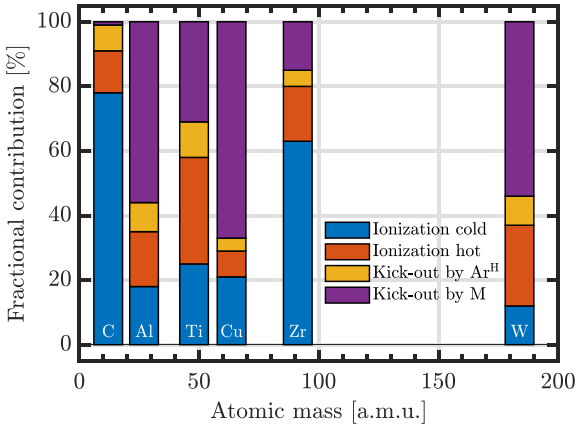

Figure 17. The fractional contribution of the various processes to working gas rarefaction within the ionization region versus the atomic mass. The data is for C (12 amu) ($J_{D,peak} = 1$ A cm^{-2}, $t_{pulse} = 50$ μs, $p_g = 1.0$ Pa), Ti (47.9 amu) ($J_{D,peak} = 1.0$ A cm^{-2}, $t_{pulse} = 100$ μs, $p_g = 1.0$ Pa), Cu (63.5 amu) ($J_{D,peak} = 1$ A cm^{-2}, $t_{pulse} = 40$ μs, $p_g = 1.0$ Pa), Al (27.0 amu) ($J_{D,average} = 1.0$ A cm^{-2}, $t_{pulse} = 100$ μs, $p_g = 2.0$ Pa), Cu (63.5 amu) ($J_{D,peak} = 1$ A cm^{-2}, $t_{pulse} = 40$ μs, $p_g = 1.0$ Pa), Zr (91.2 amu) ($J_{D,peak} = 1$ A cm^{-2}, $t_{pulse} = 50$ μs, $p_g = 1.0$ Pa), and W (183.8 amu) ($J_{D,peak} = 0.73$ A/cm^2 $t_{pulse} = 100$ μs, $p_g = 1.0$ Pa). M denotes the target atom.

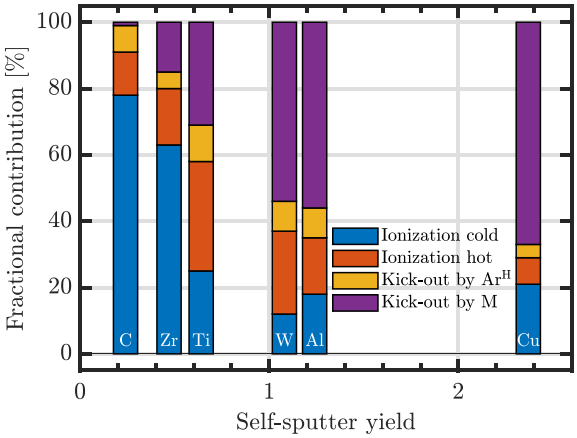

Figure 18. The fractional contribution of the various processes to working gas rarefaction within the ionization region versus self-sputter yield. The data is for C (0.24, 12 amu) ($J_{D,peak} = 1$ A cm^{-2}, $t_{pulse} = 50$ μs, $p_g = 1.0$ Pa), Zr (0.47, 91.2 amu) ($J_{D,peak} = 1$ A cm^{-2}, $t_{pulse} = 50$ μs, $p_g = 1.0$ Pa), Ti (0.64, 47.9 amu) ($J_{D,peak} = 1.0$ A cm^{-2}, $t_{pulse} = 100$ μs, $p_g = 1.0$ Pa), W (1.14, 183.8 amu) ($J_{D,peak} = 0.73$ A/cm^2 $t_{pulse} = 100$ μs, $p_g = 1.0$ Pa), Al (1.19, 27.0 amu) ($J_{D,average} = 1.0$ A cm^{-2}, $t_{pulse} = 100$ μs, $p_g = 2.0$ Pa), and Cu (2.37, 63.5 amu) ($J_{D,peak} = 1$ A cm^{-2}, $t_{pulse} = 40$ μs, $p_g = 1.0$ Pa). M denotes the target atom.

pulse and the afterglow. Table 1 summarizes the atomic properties, for the six target atoms explored. The role of electron impact ionization by primary electrons is significant for most of the target materials explored, while its contribution is however smaller for a discharge with copper and tungsten targets. Electron impact ionization by hot (secondary) electrons has ∼10% contribution when operating with a graphite target while for titanium and tungsten targets the contribution is ∼30%. We also note, for the zirconium case that the role of electron impact ionization is large, or well over 80%, when both primary and secondary electrons are taken into account, while kick-out has only a small contribution. For titanium the overall contribution of electron impact ionization is high or almost 60%. The role of kick-out, or sputter wind, plays a significant role in a discharge with target made of the heaviest target atom, tungsten (183.8 amu), and a larger and indeed rather significant role for a discharge with a copper (63.5 amu) target, while for a discharge with a zirconium (91.2 amu) target the contribution is small. There is therefore no apparent dependence of the various contributions on the target atom mass as can be seen in figure 17.

The missing correlation between target material mass and the contribution to the overall gas rarefaction by the kick-out mechanism is to be expected, as our kick-out model does not explicitly depend on the mass ratios. The justification is based on the fact that argon species are quickly lost on time scales that are short compared to typical pulse lengths (see section 2.1). This short residence time of an argon species in the IR after a collision is in our model therefore approximated by zero. In addition there is at most one collision between a sputtered species from the target and an argon species, due to the long mean free path compared to typical heights of the IR (see section 2.1). The momentum of a sputtered species is therefore unlikely to be shared between more than one argon species. This leads us to the conclusion that the mass ratio is only of secondary importance for determining the contribution of kick-out to the overall gas rarefaction.

Figure 18 shows the fractional contributions of the various processes to working gas rarefaction versus the self-sputter yield of the various target ions. Note that we have chosen to plot the data versus the self-sputter yield, although for argon-dominated discharges, the sputter yield would be the more relevant parameter. For the materials under investigation here, the numerical value of both is very similar, which is why the plot and the conclusions drawn from it would not change if we had used the sputter yield instead of the self-sputter yield. We see that the fractional contribution of kick-out increases with increased self-sputter yield. The total contribution of electron impact ionization decreases with increased self-sputter yield. The sputter yield or the self-sputter yield appears to be the primary factor for which process is the dominating contributor to working gas rarefaction. This is the reason why kick-out is so significant for copper, which has high sputter yield, even though the mass ratio and cohesive energy are smaller than for Zr. In general we see that for the metal targets the kick-out is mainly due to metal atoms sputtered from the target and that kick-out by hot argon atoms has smaller contribution. This is different for the graphite target where hot argon atoms are the dominant contributor by far and carbon atoms only have a small contribution due to its low sputter yield.

A secondary trend is visible in the data in figure 18. From copper with a high sputter yield, to titanium with a moderate sputter yield, the contribution of electron impact ionization increases as discussed in the preceding paragraph. At the same time the share of electron impact ionization from the hot electron population increases. This is due to the IR becoming more argon-dominated as opposed to metal-dominated. As the bombardment of a metal target with argon ions produces secondary electrons, while the bombardment of singly ionized metal ions does not, there is a higher density of hot electrons in these discharges, explaining the stronger contribution of ionization from this electron population for titanium compared to copper. The continuation of this trend cannot be seen for zirconium, nor for graphite.

The above observations, and the discussion above on the working gas rarefaction, highlights its importance for the deposition processes based on magnetron sputtering. In some of the earlier studies of working gas rarefaction [27, 33, 81] the deposition flux is suggested to be influenced in both its magnitude and kinetic energy by the working gas rarefaction. On the one hand, the reduced density of heavy species in a pronounced rarefaction window decreases the energy dissipation of sputtered species on their path through the IR and to the substrate [33], while on the other hand, fewer particles are scattered, possibly increasing the deposition rate in the axial direction [27, 81]. Finally, the reduction of heavy species in front of the target also reduces electron-neutral collision frequency and, therefore, reduces classical (collisional) diffusion of electrons across the magnetic field lines, which is suggested to promote the appearance of plasma instabilities, termed spokes, to provide an alternative path for electron transport across the magnetic field lines [82–85]. These spokes have been suggested to positively influence the release of target ions toward the substrate [86]. Studying the effect of the degree of gas rarefaction on the thin film deposition process is left for the future.

5. Conclusion

The IRM has been applied to determine the degree of working gas rarefaction and the relative contribution of various processes to working gas rarefaction in HiPIMS discharges with different target materials. The dominating contribution of the various processes to working gas rarefaction varies between the different target materials. For targets with low sputter yield electron impact ionization is the dominating process, while for high sputter yield target materials, tungsten as well as copper targets, kick-out of argon atoms by the metal atoms is the dominating process, with over 60% contribution. For the metal targets the magnitude of the kick-out is mainly due to metal atoms sputtered from the target and kick-out by hot argon atoms has a smaller contribution. For the graphite target, the small kick-out contribution is dominated by a kick-out by the hot argon atoms, while carbon atoms only have a small contribution. The sputter yield is the primary factor that dictates which process is the most important when it comes to working gas rarefaction. We also see that the degree of working gas rarefaction depends on the working gas pressure as demonstrated for a discharge with an aluminum target. Working gas rarefaction is much more significant for the lower pressures and the kick-out mechanism is a much more important at higher working gas pressure. Furthermore, we note that in most cases there is a significant fraction of hot and warm argon atoms within the IR. This value is highest or 67% when operating with the graphite target. However, this fraction is smaller for the copper target (16%) and the tungsten target (26%), as much of the sputtering is self-sputtering. This may explain the high neutral gas temperature that has been observed experimentally [42].

Data availability statement

All data that support the findings of this study are included within the article (and any supplementary files).

Acknowledgments

This work was partially supported by the University of Iceland Research Fund for Doctoral students, the Icelandic Research Fund Grant Nos. 196141 and 217999, the University of Iceland Research Fund Grant No. 93940 and the Swedish Government Strategic Research Area in Materials Science on Functional Materials at Linköping University (Faculty Grant SFO-Mat-LiU No. 2009-00971).

ORCID iDs

Kateryna Barynova https://orcid.org/0009-0009-0894-6160
Martin Rudolph https://orcid.org/0000-0002-0854-6708
Swetha Suresh Babu https://orcid.org/0000-0001-5360-5562
Joel Fischer https://orcid.org/0000-0001-9116-6302
Daniel Lundin https://orcid.org/0000-0001-8591-1003
Michael A Raadu https://orcid.org/0000-0002-1299-5039
Nils Brenning https://orcid.org/0000-0003-1308-9270
Jon Tomas Gudmundsson https://orcid.org/0000-0002-8153-3209

References

[1] Rossnagel S M 1999 *IBM J. Res. Dev.* **43** 163
[2] Kelly P J and Arnell R D 2000 *Vacuum* **56** 159
[3] Gudmundsson J T 2020 *Plasma Sources Sci. Technol.* **29** 113001
[4] Gudmundsson J T, Anders A and von Keudell A 2022 *Plasma Sources Sci. Technol.* **31** 083001
[5] Gudmundsson J T 2010 *Vacuum* **84** 1360
[6] Gudmundsson J T, Brenning N, Lundin D and Helmersson U 2012 *J. Vac. Sci. Technol.* A **30** 030801
[7] D Lundin, T Minea and J T Gudmundsson ed 2020 *High Power Impulse Magnetron Sputtering: Fundamentals, Technologies, Challenges and Applications* (Elsevier)
[8] Cada M, Gudmundsson J T and Lundin D 2020 Electron dynamics in high power impulse magnetron sputtering discharges *High Power Impulse Magnetron Sputtering: Fundamentals, Technologies, Challenges and Applications*

ed D Lundin, T Minea and J T Gudmundsson (Elsevier) pp 81–110
[9] Rudolph M, Brenning N, Hajihoseini H, Raadu M A, Minea T M, Anders A, Lundin D and Gudmundsson J T 2022 *J. Phys. D: Appl. Phys.* **55** 015202
[10] Lundin D, Cada M and Hubicka Z 2015 *Plasma Sources Sci. Technol.* **24** 035018
[11] Hajihoseini H, Cada M, Hubicka Z, Ünaldi S, Raadu M A, Brenning N, Gudmundsson J T and Lundin D 2019 *Plasma* **2** 201
[12] Samuelsson M, Lundin D, Jensen J, Raadu M A, Gudmundsson J T and Helmersson U 2010 *Surf. Coat. Technol.* **202** 591
[13] Alami J, Petersson P O Å, Music D, Gudmundsson J T, Bohlmark J and Helmersson U 2005 *J. Vac. Sci. Technol.* A **23** 278
[14] Helmersson U, Lattemann M, Bohlmark J, Ehiasarian A P and Gudmundsson J T 2006 *Thin Solid Films* **513** 1
[15] Greczynski G, Mráz S, Schneider J M and Hultman L 2020 *J. Appl. Phys.* **127** 180901
[16] Thompson M W 1968 *Phil. Mag.* **18** 377
[17] Hofer W O 1991 Angular, energy, and mass distribution of sputtered particles *Sputtering by Particle Bombardment III: Characteristics of Sputtered Particles, Technical Applications* (*Topics in Applied Physics* vol 64) ed R Behrisch and K Wittmaack (Springer) pp 15–90
[18] Gnaser H 2007 Energy and angular distributions of sputtered species *Sputtering by Particle Bombardment: Experiments and Computer Calculations From Threshold to MeV Energies* (*Topics in Applied Physics* vol 110) ed R Behrisch and W Eckstein (Springer) ch 5, pp 231–328
[19] Hoffman D W 1985 *J. Vac. Sci. Technol.* A **3** 561
[20] Rossnagel S M 1988 *J. Vac. Sci. Technol.* A **6** 19
[21] Rossnagel S M and Kaufman H R 1988 *J. Vac. Sci. Technol.* A **6** 223
[22] Rossnagel S M 1988 *J. Vac. Sci. Technol.* A **6** 1821
[23] Drüsedau T P 2002 *J. Vac. Sci. Technol.* A **20** 459
[24] Palmero A, Rudolph H and Habraken F H P M 2005 *Appl. Phys. Lett.* **87** 071501
[25] Palmero A, Rudolph H and Habraken F H P M 2006 *Thin Solid Films* **515** 631
[26] Palmero A, Rudolph H and Habraken F H P M 2006 *Appl. Phys. Lett.* **89** 211501
[27] Kobayashi T 2001 *Appl. Surf. Sci.* **169–170** 405
[28] Serikov V V, Kawamoto S and Nanbu K 1999 *IEEE Trans. Plasma Sci.* **27** 1389
[29] Kolev I and Bogaerts A 2008 *J. Appl. Phys.* **104** 093301
[30] Lundin D, Brenning N, Jadernas D, Larsson P, Wallin E, Lattemann M, Raadu M A and Helmersson U 2009 *Plasma Sources Sci. Technol.* **18** 045008
[31] Alami J, Sarakinos K, Mark G and Wuttig M 2006 *Appl. Phys. Lett.* **89** 154104
[32] Vlcek J, Pajdarová A D and Musil J 2004 *Contrib. Plasma Phys.* **44** 426
[33] Palmucci M, Britun N, Konstantinidis S and Snyders R 2013 *J. Appl. Phys.* **114** 113302
[34] Hecimovic A, de los Arcos T, Schulz-von der Gathen V, Böke M and Winter J 2012 *Plasma Sources Sci. Technol.* **21** 035017
[35] Liebig B, Braithwaite N S J, Kelly P J and Bradley J W 2010 *Thin Solid Films* **519** 1699
[36] Shimizu T, Takahashi K, Boyd R, Viloan R P, Keraudy J, Lundin D, Yang M and Helmersson U 2021 *J. Appl. Phys.* **129** 155305
[37] Horwat D and Anders A 2010 *J. Appl. Phys.* **108** 123306
[38] Ferrec A, Keraudy J and Jouan P-Y 2016 *Appl. Surf. Sci.* **390** 497
[39] Greczynski G, Zhirkov I, Petrov I, Greene J E and Rosen J 2017 *J. Vac. Sci. Technol.* A **35** 060601
[40] Greczynski G, Zhirkov I, Petrov I, Greene J E and Rosen J 2018 *J. Vac. Sci. Technol.* A **36** 020602
[41] Li X, Bakhit B, Johansson Jõesaar M P, Hultman L, Petrov I and Greczynski G 2021 *Surf. Coat. Technol.* **415** 127120
[42] Vitelaru C, Lundin D, Stancu G D, Brenning N, Bretagne J and Minea T 2012 *Plasma Sources Sci. Technol.* **21** 025010
[43] Kadlec S 2007 *Plasma Process. Polym.* **4** S419
[44] Kozák T and Lazar J 2018 *Plasma Sources Sci. Technol.* **27** 115012
[45] Kozák T 2023 *Plasma Sources Sci. Technol.* **32** 035007
[46] Huo C, Lundin D, Gudmundsson J T, Raadu M A, Bradley J W and Brenning N 2017 *J. Phys. D: Appl. Phys.* **50** 354003
[47] Huo C, Raadu M A, Lundin D, Gudmundsson J T, Anders A and Brenning N 2012 *Plasma Sources Sci. Technol.* **21** 045004
[48] Huo C, Lundin D, Raadu M A, Anders A, Gudmundsson J T and Brenning N 2014 *Plasma Sources Sci. Technol.* **23** 025017
[49] Gudmundsson J T, Lundin D, Stancu G D, Brenning N and Minea T M 2015 *Phys. Plasmas* **22** 113508
[50] Stancu G D, Brenning N, Vitelaru C, Lundin D and Minea T 2015 *Plasma Sources Sci. Technol.* **24** 045011
[51] Rudolph M, Hajihoseini H, Raadu M A, Gudmundsson J T, Brenning N, Minea T M, Anders A and Lundin D 2021 *J. Appl. Phys.* **129** 033303
[52] Gudmundsson J T, Fischer J, Hinriksson B P, Rudolph M and Lundin D 2022 *Surf. Coat. Technol.* **442** 128189
[53] Suresh Babu S, Rudolph M, Lundin D, Shimizu T, Fischer J, Raadu M A, Brenning N and Gudmundsson J T 2022 *Plasma Sources Sci. Technol.* **31** 065009
[54] Suresh Babu S, Rudolph M, Ryan P J, Fischer J, Lundin D, Bradley J W and Gudmundsson J T 2023 *Plasma Sources Sci. Technol.* **32** 034003
[55] Eliasson H, Rudolph M, Brenning N, Hajihoseini H, Zanáska M, Adriaans M J, Raadu M A, Minea T M, Gudmundsson J T and Lundin D 2021 *Plasma Sources Sci. Technol.* **30** 115017
[56] Suresh Babu S, Fischer J, Rudolph M, Lundin D and Gudmundsson J T 2024 *J. Vac. Sci. Technol.* A **42** accepted
[57] Raadu M A, Axnäs I, Gudmundsson J T, Huo C and Brenning N 2011 *Plasma Sources Sci. Technol.* **20** 065007
[58] Rudolph M, Revel A, Lundin D, Hajihoseini H, Brenning N, Raadu M A, Anders A, Minea T M and Gudmundsson J T 2021 *Plasma Sources Sci. Technol.* **30** 045011
[59] Gudmundsson J T, Lundin D, Brenning N, Raadu M A, Huo C and Minea T M 2016 *Plasma Sources Sci. Technol.* **25** 065004
[60] Anders A 2010 *J. Vac. Sci. Technol.* A **28** 783
[61] Schmid M 2024 A simple sputter yield calculator (Surface Physics, Institute of Applied Physics, Technischen Universität Wien) (available at: www2.iap.tuwien.ac.at/www/surface/sputteryield)
[62] Matsunami N, Yamamura Y, Itikawa Y, Itoh N, Kazumata Y, Miyagawa S, Morita K, Shimizu R and Tawara H 1983 Energy dependence of the yields of ion-induced sputtering of monatomic solids *Technical Report* IPPJ-AM-32 (Institute of Plasma Physics, Nagoya University)
[63] Yamamura Y and Ishida M 1995 *J. Vac. Sci. Technol.* A **13** 101
[64] Rudolph M, Lundin D, Foy E, Debongnie M, Hugon M-C and Minea T 2018 *Thin Solid Films* **658** 46
[65] Anders A, Capek J, Hála M and Martinu L 2012 *J. Phys. D: Appl. Phys.* **45** 012003
[66] Huo C, Lundin D, Raadu M A, Anders A, Gudmundsson J T and Brenning N 2013 *Plasma Sources Sci. Technol.* **22** 045005
[67] Phelps A V, Greene C H, Burke J P and Phelps A V 2000 *J. Phys. B: At. Mol. Opt. Phys.* **33** 2965

[68] Clementi E, Raimondi D L and Reinhardt W P 1967 *J. Chem. Phys.* **47** 1300
[69] Kittel C 2005 *Introduction to Solid State Physics* 8th edn (Wiley)
[70] Antunes V G, Rudolph M, Kapran A, Hajihoseini H, Raadu M A, Brenning N, Gudmundsson J T, Lundin D and Minea T 2023 *Plasma Sources Sci. Technol.* **32** 075016
[71] Renner M, Fischer J, Hajihoseini H, Gudmundsson J T, Rudolph M and Lundin D 2023 *J. Vac. Sci. Technol.* A **41** 033009
[72] Hajihoseini H, Brenning N, Rudolph M, Raadu M A, Lundin D, Fischer J, Minea T M and Gudmundsson J T 2022 *J. Vac. Sci. Technol.* A **41** 013002
[73] Anders A, Andersson J and Ehiasarian A 2007 *J. Appl. Phys.* **102** 113303
[74] Brenning N, Gudmundsson J T, Raadu M A, Petty T J, Minea T and Lundin D 2017 *Plasma Sources Sci. Technol.* **26** 125003
[75] Butler A, Brenning N, Raadu M A, Gudmundsson J T, Minea T and Lundin D 2018 *Plasma Sources Sci. Technol.* **27** 105005
[76] Kouznetsov V, Macák K, Schneider J M, Helmersson U and Petrov I 1999 *Surf. Coat. Technol.* **122** 290
[77] Fischer J, Renner M, Gudmundsson J T, Rudolph M, Hajihoseini H, Brenning N and Lundin D 2023 *Plasma Sources Sci. Technol.* **32** 125006
[78] Cemin F, Lundin D, Cammilleri D, Maroutian T, Lecoeur P and Minea T 2016 *J. Vac. Sci. Technol.* A **34** 051506
[79] Hajihoseini H, Cada M, Hubicka Z, Ünaldi S, Raadu M A, Brenning N, Gudmundsson J T and Lundin D 2020 *J. Vac. Sci. Technol.* A **38** 033009
[80] Rudolph M, Brenning N, Hajihoseini H, Raadu M A, Fischer J, Gudmundsson J T and Lundin D 2022 *J. Vac. Sci. Technol.* A **40** 043005
[81] Drüsedau T P, Löhmann M and Garke B 1998 *J. Vac. Sci. Technol.* A **16** 2728
[82] Lundin D, Helmersson U, Kirkpatrick S, Rohde S and Brenning N 2008 *Plasma Sources Sci. Technol.* **17** 025007
[83] Anders A, Ni P and Rauch A 2012 *J. Appl. Phys.* **111** 053304
[84] Hecimovic A and von Keudell A 2018 *J. Phys. D: Appl. Phys.* **51** 453001
[85] Rudolph M, Kalanov D, Diyatmika W and Anders A 2021 *J. Appl. Phys.* **130** 243301
[86] Biskup B, Maszl C, Breilmann W, Held J, Böke M, Benedikt J and von Keudell A 2018 *J. Phys. D: Appl. Phys.* **51** 115201

Article II

Self-regulating electron temperature in high-power impulse magnetron sputtering discharges and its effect on the metal ion escape

Kateryna Barynova, Nils Brenning, Swetha Suresh Babu, Joel Fischer, Daniel Lundin, Michael A. Raadu, Jon Tomas Gudmundsson and Martin Rudolph

Plasma Sources Science and Technology 34(6) (2025) 06LT01

Letters

IOP Publishing

Plasma Sources Science and Technology

Plasma Sources Sci. Technol. **34** (2025) 06LT01 (7pp)

https://doi.org/10.1088/1361-6595/adde82

Letter

Self-regulating electron temperature in high-power impulse magnetron sputtering discharges and its effect on the metal ion escape

Kateryna Barynova[1], Nils Brenning[2,3], Swetha Suresh Babu[1], Joel Fischer[3], Daniel Lundin[3], Michael A Raadu[2], Jon Tomas Gudmundsson[1,2] and Martin Rudolph[4,*]

[1] Science Institute, University of Iceland, Dunhaga 3, IS-107 Reykjavik, Iceland
[2] Division of Space and Plasma Physics, School of Electrical Engineering and Computer Science, KTH Royal Institute of Technology, SE-10044 Stockholm, Sweden
[3] Plasma and Coatings Physics Division, IFM-Materials Physics, Linköping University, SE-581 83 Linköping, Sweden
[4] Leibniz Institute of Surface Engineering (IOM), Permoserstraße 15, 04318 Leipzig, Germany

E-mail: martin.rudolph@iom-leipzig.de

Received 21 March 2025, revised 11 May 2025
Accepted for publication 29 May 2025
Published 9 June 2025

Abstract

We have studied the impact of target material on the electron temperature of high power impulse magnetron sputtering (HiPIMS) discharges. The study is based on results from modeling 35 discharges with seven different target materials, using the ionization region (IR) model, a global plasma chemistry model for HiPIMS discharges. We find that the typical evolution of electron temperatures during a HiPIMS pulse stabilizes at the end of the pulse as a result of a balance between electron heating and electron collisional cooling. The underlying cause is a self-regulating mechanism: the monotonically increasing rate coefficients for relevant electron temperatures in HiPIMS discharges ensure that a higher electron temperature enhances electron collisional cooling, while a lower electron temperature reduces it. We furthermore find the steady state electron temperature to be inversely correlated to the sputter yield of the target material. This is a result of the atomic composition in the IR shifting from argon-dominated at low sputter yields to metal-rich at high sputter yields. As the metal ionization rate coefficients are larger at lower electron temperatures compared to that of the argon ionization rate coefficient, the self-regulating mechanism maintains a lower electron temperature in metal-rich discharges. This has implications for the metal ion escape in a HiPIMS discharge, since the ionization mean free path of sputtered atoms depends on the electron temperature. As a result, ionization in metal-rich discharges (lower electron temperature) occurs, on average, further away from the target surface, where the remaining potential hill to climb, in order for a metal

* Author to whom any correspondence should be addressed.

ion to escape to the bulk plasma, is lower. Metal ions in those discharges can therefore escape more easily to the substrate region compared to metal ions in argon-dominated discharges.

Keywords: magnetron sputtering, high power impulse magnetron sputtering, sputtering, plasma chemistry

1. Introduction

Magnetron sputtering is a widely used process for thin-film deposition, extensively employed both in laboratory research and in industrial applications. It is based on a low-pressure plasma discharge in which ions of a working gas, typically argon, are created and accelerated toward a solid target containing the source material. Sputtering from the target releases atoms of the target into the gas phase that can condense on a substrate to form a thin film. High-power impulse magnetron sputtering (HiPIMS) achieves high discharge current densities, on the order of 1 A cm^{-2} over the target area, by pulsing the plasma discharge at a low duty cycle [1, 2]. This process generates peak plasma densities in the range from 10^{18} m^{-3} to a few times 10^{19} m^{-3}, creating a dense plasma region through which sputtered atoms pass with a high probability of becoming ionized [3, 4]. The resulting highly ionized flux of film-forming species enables the deposition of dense [5], crystalline [6], well-adhering thin films [7], and the possibility to tailor film stress [8].

Although the role of high plasma densities in HiPIMS discharges is well understood, the influence of electron temperature remains less explored. Since ionization of the sputtered material in the ionization region (IR) near the target surface is governed not only by the electron density but also by the electron temperature, a deeper understanding of its variation and impact is essential. To address this, we analyze the role of electron temperature using results from the IR Model (IRM), a semi-empirical global plasma chemistry model for HiPIMS discharges [9], from 35 different experimental discharges. These discharges encompass seven different target materials, namely carbon [10], zirconium [11], titanium [12–15], tungsten [16], aluminum [17], chromium [18], and copper [19, 20]. The discharges were operated using argon as a working gas with typical working gas pressures between 0.3 Pa and 2.7 Pa. Discharge current densities were between 0.2 A cm^{-2} and 2.8 A cm^{-2} normalized to the target surface area. Table 1 lists the experimental parameters for all the discharges analyzed here, along with a reference to the original experimental work. Note that for this work all the discharge parameters were re-calculated and analyzed using the most up to date version of the IRM [9].

The IRM allows us to analyze trends in electron temperature T_e in these discharges across different target materials. We start by analyzing the steady state electron temperature that is established when electron heating and cooling rates balance each other. This is typically reached after a few tens of μs, as for example seen by Thomson scattering experiments (figure 5(b) in Ryan *et al* [21]), probe measurements (figures 7–9 in Held *et al* [22]) and in results of the IRM (figure 8 in Eliasson *et al* [10] or figure 8 in Suresh Babu *et al* [16]).

Figure 1 shows the steady state electron temperature T_e as a function of the self-sputter yield Y_{SS}. Even though external process conditions, such as working gas pressure, target size, magnetic field configuration, and HiPIMS pulse conditions varied (see table 1), the prevailing trend is that an increasing sputter yield results in a decreasing steady state electron temperature, a trend that has been pointed out earlier by Brenning *et al* [23]. A similar trend has also been experimentally observed by Held *et al* [22] in their analysis of HiPIMS discharges with titanium, aluminum, and chromium targets. In their study, the electron temperature, at the end of the pulse, stabilized at approximately 4.5 eV for Ti, 2.6 eV for Al, and 1.5 eV for Cr, following an order that correlates with increasing sputter yield.

Both Brenning *et al* [23] and Held *et al* [22] attribute the lower electron temperature for high sputter yield target materials to the higher metal density in the IR and the resulting higher collisional losses leading to increased electron cooling. We note, though, that the electron temperature is a result of electron cooling *and* heating at the same time. We therefore suggest taking a comprehensive look at the electron temperature balance throughout the pulse for two typical discharges modeled by the IRM: one with a low sputter yield and one with a high sputter yield target material. Figures 2(a) and (b) show the electron temperature evolution of a discharge with a zirconium target ($Y_{SS} = 0.60$) and a chromium target ($Y_{SS} = 1.47$), respectively. After an initial transient during the early stage of the HiPIMS discharge pulse, the electron temperatures level out. In figures 2(c) and (d), the individual contributions to heating and cooling of the electron population are shown. The heating of the electron population in the IRM is modeled as a combination of Ohmic heating [24] and the heating by originally hot secondary electrons that have lost the majority of their energy in collisions [25]. For both discharges, Ohmic heating by far dominates the overall heating of the electron population, as it is the primary electron heating mechanism in magnetron sputtering discharges [24–27].

The cooling of the cold electron population occurs through collisions with argon species (Ar(3p^6), Ar^W(3p^6), Ar^H(3p^6), Ar(4s[3/2]$_2$), Ar(4s′[1/2]$_0$), and Ar$^+$) and through collisions with metal species (M(ground state) and M$^+$). Figures 2(c) and (d) present the contributions from both terms separately. At the beginning of the pulse, the cooling is dominated by collisions

Table 1. The discharges included in the study, the operating parameters and the internal discharge parameters ionization probability α_t, the back-attraction probability β_t, determined using the IRM [9]. Reference is given to the original work.

Target	t_{pulse} (μs)	p_g (Pa)	$J_{D,peak}$ (A cm^{-2})	V_D (V)	α_t (%)	$\beta_{t,pulse}$ (%)	References
C	50	1	1	610	11	92	[10]
C	50	1	2	620	18	95	[10]
C	50	1	3	630	23	98	[10]
Ti	400	0.5	2.8	500	93	98	[14]
Ti	100	1	1	640	87	95	[41]
Ti	100	1	0.4	650	78	95	[41]
Ti	100	1	0.2	655	57	95	[41]
Ti	100	1	0.5	520	81	86	[41]
Ti	100	1	0.5	650	81	85	[41]
Ti	100	1	0.5	660	82	79	[41]
Zr	50	1	1	550	86	74	[11]
Zr	100	1	1	550	85	68	[11]
Zr	100	1	0.5	485	73	75	[11]
Zr	50	1	0.6	485	76	72	[11]
Zr	50	1	1.9	575	92	76	[11]
W	100	1	0.33	500	60	94	[16, 42]
W	100	1	0.54	600	68	94	[16, 42]
W	100	1	0.68	700	74	83	[16, 42]
W	100	1	0.73	800	77	74	[16, 42]
W	100	1.6	1.7	900	87	78	[11, 21, 43]
Al	100	0.5	1.4	740	88	73	[14]
Al	100	2	1.2	650	83	78	[14]
Cr	25	0.3	1.0	1020	88	60	[18]
Cr	50	0.3	1.0	950	82	64	[18]
Cr	75	0.3	1.0	1000	81	64	[18]
Cr	100	0.3	1.0	1000	80	65	[18]
Cr	150	0.3	1.0	1000	76	70	[18]
Cr	200	0.3	1.0	990	74	73	[18]
Cr	100	0.3	0.7	770	75	81	[18]
Cr	100	0.3	0.4	680	68	89	[18]
Cu	40	0.5	1	575	62	62	[44]
Cu	40	0.5	1	900	57	58	[19]
Cu	80	0.4	0.9	815	62	54	[19]
Cu	80	2.7	1.3	880	62	52	[19]
Cu	85	0.4	0.9	1000	68	53	[45]

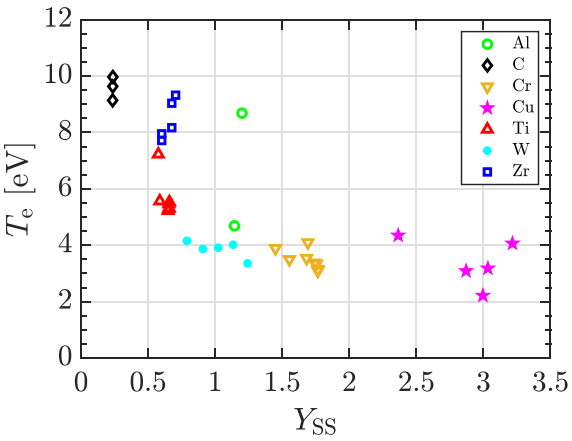

Figure 1. The electron temperature T_e in steady state as a function of the self-sputter yield Y_{SS}. The data points are taken from modeled HiPIMS discharges using a graphite [10], a zirconium [11], a titanium [12, 13], a tungsten [16], an aluminum [17], a chromium [18], and a copper [19] target. The experimental operating parameters for the modeled discharges are listed in table 1.

with argon species for both discharges. Later in the pulse, for the discharge with a zirconium target, electron cooling continues to be primarily governed by collisions with argon, remaining the dominant mechanism until the pulse ends. On the contrary, for the discharge with a chromium target, collisional cooling with argon becomes almost negligible, and the electron population is cooled to a large extent by collisions with metal atoms. The shift from an argon-dominated to a metal-rich discharge in the case of chromium is due to the appearance of sputtered metal species in the IR after the pulse onset (figure 2(f)).

Looking closer at figures 2(c) and (d) reveals striking similarities, both in shape and magnitude of the overall heating and cooling rates, throughout the entire pulse. Any variations in the electron temperature are due to only small differences in these rates. In fact, the strong correlation between heating and cooling rates suggests the presence of a self-regulating mechanism that maintains the electron temperature at a given value. We attribute the underlying cause of this self-regulation to the monotonically increasing electron impact excitation and ionization rate coefficients, as illustrated in figure 3 for metal and argon ionization in the relevant low electron temperature range. In the case that T_e increases, the rate coefficients increase as well, which enhances collisional cooling and limits a further increase of T_e. Conversely, a reduction in T_e lowers the rate coefficients and thereby reduces collisional cooling. This negative feedback mechanism results in heating and cooling rates tending to balance each other, which eventually results in the convergence of the electron temperature to a steady state value.

While the steady increase of the electron impact rate coefficient explains the convergence of electron temperature during the pulse, it does not explain the absolute difference in steady state electron temperatures between the discharges with a Zr and a Cr target. The absolute difference in steady state electron temperatures arises because electron heating is balanced by collisional cooling at *different electron temperatures.*

For example, let us look at the collisional cooling of the two discharges at the end of the discharge pulse. We note that the collisional cooling rate is the product of the rate coefficients for electron impact excitation and ionization with the atomic and electron densities. (In the following example, we neglect the contribution from electron impact excitation.) The IR of the discharge with the Zr target is dominated by argon atoms, or $n_{n,Ar} = 5.4 \times 10^{19}$ m^{-3} compared to $n_{n,Zr} = 3.2 \times 10^{18}$ m^{-3}. Its electron density is $n_{n,e} = 3.8 \times 10^{18}$ m^{-3}. In the case of the discharge with a Cr target, the argon and metal atom densities in the IR are of the same order of magnitude, or

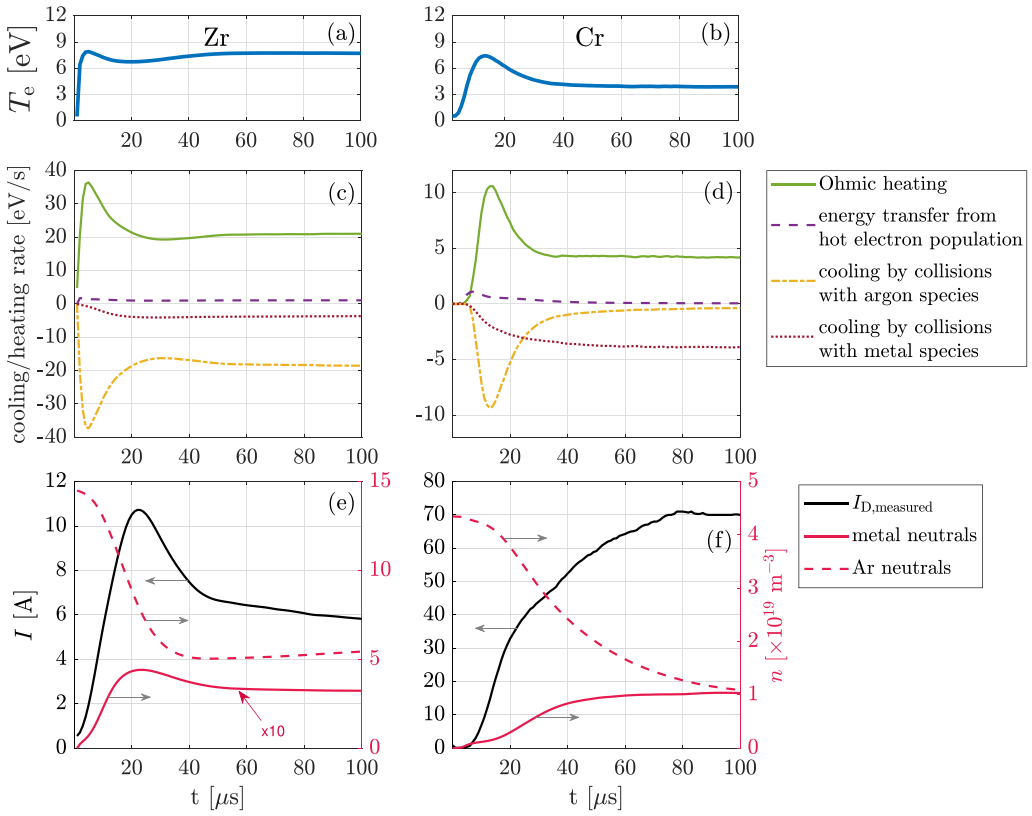

Figure 2. Detailed examples of the electron temperature evolution for discharges with (a) a zirconium target ($Y_{SS} = 0.60$) and (b) a chromium target ($Y_{SS} = 1.47$). The rate of change of the electron temperature due to contributions by electron heating mechanisms and collisional cooling mechanisms are shown in panel (c) for the the discharge with azirconium target and in panel (d) for the discharge with a chromium target, respectively. Panels (e) and (f) show the corresponding experimental and modeled discharge currents as well as the evolution of the gas and metal neutrals densities. Discharge conditions: Zr target (diameter $d = 2$ inch), pulse length $t_{pulse} = 100$ μs, discharge voltage $V_D = -550$ V, working gas pressure $p_{gas} = 1$ Pa [11], Cr target (diameter $d = 6$ inch), pulse length $t_{pulse} = 100$ μs, discharge voltage $V_D = -1000$ V, working gas pressure $p_{gas} = 0.3$ Pa [18].

$n_{n,Ar} = 1.1 \times 10^{19}$ m^{-3} and $n_{n,Cr} = 1.0 \times 10^{19}$ m^{-3}. The electron density in that discharge is $n_{n,e} = 6.6 \times 10^{18}$ m^{-3}. Setting aside the electron densities that differ only by a factor of 2, the product of the high Cr density with the high ionization rate coefficient for Cr (figure 3), results in a high collisional cooling being established at a considerable lower electron temperature compared to the discharge with a Zr target. For the latter, argon is the dominating species in the IR. Its much lower ionization rate coefficient (figure 3) results in the electron cooling balancing the heating only at high electron temperature. The primary cause for the difference in electron temperature between discharges with different target materials is thus the difference in the temperature-dependent electron cooling rate, that is determined by the atomic composition of the IR (metal vs. argon species), which is ultimately dependent on the sputter yield of the target material.

Variations in T_e at the beginning and in the middle of the pulse seen in figures 2(a) and (b) can be explained using the same argument. Each pulse features a highly dynamic atomic composition within the IR [26, 28, 29]. At the pulse onset, the IR is free of metal atoms and filled by argon species only, which is reflected by an initial peak in the electron temperature, as observed for both the discharge with a zirconium target (≈ 5 μs) and the discharge with a chromium target (≈ 13 μs) in figure 2. Argon ion bombardment of the target results in sputtering and raises the metal species density in the IR. This is reflected by a reduction in electron temperature after the initial peak. For the discharge with a zirconium target, the density of the metal species reduces after the current maximum (figure 2(e)), which is reflected by the re-establishment of the initial high electron temperature. In the discharge with a chromium target, the metal density continuously increases, which

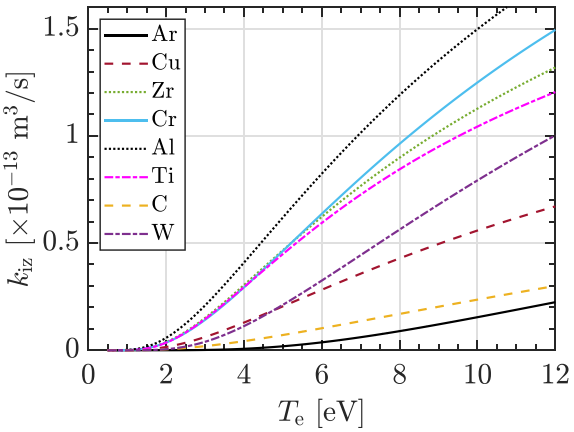

Figure 3. Rate coefficients for electron impact ionization of metal and argon atoms in the low electron temperature range. The rate coefficients are calculated assuming a Maxwellian electron energy distribution function. The cross sections used for the calculations are discussed in each model study for a graphite [10], a zirconium [11], a titanium [12, 13], a tungsten [16], an aluminum [17], a chromium [18], and a copper [19] target.

lowers the electron temperature until steady state is reached. In conclusion, the variation in the atomic composition of the IR is reflected in the changes of T_e during the pulse. Only later in the pulse, when atomic densities reach steady state, T_e also stabilizes.

Note, that the atomic composition in the IR is not solely determined by the sputter yield of the target material, but by a more complex recycling loop [23, 30] in which atoms in the IR are ionized and back-attracted to the target. Argon ions either backscatter from the target [31, 32] or implant into the target, and subsequently diffuse back (as neutrals) into the IR [23, 30]. Upon re-entering the IR, they can be ionized and back-attracted again to the target, which effectively traps them in a gas recycling loop. In addition, a metal recycling loop exists that starts with sputtering fresh metal atoms into the IR, where they can be ionized and back-attracted to the target. The ion bombardment of the target then maintains the metal recycling loop. It is only because of these two material recycling loops, that the high discharge currents in HiPIMS discharges are possible [23]. One could ask why the discharge currents in discharges with strong metal recycling ($Y_{SS} > 1$) are not strongly amplified from these loops. Oks and Anders [29] have pointed out the importance of electron cooling by metal atoms for stabilizing current fluctuations. We can here add that the systematically lower electron temperatures observed in discharges with high sputter yield materials prevent an uncontrolled amplification of the discharge current.

The observed correlation between electron temperature and target self-sputter yield impacts the deposition rate. Strong ionization of sputtered metal atoms results in a significant fraction of those ions being back-attracted to the target instead of reaching the substrate [33]. However, as T_e decreases, the mean free path for electron impact ionization increases [14, 34]. The ionization mean free path for the sputtered atoms is given by $\lambda_{mfp} = v_{sputter}/(n_e k_{iz})$, where $v_{sputter}$ is the velocity of the sputtered atom, $k_{iz}(T_e)$ is the electron temperature-dependent ionization rate coefficient (figure 3), and n_e is the electron density. In the discharge with a zirconium target shown in figure 2, the electron temperature at the end of the pulse is 7.7 eV. The rate coefficient for zirconium ionization at this electron temperature is 0.86×10^{-13} m^3 s^{-1} (figure 3). For the discharge with a chromium target in figure 2, the electron temperature is 3.9 eV, corresponding to a chromium ionization rate coefficient of 0.27×10^{-13} m^3 s^{-1}. Typically, sputter velocities correspond to ~1/2 the cohesive energy of the target material [35] and are similar for most metals. Thus, for a given electron density, the factor ≈3 in the two rate coefficients corresponds to a factor three longer ionization mean free path in the discharge with a chromium target compared to the discharge with a zirconium target.

The shift in the location of ionization of sputtered species has indeed been experimentally observed by Held *et al* [22] using spectroscopic imaging. They found that most metal atoms were ionized within 0.5 mm of the target in a HiPIMS discharge with a titanium target, whereas for aluminum and chromium targets, this distance was significantly greater. They attributed the trend to the variation in T_e, which decreased from 4.5 eV for titanium to 1.5 eV for chromium. They hypothesized that this shift may impact the deposition rate, as the electric field responsible for ion back-attraction weakens with distance from the target [36, 37]. Ions created further away from the target have thus to overcome a smaller potential hill which facilitates metal ion escape toward the substrate.

Using the IRM, we can show that this is indeed the case. The target ion back-attraction in the IRM is formally described as the probability β_t that an ion created in the IR is back-attracted toward the target [12, 38, 39]. The probability that an ion is back-attracted *during the pulse* is described as $\beta_{t,pulse}$ [13]. Figure 4 shows $\beta_{t,pulse}$ for the discharges studied here as a function of sputter yield. The overall trend is clear and shows a significant decrease in $\beta_{t,pulse}$ with increasing sputter yield. Due to the broad spread of values for one cathode material, the trend may not always strictly hold for a point-to-point comparison, though, which can be attributed to the influence of other process parameters on $\beta_{t,pulse}$ [15]. Values for $\beta_{t,pulse}$ start at around 0.95 for low sputter yield carbon discharges and drop to approximately 0.55 for high sputter yield copper discharges. To put these numbers into perspective, keep in mind, that while $\beta_{t,pulse}$ describes the ion back-attraction probability, $(1 - \beta_{t,pulse})$ describes the ion escape probability. A decrease of $\beta_{t,pulse}$ from 0.95 to 0.55 results in an increase of $(1 - \beta_{t,pulse})$ from 0.05 to 0.45, i.e. by a factor of 9. Hence, as the metal ion back-attraction during the pulse is severely reduced, so is the loss in deposition rate for high sputter yield target materials. This applies in particular to chromium and copper, two materials of significant current interest [18, 34].

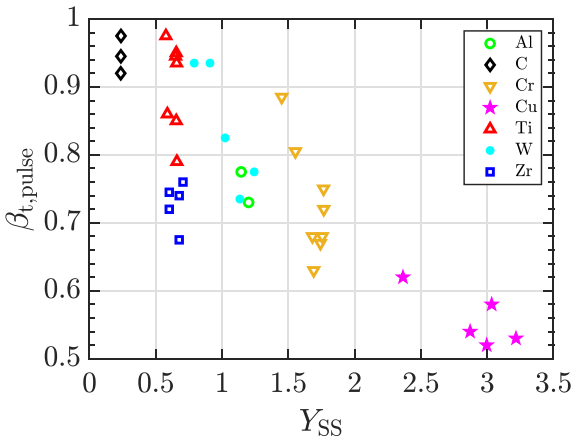

Figure 4. The target ion back-attraction probability as a function of self-sputter yield. The data points are taken from modeled HiPIMS discharges using a graphite [10], a zirconium [11], a titanium [12, 13], a tungsten [16], an aluminum [17], a chromium [18], and a copper [19] target. The experimental operating parameters for the modeled discharges are listed in table 1.

Brenning *et al* [15] have argued that already small differences in β_t are of practical importance for the optimization of HiPIMS processes. This is not only because percentagewise the increase in ion escape $(1-\beta_t)$ is disproportionally higher than the decrease in β_t. In addition, they show that a low β_t can be used as a single figure of merit for HiPIMS discharges, in a way, that a discharge with a lower β_t can always be tuned to provide a better combination of deposition rate and ionized flux fraction. In this regard, one should ask the question of how the trend shown in figure 4 can be exploited for the practical application of HiPIMS processes in thin film deposition. An obvious idea would be to replace the target material for one with a higher sputter yield. The applications in which one can freely choose the material to be deposited are likely limited, though. Another idea would be to increase the target ion bombardment energy to increase the sputter yield. Brenning *et al* [15, 40] empirically found a lower β_t for higher discharge currents, an effect which could be explained by the trend in figure 4. A third possibility would be to alloy the target material in order to increase its effective sputter yield, if the application in view is tolerant to foreign atoms in the thin film.

To conclude, we have classified HiPIMS discharges according to the self-sputter yield Y_{SS} of their target material. Discharges with high Y_{SS} target materials, such as chromium or copper, have a low electron temperature T_e. They are rich in easily ionized metal atoms. Collisional cooling is therefore already effective at low T_e in balancing electron heating. This low T_e results in a long mean free path for ionization of metal atoms sputtered off the target. Consequently, the sputtered species are ionized farther away from the cathode where the electric potential is flatter compared to the target vicinity. Metal ion escape toward the substrate is therefore more easily achieved, which reduces the loss in deposition rate. Contrary, discharges with low Y_{SS} target materials, such as carbon or titanium, are argon-dominated. Collisional cooling is here only effective at high T_e due to the high ionization potential of argon. In this class of discharges, sputtered metals ionize close to the target vicinity where they are subjected to strong back-attracting fields, increasing the loss in deposition rate.

Data availability statement

The data that support the findings of this study are available upon reasonable request from the authors.

Acknowledgments

This work was partially supported by the Icelandic Research Fund Grant Nos. 196141 and 2511073, the University of Iceland Research Fund Grant No. 93940, University of Iceland Research Fund for Doctoral Students and the Swedish Government Strategic Research Area in Materials Science on Functional Materials at Linköping University (Faculty Grant SFO-Mat-LiU No. 2009-00971).

Conflict of interest

The authors have no conflicts to disclose.

ORCID iDs

Kateryna Barynova https://orcid.org/0009-0009-0894-6160
Nils Brenning https://orcid.org/0000-0003-1308-9270
Swetha Suresh Babu https://orcid.org/0000-0001-5360-5562
Joel Fischer https://orcid.org/0000-0001-9116-6302
Daniel Lundin https://orcid.org/0000-0001-8591-1003
Jon Tomas Gudmundsson https://orcid.org/0000-0002-8153-3209
Martin Rudolph https://orcid.org/0000-0002-0854-6708

References

[1] Helmersson U, Lattemann M, Bohlmark J, Ehiasarian A P and Gudmundsson J T 2006 *Thin Solid Films* **513** 1
[2] Gudmundsson J T, Brenning N, Lundin D and Helmersson U 2012 *J. Vac. Sci. Technol. A* **30** 030801
[3] Lundin D, Helmersson U, Kirkpatrick S, Rohde S and Brenning N 2008 *Plasma Sources Sci. Technol.* **17** 025007
[4] Rudolph M, Brenning N, Hajihoseini H, Raadu M A, Fischer J, Gudmundsson J T and Lundin D 2022 *J. Vac. Sci. Technol. A* **40** 043005
[5] Samuelsson M, Lundin D, Jensen J, Raadu M A, Gudmundsson J T and Helmersson U 2010 *Surf. Coat. Technol.* **202** 591
[6] Alami J, Petersson P O Å, Music D, Gudmundsson J T, Bohlmark J and Helmersson U 2005 *J. Vac. Sci. Technol. A* **23** 278
[7] Ehiasarian A P, Wen J G and Petrov I 2007 *J. Appl. Phys.* **101** 054301

[8] Cemin F, Abadias G, Minea T, Furgeaud C, Brisset F, Solas D and Lundin D 2017 *Acta Mater.* **141** 120
[9] Barynova K, Suresh Babu S, Rudolph M, Fischer J, Lundin D, Raadu M A, Brenning N and Gudmundsson J T 2024 *Plasma Sources Sci. Technol.* **33** 065010
[10] Eliasson H, Rudolph M, Brenning N, Hajihoseini H, Zanáška M, Adriaans M J, Raadu M A, Minea T M, Gudmundsson J T and Lundin D 2021 *Plasma Sources Sci. Technol.* **30** 115017
[11] Suresh Babu S, Fischer J, Barynova K, Rudolph M, Lundin D and Gudmundsson J T 2024 *J. Vac. Sci. Technol. A* **42** 043007
[12] Rudolph M, Hajihoseini H, Raadu M A, Gudmundsson J T, Brenning N, Minea T M, Anders A and Lundin D 2021 *J. Appl. Phys.* **129** 033303
[13] Rudolph M, Brenning N, Raadu M A, Hajihoseini H, Gudmundsson J T, Anders A and Lundin D 2020 *Plasma Sources Sci. Technol.* **29** 05LT01
[14] Lundin D, Čada M and Hubička Z 2015 *Plasma Sources Sci. Technol.* **24** 035018
[15] Brenning N, Butler A, Hajihoseini H, Rudolph M, Raadu M A, Gudmundsson J T, Minea T and Lundin D 2020 *J. Vac. Sci. Technol. A* **38** 033008
[16] Suresh Babu S, Rudolph M, Lundin D, Shimizu T, Fischer J, Raadu M A, Brenning N and Gudmundsson J T 2022 *Plasma Sources Sci. Technol.* **31** 065009
[17] Raadu M A, Axnäs I, Gudmundsson J T, Huo C and Brenning N 2011 *Plasma Sources Sci. Technol.* **20** 065007
[18] Barynova K, Shimizu T, Zanáška M, Viloan R P B, Rudolph M, Lundin D and Gudmundsson J T 2025 *Plasma Sources Sci. Technol.* (in preparation)
[19] Gudmundsson J T, Fisher J, Hinriksson B P, Rudolph M and Lundin D 2022 *Surf. Coat. Technol.* **442** 128189
[20] Fischer J, Renner M, Gudmundsson J T, Rudolph M, Hajihoseini H, Brenning N and Lundin D 2023 *Plasma Sources Sci. Technol.* **32** 125006
[21] Ryan P J, Bradley J W and Bowden M D 2019 *Phys. Plasmas* **26** 040702
[22] Held J, Schulz-von der Gathen V and von Keudell A 2023 *Plasma Sources Sci. Technol.* **32** 065006
[23] Brenning N, Gudmundsson J T, Raadu M A, Petty T J, Minea T and Lundin D 2017 *Plasma Sources Sci. Technol.* **26** 125003
[24] Huo C, Lundin D, Raadu M A, Anders A, Gudmundsson J T and Brenning N 2013 *Plasma Sources Sci. Technol.* **22** 045005
[25] Huo C, Lundin D, Gudmundsson J T, Raadu M A, Bradley J W and Brenning N 2017 *J. Phys. D: Appl. Phys.* **50** 354003
[26] Huo C, Raadu M A, Lundin D, Gudmundsson J T, Anders A and Brenning N 2012 *Plasma Sources Sci. Technol.* **21** 045004
[27] Brenning N, Gudmundsson J T, Lundin D, Minea T, Raadu M A and Helmersson U 2016 *Plasma Sources Sci. Technol.* **25** 065024
[28] Anders A, Andersson J and Ehiasarian A 2007 *J. Appl. Phys.* **102** 113303
[29] Oks E and Anders A 2009 *J. Appl. Phys.* **105** 093304
[30] Anders A, Čapek J, Hála M and Martinu L 2012 *J. Phys. D: Appl. Phys.* **45** 012003
[31] Rudolph M, Lundin D, Foy E, Debongnie M, Hugon M-C and Minea T 2018 *Thin Solid Films* **658** 46
[32] Takagi Y, Sakashita Y, Toyoda H and Sugai H 2006 *Vacuum* **80** 581
[33] Brenning N, Lundin D, Raadu M A, Huo C, Vitelaru C, Stancu G D, Minea T and Helmersson U 2012 *Plasma Sources Sci. Technol.* **21** 025005
[34] Hopwood J 1998 *Phys. Plasmas* **5** 1624
[35] Hofer W O 1991 *Sputtering by Particle Bombardment III: Characteristics of Sputtered Particles, Technical Applications* (*Topics in Applied Physics* vol 64) ed R Behrisch and K Wittmaack (Springer) pp 15–90
[36] Mishra A, Kelly P J and Bradley J W 2010 *Plasma Sources Sci. Technol.* **19** 045014
[37] Rauch A, Mendelsberg R J, Sanders J M and Anders A 2012 *J. Appl. Phys.* **111** 083302
[38] Christie D J 2005 *J. Vac. Sci. Technol. A* **23** 330
[39] Vlček J and Burcalová K 2010 *Plasma Sources Sci. Technol.* **19** 065010
[40] Brenning N, Hajihoseini H, Rudolph M, Raadu M A, Gudmundsson J T, Minea T M and Lundin D 2021 *Plasma Sources Sci. Technol.* **30** 015015
[41] Hajihoseini H, Čada M, Hubička Z, Ünaldi S, Raadu M A, Brenning N, Gudmundsson J T and Lundin D 2019 *Plasma* **2** 201
[42] Shimizu T, Takahashi K, Boyd R, Viloan R P, Keraudy J, Lundin D, Yang M and Helmersson U 2021 *J. Appl. Phys.* **129** 155305
[43] Ryan P J 2019 Electron diagnostics of magnetron discharges *PhD Thesis* University of Liverpool, Liverpool, England (http://dx.doi.org/10.17638/03070217)
[44] Cemin F, Lundin D, Cammilleri D, Maroutian T, Lecoeur P and Minea T 2016 *J. Vac. Sci. Technol. A* **34** 051506
[45] Gudmundsson J T, Sigurjonsson P, Larsson P, Lundin D and Helmersson U 2009 *J. Appl. Phys.* **105** 123302

Article III

High power impulse magnetron sputtering from a chromium target

Kateryna Barynova, Tetsuhide Shimizu, Rommel Paulo B. Viloan, Michal Zanáška, Joel Fischer, Martin Rudolph, Daniel Lundin and Jon Tomas Gudmundsson

Plasma Sources Science and Technology 35(2) (2026) 025028

IOP Publishing Plasma Sources Sci. Technol. 35 (2026) 025028 https://doi.org/10.1088/1361-6595/ae42e5

Plasma Sources Science and Technology

OPEN ACCESS

RECEIVED
20 August 2025

REVISED
16 January 2026

ACCEPTED FOR PUBLICATION
6 February 2026

PUBLISHED
20 February 2026

PAPER

High power impulse magnetron sputtering from a chromium target

Kateryna Barynova[1], Tetsuhide Shimizu[2], Rommel Paulo B Viloan[3], Michal Zanáška[3], Joel Fischer[3,4], Martin Rudolph[5], Daniel Lundin[3] and Jon Tomas Gudmundsson[1,6,*]

[1] Science Institute, University of Iceland, Dunhaga 3, IS-107 Reykjavik, Iceland
[2] Department of Mechanical Systems Engineering, Graduate School of Systems Design, Tokyo Metropolitan University, 6-6, Asahigaoka, Hino-shi, 191-0065 Tokyo, Japan
[3] Thin Film Physics Division, IFM-Materials Physics, Linköping University, Linköping, SE-581 83, Sweden
[4] Evatec AG, Hauptstrasse 1a, Trübbach CH-9477, Switzerland
[5] Leibniz Institute of Surface Engineering (IOM), Permoserstraße 15, 04318 Leipzig, Germany
[6] Department of Electromagnetics and Plasma Physics, School of Electrical Engineering and Computer Science, KTH Royal Institute of Technology, SE-10044 Stockholm, Sweden
[*] Author to whom any correspondence should be addressed.

E-mail: tumi@hi.is

Keywords: magnetron sputtering discharge, high power impulse magnetron sputtering (HiPIMS), chromium, ionized flux fraction

Abstract

High power impulse magnetron sputtering discharges with a chromium target are studied experimentally. For a given pulse length the deposition rate decreases and the ionized flux fraction increases with increased discharge current density ranging between 0.4 – 1.0 A cm^{-2}. Furthermore, the deposition rate is highest for a pulse length of 50 μs and decreases when shortening the pulses down to 25 μs or increasing the pulse length up to 200 μs. The measured chromium ionized flux fraction ranges between 10% – 50%. The ionized flux fraction is highest for the highest peak discharge current density, and the shortest pulse length studied. In order to understand the experimental findings the discharges were analyzed by applying the ionization region model (IRM). The IRM is a semi-empirical, time-dependent, volume-averaged, plasma chemistry model that covers the ionization region (IR) of the magnetron sputtering discharge and uses the measured cathode voltage and current waveforms as input data. The IRM results indicate that the singly charged chromium ion is the dominant ion in the IR and the discharges operate in metal recycling mode. The ionization probability of the sputtered species increases with increased peak discharge current density. It also increases at first with decreased pulse length, reaches a peak and then decreases with further decrease in the pulse length. The back-attraction probability of the sputtered species decreases with decreasing pulse length, and with increasing peak discharge current density.

1. Introduction

Chromium Cr([Ar]3d^{5}4s^1) is a transition metal of Group VI, which in thin film form is known for its high corrosion resistance and high hardness. Chromium coatings are popular as decorative surfaces, due to their mirrorlike surface finishing, and they provide good wear resistance and corrosion-protection. For these applications chromium coatings are commonly deposited using electroplating [1], however, due to environmental concerns, there have been attempts to develop physical vapor deposition (PVD) processes. Among the most promising PVD processes for chromium deposition is magnetron sputter deposition [2, 3]. Magnetron sputtering [4–6] is a widely applied PVD technique [7] for the deposition of thin films and coatings, where the film-forming material is sputtered from a solid target by ion bombardment. Often these discharges are driven by direct current (dc) power supplies or radio frequency (rf) sinusoidal generators. In these cases, the ions that bombard the target and the substrate are ions of the noble working gas [4]. By pulsing the discharge a higher plasma density can be achieved, and if the discharge is driven by high power pulses, at low repetition frequency, and short duty cycle, the plasma can be

dense enough to ionize a significant proportion of the sputtered species. In that case, the ions bombarding the cathode target and the substrate are both ions of the working gas and ions of the target material. This approach is called high power impulse magnetron sputtering (HiPIMS) [8, 9], a technique that was developed to provide highly ionized flux of the sputtered species to the deposition process [10]. In HiPIMS operation with a metal target the ionized flux fraction can be high, typically in the range 10% – 80%, and the ionized flux fraction increases with increased discharge current density and decreased working gas pressure, as has been demonstrated experimentally for a number of target materials [10–14]. Chromium films and coatings have been deposited by HiPIMS [15–19] as well as deep oscillation magnetron sputtering [20, 21] over the years, and have been demonstrated to show superior properties, increased film mass density [15, 17], improved high-temperature steam oxidation resistance [17], control of crystallographic orientation [19], enhanced mechanical properties [21], and improved corrosion resistance [18], over dc magnetron sputter deposited films. The improved thin film properties are attributed to the increased ionization of the sputtered species in the HiPIMS process. However, as also demonstrated in the study by Samuelsson *et al* [15] the improved film properties come with reduced deposition rate.

Numerious studies of HiPIMS discharges with a chromium target have been conducted, both experimental characterization [22–25] and discharge modeling [26–29]. Alami *et al* [22] measured the temporal evolution of the emission lines representing the various species in a HiPIMS discharge with a chromium target, and observed a significant increase in the Cr^0 and Cr^+ emission intensity, and almost an order-of-magnitude drop in the Ar^0 emission intensity, with increasing discharge current density, confirming significant working gas rarefaction. Zgheib *et al* [26, 30] developed a time-dependent global plasma model of the ionization region (IR) in a HiPIMS discharge with a chromium target and with argon as the working gas. Their study indicated a higher density of the metal ions Cr^+ than the ions of the working gas Ar^+, as well as the appearance of working gas rarefaction. This model was later coupled with a Monte Carlo treatment to study the ion transport in the discharge [28]. Held *et al* [25] presented a simplified IR model (IRM) and explored among other discharge properties, the electron energy, and connect low average electron energy to high sputter yield and ionization of the sputtered metal atoms farther away from the target surface. Furthermore, Gao *et al* [27] presented a time-dependent global plasma chemistry model, which was more recently developed into a time-dependent hybrid plasma model [29].

In HiPIMS operation there is an inescapable trade-off between high deposition rate and high ionized flux fraction, known as the HiPIMS compromise [31]. To optimize a HiPIMS deposition process for a given target material five operational parameters can be adjusted: working gas pressure, discharge current density, pulse length, magnetic field strength, and magnetic unbalance [31]. It was suggested by Butler *et al* [32] that it should be possible to increase the deposition rate, while maintaining a high ionized flux fraction, by shortening the pulse length. This idea was based on the fact that the ions still in the magnetic trap (the IR) at the end of the pulse are not back-attracted to the target once the discharge voltage pulse is switched off. Consequently, for these afterglow ions that have a velocity directed away from the target the probability of reaching the substrate is high. This idea was further tested numerically on experimental discharges with a titanium target [12] by Rudolph *et al* [33], using the time-dependent IRM [34]. The model results showed that, by shortening the pulse length, in a HiPIMS discharge with a titanium target, the outward flux of film-forming species could be increased significantly. The model predicted a gain in deposition rate of close to 50%, when using 40 μs instead of 100 μs-long pulses at a constant average power and close-to-constant peak discharge current. The model results also suggested that this increase in deposition rate can be achieved without compromising the ionized flux fraction. In a following study, these results were experimentally confirmed by Shimizu *et al* [35]. In this current study, the effect of shortening the pulse length on the deposition rate and the ionized flux fraction is explored through experiments, followed by using the IRM for a HiPIMS discharge with argon as the working gas and a chromium target, to gain understanding of the experimental findings. The model provides insights into the temporal evolution of the species densities and the discharge current composition. It also provides information on the voltage drop across the IR, the ionization probability, as well as the back-attraction probability of the sputtered species [34]. The paper is structured as follows: In section 2 we discuss the experimental setup and section 4 discusses the findings of the experimental campaign. The basics of the IRM and the addition of the chromium reaction set are reviewed in sections 3 and 5 discusses the results of the model studies. The findings of this work are summarized in section 6.

2. Experimental setup

The experiments were performed in a cylindrical stainless steel vacuum chamber (44 cm in diameter and 75 cm in height) evacuated by a turbomolecular pump to a base pressure below 2×10^{-4} Pa. The magnetron assembly was mounted on the top circular flange with the target surface facing downwards. The magnetron assembly was a standard slightly unbalanced type (magnetic field strength and geometry has been given elsewhere [36]). A chromium disk of 150 mm in diameter and a thickness of 6 mm mounted onto the magnetron assembly was used as the sputtering target. Argon with a 99.9997% purity was introduced through a leak valve. A working gas pressure of 0.3 Pa was used for all experiments. Unipolar HiPIMS pulses were supplied by a HiPSTER 6 pulsing unit (Ionautics AB, Sweden). The pulsing unit was fed by a HiPSTER 6 – DCPSU 6 kW dc power supply. The discharge current and voltage waveforms were monitored and recorded onto a Tektronix TDS2004C digital oscilloscope, which was connected to the discharge voltage and current sensors of the HiPIMS pulsing unit. The average sputtering power delivered to the target was kept at 1.5 kW by adjusting the pulse repetition frequency between 50 – 2100 Hz. More details on the experimental setup are given by Shimizu *et al* [35].

Reference measurements were carried out operating a dc magnetron sputtering discharge at the same experimental conditions, which included maintaining the power at 1.5 kW. The resulting discharge voltage waveforms for the HiPIMS discharges are shown in figure 1 and the discharge current waveforms are shown in figure 2, as the pulse length was varied in the range between 25 and 200 μs, for peak discharge current density $J_{D,peak}$ of 0.4 A cm^{-2}, 0.7 A cm^{-2}, and 1.0 A cm^{-2}. To estimate the peak discharge current density we divide the measured discharge current by the entire target area (180 cm^2). For each set of measurements the peak discharge current density was maintained by adjusting the discharge voltage.

A quartz crystal micro-balance (QCM) (SQM-160 thin film deposition monitor) with a native frequency of 5 MHz and a gold coated surface was applied to determine the deposition rate. The QCM faced the target racetrack region at a distance of 10 cm (a typical substrate position). For each series of varying pulse lengths, with a fixed peak discharge current density $J_{D,peak}$, the total mass deposition rate M_{total} (including both deposited neutrals and ions) was obtained by the QCM. The total mass deposition rate was calibrated against the deposition rate calculated by measuring the film thickness of selected samples deposited at a pulse length of 75 μs (0.4 A cm^{-2}) and 100 μs (0.4 and 0.7 A cm^{-2}) using a scanning electron microscope (Zeiss 1540EsB).

A gridless ion meter was used to determine the ionized flux fraction (F_{flux}). The device is based on the same QCM system used for measuring the deposition rate and a detailed description is given elsewhere [35, appendix A.2.]. The ionized fraction of the metal flux was obtained using the formula [12]

$$F_{flux} = \frac{M_{total} - M_{neutral}}{M_{neutral}} \quad (1)$$

where $M_{neutral}$ is the mass deposition rate of neutral metal atoms only (i.e. excluding positive metal ions), by biasing the QCM, as discussed elsewhere [37]. The mass deposition rates M_{total} and $M_{neutral}$ were determined by a linear fit of the non-calibrated film thickness signal from the QCM readout unit recorded for 3 min with approximately 0.3 s steps. The error is estimated to be up to 15% for a single measurement based on the accuracy of the mass deposition rate determination [38].

3. The IRM

The IRM is a time-dependent volume-averaged plasma chemistry model that covers the IR of the magnetron sputtering discharge [34, 39, 40]. The IRM is a semi-empirical model as the measured cathode voltage and current waveforms are applied as input data. The essence of the IRM is to determine the temporal development of all the species densities and the electron temperature. The temporal evolution of the heavy species densities and the electron temperature are defined by a set of ordinary differential equations. The electron density is determined by applying the quasi-neutrality condition. The model assumes two populations of electrons, the cold electrons, created in the bulk ionization processes, and hot electrons, originating from secondary electrons emitted from the target due to ion bombardment and accelerated across the cathode sheath. Each of the electron populations is assumed to have a Maxwellian energy distribution. In an earlier study this assumption was compared to calculations using a Boltzmann solver, for a discharge with a titanium target, yielding a good agreement [41]. The basic formulation of the IRM, including the reaction rates for the various surface and volume processes that

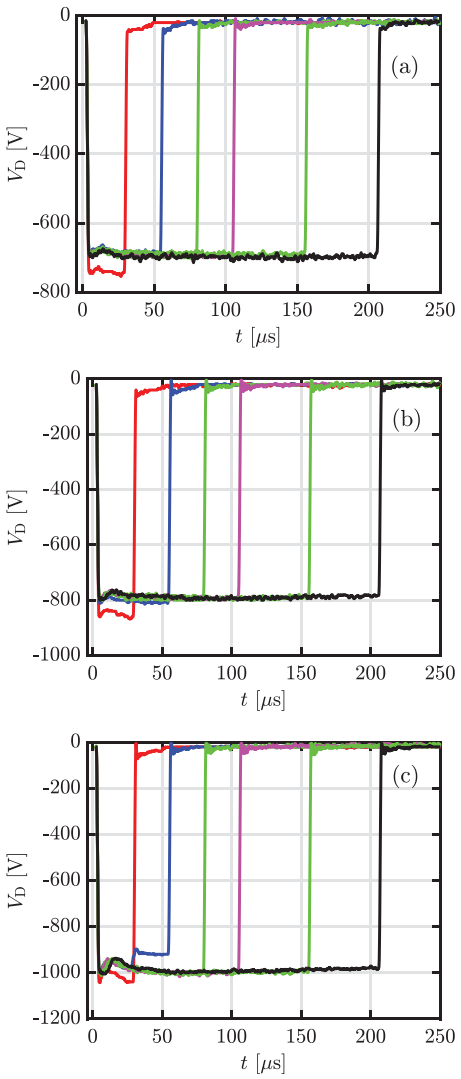

Figure 1. The discharge voltage waveforms when varying the pulse length between 25 and 200 μs. The discharge voltage was adjusted to maintain a peak discharge current current density $J_{D,peak}$ at (a) 0.4 A cm^{-2}, (b) 0.7 A cm^{-2}, and (c) 1.0 A cm^{-2}. The working gas was argon at a pressure of 0.3 Pa and the target was a 150 mm diameter chromium disk. The pulse repetition frequency was adjusted to maintain a constant time-averaged power of 1.5 kW.

are taken into account, has been summarized by Huo *et al* [34]. Note that the interaction of the discharge species with surfaces, in particular the sputter yield of the cathode target, and the target secondary electron emission yield, has a significant influence on discharge properties, including discharge composition [42], electron power absorption [42], the back-attraction probability [43], and processes that lead to working gas rarefaction [40]. Modifications to the IRM have been made more recently regarding the treatment of afterglow [33], updated reaction rates [41], and a modification of the term that describes the expulsion of sputtered species that contribute to the rarefaction of the working gas [40]. The updated IRM is applied for this current study.

In this current study, the working gas is argon, and the discharge is composed of the atoms and ions of the argon working gas, the sputtered chromium species and their ions, and electrons. The argon species included in the model are cold argon atoms in the ground state Ar^C, metastable argon atoms (both $Ar(4s[3/2]_2)$ and $Ar(4s'[1/2]_0)$), Ar^+ and Ar^{2+} ions, and warm Ar^W and hot Ar^H argon atoms

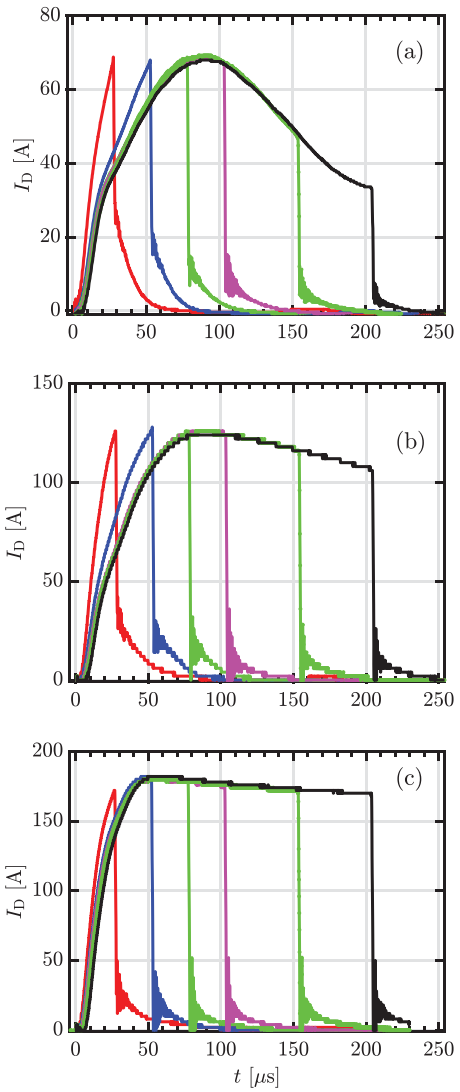

Figure 2. The discharge current waveforms when varying the pulse length between 25 and 200 μs. The discharge voltage was adjusted to maintain a peak discharge current current density $J_{D,peak}$ at (a) 0.4 A cm^{-2}, (b) 0.7 A cm^{-2}, and (c) 1.0 A cm^{-2}. The working gas was argon at a pressure of 0.3 Pa and the target was a 150 mm diameter chromium disk. The pulse repetition frequency was adjusted to maintain a constant time-averaged power of 1.5 kW.

in the ground state. The latter two populations of argon atoms originate from argon ions that bombard the target and then return to the discharge as neutrals. The hot argon population represents the reflected argon atoms at the target [44, 45] and is assumed to have an average energy of 2 eV (motivated by Raadu *et al* [39]). The warm population Ar^W is assumed to have energy similar to the thermal energy of the target surface, about 0.1 eV (∼1000 K) [46] and is due to argon ions that penetrate the target surface, and then slowly diffuse back as atoms. More details on the argon discharge, the reaction set, and rate coefficients can be found in recent publications [47, 48]. The chromium species in the discharge include chromium atoms in the ground state, and the ions Cr^+ and Cr^{2+}. The sputtered chromium atoms are assumed to enter the IR with a velocity corresponding to the energy of roughly $1/2 \times \mathcal{E}_{\text{cohesive}} = 1/2 \times 4.10\,\text{eV} = 2.05\,\text{eV}$ [49, p. 50], where $\mathcal{E}_{\text{cohesive}}$ is the cohesive energy of the target material. This is the most probable energy of the Sigmund–Thompson distribution for sputtered species, which is roughly half the cohesive energy of the solid target [50, 51].

The rate coefficients for electron impact ionization are calculated using cross sections assuming a Maxwellian electron energy distribution. For electron impact ionization of the chromium atom we use

Table 1. The reactions and rate coefficients used in the IRM involving chromium determined for both hot and cold electrons. The rate coefficients are calculated assuming a Maxwellian electron energy distribution function and fit in the range $T_e = 1 - 7$ eV for cold electrons and 200 – 1000 eV for hot electrons.

	Reaction	Threshold [eV]	Rate coefficient [m^3/s]	Electron group	Reference
(R1)	$e + Cr \rightarrow Cr^+ + e$	6.7666	$8.95 \times 10^{-14} T_e^{0.4682} \exp(-7.0786/T_e)$	cold	[52, 53]
			$4.0586 \times 10^{-13} - 2.6729 \times 10^{-16} \times T_e$	hot	
(R2)	$e + Cr^+ \rightarrow Cr^{2+} + 2e$	16.4857	$9.2132 \times 10^{-15} T_e^{0.5702} \exp(-14.3882/T_e)$	cold	[54]
			$9.2457 \times 10^{-14} - 5.7450 \times 10^{-17} \times T_e$	hot	
(R3)	$e + Cr \rightarrow Cr^{2+} + 3e$	23.25	$2.9309 \times 10^{-16} T_e^{1.2029} \exp(-20.8886/T_e)$	cold	[53]
			$5.6848 \times 10^{-14} - 3.6485 \times 10^{-17} \times T_e$	hot	
(R4)	$Ar^+ + Cr \rightarrow Ar + Cr^+$		6.2×10^{-16}		[55]
(R5)	$Ar(4s'[1/2]_0) + Cr \rightarrow Ar + Cr^+ + e$		2.38×10^{-16}		[55]
(R6)	$Ar(4s[3/2]_2) + Cr \rightarrow Ar + Cr^+ + e$		2.38×10^{-16}		[55]

Table 2. The lowest few excited states of the chromium atom that are used to calculate the collisional loss per electron–ion pair created.

Configuration	Term	Threshold [eV]
$3d^5(^6S)4s$	a^7S	ground state
$3d^5(6S)4s$	a^5S	0.9414
$3d^4 4s^2$	a^5D	0.9610–1.0300
$3d^5(^4G)4s$	a^5G	2.5438–2.5446
$3d^5(^4P)4s$	a^5P	2.7079–2.7099
$3d^4 4s^2$	a^3P	2.8719–2.9871
$3d^5(^6S)4p$	z^7P°	2.8894–2.9134
$3d^4 4s^2$	a^3H	2.9674–3.0004

the cross section recommended by Lennon *et al* [52] for electron energies below 15 eV, and for higher electron energies the cross section measured by Nelson [53] is used. For electron impact ionization of the Cr^+ ion to create the doubly ionized Cr^{2+} we use the cross section measured by Man *et al* [54] and for electron impact ionization of the neutral chromium atom to create the doubly ionized Cr^{2+} we use the cross section measured by Nelson [53]. The rate coefficient for charge transfer between Ar^+ and Cr is taken from the calculation of Bogaerts *et al* [55], using the adjusted value. The rate coefficients for Penning ionization are also taken from the same calculations. For the primary electrons the rate coefficients are fitted for T_e between 1 and 7 eV and for the hot electrons in the range 200 – 1000 eV. All the electron impact rate coefficients for reactions involving chromium species are listed in table 1.

Due to the significant amount of chromium in the discharge, we need to calculate and account for the collisional energy loss for each electron-chromium ion pair created $\mathcal{E}_c$ in the electron energy balance [56, section 3.5.2]. For this purpose, we use the same electron impact ionization cross section mentioned above and we assume the cross section for electron elastic scattering on Cr atoms to be the same as for tungsten atoms [57]. We include the seven lowest excited levels of the chromium atom listed in table 2 to account for electron energy loss. As the electron impact excitation cross sections for the chromium atom are mostly unknown we assume that each excitation cross section follows the Thomson cross section [56, p. 58] with a peak at 1/5 of the peak of the ionization cross section. If the electron impact excitation cross sections are overestimated (underestimated), the collisional energy loss per electron–ion pair created from Cr atoms is overestimated (underestimated) slightly, and the Cr^+ ion density and the electron density are underestimated (overestimated). We will see later that the Cr^+ ion is the dominating ion in the discharge, so this assumption can have some influence on the overall results.

The sputter yield for Ar^+ and Cr^+ ions bombarding a chromium target was estimated using the TU Wien Sputter Yield Calculator [58], which is based on the empirical equations for sputter yields at normal incidence developed by Matsunami *et al* [59].

For the secondary electron emission yield due to bombardment of the target by argon ions, we use the fit given for clean metals by Phelps and Petrović [60]. For the chromium ions bombarding the chromium target, the secondary electron emission yield is essentially zero. For the secondary electron emission due to the bombardment of the target by Cr^{2+} ions we use the fit given by Baragiola *et al* [61]

$$\gamma_{see} = 0.032 \times (0.78\mathcal{E}_{iz} - 2\phi) \quad (2)$$

where $\mathcal{E}_{iz}$ is the ionization energy of the ion and the work function is $\phi = 4.6$ eV for chromium [62]. This gives a secondary electron emission yield $\gamma_{see,2+} = 0.23$, due to bombardment by doubly ionized chromium.

The IRM relies on three free parameters that have to be adjusted to fit the calculated discharge current to the measured discharge current: (i) the ion back-attraction probability for the metal ions $\beta_{t,pulse}$ and gas ions $\beta_{g,pulse}$, (ii) the potential drop across the IR, V_{IR}, and (iii) the electron recapture probability r. In practice, V_{IR} is determined using the ratio $f = V_{IR}/V_D$, where V_D is the discharge voltage [34]. For the cases presented here, we assume $r = 0.7$, since it has been suggested by Buyle *et al* [63], based on a Monte Carlo model calculations, that the electron recapture probability lies between 65%–75% for a planar magnetron sputtering discharge. Note that for a metal target, that operates in self-sputter recycling mode, the value of the electron recapture probability r does not influence the model results much as the metal ions dominate the discharge and they do not create secondary electrons. Furthermore, we assume $\beta_{t,pulse} = \beta_{g,pulse}$, where t stands for target and g stands for working gas, as in previous studies [34, 39, 48].

We can lock the model, and confine the two remaining free parameters (f and $\beta_{t,pulse}$), using the experimentally measured discharge current waveform and the measured ionized flux fraction as suggested by Butler *et al* [32]. The ionized flux fraction onto a given surface facing the sputter target is related to the time-integrated total number of metal atoms and metal ions leaving the IR for the diffusion region (DR) during the discharge pulse through

$$F_{flux} = \left(1 + \left(\frac{\xi_{tn}}{\xi_{ti}}\right) \frac{\int_T \tilde{\Gamma}_M^{DR}(t)\,dt}{\int_T \tilde{\Gamma}_{M+}^{DR}(t)\,dt}\right)^{-1} \tag{3}$$

where $\tilde{\Gamma}_M^{DR}(t)$ is the total flux of metal neutrals and $\tilde{\Gamma}_{M+}^{DR}(t)$ is the total flux of metal ions into the DR, T is the pulse period, ξ_{ti} is the transport parameter for ions, and ξ_{tn} is the transport parameter for neutrals [64–66]. This approach is applied to all the discharges modeled in this work. The transport parameter ratio has been determined experimentally for a HiPIMS discharge with a titanium target to be roughly $\xi_{tn}/\xi_{ti} \approx 1.25$ for a substrate located 3 cm from the target surface and $\xi_{tn}/\xi_{ti} \approx 2$ for a substrate located 7 cm from the target surface [65]. Based on these findings we use the value of 2 for flux measurements made 10 cm from the target surface.

Keep in mind that the IRM is a volume-averaged model, that we are applying to describe a spatially varying plasma in the IR. In reality the plasma density decays axially with distance from the target surface (see e.g. Dubois *et al* [67]) and rotating ionization zones (or spokes) travel azimuthally along the racetrack [68]. Furthermore, the cross sections and rate coefficients used all have some uncertainty and in some cases rather significant. For this reason the model results should be taken as an indication of trends or scalings rather than absolute values.

4. Experimental results

The measured discharge voltage waveforms are shown in figure 1 for three different peak discharge current densities (0.4, 0.7 and 1.0 A cm^{-2}) and varying pulse lengths (25 – 200 μs). For a given peak discharge current density the discharge voltage is the same for all pulse lengths, except for the shortest pulse where the discharge voltage is slightly higher, as higher discharge voltage is required to reach the desired peak discharge current within a shorter time. The corresponding discharge current waveforms are shown in figure 2, for three different peak discharge current densities, as the pulse lengths vary. For the shortest pulses the discharge current waveform appears to be triangular as the current is still rising when the voltage is shut off. For longer pulses the discharge current reaches a peak and then decreases again. The drop in the discharge current towards the end of the pulse is most significant for the lowest peak discharge current density (figure 2(a)) and the drop in discharge current is greater with longer pulse. This is in agreement with what has been reported on the discharge current waveform for discharges with a chromium target in the past [69, 70]. Lundin *et al* [23] reported on an initial high-current peak followed by a stable plateau at lower current level for working gas pressure below 1 Pa, but a gradual drop in current for higher pressure for 500 μs long pulses. Note that this is different from what was observed experimentally for a discharge with a titanium target, where the discharge current either peaked at the end of the pulse, or peaked before but remained high until the end of the pulse [35].

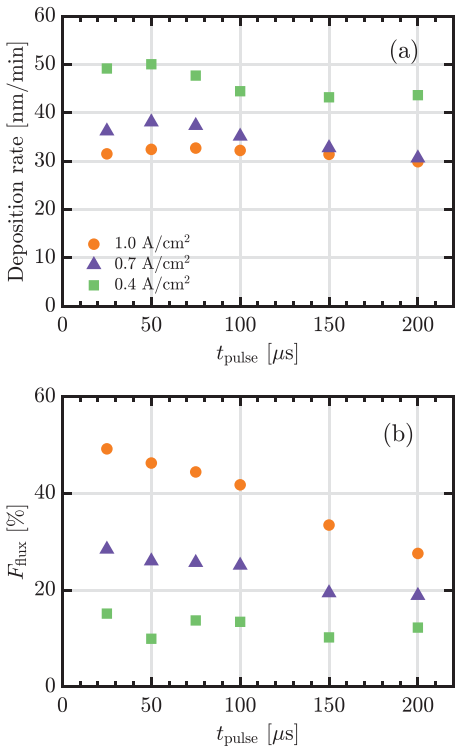

Figure 3. (a) The deposition rate and (b) the ionized flux fraction versus the pulse length for peak discharge current density of 0.4 A cm^{-2}, 0.7 A cm^{-2}, and 1.0 A cm^{-2}, for argon working gas pressure of 0.3 Pa. The target was 150 mm diameter chromium disk. The pulse repetition frequency was adjusted to maintain a constant time-averaged power of 1.5 kW.

The two key flux parameters, the deposition rate and the ionized flux fraction, determine the throughput of the deposition process, and the quality of the deposited films. Figure 3 shows the measured deposition rate and the measured ionization flux fraction versus the pulse length for three different peak current densities $J_{D,peak}$. It can be seen in figure 3(a) that for any given pulse length investigated we observe a decrease of the deposition rate when the peak discharge current density is increased, which is consistent with what is commonly reported in the literature [13, 35, 71, 72].

In addition, it can be seen that, when the maximum discharge current density is kept constant, the deposition rate increases with decreasing pulse length and reaches a maximum for pulse length of around 50 μs. However, if the pulse length is shortened even further, the deposition rate decreases. At 0.4 A cm^{-2} the increase to the maximum in deposition rate is 15%, at 0.7 A cm^{-2} the increase is 24.3% and in both cases the maximum appears for 50 μs long pulses, and at 1.0 A cm^{-2} the increase is 9.5% and the peak appears for 75 μs long pulse. An increase in deposition rate with decreased pulse length at fixed average power for a discharge with a titanium target had been reported earlier by Konstantinidis *et al* [73]. These results for the deposition rate are very similar to what was observed experimentally for discharges with a titanium target [35] and had earlier been predicted using the IRM [33]. However, for a discharge with a titanium target the increase in deposition rate was more significant or 45% – 54% [35]. Also note that the deposition rate for a chromium target is higher than for a titanium target for a given peak current density and pulse length, which is to be expected as the sputter yield is roughly three times larger for chromium than for titanium.

The measured ionized flux fraction is shown in figure 3(b) as a function of pulse length for the three different peak discharge current densities. An increase in the ionized flux fraction with increasing $J_{D,peak}$ is observed. The increase in the ionized flux fraction with an increase in $J_{D,peak}$ is commonly observed in HiPIMS operation, and has been demonstrated experimentally for a number of metal targets [11–13, 35, 74]. Here, it is also seen that the ionized flux fraction increases with decreasing pulse length and the increase is much more significant for the highest $J_{D,peak}$. At 0.4 A cm^{-2} the increase in the ionized flux fraction is 23.7%, at 0.7 A cm^{-2} the increase is 50.5%, and at 1.0 A cm^{-2} the increase is 78.4%, as the pulse length is varied from 200 μs to 25 μs. The peak in ionized flux fraction appears always for the

shortest pulses. This is consistent with the measured ionized flux fraction for a titanium target reported by Shimizu *et al* [35] but only for peak discharge current density of 1.0 A cm^{-2}.

5. Model results

The IRM was applied to explore all the discharges studied experimentally, with varying peak discharge current density and pulse lengths, and discussed in section 4. For these discharges the IRM results provide the temporal evolution of the species that constitute the plasma discharge, the discharge current composition, the electron power absorption mechanisms, the dominant recycling mechanism, and the working gas rarefaction.

5.1. Composition of the film-forming flux to the substrate

First we explore the flux of the film forming species out of the IR. Figure 4 shows the metal flux out of the IR into the DR Γ^{DR}_{M,M^+}, normalized by the deposition flux for the 200 μs long pulse, versus the pulse length, for two cases of peak discharge current densities, 0.4 A cm^{-2} (lowest) and 1.0 A cm^{-2} (highest). A direct effect of shortening the pulses is a decrease in the deposition rate per pulse, which is expected since the frequency is adjusted to keep the average power constant, since less energy is put into each pulse. However, the contributions to the deposition rate from the pulse and the afterglow, behave very differently. The contribution from the afterglow remains roughly constant for a given peak current density, while the contribution during the pulse increases with increasing pulse length. The relative contribution of the afterglow is smaller at the higher peak discharge current density (1.0 A cm^{-2}) than at the lower peak discharge current density (0.4 A cm^{-2}), as can be seen by comparing figures 4(a) and (b). Furthermore, the ion contribution during the pulse is significantly higher at the higher peak discharge current density (1.0 A cm^{-2}) than at the lower peak discharge current density (0.4 A cm^{-2}). For peak discharge current density of 0.4 A cm^{-2} (figure 4(a)) at a pulse length of 25 μs the contribution from the afterglow is similar (49%) to the contribution during the pulse, for a pulse length of 50 μs and longer, the pulse contribution is dominating (67% for 50 μs) and its contribution increases with increased pulse length.

5.2. Current composition

In dc magnetron sputtering most of the ions that constitute the discharge are ions of the noble working gas and all the sputtering is due to ions of the working gas, the primary ions. In a HiPIMS discharge both ions of the working gas and ions of the target material participate in the sputter process. This can be seen in figure 5, which shows the temporal evolution of the discharge current composition at the target surface for two different pulse lengths (25 μs and 200 μs) and two different peak discharge current densities (0.4 and 1.0 A cm^{-2}). It can be seen that the discharge is initiated by the ionization of the argon working gas, but the Ar^+ ions only appear to be significant early in the pulse, while they have a relatively small contribution overall, and later in the pulse Cr^+ ions are dominating. The contributions from Ar^{2+} and Cr^{2+} ions and secondary electron emission are much smaller, almost negligible. Furthermore, the contribution of Ar^+ ions, despite being small, is relatively larger for shorter pulses. This is in agreement what was observed by Alami *et al* [22] which measured the temporal evolution of the emission lines representing the various species in a HiPIMS discharge with a chromium target. They observed a significant increase in the Cr^0 emission intensity, and an even more significant increase in the Cr^+ emission intensity, as the peak discharge current density was increased, indicating the significance of Cr^+ ions in the discharge, when operating with a chromium target applying 50 μs long pulses with an average current density of up to 2.8 A cm^{-2}, and a working gas pressure of 0.8 Pa. This also agrees with the results of the model study by Zgheib *et al* [26] which also showed the Cr^+ ions to dominate over Ar^+ ions for short pulses at 0.67 Pa. However, they found that at higher pressure (4 Pa), the absolute Ar^+ ion density became higher than that of Cr^+ ions.

We see in figure 5 that there is a time lag between the model results and the experimental curve. This is in particular noticeable for the shorter pulses. In fact the first few microsecods of the pulse the arbitrary choice of the seed electron density may affect the calculated density values, so these first few microseconds of the model results are uncertain [75].

5.3. Ionization and back-attraction probabilities

The connection between the external control parameters, such as working gas pressure, pulse power density, the magnetic field strength, and the pulse configuration, and the two flux parameters, the

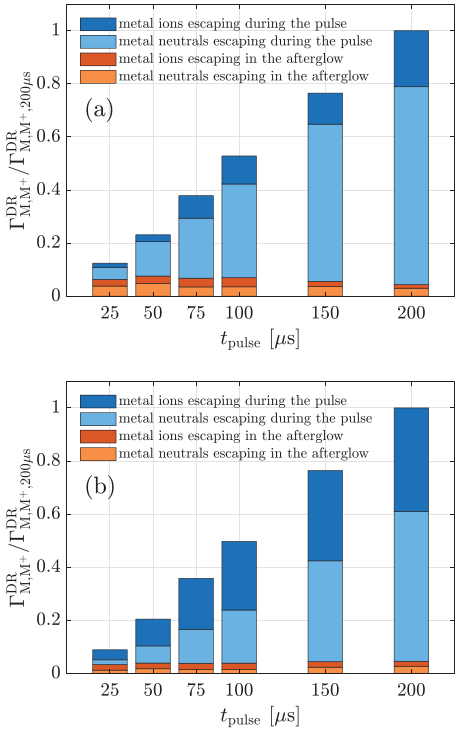

Figure 4. The metal flux out of the ionization region towards the DR (Γ^{DR}_{M,M^+}) for an individual pulse for varying pulse lengths normalized to the deposition rate for 200 μs-long pulses when the discharge voltage is kept constant for the peak discharge current density of (a) 0.4 A cm^{-2} and (b) 1.0 A cm^{-2}. The two top bars in dark blue and light blue show the contribution from the pulse and two bottom bars in dark orange and light orange show the contribution from the afterglow. The right-hand axis shows the power per pulse compared to the same 200 μs reference pulse.

deposition rate and the ionized flux fraction, is typically studied using the two internal discharge parameters, the probability of ionization of the target atom α_t and the probability of back-attraction of the target ion β_t [12, 66]. The latter is one of the fitting parameters of the model, which is here determined, or locked, by constraining the model by the measured ionized flux fraction F_{flux}, using equation (3). Knowledge of these two internal discharge parameters provides a quantitative insight into the quality of a deposition process and its efficiency. Here, we explore how these internal discharge parameters depend on the pulse length and the peak discharge current density. These parameters are shown in figure 6, versus the pulse length for varying peak discharge current densities 0.4 A cm^{-2}, 0.7 A cm^{-2}, and 1.0 A cm^{-2}. We see that the ionization probability α_t increases with increased peak discharge current density, as we have demonstrated earlier for a discharge with a titanium target [76]. For a fixed peak current density, the ionization probability increases at first as the pulse length is shortened, and then decreases again for short pulses. The peak in ionization probability appears for roughly 100 μs long pulse for peak discharge current density of 0.4 and 0.7 A cm^{-2}, and at 50 μs for peak discharge current density of 1.0 A cm^{-2}. This dependence on the pulse length was discussed earlier by Brenning *et al* [31] which explained this dependence for shorter pulses, with a larger fraction of the sputtered atoms being created at the beginning of the pulse, and therefore these atoms have a smaller ionization probability due to the initial low plasma density. This can explain the drop in the ionization probability for very short pulses (see also discussion by Fischer *et al* [77]). Furthermore, the drop in ionization probability for the longer pulses is, at least partially, due to the drop in the discharge current towards the end of the longer pulses, seen in figure 2 and discussed in the beginning of section 4.

Figure 6(b) shows the back-attraction probability of the sputtered species versus pulse length for peak discharge current density of 0.4, 0.7 and 1.0 A cm^{-2}. It can be seen that the back-attraction probability β_t decreases with increased peak discharge current density. Recall, that a decrease in the back-attraction of the sputtered species has a positive influence on both the deposition rate and the ionized flux fraction [31, 78]. The lower back-attraction probability with increasing peak discharge current

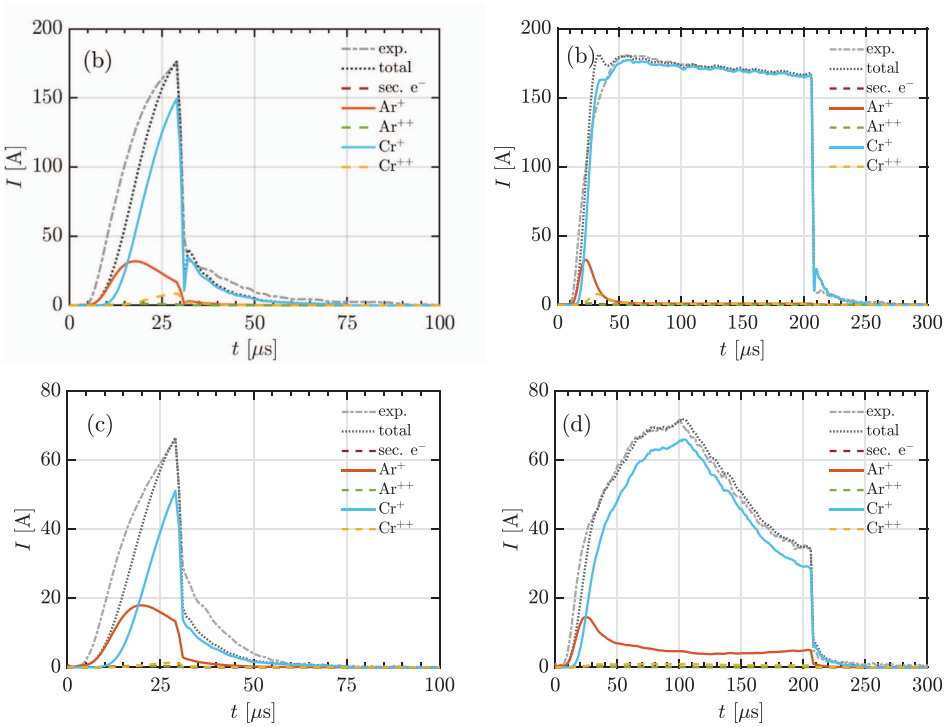

Figure 5. The discharge current composition at the target surface for peak discharge current density of 1.0 A cm^{-2} and pulse length (a) 25 μs and (b) 200 μs, and for peak discharge current density of 0.4 A cm^{-2} and pulse length (c) 25 μs and (d) 200 μs. The argon working gas pressure was 0.3 Pa and the target was 150 mm diameter chromium disk. The pulse repetition frequency was adjusted to maintain a constant time-averaged power of 1.5 kW.

density had been hinted by Brenning *et al* [31] when discussing the optimization of the HiPIMS discharge. Furthermore, we have recently demonstrated, based on modeling discharges with a number of varying target materials, that the back-attraction probability decreases with increasing self-sputter yield of the target material [43]. Therefore, increased discharge current density, which is driven by increased discharge voltage, consequently leads to higher sputter yield and lower back-attraction probability β_t. We also see in figure 6(b) that the back-attraction probability β_t increases with increasing pulse length. For longer pulses and low peak discharge current density the drop in the discharge current towards the end of the pulse decreases the contribution from the afterglow to the flux of the film forming species, which can at least partially explain the increase in the back-attraction probability for longer pulses. Earlier, we had demonstrated an increase in the ionization probability α_t and a decrease in the back-attraction probability β_t with decreasing pulse length, when modeling a HiPIMS discharge with a tungsten target [79]. Note that in the afterglow, the target potential is close to 0 V, and therefore the ion back-attracting electric field vanishes and we assume that the sputtered ionic species have a directional velocity away from the target. Therefore, the effective back-attraction probability, which includes both the pulse and the afterglow, is somewhat lower than the back-attraction probability during the pulse which is shown in figure 6(b).

We explore further the contribution of argon ions to the sputter process by plotting (with symbols) in figure 7 the fraction of the total ion current at the target surface that is due to working gas ions

$$\zeta = \frac{J_{Ar^+} + J_{Ar^{2+}}}{\sum_i J_i} \tag{4}$$

where i denotes the various ions that bombard the target surface, Ar^+, Ar^{2+}, Cr^+, and Cr^{2+}. This fraction is simplified by assuming that the contribution of secondary electron emission to the current at the target surface is small, and can be neglected. The fraction of argon ions bombarding the target surface increases with decreasing pulse length and decreasing discharge current density. For the shortest pulse length of 25 μs and lowest discharge current density of 0.4 A cm^{-2} the argon ions (Ar^+ and Ar^{2+} ions) exhibit roughly 41% contribution, while for pulse length of 150 μs and longer the contribution

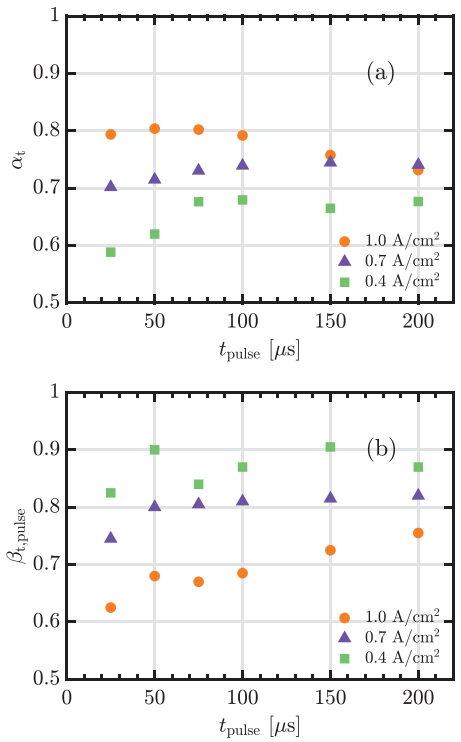

Figure 6. (a) The ionization probability α_t and (b) the back-attraction probability $\beta_{t,pulse}$ determined by the IRM versus the pulse length. The working gas was argon at 0.3 Pa and the target was 150 mm diameter chromium disk. The pulse repetition frequency was adjusted to maintain a constant time-averaged power of 1.5 kW.

is roughly 11%. At higher current density the contribution is around 30% at 25 μs and below 10% for pulse length 75 μs and longer. Again, this confirms that the discharges are dominated by Cr^+ ions.

This formulation can be simplified further by assuming that a fraction $\zeta = J_{Ar^+}/J_{D,i}$ of the total ion current at the target surface is due to singly charged ions of the working gas which sputter the target with sputter yield Y_{tg}, and the remaining fraction of the discharge current $(1-\zeta)$ is due to singly charged ions of the species of the target material sputtered (self-sputtering) with sputter yield Y_{SS}. This assumption can be justified as we can see in figure 5 that the contribution of the doubly charged ions is small. The total flux of sputtered species from the target depends on the ion composition as the sputter yield depends on the ion type bombarding the target [12]

$$\Gamma_0 = \frac{\langle I_D \rangle}{e}\left(\zeta Y_{tg}(V_D) + (1-\zeta)\, Y_{SS}(V_D)\right). \tag{5}$$

All the parameters in this expression are known from the experiment and sputter yield data, and are easily accessible, except the fraction ζ of the ion current to the target that is carried by Ar^+ ions, which is determined by the IRM. For the simplified case the fraction of the ion current carried by Ar^+ ions can be estimated using [80]

$$\zeta = \frac{J_{Ar^+}}{J_{Cr^+} + J_{Ar^+}} = \frac{1-\alpha_t\beta_t Y_{SS}}{1+\alpha_t\beta_t\left(Y_{tg}-Y_{SS}\right)} \tag{6}$$

where Y_{tg} is the sputter yield for ions of the working gas, Y_{SS} is the self-sputter yield, α_t is the ionization probability and β_t is the back-attraction probability. The fraction of Ar^+ ions in the total ion current towards the target determined using equation (6) is shown versus pulse length with solid lines in figure 7, for varying discharge current density. This simplified formulation somewhat underestimates the argon ion contribution, in particular for the shortest pulse length. This is probably due to the increased relative contribution of the afterglow as the pulse length is shortened, as we can see in figure 4, and not

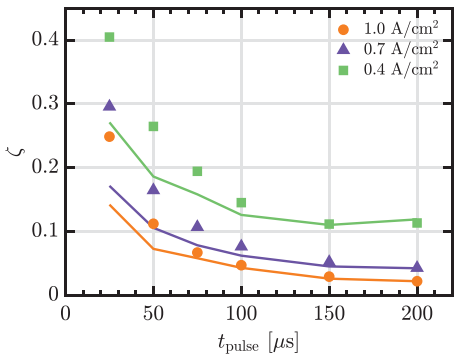

Figure 7. The fraction of Ar^+ ions in the total ion current onto the target ζ versus the pulse length for peak discharge current density of 0.4 A cm^{-2}, 0.7 A cm^{-2}, and 1.0 A cm^{-2}. The working gas was argon at 0.3 Pa and the target was 150 mm diameter chromium disk. The symbols denote calculations using the integrated current at the target surface from the IRM calculations and equation (4) and the solid lines are estimates using equation (6).

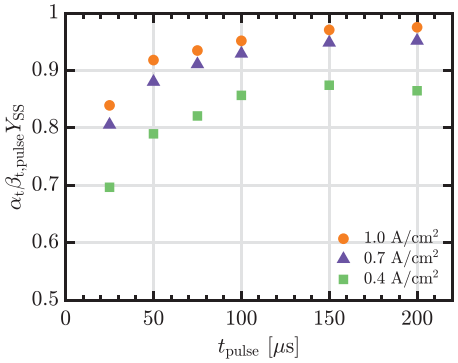

Figure 8. The parameter $\alpha_t\beta_{t,\mathrm{pulse}}Y_{SS}$ versus the pulse length for peak discharge current density of 0.4 A cm^{-2}, 0.7 A cm^{-2}, and 1.0 A cm^{-2}. The working gas was argon at 0.3 Pa and the target was 150 mm diameter chromium disk.

accounted for in determining the ionization probability α_t and the back-attraction probability β_t used in equation (6). Equation (6) should therefore not be applied for very short pulses.

The condition for sustained self-sputtering, sputtering that relies exclusively on self-sputtering, is given as [69, 80]

$$\alpha_t\beta_t Y_{SS} \geqslant 1 \tag{7}$$

For sustained self-sputtering the noble working gas is only needed to get the process started. Since $\alpha_t < 1$ and $\beta_t < 1$ the condition $Y_{SS} > 1$ is necessary but not sufficient for sustained self-sputtering. Figure 8 shows the parameter $\alpha_t\beta_t Y_{SS}$ versus the pulse length for all the discharges studied. We see that this parameter increases with increased pulse length for a given peak discharge current density. For a given pulse length it increases with increased peak discharge current density. We also note that for the longest pulses and highest peak current density (0.7 and 1.0 A cm^{-2}) the value approaches one. In this case, the discharge is close to operation in sustained self-sputtering mode [69]. On the other hand, at the lowest peak current density of 0.4 A cm^{-2} it remains well below 1 even for the longest pulses. The discharge in this case does not reach sustained self-sputtering. We note that the significant deviation of the parameter $\alpha_t\beta_t Y_{SS}$ from unity correlates with a strongly decreasing discharge current after the initial discharge current peak (see figure 2). After the argon gas is consumed and evacuated from the target vicinity, the discharge is run at a too small discharge power to produce sufficient metal atoms and metal ions in order to sustain the high discharge current in the later phase of the discharge pulse.

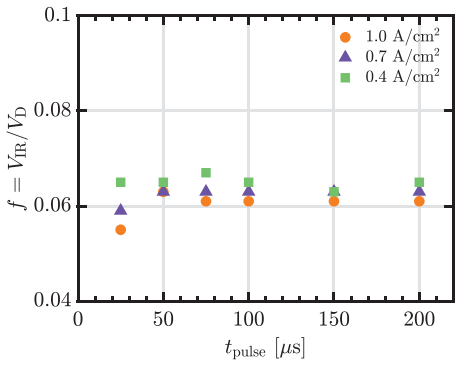

Figure 9. The fraction V_{IR}/V_D versus the pulse length for peak discharge current density of 0.4 A cm^{-2}, 0.7 A cm^{-2}, and 1.0 A cm^{-2}, for argon working gas pressure of 0.3 Pa. The target is a 150 mm diameter chromium disk.

5.4. Electron power absorption

In an early study using the IRM two routes of electron energization were quantified: sheath energization by secondary emitted electrons accelerated across the cathode sheath, and Ohmic $\mathbf{J}_e \cdot \mathbf{E}$ heating of electrons that carry the current in an extended presheath or the IR [81]. The IRM provides information on the voltage drop across the IR, V_{IR}. The fraction of the applied discharge voltage that is dropped across the IR is shown versus pulse length for the three different peak discharge current densities in figure 9. The voltage drop fraction $f = V_{IR}/V_D$ is in the range 5.4% – 6.7% for all the cases explored. The voltage fraction is slightly higher for lower peak discharge current density and slightly lower for higher peak discharge current density. The voltage fraction is similar to the fractional potential drop for a discharge with a tungsten target, which was found to be in the range 6% – 8%, also decreasing with increasing peak discharge current density [48]. For discharges with a zirconium target the fractional potential drop was found to be higher or in the range 10% – 16% of the applied discharge voltage and be slightly lower at 0.5 Pa than at 1 Pa [82]. For a discharge with aluminum target it was observed that about 15% – 25% of the discharge voltage, falls across the plasma outside the cathode sheath region, and that Ohmic electron heating in the IR always dominates, with a large margin, over secondary emitted electron energization in the cathode sheath [34, 81]. For discharges with a copper target the fractional potential drop was found to lie in the range 14% – 17% [83], and for a graphite target this fraction was found to be 14% [47], for a working gas pressure of $p_g \sim 1$ Pa and $J_{D,peak} \sim 1$ A cm^{-2}.

As mentioned above it is possible to quantify two mechanisms of electron power absorption: secondary electron acceleration across the sheath and Ohmic heating within the IR, which is due to the voltage drop across the IR, V_{IR}. Consequently, the total power transfer to the electrons is given by

$$P_e = P_{Sh} + P_{Ohm} \tag{8}$$

where P_e is split up into sheath energization P_{Sh} and Ohmic heating P_{Ohm} within the IR. This is achieved by splitting the discharge voltage up into the potential drop over the sheath and the potential drop over the IR, $V_D = V_{Sh} + V_{IR}$. In each volume, the electrons absorb a part of the total electric power, $I_{e,Sh}V_{Sh}$ and $I_{e,IR}V_{IR}$, respectively, that is given by the fraction of the discharge current the electrons carry. The electron current in the sheath is determined using the model-calculated ion currents to the target and the corresponding secondary electron emission yields as

$$P_{Sh} = I_{e,Sh}V_{Sh} = \left(I_{Ar^+}\gamma_{Ar^+,eff} + \frac{1}{2}I_{Ar^{2+}}\gamma_{Ar^{2+},eff} + \frac{1}{2}I_{M^{2+}}\gamma_{M^{2+},eff}\right)V_{Sh} \tag{9}$$

where $\gamma_{Ar^+,eff} = \gamma_{Ar^+}m\epsilon_e(1-r)$ is the effective secondary electron emission yield for Ar^+-ions bombarding the target, and $\gamma_{Ar^{2+},eff} = \gamma_{Ar^{2+}}m\epsilon_e(1-r)$ and $\gamma_{M^{2+},eff} = \gamma_{M^{2+}}m\epsilon_e(1-r)$ are the effective secondary electron emission yields for doubly ionized argon and metal ions bombarding the target, respectively, and ϵ_e represents the fraction of the electron energy that is used for ionization before being lost from the discharge process [84]. The number of electrons that actually leave the cathode is reduced by the recapture probability r, while a factor m (equal or greater than unity) accounts for ionization within the sheath [84, 85]. We here assume that $m\epsilon_e = 1$. The factor 1/2 in front of the second and third terms

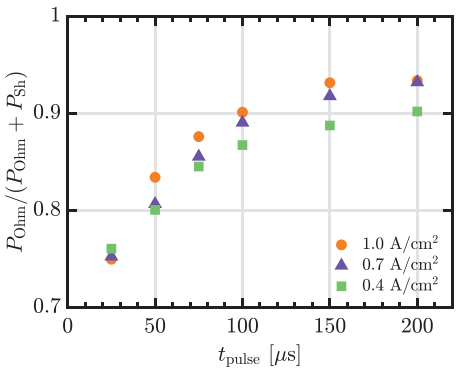

Figure 10. Share of electron power absorption due to Ohmic heating of the electrons versus t_{pulse} for different current densities. The working gas was argon at pressure of 0.3 Pa and the target was 150 mm diameter chromium disk.

accounts for the fact that each M^{2+} and Ar^{2+} ion carries a charge $2e$. The sheath potential is given by $V_{\mathrm{Sh}} = V_{\mathrm{D}} - V_{\mathrm{IR}}$. In the IR the electron power absorption is due to Ohmic heating [81] given by

$$P_{\mathrm{Ohm}} = I_{\mathrm{e,IR}} V_{\mathrm{IR}} = \left\langle \frac{I_{\mathrm{e}}}{I_{\mathrm{D}}} \right\rangle I_{\mathrm{D}} V_{\mathrm{IR}} \tag{10}$$

where $\langle I_{\mathrm{e}}/I_{\mathrm{D}} \rangle \sim 1/2$ is the volume average of the fraction of the discharge current in the IR that is carried by electrons. At the cathode sheath edge the electron current is small, while at the boundary to the DR the electrons carry almost the entire discharge current. The average electron current over the IR is therefore on average $I_{\mathrm{D}}/2$ (see Huo *et al* [81]). The share of the electron power absorption that is due to Ohmic heating is shown versus pulse length for the different current densities in figure 10. We see that the contribution of Ohmic heating is very high, in the range 75% – 93%, and it increases with increasing pulse length and increasing peak discharge current density. Earlier, we had observed similar fraction for the electron power absorption due to Ohmic heating for discharges with aluminum [34, 81] and titanium [34] targets. In a more recent study of a discharge with a titanium target we found the share of Ohmic heating to be lower or in the range of 70% – 60%, decreasing with decreasing magnetic field strength [76].

5.5. Working gas rarefaction

As discussed in the introduction, Alami *et al* [22] observed significant working gas rarefaction when operating a HiPIMS discharge with a chromium target, as they observed almost an order-of-magnitude drop in the Ar^0 emission intensity towards the end of the pulse. The model results for chromium also show significant working gas rarefaction. Several processes can lead to working gas rarefaction, including momentum transfer from the sputtered species to the working gas atoms, momentum transfer from the hot argon atoms to the working gas atoms, in both cases followed by removal from the IR (kick-out), and ionization by secondary or primary electrons [40, 86]. The momentum transfer from high energy species to the colder working gas atoms followed by removal from the IR is sometimes called sputtering wind [87]. In figure 11 the various processes that contribute to the rarefaction of the working gas within the IR are displayed for the three peak discharge current densities for a pulse length of 100 μs. It can be seen that kick-out of the argon atoms by the sputtered Cr atom is the main process leading to working gas rarefaction, while the second most important process is electron impact ionization by the bulk electrons. This agrees with what we have observed for high sputter yield target materials like copper [40]. A detailed analysis of working gas rarefaction in HiPIMS discharges with varying targets, and how the contributions of the various processes varies with the sputter yield of the target material, is given by Barynova *et al* [40].

5.6. Species recycling

It is known that in HIPIMS operation the discharge current is large and this large discharge current is driven by recycling of species [88]. In this work the peak discharge current density is in the range 0.4–1.0 A cm^{-2}. There is an upper limit on the discharge current density that corresponds to where all the incoming argon atoms from the surrounding gas reservoir are ionized and drawn to the target. This

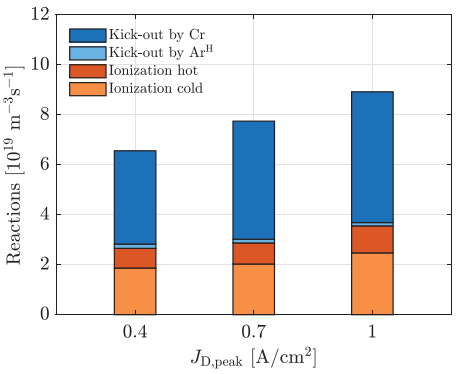

Figure 11. Contribution of the various processes, kick-out by the Cr atoms, kick-out by the hot argon atoms Ar^H, electron impact ionization by bulk electrons, and electron impact ionization by secondary electrons, to working gas rarefaction within the IR. The argon working gas pressure is 0.3 Pa, the pulse length 100 μs and the target a 150 mm diameter chromium disk.

upper limit defines the critical current density of $J_{crit} = 0.2\,A\,cm^{-2}$ at 1 Pa and $T_g = 300\,K$ [88, 89]. This corresponds to $J_{crit} = 60\,mA\,cm^{-2}$ for the discharges explored here, operated at 0.3 Pa. It is therefore clear that for all the cases discussed here, the discharges are operated well above this critical current density limit and ion recycling has to take place to reach the high discharge current densities observed [88]. As seen in figure 5 the singly charged chromium ions contribute most significantly to the discharge current at the target surface, and therefore the discharge operates on self-sputter recycling.

6. Summary

We have explored the effect of shortening the pulse length in a HiPIMS discharge operated with argon as the working gas and chromium target, both experimentally and by applying the IRM. Experimentally, it is observed that for a given pulse length the deposition rate decreases and the ionized flux fraction increases with increased discharge current density. The measured ionized flux fraction of the sputtered chromium is found to be in the range 10% – 50%, highest for the highest peak discharge current density, and the shortest pulse length studied.

The model study shows that the Cr^+ ion is the dominant charged species at the target surface during the pulse and the discharge operates mainly on self-sputter recycling. The model results also show that the ionization probability of the sputtered species increases with increased peak current discharge density, but increases at first with increased pulse length, reaches a peak and then decreases with further increase in the pulse length. The back-attraction probability of the sputtered species decreases with decreasing pulse length and with increasing peak discharge current density. The contribution of Ohmic heating is found to be very high, in the range 75% – 93%, and its contribution increases with increasing pulse length and increasing peak discharge current density. Furthermore, momentum transfer to the argon atoms in the IR from the sputtered chromium atoms, followed by a removal from the IR (kick-out), was determined to be the most significant contributor to working gas rarefaction, which agrees with what has been seen earlier for high sputter yield targets, followed by electron impact ionization by the bulk electrons.

Data availability statement

All data that support the findings of this study are included within the article (and any supplementary files).

Acknowledgments

This work was partially supported by the Icelandic Research Fund Grants Nos. 196141, 217999 and 2511073, the University of Iceland Research Fund Grant no. 93940, University of Iceland Research Fund for Doctoral Students, and the Swedish Government Strategic Research Area in Materials Science on Functional Materials at Linköping University (Faculty Grant SFO-Mat-LiU No. 2009-00971).

Conflict of interest

The authors have no conflicts to disclose.

Author contributions

Kateryna Barynova 0009-0009-0894-6160
Data curation (equal), Formal analysis (equal), Investigation (equal), Software (equal), Validation (equal), Visualization (equal), Writing – review & editing (equal)

Tetsuhide Shimizu 0000-0002-7810-3777
Conceptualization (equal), Data curation (equal), Formal analysis (equal), Investigation (equal), Methodology (equal), Project administration (equal), Supervision (equal), Validation (equal), Visualization (equal), Writing – review & editing (equal)

Rommel Paulo B Viloan 0000-0002-4642-9473
Data curation (equal), Formal analysis (equal), Investigation (equal), Methodology (equal), Validation (equal)

Michal Zanáška 0000-0002-6855-9930
Data curation (equal), Formal analysis (equal), Methodology (equal), Validation (equal)

Joel Fischer 0000-0001-9116-6302
Data curation (equal), Formal analysis (equal), Methodology (equal), Software (equal), Validation (equal), Writing – review & editing (equal)

Martin Rudolph 0000-0002-0854-6708
Conceptualization (equal), Data curation (equal), Formal analysis (equal), Investigation (equal), Methodology (equal), Project administration (equal), Software (equal), Supervision (equal), Validation (equal), Visualization (equal), Writing – original draft (equal), Writing – review & editing (equal)

Daniel Lundin 0000-0001-8591-1003
Conceptualization (equal), Data curation (equal), Formal analysis (equal), Funding acquisition (equal), Project administration (equal), Resources (equal), Supervision (equal), Validation (equal), Writing – review & editing (equal)

Jon Tomas Gudmundsson 0000-0002-8153-3209
Conceptualization (equal), Data curation (equal), Formal analysis (equal), Funding acquisition (equal), Investigation (equal), Methodology (equal), Project administration (equal), Resources (equal), Software (equal), Supervision (equal), Validation (equal), Visualization (equal), Writing – original draft (equal), Writing – review & editing (equal)

References

[1] Bikulčius G, Češunien A, Selskienė A, Pakštas V and Matijošius T 2017 *Surf. Coat. Technol.* **315** 130
[2] Navinšek B, Panjan P and Milošev I 1999 *Surf. Coat. Technol.* **116-119** 476
[3] Daure J L, Carrington M J, Shipway P H, McCartney D G and Stewart D A 2018 *Surf. Coat. Technol.* **350** 40
[4] Gudmundsson J T 2020 *Plasma Sources Sci. Technol.* **29** 113001
[5] Waits R K 1978 *J. Vac. Sci. Technol.* **15** 179
[6] Kelly P J and Arnell R D 2000 *Vacuum* **56** 159
[7] Gudmundsson J T, Anders A and von Keudell A 2022 *Plasma Sources Sci. Technol.* **31** 083001
[8] Gudmundsson J T, Brenning N, Lundin D and Helmersson U 2012 *J. Vac. Sci. Technol. A* **30** 030801
[9] Lundin D, Minea T and Gudmundsson J T 2020 *High Power Impulse Magnetron Sputtering: Fundamentals, Technologies, Challenges and Applications* (Elsevier) (https://doi.org/10.1016/C2016-0-02463-4)
[10] Kouznetsov V, Macák K, Schneider J M, Helmersson U and Petrov I 1999 *Surf. Coat. Technol.* **122** 290
[11] Lundin D, Čada M and Hubička Z 2015 *Plasma Sources Sci. Technol.* **24** 035018
[12] Hajihoseini H, Čada M, Hubička Z, Ünaldi S, Raadu M A, Brenning N, Gudmundsson J T and Lundin D 2019 *Plasma* **2** 201
[13] Fischer J, Renner M, Gudmundsson J T, Rudolph M, Hajihoseini H, Brenning N and Lundin D 2023 *Plasma Sources Sci. Technol.* **32** 125006
[14] Kapran A, Ballage C, Hubička Z and Minea T 2024 *J. Appl. Phys.* **135** 173302
[15] Samuelsson M, Lundin D, Jensen J, Raadu M A, Gudmundsson J T and Helmersson U 2010 *Surf. Coat. Technol.* **202** 591
[16] Kuo C-C, Lin C-H, Lin Y-T and Chang J-T 2020 *Coatings* **10** 542
[17] Chen D, Dai W, Liang D, Wang Q and Yan J 2025 *Thin Solid Films* **814** 140625
[18] Ammendola M *et al* 2024 *Surf. Coat. Technol.* **485** 130835
[19] Ding X, Cui M, Lian Y, Jiao J, Yang J, Zhang J, Wu Y, Tian X and Gong C 2024 *Vacuum* **227** 113386
[20] Ferreira F, Serra R, Cavaleiro A and Oliveira J C 2016 *Thin Solid Films* **619** 250

[21] Li Y G, Liu W Y and Cui L 2024 *J. Vac. Sci. Technol. A* **42** 023108
[22] Alami J, Sarakinos K, Mark G and Wuttig M 2006 *Appl. Phys. Lett.* **89** 154104
[23] Lundin D, Brenning N, Jädernäs D, Larsson P, Wallin E, Lattemann M, Raadu M A and Helmersson U 2009 *Plasma Sources Sci. Technol.* **18** 045008
[24] Šlapanská M, Hecimovic A, Gudmundsson J T, Hnilica J, Breilmann W, Vašina P and von Keudell A 2020 *J. Phys. D: Appl. Phys.* **53** 155201
[25] Held J, Schulz-von der Gathen V and von Keudell A 2023 *Plasma Sources Sci. Technol.* **32** 065006
[26] Zgheib J, Jouan P Y and Rhallabi A 2021 *J. Vac. Sci. Technol. A* **39** 043004
[27] Gao J Y, Ferreira F and Lei M K 2022 *J. Appl. Phys.* **132** 203303
[28] Zgheib J, Jouan P-Y and Rhallabi A 2024 *J. Vac. Sci. Technol. A* **42** 033004
[29] Gao J Y, Ferreira F and Lei M K 2024 *J. Appl. Phys.* **135** 033301
[30] Zgheib J 2021 Characterization and modeling of a high power impulse magnetron sputtering discharge, application to thin films deposition *PhD Thesis* Université de Nantes (available at: https://theses.hal.science/tel-05383585v1)
[31] Brenning N, Butler A, Hajihoseini H, Rudolph M, Raadu M A, Gudmundsson J T, Minea T and Lundin D 2020 *J. Vac. Sci. Technol. A* **38** 033008
[32] Butler A, Brenning N, Raadu M A, Gudmundsson J T, Minea T and Lundin D 2018 *Plasma Sources Sci. Technol.* **27** 105005
[33] Rudolph M, Brenning N, Raadu M A, Hajihoseini H, Gudmundsson J T, Anders A and Lundin D 2020 *Plasma Sources Sci. Technol.* **29** 05LT01
[34] Huo C, Lundin D, Gudmundsson J T, Raadu M A, Bradley J W and Brenning N 2017 *J. Phys. D: Appl. Phys.* **50** 354003
[35] Shimizu T, Zanáška M, Villoan R P, Brenning N, Helmersson U and Lundin D 2021 *Plasma Sources Sci. Technol.* **30** 045006
[36] Bohlmark J, Helmersson U, VanZeeland M, Axnäs I, Alami J and Brenning N 2004 *Plasma Sources Sci. Technol.* **13** 654
[37] Wu L, Ko E, Dulkin A, Park K J, Fields S, Leeser K, Meng L and Ruzic D N 2010 *Rev. Sci. Instrum.* **81** 123502
[38] Kubart T, Čada M, Lundin D and Hubička Z 2014 *Surf. Coat. Technol.* **238** 152
[39] Raadu M A, Axnäs I, Gudmundsson J T, Huo C and Brenning N 2011 *Plasma Sources Sci. Technol.* **20** 065007
[40] Barynova K, Suresh Babu S, Rudolph M, Fischer J, Lundin D, Raadu M A, Brenning N and Gudmundsson J T 2024 *Plasma Sources Sci. Technol.* **33** 065010
[41] Rudolph M, Revel A, Lundin D, Hajihoseini H, Brenning N, Raadu M A, Anders A, Minea T M and Gudmundsson J T 2021 *Plasma Sources Sci. Technol.* **30** 045011
[42] Gudmundsson J T, Lundin D, Brenning N, Raadu M A, Huo C and Minea T M 2016 *Plasma Sources Sci. Technol.* **25** 065004
[43] Barynova K, Brenning N, Suresh Babu S, Fischer J, Lundin D, Raadu M A, Gudmundsson J T and Rudolph M 2025 *Plasma Sources Sci. Technol.* **34** 06LT01
[44] Yamamura Y and Ishida M 1995 *J. Vac. Sci. Technol. A* **13** 101
[45] Rudolph M, Lundin D, Foy E, Debongnie M, Hugon M-C and Minea T 2018 *Thin Solid Films* **658** 46
[46] Anders A, Čapek J, Hála M and Martinu L 2012 *J. Phys. D: Appl. Phys.* **45** 012003
[47] Eliasson H, Rudolph M, Brenning N, Hajihoseini H, Zanáška M, Adriaans M J, Raadu M A, Minea T M, Gudmundsson J T and Lundin D 2021 *Plasma Sources Sci. Technol.* **30** 115017
[48] Suresh Babu S, Rudolph M, Lundin D, Shimizu T, Fischer J, Raadu M A, Brenning N and Gudmundsson J T 2022 *Plasma Sources Sci. Technol.* **31** 065009
[49] Kittel C 2005 *Introduction to Solid State Physics* 8th edn (Wiley)
[50] Hofer W O 1991 Angular, energy, and mass distribution of sputtered particles *Sputtering by Particle Bombardment III: Characteristics of Sputtered Particles, Technical Applications* (*Topics in Applied Physics*) vol 64, ed R Behrisch and K Wittmaack (Springer) pp 15–90
[51] Gnaser H 2007 Energy and angular distributions of sputtered species *Sputtering by Particle Bombardment: Experiments and Computer Calculations From Threshold to MeV Energies* (*Topics in Applied Physics*) vol 110, ed R Behrisch and W Eckstein (Springer) ch 5, pp 231–328
[52] Lennon M A, Bell K, Gilbody H B, Hughes J G, Kingston A E, Murray M and Smith F J 1988 *J. Phys. Chem. Ref. Data* **17** 1285
[53] Nelson A N 1976 Electron impact ionization cross sections of gold, chromium and iron *Technical Report AFML-TR-75-198* Massachusetts Institute of Technology
[54] Man K F, Smith A C H and Harrison M F A 1987 *J. Phys. B: Phys.* **20** 2571
[55] Bogaerts A, Temelkov K A, Vuchkov N K and Gijbels R 2007 *Spectrochim. Acta B* **62** 325
[56] Lieberman M A and Lichtenberg A J 2025 *Principles of Plasma Discharges and Materials Processing* 3rd edn (Wiley)
[57] Blanco F, Ferreira da Silva F, Limao-Vieira P and García G 2017 *Plasma Sources Sci. Technol.* **26** 085004
[58] Schmid M 2024 A simple sputter yield calculator *Surface Physics, Institute of Applied Physics* (Technischen Universität Wien) (available at: www2.iap.tuwien.ac.at/www/surface/sputteryield)
[59] Matsunami N, Yamamura Y, Itikawa Y, Itoh N, Kazumata Y, Miyagawa S, Morita K, Shimizu R and Tawara H 1984 *At. Data Nucl. Data Tables* **31** 1
[60] Phelps A V and Petrović Z L 1999 *Plasma Sources Sci. Technol.* **8** R21
[61] Baragiola R A, Alonso E V, Ferron J and Oliva-Florio A 1979 *Surf. Sci.* **90** 240
[62] Wahlin H B 1948 *Phys. Rev.* **73** 1458
[63] Buyle G, Depla D, Eufinger K and De Gryse R 2004 *J. Phys. D: Appl. Phys.* **37** 1639
[64] Christie D J 2005 *J. Vac. Sci. Technol. A* **23** 330
[65] Hajihoseini H, Brenning N, Rudolph M, Raadu M A, Lundin D, Fischer J, Minea T M and Gudmundsson J T 2022 *J. Vac. Sci. Technol. A* **41** 013002
[66] Rudolph M, Hajihoseini H, Raadu M A, Gudmundsson J T, Brenning N, Minea T M, Anders A and Lundin D 2021 *J. Appl. Phys.* **129** 033303
[67] Dubois T, Tsikata S and Minea T 2022 *Plasma Sources Sci. Technol.* **31** 115018
[68] Panjan M and Anders A 2017 *J. Appl. Phys.* **121** 063302
[69] Anders A, Andersson J and Ehiasarian A 2007 *J. Appl. Phys.* **102** 113303
[70] Čapek J, Hála M, Zabeida O, Klemberg-Sapieha J E and Martinu L 2012 *J. Appl. Phys.* **111** 023301
[71] Kozák T, Vlček J and Kos Š 2013 *J. Phys. D: Appl. Phys.* **46** 105203
[72] Tiron V, Velicu I-L, Vasilovici O and Popa G 2015 *J. Phys. D: Appl. Phys.* **48** 495204
[73] Konstantinidis S, Dauchot J P, Ganciu M, Ricard A and Hecq M 2006 *J. Appl. Phys.* **99** 013307

[74] Rudolph M, Brenning N, Hajihoseini H, Raadu M A, Fischer J, Gudmundsson J T and Lundin D 2022 *J. Vac. Sci. Technol. A* **40** 043005
[75] Lundin D, Gudmundsson J T, Brenning N, Raadu M A and Minea T M 2017 *J. Appl. Phys.* **121** 171917
[76] Rudolph M, Brenning N, Hajihoseini H, Raadu M A, Minea T M, Anders A, Lundin D and Gudmundsson J T 2022 *J. Phys. D: Appl. Phys.* **55** 015202
[77] Fischer J, Gudmundsson J T, Rudolph M, Raadu M A and Lundin D 2026 *Plasma Sources Sci. Technol.* **35** 025024
[78] Brenning N, Hajihoseini H, Rudolph M, Raadu M A, Gudmundsson J T, Minea T M and Lundin D 2021 *Plasma Sources Sci. Technol.* **30** 015015
[79] Suresh Babu S, Rudolph M, Ryan P J, Fischer J, Lundin D, Bradley J W and Gudmundsson J T 2023 *Plasma Sources Sci. Technol.* **32** 034003
[80] Hosokawa N, Tsukada T and Kitahara H 1980 Effect of discharge current and sustained self-sputtering *8th Int. Vacuum Congress* (*Cannes, France, 22–26 September1980*) pp 11–14
[81] Huo C, Lundin D, Raadu M A, Anders A, Gudmundsson J T and Brenning N 2013 *Plasma Sources Sci. Technol.* **22** 045005
[82] Suresh Babu S, Fischer J, Barynova K, Rudolph M, Lundin D and Gudmundsson J T 2024 *J. Vac. Sci. Technol. A* **42** 043007
[83] Gudmundsson J T, Fischer J, Hinriksson B P, Rudolph M and Lundin D 2022 *Surf. Coat. Technol.* **442** 128189
[84] Thornton J A 1978 *J. Vac. Sci. Technol.* **15** 171
[85] Depla D, Mahieu S and De Gryse R 2009 *Thin Solid Films* **517** 2825
[86] Huo C, Raadu M A, Lundin D, Gudmundsson J T, Anders A and Brenning N 2012 *Plasma Sources Sci. Technol.* **21** 045004
[87] Hoffman D W 1985 *J. Vac. Sci. Technol. A* **3** 561
[88] Brenning N, Gudmundsson J T, Raadu M A, Petty T J, Minea T and Lundin D 2017 *Plasma Sources Sci. Technol.* **26** 125003
[89] Huo C, Lundin D, Raadu M A, Anders A, Gudmundsson J T and Brenning N 2014 *Plasma Sources Sci. Technol.* **23** 025017

Article IV

High power impulse magnetron sputtering of a zirconium target.

Swetha Suresh Babu, Joel Fischer, Kateryna Barynova, Martin Rudolph, Daniel Lundin, and Jon Tomas Gudmundsson

Journal of Vacuum Science and Technology A 42, 043007 (2024)

High power impulse magnetron sputtering of a zirconium target

Cite as: J. Vac. Sci. Technol. A 42, 043007 (2024); doi: 10.1116/6.0003647
Submitted: 25 March 2024 · Accepted: 30 May 2024 ·
Published Online: 25 June 2024

View Online Export Citation CrossMark

Swetha Suresh Babu,[1] Joel Fischer,[2] Kateryna Barynova,[1] Martin Rudolph,[3] Daniel Lundin,[2] and Jon Tomas Gudmundsson[1,4]

AFFILIATIONS

[1]Science Institute, University of Iceland, Dunhaga 3, Reykjavik IS-107, Iceland
[2]Plasma and Coatings Physics Division, IFM-Materials Physics, Linköping University, Linköping SE-581 83, Sweden
[3]Leibniz Institute of Surface Engineering (IOM), Permoserstraße 15, Leipzig 04318, Germany
[4]Division of Space and Plasma Physics, School of Electrical Engineering and Computer Science, KTH Royal Institute of Technology, Stockholm SE-10044, Sweden

ABSTRACT

High power impulse magnetron sputtering (HiPIMS) discharges with a zirconium target are studied experimentally and by applying the ionization region model (IRM). The measured ionized flux fraction lies in the range between 25% and 59% and increases with increased peak discharge current density ranging from 0.5 to 2 A/cm^2 at a working gas pressure of 1 Pa. At the same time, the sputter rate-normalized deposition rate determined by the IRM decreases in accordance with the HiPIMS compromise. For a given discharge current and voltage waveform, using the measured ionized flux fraction to lock the model, the IRM provides the temporal variation of the various species and the average electron energy within the ionization region, as well as internal discharge parameters such as the ionization probability and the back-attraction probability of the sputtered species. The ionization probability is found to be in the range 73%–91%, and the back-attraction probability is in the range 67%–77%. Significant working gas rarefaction is observed in these discharges. The degree of working gas rarefaction is in the range 45%–85%, higher for low pressure and higher peak discharge current density. We find electron impact ionization to be the main contributor to working gas rarefaction, with over 80% contribution, while kick-out by zirconium atoms and argon atoms from the target has a smaller contribution. The dominating contribution of electron impact ionization to working gas rarefaction is very similar to other low sputter yield materials.

I. INTRODUCTION

The magnetron sputtering discharge[1–3] is a highly successful and widely used thin film deposition technique that belongs to the group of physical vapor deposition methods.[4] The source of the film-forming material is a solid target out of which the atoms are released by ion bombardment. The magnetron sputtering discharge is based on forming a dense plasma in the target vicinity by a static magnetic field that traps the electrons.[1,2,5] This dense plasma is easily observable and appears as a brightly glowing torus located adjacent to the target surface. This brightly glowing region is referred to as the ionization region (IR).[6] Ions accelerated from this dense plasma sputter the film-forming material from the cathode target.

When operated as a dc magnetron sputtering (dcMS) discharge, the ions of the working gas bombard the target and the sputtered species that reach the substrate are mostly neutral atoms. The ions bombarding the substrate are ions of the working gas. By applying high voltage pulses of low duty cycle to the cathode target, the discharge current density in the pulse can become high, and therefore, a high electron density is created in the IR.[7–12] Consequently, a significant fraction of the sputtered atoms coming off the target becomes ionized as they pass through the dense plasma of the ionization region. In this case, ions of both the working gas and the target material bombard the target. This also makes ions of the film-forming material available for deposition onto the substrate. This variant of magnetron sputtering is referred to as high power impulse magnetron sputtering (HiPIMS).[7,10] It is one approach to create a highly ionized flux of the film-forming material.[7,13] When the atoms of the film-forming material in the deposition flux are ionized, the energy and direction of the ions

bombarding the substrate can be controlled by biasing the substrate.[13–15] Control of the ion bombarding energy means that the need for external substrate heating can be significantly reduced or even eliminated.[16–18] Furthermore, selective microstructural texturing is made possible.[18–20]

Zirconium (Zr([Kr]$4d^2s^2$)) is a group-IV transition metal element. The stable crystalline state of zirconium at room temperature and ambient pressure is a hexagonal close-packed (hcp) structure (α-Zr phase). With increased temperature, it transforms martensitically into the body-centered cubic (bcc) structure (β-Zr phase) at 1136 K.[21] In comparison with other elemental metals, zirconium in solid form exhibits good thermal conductivity, high melting point, low thermal expansion, and good mechanical strength. Furthermore, zirconium has a very low neutron scattering cross section and a high solid solubility of oxygen and hydrogen. Therefore, zirconium and its alloys in bulk and thin film forms are widely used in the nuclear industry.[22,23] Furthermore, as zirconium has excellent corrosion resistance and acceptable biocompatibility, titanium–zirconium (Ti–Zr) binary alloys have been proposed for biomedical applications.[24,25]

Zirconium thin films with hexagonal close packed crystal structure (α-Zr) have been deposited by dc magnetron sputtering,[26–28] asymmetric bipolar pulsed magnetron sputtering,[29,30] and HiPIMS.[19,20] Noteworthy is the work of Fankhauser *et al.*[28] which deposited epitaxial Zr(0001) thin films onto Al_2O_3(0001) using dc magnetron sputtering. When deposited by HiPIMS, at substrate temperature in the range 300–873 K, Kuo *et al.*[20] find zirconium films to be polycrystalline and exhibit predominantly [0 0 0 1] texture. The crystallite size is found to increase with increasing substrate temperature during deposition.[29,30] Kuo *et al.*[20] also explored the influence of the pulse width and substrate bias on the properties of zirconium films deposited by HiPIMS and showed that the predominant texture can become [1 0 $\bar{1}$ 1] by synchronizing bias on the substrate and longer pulse lengths. Lustosa *et al.*[25] deposited Ti-Zr alloy using HiPIMS, exploring how the hardness varied with pulsing frequency. The hardness decreased and lower contact angles and better hydrophilic properties were observed when the alloy was deposited at lower pulsing frequencies.

Here, we develop an ionization region model (IRM) of a HiPIMS discharge with argon as the working gas and a zirconium target. The model provides insights into the discharge physics and chemistry, notably the temporal evolution of the species densities and the discharge current composition, a voltage drop across the IR, the ionization probability, as well as the back-attraction probability of the sputtered species.[31] Earlier, the IRM has been applied to study discharges with graphite,[32] aluminum,[31,33] titanium,[31,34] copper,[35] and tungsten[36,37] targets. These studies indicate that the process that dominates working gas rarefaction depends strongly on the sputter yield and/or self-sputter yield,[38] with little dependence on the mass of the target atoms, contrary to reports by other authors.[39,40] For example, rarefaction in a discharge with a tungsten target, having a high atomic mass and a moderate sputter yield, behaves very similar to a discharge using an aluminum target, having a low atomic mass and a similar sputter yield to tungsten.[38] Similarly, the back-attraction probability appears to depend on the sputter yield of the target material.[35] To fully disentangle the effect of mass and sputter yield, we here develop a model of a HiPIMS discharge with a zirconium target and apply it to a few discharges with experimentally determined discharge voltage and current waveforms and measured ionized flux fraction. Zirconium has a moderate atomic mass, lower than tungsten and higher than copper, and a low sputter yield. Therefore, it is important to understand a HiPIMS discharge with a zirconium target to provide a piece of the puzzle on how working gas rarefaction, the deposition rate, and the back-attraction probability depend on the atom mass and the sputter yield of the target material.

The paper is structured as follows: In Sec. II A, we discuss the experimental setup. The basics of the ionization region model and the addition of the zirconium reaction set are reviewed in Sec. II B. Section III A discusses the experimental findings and Sec. III B the results of the model studies. The findings of this work are summarized in Sec. IV.

II. EXPERIMENTAL APPARATUS AND METHOD

A. Experimental setup

The sputter target was a 2 in. zirconium disk mounted on an unbalanced magnetron assembly. The base pressure was maintained below 2×10^{-4} Pa by a turbomolecular pump backed by a roughing pump. The working gas pressure was set to 0.5 and 1 Pa by regulating the argon gas flow. A dc power supply together with a HiPSTER 6 pulsing unit (Ionautics, Sweden) was used to apply voltage pulses to the cathode target. The peak discharge current was kept fixed and an average discharge power $\langle P_D \rangle$ was maintained at 60 W by varying the repetition frequency. The pulse was kept at a constant length of either 50 or 100 μs. For comparison, measurements were also made for a dcMS discharge at the same pressures and average power and a discharge voltage of $V_{D,dcMS} = 255$ V.

The flux parameters were determined using an ion meter, which consisted of a magnetic schielding, a grounded casing, and a quartz crystal micro-balance (QCM) sensor which could be biased to achieve charge selectivity. The ion meter could measure either the deposition rate from ions and neutrals or from neutrals only by varying the voltage applied to the biased top QCM electrode. The ion meter (or gridless QCM/m-QCM) and its design and operation principles are described in detail elsewhere.[41,42] For the measurements, the ion meter was placed at distances of 3, 4, 6, 8, and 10 cm above the racetrack and facing the target surface.

B. Ionization region model

The IRM of a high power impulse magnetron sputtering discharge is a volume-averaged plasma chemistry model that provides the temporal variation of the various species densities and the electron energy. It is a semi-empirical model that requires experimentally determined discharge voltage and current waveforms, the working gas pressure, the target and its dimensions, and the dimensions of the ionization region as input. The IRM only covers the target and the ionization region, which is defined as an annular cylinder of width $w_{RT} = r_{c2} - r_{c1}$ positioned above the racetrack, and a length $L = z_2 - z_1$, extending from z_1 to z_2 axially away from the target.

The IRM, originally described by Raadu *et al.*[43] in 2011, has been under constant development ever since, and its main features

are summarized by Huo *et al.*[31] In the IRM, the temporal development of the species densities and electron temperature is defined by a set of ordinary differential equations.[31,43] The electron density is found by applying the quasineutrality condition. The details of the IRM, including the reaction rates for the various surface and volume processes that are taken into account, are summarized by Huo *et al.*[31] More recent modifications concerning the treatment of the afterglow[44] and updated reaction rates[45] have been made, as well as a modification to the term that describes the kick-out by the sputtered species and contributes to working gas rarefaction as discussed by Barynova *et al.*.[38] This last modification is needed to analyze the contributions from electron impact ionization and kick-out to working gas rarefaction. The updated IRM is applied for this current study.

There are three free parameters or fitting parameters that are adjusted in the IRM: (i) the ion back-attraction probability for the metal ions $\beta_{t,pulse}$ and gas ions $\beta_{g,pulse}$; (ii) the potential drop across the IR, V_{IR}; and (iii) the electron recapture probability r. In practice, V_{IR} is determined using the ratio $f = V_{IR}/V_D$, where V_D is the discharge voltage.[31] For the cases presented here, we assume $r = 0.7$, since it has been suggested by Buyle *et al.*,[46] based on a Monte Carlo model calculations, that the electron recapture probability is typically between 65% and 75% for a planar magnetron sputtering discharge. Note that for a metal target, the value of the electron recapture probability r does not influence the model results significantly. Furthermore, we assume $\beta_{t,pulse} = \beta_{g,pulse}$ as in previous studies.[31,36,43] It has been argued, based on the direct simulation Monte Carlo calculation, that this may be a rough approximation and that the back-attraction probability for the ions of the working gas is close to unity.[47] This will not have much influence on the overall findings reported in this current work.

We can lock the model and confine the two fitting parameters, using the experimentally measured discharge current waveform and the measured ionized flux fraction as discussed by Butler *et al.*.[48] The ionized flux fraction onto a given surface facing the discharge is related to the time-integrated total number of metal atoms and metal ions leaving the IR for the diffusion region (DR) during the discharge pulse through

$$F_{flux} = \left(1 + \left(\frac{\xi_{tn}}{\xi_{ti}}\right)\frac{\int_T \tilde{\Gamma}_M^{DR}(t)dt}{\int_T \tilde{\Gamma}_{M^+}^{DR}(t)dt}\right)^{-1}, \quad (1)$$

where $\tilde{\Gamma}_M(t)$ is the total flux of metal neutrals and $\tilde{\Gamma}_{M^+}(t)$ is the total flux of metal ions into the diffusion region, T is the pulse period, and the collection of metal neutrals and ions on the given surface is described through the ratio of the transport parameters ξ_{tn}/ξ_{ti}, where ξ_{ti} is the transport parameter for ions, and ξ_{tn} is the transport parameter for neutrals, of the sputtered species[49,50] (see, in particular, Fig. 1 of Rudolph *et al.*[34]). The transport parameter ratio has been determined experimentally for a HiPIMS discharge with a titanium target to be roughly $\xi_{tn}/\xi_{ti} \approx 1.25$ for a substrate located 3 cm from the target surface and $\xi_{tn}/\xi_{ti} \approx 2$ for a substrate located 7 cm from the target surface.[50] We use these values and assume a value of 2 for flux measurements made in the range 7–10 cm from the target surface and use a linear fit to determine values for 4 and 6 cm distance.

As discussed above, the model results include the back-attraction probability during the pulse from a potential drop across the IR, V_{IR}. This potential barrier prevents some of the ions in the IR from reaching the substrate, lowering the deposition rate. This potential barrier is eliminated when the pulse is shut off. Therefore, we assume β_t to be zero in the afterglow and consequently the back-attraction probability is defined as[44]

$$\beta_t(t) = \begin{cases} \beta_{t,pulse} & \text{during the pulse,} \\ 0 & \text{in the afterglow.} \end{cases} \quad (2)$$

After the pulse is switched off, the metal ions are assumed to have a velocity that is similar to that of the sputtered metal species.

1. Species considered and reactions involving zirconium

The discharge formed is composed of the argon working gas atoms and ions, the sputtered zirconium species and their ions, as well as electrons. The working gas species included in the model for the argon discharge are cold argon atoms in the ground state Ar^C, metastable argon atoms [both $Ar(4s[3/2]_2)$ and $Ar(4s'[1/2]_0)$], Ar^+ and Ar^{2+} ions, and warm Ar^W and hot Ar^H argon atoms. The latter two populations of argon atoms originate from argon ions that bombard the target and then return to the discharge as neutrals. The hot argon population represents reflected argon atoms at the target.[51,52] They are assumed to have an average energy of 2 eV as motivated by Raadu *et al.*[43] The warm population Ar^W, which is assumed to have energy similar to the thermal energy of the surface, with about 0.1 eV (~1000 K),[53] is due to argon ions that penetrate the target surface and then slowly diffuse back as atoms. The argon discharge, the reaction set, and rate coefficients can be found in recent publications.[32,36]

For the zirconium discharge, we include zirconium atoms in the ground state and the ions Zr^+ and Zr^{2+}. The sputtered zirconium atoms enter the IR with a velocity corresponding to the energy of $1/2 \times \mathcal{E}_{cohesive} = 1/2 \times 6.25\,eV = 3.125\,eV$,[54] (p. 50), where $\mathcal{E}_{cohesive}$ is the cohesive energy of the target material. We note here that the cohesive energy of zirconium is almost as high as that of graphite.[32] For a HiPIMS discharge using a graphite target, we have partially attributed the low ionized flux fraction to the high cohesive energy of graphite, resulting in a low residence time of the carbon atoms within the ionization region. Here, in the case of zirconium, the velocity with which the atoms leave the target remains moderate, as the mass of zirconium is high with $91m_p$, where m_p is the proton mass. Therefore, the probability of ionization of zirconium is expected to be higher than that of carbon. Consequently, we expected a substantial density of both zirconium atoms and ions in the discharge, in particular, late in the pulse.

Due to this composition of the discharge, we need to calculate and account for the collisional loss for each electron-ion pair created $\mathcal{E}_c$ for zirconium in the electron energy balance. For this purpose, we use the electron impact ionization cross section calculated by Deutsch *et al.*[55] with an ionization potential of 6.63 V. Our calculations of the collisional energy loss also include the seven lowest excited levels of the atom listed in Table II. As the electron impact excitation cross sections for the zirconium atom

are mostly unknown, we assume that each excitation cross section follows the Thomson cross section[56] (p. 71) with a peak at 1/5 of the peak of the ionization cross section. If the electron impact excitation cross sections are overestimated (underestimated), the collisional energy loss per electron-ion pair created from Zr atoms is overestimated (underestimated) slightly, and the Zr^+ ion density and the electron density are underestimated (overestimated). However, as we will see later that the Zr^+ ion is not the dominating ion in the discharge, so this assumption does not have much influence on the overall results. We assume the cross section for electron elastic scattering on Zr atoms to be the same as for tungsten.[57] For electron energies above 50 eV, the total electron elastic cross section agrees well with the elastic cross section for zirconium calculated using the NIST Electron Elastic-Scattering Cross-Section Database SRD 64.[58] To find an electron impact ionization cross section for Zr^+ to create the doubly ionized Zr^{2+}, we use the cross section for the first ionization of the zirconium atom from Deutsch *et al.*[55] and scale it down by a factor of 10 and shift the energy axis by the difference in ionization energy between Zr^+ and Zr^{2+}. The reactions and the rate coefficients for electron impact ionization of Zr and Zr^+ by both primary (cold) and secondary (hot) electrons are listed in Table III. The rate coefficients for electron impact collisions are calculated assuming a Maxwellian EEDF. The fits are valid in the range 1–7 eV for the cold electrons and in the range 200–1000 eV for the hot electrons.

The sputter yield for Ar^+ and Zr^+ ions bombarding a zirconium target was estimated using the TU Wien Sputter Yield Calculator,[59] which is based on the empirical equations for sputter yields at normal incidence developed by Matsunami *et al.*[60] The calculated sputter yields were fitted using a power-law equation

$$Y = a\mathcal{E}_i^b, \tag{3}$$

where a and b are the fitting parameters. Here, $a = 0.003538$ and $b = 0.7936$ for Ar^+ sputtering of zirconium and for self-sputtering of zirconium $a = 0.001896$ and $b = 0.9316$.

For the secondary electron emission yield due to bombardment of the target by argon ions, we use the fit given for clean metals by Phelps and Petrović.[61] For the zirconium ions bombarding the zirconium target, the secondary electron emission yield is essentially zero. Furthermore, we neglect secondary electron emission due to the bombardment of the target by Zr^{2+} ions.

III. RESULTS AND DISCUSSION

A. Experimental results

Figure 1 shows the measured ionized flux fraction vs the discharge current density at a working gas pressure of 0.5 and 1 Pa. We see that at 1 Pa the ionized flux fraction is in the range 25%–61% and increases with increased discharge current density in the range 0.5–2.0 A/cm^2. The ionized flux fraction was measured at 3 cm from the target surface, facing the race track, representing the edge of the ionization region,[6] and 10 cm from the target surface, representing a typical substrate distance. The ionized flux fraction was also measured at 4, 6, and 8 cm from the target surface for $J_{D,peak} = 1$ A/cm^2. All the measured ionized flux fraction values are listed in Table I and shown in Fig. 1. We see that the ionized flux fraction is slightly higher when measured at 3 cm from the target than when measured at 10 cm from the target surface. This can be understood from a larger ion sputter cone compared to the neutral sputter cone.[34,50] The lower pressure (0.5 Pa) delivers a slightly higher ionized flux fraction as shown by the open circles in Fig. 1. Furthermore, longer pulses (100 μs) also give higher ionized flux fraction, except at the lowest peak discharge current density (0.5 A/cm^2). This contradicts the recent findings of Shimizu *et al.*[63] that observed, while studying a HiPIMS discharge with titanium target, that there is an increase in the ionized flux fraction for decreasing pulse length for peak discharge current density $J_{D,peak} = 1.1$ A/cm^2 and that there is a small decrease in the ionized flux fraction with decreasing pulse length for low $J_{D,peak} = 0.37$ A/cm^2. In their study, the ionized flux fraction was measured to be in the range ~20 to ~40% and increased with increased peak discharge current density.

For comparison, measurements with a copper target find the ionized flux fraction to be in the range of 31%–62% at the substrate position (9 cm from the target) and increase with increased peak discharge current density in a discharge operated at 1 Pa for a 50 μs long pulse and $J_{D,peak}$ in the range 1–1.5 A/cm^2.[64] For aluminum and titanium targets, Lundin *et al.*[65] measured the ionized flux fraction to increase from about 20% to roughly 70% as the average discharge current density $J_{D,average}$ was varied from 0.5 to 2.0 A/cm^2, for working gas pressure of 0.5 and 2.0 Pa, and 100 μs long pulses 4 cm from the target surface. Lower working gas pressure resulted in a slightly higher ionized flux fraction, a trend that has also been observed for a discharge with a copper target,[64] as well as titanium and aluminum targets.[65] This latter effect is also seen for the zirconium target in Fig. 1.

The measured normalized deposition rate vs the peak discharge current density is shown in Fig. 2. The measured normalized deposition rate is the deposition rate for HiPIMS operation divided by the deposition rate determined from dc magnetron sputtering operated at the same average power. We see in Fig. 2 that the measured normalized deposition rate decreases with increased peak discharge current density. This is commonly observed in HiPIMS operations. For a given pulse length and average power, the deposition rate decreases as the peak discharge current density increases.[36,63,65,66] The normalized deposition rate for a given discharge current density is higher when measured 10 cm from the target surface than when measured at 3 cm. It can also be seen in Fig. 2 that the normalized deposition rate is slightly lower for the lower working gas pressure (0.5 Pa) (open circles). The normalized deposition rate is also slightly higher for the longer pulse length (100 μs). This again contradicts the findings of Shimizu *et al.*[63] for a HiPIMS discharge with a titanium target as they observed a decrease in the normalized deposition rate as the pulse length was increased from 50 μs at $J_{D,peak} = 1.1$ A/cm^2. In general, for a fixed peak discharge current density, they found that the deposition rate increases with decreasing pulse length and reaches a maximum at around 25–50 μs, a trend that had been predicted earlier using the IRM.[44] They also found that further shortening the pulse length decreases the deposition rate.[63]

Overall, we observe that the ionized flux fraction increases (Fig. 1) and the normalized deposition rate decreases (Fig. 2) as the peak discharge current density is increased. This is a manifestation

TABLE I. Discharge parameters, the measured ionized flux fraction F_{flux}, and the measured deposition rate normalized to the deposition rate in a dcMS, operated at the same power and pressure, F_{dep}, at the axial position z_{QCM}, and the internal discharge parameters ionization probability α_t, the back-attraction probability β_t and the peak in the degree of working gas rarefaction derived from the modeling of HiPIMS discharges with zirconium target for 0.5 and 1 Pa pressure.

t_{pulse} (μs)	Pressure (Pa)	$J_{D,\,peak}$ (A/cm^2)	V_D (V)	z_{QCM} (cm)	α_t (%)	$\beta_{t,\,pulse}$ (%)	β_t (%)	F_{flux} (%)	F_{dep} (%)	$1-n_{Ar}/n_{Ar}$, 0 (%)
50	1	1	550	10	86	73	71	45	23	72
100	1	1	549	10	85	68	67	48	27	78
100	1	0.5	485	10	73	76	75	25	43	49
50	1	0.5	485	10	75	73	71	31	39	50
50	1	2	575	10	91	79	76	59	13	80
50	0.5	1	488	10	88	70	68	54	21	85
50	1	1	548	10	88	78	76	46	23	72
50	1	1	538	10	85	76	74	43	22	67
50	1	1	535	8	85	74	72	46	—[a]	68
50	1	1	534	6	86	70	68	53	—[a]	74
50	1	1	529	4	86	75	73	54	—[a]	69
50	1	1	529	3	85	78	75	52	21	65
100	1	1	536	3	84	73	72	53	23	71
50	1	0.5	467	3	73	80	77	34	36	45
100	1	0.5	488	3	75	75	74	38	36	52
50	1	1	488	3	86	73	71	58	23	70
50	0.5	1	488	3	88	75	72	61	16	81

[a]No dcMS reference measurements were made.

of the HiPIMS compromise, which states that the increased ionized flux fraction comes at the cost of a lower deposition rate.[67]

B. Modeling results

As discussed in Sec. II B, the IRM is a semi-empirical model and has three unknown fitting parameters: the ion back-attraction probability, the potential drop across the IR, and the electron recapture probability. The last parameter is given a fixed value as discussed above. This leaves the ($\beta_{t,pulse}$, $f = V_{IR}/V_D$) parameter space as the one to be explored through a model fitting procedure, where we find the best fit to the experimentally determined discharge current waveform. The best fit is determined using a fitting map showing the fraction of the discharge voltage that drops across the ionization region f, vs the back-attraction probability of an ion of the sputtered species $\beta_{t,pulse}$ during the pulse. The fitting procedure is shown in Fig. 3 for one particular discharge with a zirconium target for a 50 μs long pulse with peak discharge current density $J_{D,peak} = 1$ A/cm^2, and working gas pressure of 1 Pa, and the ionized flux fraction used to lock the model was measured 10 cm from the target surface (the discharge parameters listed in the first line of Table I). The parameters that define the size of the IR were set as follows: $r_{c1} = 6$ mm, $r_{c2} = 19$ mm, $z_1 = 2$ mm, and $z_2 = 13$ mm. The figure of merit (FOM), shown in Fig. 3, is calculated as the weighted sum of square residuals normalized by the weighted total sum of squares (see Gudmundsson *et al.*[35]). The regions on the fitting map where the modeled discharge current matches the experimental discharge current the best is shown as a yellow zone. This yellow zone indicates the combination of $f = V_{IR}/V_D$ and $\beta_{t,pulse}$ where the weighted square deviation of the discharge current is the smallest. The ionized flux fraction is shown as black contour lines. As this yellow zone is large, an additional constraint from an experimentally determined quantity is necessary. This is done by using the measured ionized flux fraction to lock the model as suggested by Butler *et al.*[48] [see Eq. (1)]. We use the ionized flux fraction measured (45%) at 10 cm from the target surface over the racetrack to lock the model. The measured discharge current waveform and the measured discharge voltage waveform are shown by solid lines in Fig. 4. The resulting best fit determined by the IRM for the discharge current waveform and the measured ionized flux fraction is shown with a dashed line in Fig. 4. The modeled discharge current matches the experimental discharge current very well.

TABLE II. Lowest few excited states of the zirconium atom that are used to calculate the collisional loss per electron-ion pair created.

Configuration	Term	Threshold (eV)
$4d^25s^2$	a ^{3}F	0–0.15
$4d^25s^2$	a ^{3}P	0.52–0.54
$4d^3(^4F)5s$	a ^{5}F	0.60–0.73
$4d^25s^2$	a ^{1}D	0.63
$4d^25s^2$	a ^{1}G	1.00
$4d^3(^4F)5s$	a ^{1}G	1.44–1.53
$4d^3(^3G)5s$	a ^{1}G	1.55–1.58

The temporal evolution of the species densities calculated by the IRM for the discharge fitted in Fig. 3 is shown in Fig. 5, the neutral species densities in Fig. 5(a) and the ions in Fig. 5(b). As to be expected, the ground state working gas argon atoms dominate the discharge. The cold argon ground state density [denoted $Ar^C(3p^6)$ in Fig. 5(a)] decreases steadily to a minimum and then

TABLE III. Reactions and rate coefficients used in the IRM involving zirconium determined for both hot and cold electrons. The rate coefficients are calculated assuming a Maxwellian electron energy distribution function and fit in the range $T_e = 1 - 7$ eV for cold electrons and 200–1000 eV for hot electrons.

	Reaction	Threshold (eV)	Rate coefficient (m^3/s)	Electron group	Reference
(R1)	$e + Zr \rightarrow Zr^+ + e$	6.63	$1.69 \times 10^{-13} T_e^{0.171} \exp(-7.825/T_e)$	Cold	55
			$3.04 \times 10^{-13} - 2.18 \times 10^{-16} \times T_e$	Hot	
(R2)	$e + Zr^+ \rightarrow Zr^{2+} + e$	13.13	$3.06 \times 10^{-14} T_e^{0.042} \exp(-14.39/T_e)$	Cold	
			$3.09 \times 10^{-14} - 2.21 \times 10^{-17} \times T_e$	Hot	
(R3)	$Ar^+ + Zr \rightarrow Ar + Zr^+$		2×10^{-16}		62
(R4)	$Ar(4s'[1/2]_0) + Zr \rightarrow Ar + Zr^+ + e$		5.3×10^{-15}		
(R5)	$Ar(4s[3/2]_2) + Zr \rightarrow Ar + Zr^+ + e$		5.3×10^{-15}		

rises slightly to the end of the pulse. The minimum in Ar^C density appears close to the maximum in the discharge current. We see that there is an increase in the density of both the hot (Ar^H) and warm (Ar^W) argon atoms, during the pulse, followed by a decay in the afterglow. Furthermore, the warm argon atom density approaches the cold argon density during its minimum. We also see in Fig. 5(a) that the zirconium atom density increases rapidly early in the pulse and then decays slowly to the end of the pulse, when the sputtering by energetic ion bombardment comes to an end. In the afterglow, the density of the ground state zirconium atoms decreases sharply at first and then slower. As seen in Fig. 5(a) toward the end of the pulse the working gas is rarefied, and the zirconium atoms pass through at high speed, while after the pulse is off there is back diffusion of argon that shortens the mean free path of the zirconium atoms and slows them down which appears as a slower decay of the zirconium atom density. Recall that the zirconium atoms enter the IR with a velocity that is directed away from the target surface and this dictates the decay rate in the afterglow. We note that the hot argon atoms, which also have a directed velocity away from the target surface, have a similar decay rate, while warm argon atoms that have lower velocity decay slower in the afterglow. The temporal behavior of the densities of the metastable argon atoms show an increase in the beginning of the pulse a drop and a peak at the end of the pulse and then a much slower decay in the afterglow, but the densities are much lower. As mentioned, the temporal evolution of the neutral argon density in Fig. 5(a) shows a significant drop toward the end of the pulse. This is what is referred to as working gas rarefaction. Working gas rarefaction is known to occur in magnetron sputtering discharges[68,69] and has been observed experimentally in HiPIMS operation.[70–72] Note that the total neutral argon density within the IR is the sum of the cold, warm, and hot argon atoms in the ground state, and the two metastable states. Hence, working gas rarefaction is not only the drop in the cold argon atom density shown in Fig. 5(a), it is the drop in the total neutral argon density. The calculated values for the degree of working gas rarefaction, including all the neutral argon atom populations, are listed in Table I for all the cases explored.

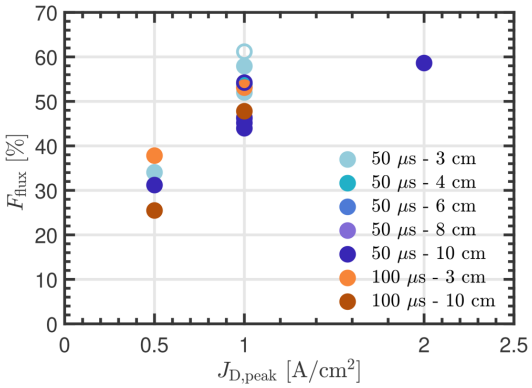

FIG. 1. Measured ionized flux fraction vs the peak discharge current density. The working gas pressure was 0.5 Pa (open circles) and 1 Pa (solid dots), and the pulse length was 50 and 100 μs and the ionized flux fraction was measured 3, 4, 6, 8, and 10 cm from the target surface.

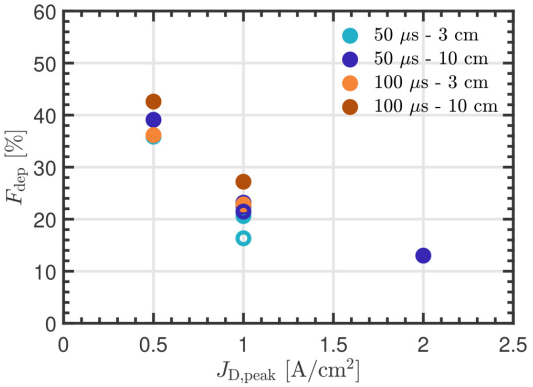

FIG. 2. Measured normalized deposition rate vs the peak discharge current density. The working gas pressure was 0.5 Pa (open circles) and 1 Pa (solid dots) and the pulse length was 50 and 100 μs, measured 3 and 10 cm from the target surface.

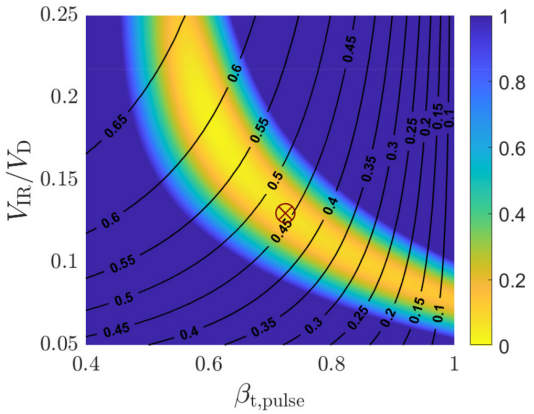

FIG. 3. FOM and the ionized flux fraction F_{flux}, displayed as a color map and contour lines, respectively, for a grid scan over $\beta_{t,pulse}$ and $f = V_{IR}/V_D$ for a zirconium target, a 50 μs long pulse, peak discharge current density $J_{D,peak} = 1$ A/cm^2, working gas pressure of 1 Pa, and the ionized flux fraction used to lock the model was measured 10 cm from the target surface. The parameter combination giving the best fit while meeting the F_{flux} constraint is highlighted with a red $\times$ inside a circle.

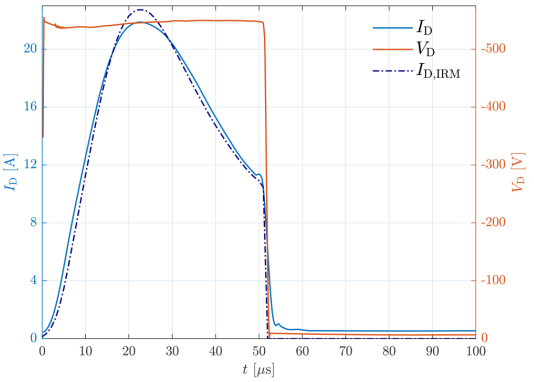

FIG. 4. Measured temporal evolution of the cathode voltage (solid red line and the right *y*-axis) and the discharge current (solid blue line and the left *y*-axis) as well as the model fit (purple dash dot line and the left *y*-axis) for the discharge current with a zirconium target, a 50 μs long pulse, a peak discharge current density $J_{D,peak} = 1$ A/cm^2, working gas pressure of 1 Pa, and the ionized flux fraction used to lock the model was measured 10 cm from the target surface.

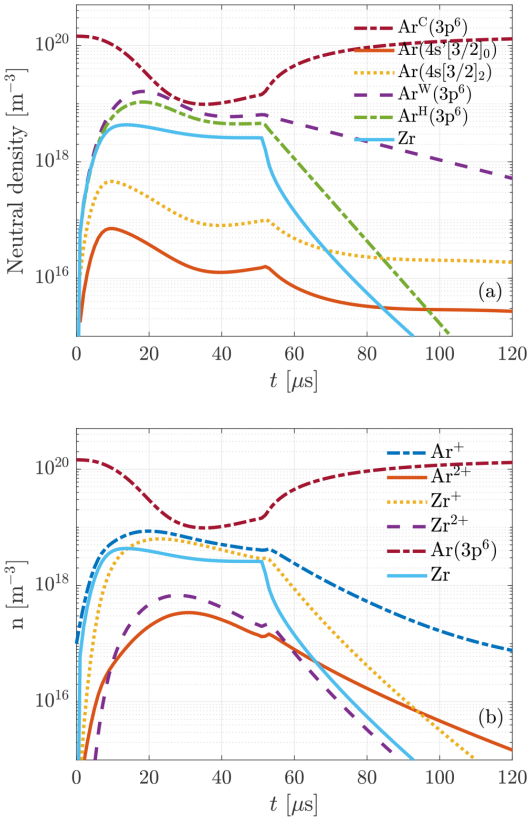

FIG. 5. Temporal evolution of the (a) neutral particle densities and (b) the ion densities for a zirconium target, a 50 μs long pulse, with peak discharge current density $J_{D,peak} = 1$ A/cm^2, working gas pressure of 1 Pa, and the ionized flux fraction used to lock the model was measured 10 cm from the target surface.

The degree of working gas rarefaction is defined as

$$\text{degree of working gas rarefaction} = 1 - \frac{n_{Ar}(t)}{n_{Ar,0}}, \quad (4)$$

where $n_{Ar,0}$ is the total argon density at the start of the pulse and $n_{Ar}(t)$ is the temporal variation of the total argon density. The peak in the degree of working gas rarefaction at $p_g = 1$ Pa and $J_{D,peak} = 1$ A/cm^2 for a 50 μs long pulse is roughly 70%, and at $J_{D,peak} = 2$ A/cm^2, it is roughly 80%. At 0.5 Pa, the peak in the degree of working gas rarefaction for $J_{D,peak} = 1$ A/cm^2 is 81%–85%. Lower working gas pressure and high peak discharge current density leads to a higher degree of working gas rarefaction. Keep in mind that the value of the degree of working gas

rarefaction depends on the volume size of the IR, so the values given are estimates.

In a separate study, we have applied the ionization region model to determine the various contributions to working gas rarefaction in HiPIMS discharges with several different cathode targets.[38] This study revealed that working gas rarefaction is driven by electron impact ionization by both primary (or cold) and hot electrons as well as by kick-out by fast neutrals coming from the target. The fast neutral species coming from the target can be either the sputtered target species or hot argon atoms. Charge exchange was found to have a negligible contribution to working gas rarefaction for all the target materials. The role of kick-out increases and the role of electron impact ionization decreases with increased sputter yield of the target material. When comparing the various contributions to working gas rarefaction for different target materials, we observed that the sputter yield is the determining factor regarding which process contributes the most to working gas rarefaction in HiPIMS operation.[38]

For the zirconium target, the contributions of the various processes to working gas rarefaction in a HiPIMS discharge vs the peak discharge current density are shown in Fig. 6. When comparing the relative contributions of each of the processes to working gas rarefaction, they are all determined by integrating the contribution of each term throughout the entire pulse and the afterglow. We see that ionization by cold primary electrons is the dominating process at all discharge current densities with a contribution in the range of 63%–65%, while ionization by secondary electrons has 14%–19% contribution, the contribution of kick-out by Zr atoms decreases from 16% to 12% and the contribution of hot argon atoms decreases from 7% to 4%, with increasing peak discharge current density in the range 0.5–2.0 A/cm^2. In this case, the location of the ionized flux fraction measurement used to lock the model was 10 cm from the target surface. We see that the peak discharge current density does not have much influence on the relative contribution of the various terms. Zirconium has a rather low sputter yield and, therefore, electron impact ionization is expected to be the most important process.[38] This confirms our expectation that the sputter yield is the primary factor in determining the dominating mechanism for argon gas rarefaction among the kick-out mechanism and the ionization by the cold and hot electron population.

The temporal evolution of the charged particle densities is shown in Fig. 5(b). The Ar^+ ion is always the dominating ion and the Zr^+ ion has always a smaller density. The densities of the doubly charged Zr^{2+} and Ar^{2+} ions are always more than an order of magnitude smaller than the density of the singly charged ions. The temporal evolution of the cold argon atoms and zirconium atoms is also shown in Fig. 5(b) to ease comparison. For most of the pulse duration, the density of Ar^+ and Zr^+ ions surpasses the density of zirconium atoms.

The temporal evolution of the discharge current composition at the target surface is shown in Fig. 7. We see that roughly 2/3 of the discharge current is carried by Ar^+ ions while only 1/3 is carried by Zr^+ ions. The contributions from Ar^{2+} and Zr^{2+} ions and secondary electron emission are smaller. The current composition is explored further in Fig. 8 where the current composition is shown for three peak discharge current densities. We see that the fractional contribution of Zr^+ and Zr^{2+} ions increases, and the

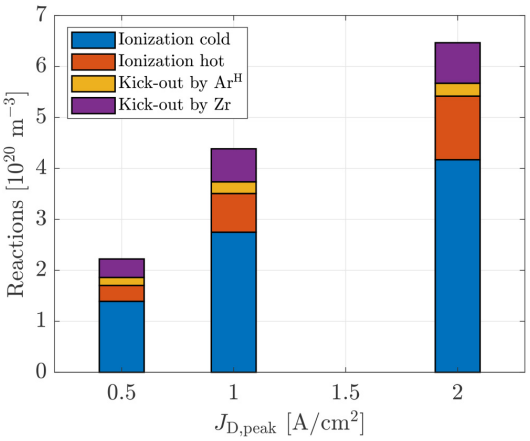

FIG. 6. Contribution of the various processes to working gas rarefaction within the ionization region for a discharge with 2 in. zirconium target vs the peak discharge current density for argon working gas pressure of 1 Pa and pulse length of 50 μs, and the ionized flux fraction used to lock the model was measured 10 cm from the target surface. Ionization cold and hot refers to electron impact ionization of argon atoms by the cold and hot electron populations, respectively.

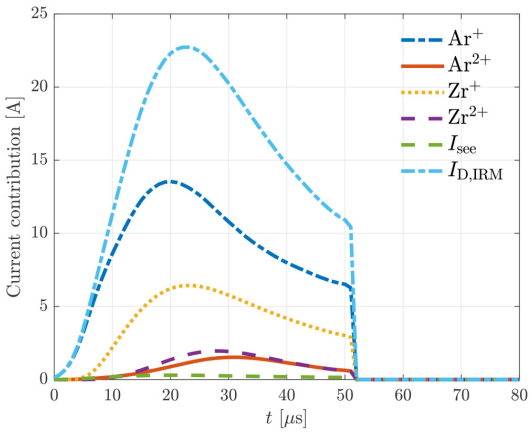

FIG. 7. Temporal evolution of the discharge current composition at the target surface for a zirconium target, for a 50 μs long pulse, with peak discharge current density $J_{D,peak} = 1$ A/cm^2, working gas pressure of 1 Pa, and the ionized flux fraction used to lock the model was measured 10 cm from the target surface.

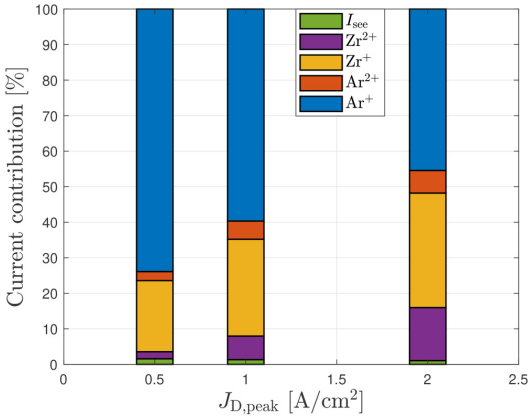

FIG. 8. Discharge current composition within the ionization region vs the peak discharge current density for a discharge with 2 in. zirconium target for argon working gas pressure of 1 Pa and pulse length of 50 μs, and the ionized flux fraction used to lock the model was measured 10 cm from the target surface.

fractional contribution of Ar^+ ions decreases, with increased peak discharge current density. At $J_{D,peak} = 0.5$ A/cm^2, the Ar^+ ion contribution is roughly 74%, at 1.0 A/cm^2 it is about 60%, and roughly 45% at $J_{D,peak} = 2$ A/cm^2. The Zr^+ ion contribution is 20%, 27%, and 32%, and the Zr^{2+} contribution increases from 2% to 6.6%, to about 15%, as the peak discharge current density is increased. The contribution of secondary electron current is always much smaller than the current carried by each of the ions. There is an upper limit on the current density that corresponds to where all the incoming argon atoms from the surrounding gas reservoir are ionized and drawn to the target. This upper limit defines the critical current density of $J_{crit} \approx 0.2$ A/cm^2 at 1 Pa and $T_g = 300$ K.[73,74] For all the cases discussed here, the discharge operates well above this limit and ion recycling has to take place to reach the high discharge current densities observed. As both argon and zirconium ions contribute significantly to the discharge current at the target surface, the discharge operates on a combination of working gas recycling and self-sputter recycling.[74]

The IRM calculations provide, in addition to the temporal variation of the species densities, various other information and discharge parameters. This includes the internal discharge parameters such as the ionization probability α_t, the back-attraction probability β_t, and the voltage drop across the IR. Earlier, we applied the IRM to study a HiPIMS discharge with 75 mm diameter tungsten target as the discharge voltage was varied.[36] There, the peak discharge current density $J_{D,peak}$ increases in the range 0.33–0.73 A/cm^2, with increased discharge voltage in the range 500–800 V. For the sputtered tungsten atoms, the ionization probability was found to increase with increased peak discharge current density and be in the range 54%–75%. For a titanium target, the ionization probability was found to increase from 45% to 84% as the peak discharge current density was varied from 0.15 to 1 A/cm^2.[11,34]

Another important internal discharge parameter is the back-attraction probability for the sputtered species after they have been ionized within the IR. The back-attraction probability β_i for an ion species i relates the ion fluxes out of the IR toward the diffusion region and the flux toward the racetrack during the pulse. The ion flux out of the IR toward the diffusion region is calculated from the flux toward the racetrack during the pulse,[31,75]

$$\int_T \tilde{\Gamma}_i^{DR}(t)dt = \left(\frac{1}{\beta_i} - 1\right)\frac{S_{RT}}{S_{DR}}\int_T \tilde{\Gamma}_i^{RT}(t)dt, \tag{5}$$

where $\int_T \tilde{\Gamma}_i^{RT}(t)dt$ is the ion flux toward the racetrack which has a surface area of S_{RT} and T is the pulse period, $\int_T \tilde{\Gamma}_i^{DR}(t)dt$ is the ion flux toward the diffusion region, and S_{DR} is the surface area of the ionization region facing the diffusion region. Here, i denotes the ion, which can be Ar^+, Zr^+, Ar^{2+}, or Zr^{2+}. A significant fraction of the ion flux onto the racetrack is made up of ionized zirconium as can be seen in Figs. 7 and 8. These are zirconium atoms that were sputtered off the target and ionized within the IR and then return to the target. For the target material, we write t as a subscript. Figure 9(b) shows the target metal ion back-attraction probability β_t vs the peak discharge current density for a HiPIMS discharge with a zirconium target. The back-attraction probability during the pulse is found to be in the range $\beta_{t,pulse} \approx 68\%$–$80\%$. The overall back-attraction probability β_t is somewhat lower or in the range 67%–77%. There is clearly some uncertainty or scatter in the calculated back-attraction probability values. This uncertainty is at least partially due to the uncertainty in the values of the transport parameters, used in Eq. (1) to determine the flux of ions and neutrals, to lock the model. Recall that we used values that were determined experimentally for a discharge with titanium target over a limited range.[50] The back-attraction probability β_t for zirconium is higher than for copper, which was found to be in the range 44%–50%,[35] but lower than for titanium target which was determined to be 83%–87%.[34] For the sputtered tungsten, the back-attraction probability β_t decreases from 87% to 67% with increasing discharge voltage or increasing discharge current density.[36]

Figure 10 shows the fractional potential drop over the IR $f = V_{IR}/V_D$ vs the peak discharge current density. The fractional potential drop is in the range 10%–16% of the applied discharge voltage. The fractional potential drop is slightly lower at 0.5 Pa than at 1 Pa and appears to decrease slightly as the peak current density is increased. The fractional potential drop reported here for a discharge with zirconium target is higher than what was determined for a discharge with tungsten target which was in the range 6%–8%, decreasing with increasing peak discharge current density.[36] For a copper target, the fractional potential drop was found to lie in the range 14%–17%,[4] and for a graphite target it was found to be 14%,[32] for a working gas pressure of $p_g \sim 1$ Pa and $J_{D,peak} \sim 1$ A/cm^2.

Figure 2 shows how the measured normalized deposition rate decreases as the peak discharge current is increased. Earlier we have defined the sputter-rate-normalized deposition rate, which is

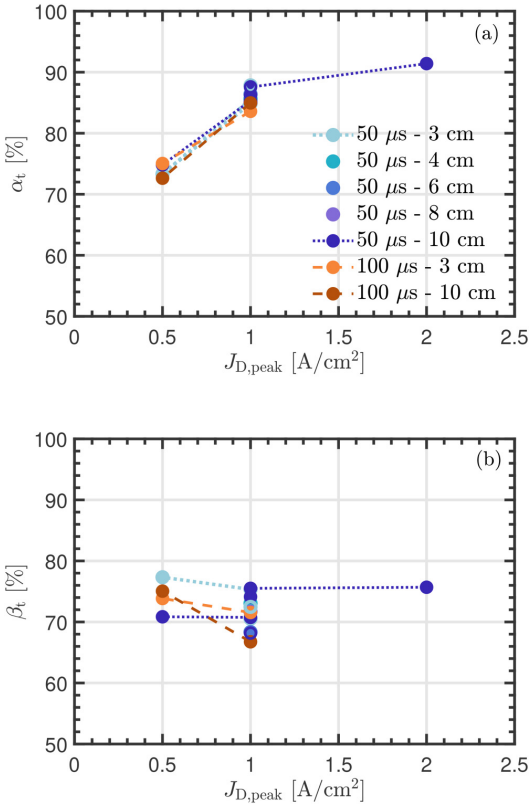

FIG. 9. (a) Ionization probability α_t and (b) the back-attraction probability β_t vs the peak discharge current density determined by the IRM for a discharge with a 2 in. zirconium target for argon working gas pressure of 0.5 Pa (open circles) and 1 Pa (solid dots) and pulse length of 50 and 100 μs and the ionized flux fraction measured 3, 4, 6, 8, and 10 cm from the target surface was used to lock the model.

given by[34]

$$F_{sput} = (1 - \alpha_t) + \left(\frac{\xi_{ti}}{\xi_{tn}}\right)\alpha_t(1 - \beta_t), \tag{6}$$

where ξ_{ti} is the transport parameter for ions and ξ_{tn} is the transport parameter for neutrals of the sputtered species.[49,50] Equation (6) can be approximated to become

$$F_{sput} = 1 - \alpha_t\beta_t = \frac{\Gamma^{DR}}{\Gamma_0}, \tag{7}$$

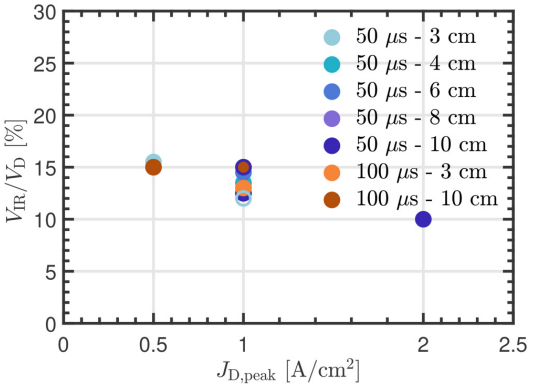

FIG. 10. Fractional potential drop over the IR $f = V_{IR}/V_D$ vs the peak discharge current density. The working gas pressure was 0.5 Pa (open circles) and 1 Pa (solid dots), the pulse length was 50 and 100 μs, and the ionized flux fraction measured 3, 4, 6, 8, and 10 cm from the target surface was used to lock the model.

for the special case when $\xi_{ti} = \xi_{tn}$.[76,77] This is the ratio of the flux of sputtered species (ions and neutrals) out of the IR toward the DR Γ^{DR} and the total flux of atoms sputtered from the target Γ_0 (atoms/s). Keep in mind that Eq. (7) does therefore not take into account ion focusing (or spreading) *en route* toward the substrate.[34,48,50] This equation states that the sputter-rate-normalized deposition rate is reduced as the ionization of the sputtered material increases.[67]

The relative ion-to-neutral transport factors ξ_{ti}/ξ_{tn} in Eq. (6) describe the relative deposited fractions of target material ions and neutrals onto a substrate. Experimentally, these parameters have been determined for HiPIMS of a titanium target to be roughly $\xi_{ti}/\xi_{tn} \approx 0.8$ for a substrate located 3 cm from the target surface and $\xi_{ti}/\xi_{tn} \approx 0.5$ for a substrate located 7 cm from the target surface.[50] A value of $\xi_{ti}/\xi_{tn} < 1$ indicates a larger spread of metal ions compared to metal neutrals, which is explained by larger scattering cross sections of ions compared to neutrals and by ions being subjected to electric fields.[34] The sputter rate-normalized deposition rate calculated using Eq. (6), using the measured relative ion-to-neutral transport factors for titanium,[50] shows roughly the same behavior as the experimentally determined normalized deposition rate but there is a slight difference in the value. This can be seen in Fig. 11 where the sputter rate-normalized deposition rate F_{sput} vs the measured normalized deposition rate F_{dep} is shown. We see that when the normalized deposition rate and the ionized flux fraction are measured 10 cm from the target surface are used to lock the model the values fall approximately on a line with slope 1 that goes through the origin, while when the flux parameters measured at 3 cm are used to lock the model F_{sput} is slightly higher than the measured F_{dep}. When the flux parameters measured at 10 cm are used to lock the model, we find the average value of the ratio F_{dep}/F_{sput} to be 0.93 with a standard deviation of 0.17, while

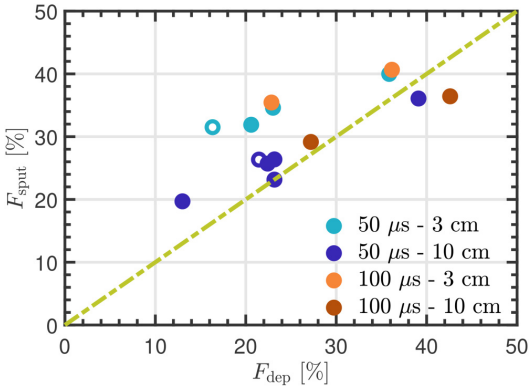

FIG. 11. Sputter-rate-normalized deposition rate $F_{\rm sput}$ calculated using Eq. (6) vs the measured normalized deposition rate $F_{\rm dep}$ for a discharge with a 2 in. zirconium target for argon working gas pressure of 0.5 Pa (open circles) and 1 Pa (solid dots) and pulse lengths of 50 and 100 μs. The dashed line has a slope of 1.

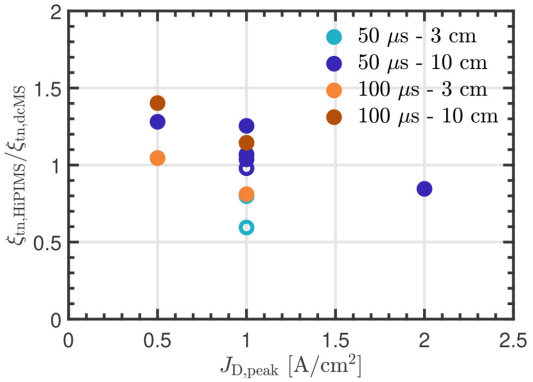

FIG. 12. Ratio of the neutral transport parameters in a HiPIMS discharge to dcMS discharge $\xi_{\rm tn,HiPIMS}/\xi_{\rm tn,dcMS}$ vs the peak discharge current density determined by the IRM for a discharge with a 2 in. zirconium target for argon working gas pressure of 0.5 Pa (open circles) and 1 Pa (solid dots) and pulse lengths of 50 and 100 μs.

the measured values at 3 cm are used to lock the model we find it to be 0.71 with a standard deviation of 0.15.

The sputter rate-normalized deposition rate $F_{\rm sput}$ and the experimentally determined normalized deposition rate $F_{\rm dep}$ are related through the relative differences in the sputter rate $\Gamma_{\rm sput,HiPIMS}/\Gamma_{\rm sput,dcMS}$ and the neutral transport parameter ratio between HiPIMS and the corresponding (same pressure and average power) dcMS discharge $\xi_{\rm tn,HiPIMS}/\xi_{\rm tn,dcMS}$ needs to be taken into account as well or

$$F_{\rm dep} = \frac{\Gamma_{\rm sput,HiPIMS}}{\Gamma_{\rm sput,\ dcMS}} \frac{\xi_{\rm tn,HiPIMS}}{\xi_{\rm tn,dcMS}} F_{\rm sput}, \tag{8}$$

where[34,64,77]

$$\frac{\Gamma_{\rm sput,HiPIMS}}{\Gamma_{\rm sput,\ dcMS}} = \frac{V_{\rm D,dcMS}}{V_{\rm D,HiPIMS}} \times \frac{\sum_i \zeta_i Y_i(z_i V_{\rm D,HiPIMS})}{Y_{\rm Ar^+\to Zr}(V_{\rm D,dcMS})}, \tag{9}$$

and $V_{\rm D,HiPIMS}$ and $V_{\rm D,dcMS}$ are the discharge voltages for the corresponding HiPIMS and dcMS discharges, respectively. The sum is taken over all the ions Ar^+, Zr^+, Zr^{2+}, and Ar^{2+}, which have sputter yields Y_i, and ζ_i is the fraction of the ion current at the target surface that is carried by a particular ion i and z_i is the charge state of that ion. The parameter $\sum_i \zeta_i Y_i(z_i V_{\rm D,HiPIMS})/Y_{\rm Ar^+\to Zr}(V_{\rm D,dcMS})$ in Eq. (9) is fairly constant and does not vary much with the varying ion fractions and pulse voltage. The average value is 1.67 with a standard deviation of 0.07. Due to a higher voltage, the average sputter during the pulse higher in HiPIMS than in dcMS. As mentioned, Eq. (8) relates the measured normalized deposition rate $F_{\rm dep}$ and the sputter rate-normalized deposition rate $F_{\rm sput}$. This information can be used to estimate the unknown neutral transport parameter ratio.[34]

The ratios of the neutral transport parameters in a HiPIMS discharge to dcMS discharge $\xi_{\rm tn,HiPIMS}/\xi_{\rm tn,dcMS}$, estimated from the measured $F_{\rm sput}$, and the calculated $F_{\rm sput}$, are shown vs the peak discharge current density, for argon working gas pressure of 0.5 and 1 Pa and pulse lengths of 50 and 100 μs, in Fig. 12. It can be seen that the ratio $\xi_{\rm tn,HiPIMS}/\xi_{\rm tn,dcMS}$ decreases slightly with increased peak discharge current density for a given pulse length and distance from the target surface. We see that the ratio $\xi_{\rm tn,HiPIMS}/\xi_{\rm tn,dcMS}$ is slightly higher if the flux parameters measured at 10 cm from the target surface are used to lock the model, compared to when they are measured 3 cm from the target surface. The ratios are smaller if we assume $\xi_{\rm ti} = \xi_{\rm tn}$ and use Eq. (7) to calculate the sputter-rate normalized deposition rate $F_{\rm sput}$ (not shown). Earlier we estimated the ratio $\xi_{\rm tn,HiPIMS}/\xi_{\rm tn,dcMS}$ to be roughly 1.9 for discharges with titanium target and justified this value by a simple estimate involving the difference in argon gas temperature in HiPIMS and dcMS operation that influences the mean free path of the sputtered Ti neutrals.[34] Note also that working gas rarefaction due to ionization losses in the HiPIMS process will add to this factor.

IV. SUMMARY

We have explored experimentally the effect of the peak discharge current density on the ionized flux fraction and normalized deposition rate in a HiPIMS discharge with a zirconium target. The ionized flux fraction increases and the normalized deposition rate decreases as the peak discharge current density increases, in accordance with the HiPIMS compromise. The measured discharge current and voltage waveforms were fed into the IRM to determine the temporal evolution of the plasma parameters and the internal discharge properties, the ionization and back-attraction probabilities. At a working gas pressure of 1 Pa, the ionization probability

was found to be in the range 73%–91% and the overall back-attraction probability to be in the range 67%–77% for a peak discharge current density in the range 0.5–2.0 A/cm^2. We explored the processes contributing to working gas rarefaction and found electron impact ionization to be the main contributor to working gas rarefaction, with over 80% contribution, while kick-out by zirconium atoms and argon atoms has a smaller contribution.

ACKNOWLEDGMENTS

This work was partially supported by the Icelandic Research Fund under Grant Nos. 196141 and 217999, the University of Iceland Research Fund under Grant No. 93940, the University of Iceland Research Fund for Doctoral Students, and the Swedish Government Strategic Research Area in Materials Science on Functional Materials at Linköping University (Faculty Grant SFO-Mat-LiU No. 2009-00971).

AUTHOR DECLARATIONS

Conflict of Interest

The authors have no conflicts to disclose.

Author Contributions

Swetha Suresh Babu: Data curation (equal); Formal analysis (equal); Investigation (equal); Methodology (equal); Software (equal); Validation (equal); Visualization (equal); Writing – review & editing (equal). **Joel Fischer:** Conceptualization (equal); Data curation (equal); Formal analysis (equal); Investigation (equal); Methodology (equal); Resources (equal); Writing – review & editing (equal). **Kateryna Barynova:** Data curation (equal); Formal analysis (equal); Investigation (equal); Methodology (equal); Software (equal); Writing – review & editing (equal). **Martin Rudolph:** Formal analysis (equal); Investigation (equal); Methodology (equal); Software (equal); Validation (equal); Writing – original draft (equal); Writing – review & editing (equal). **Daniel Lundin:** Conceptualization (equal); Funding acquisition (equal); Methodology (equal); Project administration (equal); Resources (equal); Supervision (equal); Validation (equal); Writing – review & editing (equal). **Jon Tomas Gudmundsson:** Conceptualization (equal); Data curation (equal); Formal analysis (equal); Funding acquisition (equal); Investigation (equal); Methodology (equal); Project administration (equal); Supervision (equal); Writing – original draft (equal); Writing – review & editing (equal).

DATA AVAILABILITY

The data that support the findings of this study are available within the article.

REFERENCES

[1]J. T. Gudmundsson, Plasma Sources Sci. Technol. **29**, 113001 (2020).
[2]R. K. Waits, J. Vac. Sci. Technol. **15**, 179 (1978).
[3]P. J. Kelly and R. D. Arnell, Vacuum **56**, 159 (2000).
[4]J. T. Gudmundsson, A. Anders, and A. von Keudell, Plasma Sources Sci. Technol. **31**, 083001 (2022).
[5]D. Krüger, K. Köhn, S. Gallian, and R. P. Brinkmann, Phys. Plasmas **25**, 061207 (2018).
[6]V. G. Antunes, M. Rudolph, A. Kapran, H. Hajihoseini, M. A. Raadu, N. Brenning, J. T. Gudmundsson, D. Lundin, and T. Minea, Plasma Sources Sci. Technol. **32**, 075016 (2023).
[7]J. T. Gudmundsson, N. Brenning, D. Lundin, and U. Helmersson, J. Vac. Sci. Technol. A **30**, 030801 (2012).
[8]A. Hecimovic, J. Held, V. Schulz-von der Gathen, W. Breilmann, C. Maszl, and A. von Keudell, J. Phys. D: Appl. Phys. **50**, 505204 (2017).
[9]F. Lockwood Estrin, S. K. Karkari, and J. W. Bradley, J. Phys. D: Appl. Phys. **50**, 295201 (2017).
[10]*High Power Impulse Magnetron Sputtering: Fundamentals, Technologies, Challenges and Applications*, edited by D. Lundin, T. Minea, and J. T. Gudmundsson (Elsevier, Amsterdam, 2020).
[11]M. Rudolph, N. Brenning, H. Hajihoseini, M. A. Raadu, T. M. Minea, A. Anders, D. Lundin, and J. T. Gudmundsson, J. Phys. D: Appl. Phys. **55**, 015202 (2022).
[12]M. Rudolph, N. Brenning, H. Hajihoseini, M. A. Raadu, J. Fischer, J. T. Gudmundsson, and D. Lundin, J. Vac. Sci. Technol. A **40**, 043005 (2022).
[13]U. Helmersson, M. Lattemann, J. Bohlmark, A. P. Ehiasarian, and J. T. Gudmundsson, Thin Solid Films **513**, 1 (2006).
[14]G. Greczynski, I. Petrov, J. E. Greene, and L. Hultman, J. Vac. Sci. Technol. A **37**, 060801 (2019).
[15]Z. Hubička, J. T. Gudmundsson, P. Larsson, and D. Lundin, in *High Power Impulse Magnetron Sputtering: Fundamentals, Technologies, Challenges and Applications*, edited by D. Lundin, T. Minea, and J. T. Gudmundsson (Elsevier, Amsterdam, 2020), pp. 49–80.
[16]A. Anders, Thin Solid Films **518**, 4087 (2010).
[17]B. Wicher, O. V. Pshyk, X. Li, B. Bakhit, V. Rogoz, I. Petrov, L. Hultman, and G. Greczynski, Mater. Des. **238**, 112727 (2024).
[18]G. Greczynski, L. Hultman, and I. Petrov, J. Appl. Phys. **134**, 140901 (2023).
[19]H. Luo, F. Gao, and A. Billard, Surf. Coat. Technol. **374**, 822 (2019).
[20]C.-C. Kuo, C.-H. Lin, J.-T. Chang, and Y.-T. Lin, Coatings **11**, 7 (2021).
[21]I. Schnell and R. C. Albers, J. Phys.: Condens. Matter **18**, 1483 (2006).
[22]D. R. Olander, *Fundamental Aspects of Nuclear Reactor Fuel Elements* (Technical Information Center, Office of Public Affairs Energy Research and Development Administration, Springfield, VA, 1976).
[23]*The Metallurgy of Zirconium*, edited by C. E. Coleman (International Atomic Energy Agency, Vienna, 2022).
[24]M. Niinomi, Sci. Technol. Adv. Mater. **4**, 445 (2003).
[25]C. J. R. Lustosa, J. Stryhalski, R. L. P. Gonçalves, E. Bonturim, O. Florêncio, and M. Massi, Mater. Res. **26**, e20220566 (2023).
[26]J. Chakraborty, K. K. Kumar, S. Mukherjee, and S. K. Ray, Thin Solid Films **516**, 8479 (2008).
[27]D. Pilloud, J. F. Pierson, C. Rousselot, and F. Palmino, Scr. Mater. **53**, 1031 (2005).
[28]J. Fankhauser, M. Sato, D. Yu, A. Ebnonnasir, M. Kobashi, M. S. Goorsky, and S. Kodambaka, J. Vac. Sci. Technol. A **34**, 050616 (2016).
[29]A. Singh, P. Kuppusami, R. Thirumurugesan, R. Ramaseshan, M. Kamruddin, S. Dash, V. Ganesan, and E. Mohandas, Appl. Surf. Sci. **257**, 9909 (2011).
[30]A. Singh, P. Kuppusami, R. Thirumurugesan, V. Ganesan, and E. Mohandas, Int. J. Des. Manuf. Technol. **8**, 5 (2014).
[31]C. Huo, D. Lundin, J. T. Gudmundsson, M. A. Raadu, J. W. Bradley, and N. Brenning, J. Phys. D: Appl. Phys. **50**, 354003 (2017).
[32]H. Eliasson *et al.*, Plasma Sources Sci. Technol. **30**, 115017 (2021).
[33]C. Huo, M. A. Raadu, D. Lundin, J. T. Gudmundsson, A. Anders, and N. Brenning, Plasma Sources Sci. Technol. **21**, 045004 (2012).
[34]M. Rudolph, H. Hajihoseini, M. A. Raadu, J. T. Gudmundsson, N. Brenning, T. M. Minea, A. Anders, and D. Lundin, J. Appl. Phys. **129**, 033303 (2021).
[35]J. T. Gudmundsson, J. Fischer, B. P. Hinriksson, M. Rudolph, and D. Lundin, Surf. Coat. Technol. **442**, 128189 (2022).
[36]S. Suresh Babu, M. Rudolph, D. Lundin, T. Shimizu, J. Fischer, M. A. Raadu, N. Brenning, and J. T. Gudmundsson, Plasma Sources Sci. Technol. **31**, 065009 (2022).

[37]S. Suresh Babu, M. Rudolph, P. J. Ryan, J. Fischer, D. Lundin, J. W. Bradley, and J. T. Gudmundsson, Plasma Sources Sci. Technol. **32**, 034003 (2023).
[38]K. Barynova, S. Suresh Babu, M. Rudolph, J. Fischer, D. Lundin, M. A. Raadu, N. Brenning, and J. T. Gudmundsson, "On working gas rarefaction in high power impulse magnetron sputtering," Plasma Sources Sci. Technol. (to be published) (2024).
[39]G. Greczynski, I. Zhirkov, I. Petrov, J. E. Greene, and J. Rosen, J. Vac. Sci. Technol. A **35**, 060601 (2017).
[40]X. Li, B. Bakhit, M. P. Johansson Jõesaar, L. Hultman, I. Petrov, and G. Greczynski, Surf. Coat. Technol. **415**, 127120 (2021).
[41]Z. Hubička, Š. Kment, J. Olejníček, M. Čada, T. Kubart, M. Brunclíková, P. Kšírová, P. Adámek, and Z. Remeš, Thin Solid Films **549**, 184 (2013).
[42]T. Kubart, M. Čada, D. Lundin, and Z. Hubička, Surf. Coat. Technol. **238**, 152 (2014).
[43]M. A. Raadu, I. Axnäs, J. T. Gudmundsson, C. Huo, and N. Brenning, Plasma Sources Sci. Technol. **20**, 065007 (2011).
[44]M. Rudolph, N. Brenning, M. A. Raadu, H. Hajihoseini, J. T. Gudmundsson, A. Anders, and D. Lundin, Plasma Sources Sci. Technol. **29**, 05LT01 (2020).
[45]M. Rudolph, A. Revel, D. Lundin, H. Hajihoseini, N. Brenning, M. A. Raadu, A. Anders, T. M. Minea, and J. T. Gudmundsson, Plasma Sources Sci. Technol. **30**, 045011 (2021).
[46]G. Buyle, D. Depla, K. Eufinger, and R. De Gryse, J. Phys. D: Appl. Phys. **37**, 1639 (2004).
[47]T. Kozák, Plasma Sources Sci. Technol. **32**, 035007 (2023).
[48]A. Butler, N. Brenning, M. A. Raadu, J. T. Gudmundsson, T. Minea, and D. Lundin, Plasma Sources Sci. Technol. **27**, 105005 (2018).
[49]D. J. Christie, J. Vac. Sci. Technol. A **23**, 330 (2005).
[50]H. Hajihoseini, N. Brenning, M. Rudolph, M. A. Raadu, D. Lundin, J. Fischer, T. M. Minea, and J. T. Gudmundsson, J. Vac. Sci. Technol. A **41**, 013002 (2022).
[51]Y. Yamamura and M. Ishida, J. Vac. Sci. Technol. A **13**, 101 (1995).
[52]M. Rudolph, D. Lundin, E. Foy, M. Debongnie, M.-C. Hugon, and T. Minea, Thin Solid Films **658**, 46 (2018).
[53]A. Anders, J. Čapek, M. Hála, and L. Martinu, J. Phys. D: Appl. Phys. **45**, 012003 (2012).
[54]C. Kittel, *Introduction to Solid State Physics*, 8th ed. (John Wiley & Sons, Hoboken, NJ, 2005).
[55]H. Deutsch, K. Becker, and T. Märk, Int. J. Mass Spectrom. **271**, 58 (2008).
[56]M. A. Lieberman and A. J. Lichtenberg, *Principles of Plasma Discharges and Materials Processing*, 2nd ed. (John Wiley & Sons, New York, 2005).
[57]F. Blanco, F. Ferreira da Silva, P. Limão-Vieira, and G. García, Plasma Sources Sci. Technol. **26**, 085004 (2017).
[58]NIST electron elastic-scattering cross-section database, SRD 64, version 5.0.
[59]M. Schmid, "A simple sputter yield calculator," Surface Physics, Institute of Applied Physics, Technischen Universität Wien, https://www2.iap.tuwien.ac.at/www/surface/sputteryield.
[60]N. Matsunami, Y. Yamamura, Y. Itikawa, N. Itoh, Y. Kazumata, S. Miyagawa, K. Morita, R. Shimizu, and H. Tawara, "Energy dependence of the yields of ion-induced sputtering of monatomic solids," Technical Report IPPJ-AM-32, Institute of Plasma Physics, Nagoya University, 1983.
[61]A. V. Phelps and Z. L. Petrović, Plasma Sources Sci. Technol. **8**, R21 (1999).
[62]S. C. Rae and R. C. Tobin, J. Appl. Phys. **64**, 1418 (1988).
[63]T. Shimizu, M. Zanáška, R. P. Villoan, N. Brenning, U. Helmersson, and D. Lundin, Plasma Sources Sci. Technol. **30**, 045006 (2021).
[64]J. Fischer, M. Renner, J. T. Gudmundsson, M. Rudolph, H. Hajihoseini, N. Brenning, and D. Lundin, Plasma Sources Sci. Technol. **32**, 125006 (2023).
[65]D. Lundin, M. Čada, and Z. Hubička, Plasma Sources Sci. Technol. **24**, 035018 (2015).
[66]V. Tiron, I.-L. Velicu, O. Vasilovici, and G. Popa, J. Phys. D: Appl. Phys. **48**, 495204 (2015).
[67]N. Brenning, A. Butler, H. Hajihoseini, M. Rudolph, M. A. Raadu, J. T. Gudmundsson, T. Minea, and D. Lundin, J. Vac. Sci. Technol. A **38**, 033008 (2020).
[68]S. M. Rossnagel, J. Vac. Sci. Technol. A **6**, 19 (1988).
[69]S. M. Rossnagel, J. Vac. Sci. Technol. A **6**, 1821 (1988).
[70]J. Alami, K. Sarakinos, G. Mark, and M. Wuttig, Appl. Phys. Lett. **89**, 154104 (2006).
[71]J. Vlček, A. D. Pajdarová, and J. Musil, Contrib. Plasma Phys. **44**, 426 (2004).
[72]M. Palmucci, N. Britun, S. Konstantinidis, and R. Snyders, J. Appl. Phys. **114**, 113302 (2013).
[73]C. Huo, D. Lundin, M. A. Raadu, A. Anders, J. T. Gudmundsson, and N. Brenning, Plasma Sources Sci. Technol. **23**, 025017 (2014).
[74]N. Brenning, J. T. Gudmundsson, M. A. Raadu, T. J. Petty, T. Minea, and D. Lundin, Plasma Sources Sci. Technol. **26**, 125003 (2017).
[75]N. Brenning, D. Lundin, M. A. Raadu, C. Huo, C. Vitelaru, G. D. Stancu, T. Minea, and U. Helmersson, Plasma Sources Sci. Technol. **21**, 025005 (2012).
[76]J. W. Bradley, A. Mishra, and P. J. Kelly, J. Phys. D: Appl. Phys. **48**, 215202 (2015).
[77]H. Hajihoseini, M. Čada, Z. Hubička, S. Ünaldi, M. A. Raadu, N. Brenning, J. T. Gudmundsson, and D. Lundin, Plasma **2**, 201 (2019).

Bibliography

Aijaz, A. and T. Kubart (2017). Ion induced stress relaxation in dense sputter-deposited DLC thin films. *Applied Physics Letters 111*(5), 051902.

Aijaz, A., K. Sarakinos, D. Lundin, N. Brenning, and U. Helmersson (2012). A strategy for increased carbon ionization in magnetron sputtering discharges. *Diamond and Related Materials 23*, 1–4.

Alami, J., S. Bolz, and K. Sarakinos (2009). High power pulsed magnetron sputtering: Fundamentals and applications. *Journal of Alloys and Compounds 483*(1), 530–534.

Alami, J., K. Sarakinos, G. Mark, and M. Wuttig (2006). On the deposition rate in a high power pulsed magnetron sputtering discharge. *Applied Physics Letters 89*(15), 154104.

Anders, A. (2004). Fundamentals of pulsed plasmas for materials processing. *Surface and Coatings Technology 183*(2-3), 301–311.

Anders, A. (Ed.) (2008a). *Cathodic Arcs: From Fractal Spots to Energetic Condensation*, Volume 50 of *Springer Series on Atomic, Optical, and Plasma Physics*. New York, New York: Springer Verlag.

Anders, A. (2008b). Self-sputtering runaway in high power impulse magnetron sputtering: The role of secondary electrons and multiply charged metal ions. *Applied Physics Letters 92*(20), 201501.

Anders, A. (2010a). Deposition rates of high power impulse magnetron sputtering: Physics and economics. *Journal of Vacuum Science and Technology A 28*(4), 783–790.

Anders, A. (2010b). A structure zone diagram including plasma-based deposition and ion etching. *Thin Solid Films 518*(15), 4087–4090.

Anders, A. (2011). Discharge physics of high power impulse magnetron sputtering. *Surface and Coatings Technology 205*, S1–S9.

Anders, A. (2024). Glows, arcs, ohmic discharges: An electrode-centered review on discharge modes and the transitions between them. *Applied Physics Reviews 11*(3), 031310.

Anders, A. (2026). Equilibrium and non-equilibrium heating in plasma-based deposition of thin films and coatings. *Surface and Coatings Technology 520*, 132946.

Anders, A., J. Andersson, and A. Ehiasarian (2007). High power impulse magnetron sputtering: Current-voltage-time characteristics indicate the onset of sustained self-sputtering. *Journal of Applied Physics 102*(11), 113303.

Anders, A., P. Ni, and A. Rauch (2012). Drifting localization of ionization runaway: Unraveling the nature of anomalous transport in high power impulse magnetron sputtering. *Journal of Applied Physics 111*(5), 053304.

Andersson, J. and A. Anders (2008). Gasless sputtering: Opportunities for ultraclean metallization, coatings in space, and propulsion. *Applied Physics Letters 92*(22), 221503.

Antunes, V. G., M. Rudolph, A. Kapran, H. Hajihoseini, M. A. Raadu, N. Brenning, J. T. Gudmundsson, D. Lundin, and T. Minea (2023). Influence of the magnetic field on the dimension of the ionization region in high power impulse magnetron sputtering discharges. *Plasma Sources Science and Technology 32*(7), 075016.

Ashida, S., C. Lee, and M. A. Lieberman (1995). Spatially averaged (global) model of time modulated high density argon plasma. *Journal of Vacuum Science and Technology A 13*(5), 2498–2507.

Baptista, A., F. Silva, J. Porteiro, J. Míguez, and G. Pinto (2018). Sputtering physical vapour deposition (PVD) coatings: A critical review on process improvement and market trend demands. *Coatings 8*(11), 402.

Baragiola, R. A. and P. Riccardi (2008). Electron emission from surfaces induced by slow ions and atoms. In D. Depla and S. Mahieu (Eds.), *Reactive Sputter Deposition*, Chapter 2, pp. 43–60. Berlin Heidelberg: Springer Verlag.

Barynova, K., N. Brenning, S. Suresh Babu, J. Fischer, D. Lundin, M. A. Raadu, J. T. Gudmundsson, and M. Rudolph (2025). Self-regulating electron temperature in high-power impulse magnetron sputtering discharges and its effect on the metal ion escape. *Plasma Sources Science and Technology 34*(6), 06LT01.

Barynova, K., T. Shimizu, R. P. B. Viloan, M. Zanáška, M. Rudolph, D. Lundin, and J. T. Gudmundsson (2026). High power impulse magnetron sputtering of a chromium target. *Plasma Sources Science and Technology 35*(2), 025028.

Barynova, K., S. Suresh Babu, M. Rudolph, J. Fischer, D. Lundin, M. A. Raadu, N. Brenning, and J. T. Gudmundsson (2024). On working gas rarefaction in high power impulse magnetron sputtering. *Plasma Sources Science and Technology 33*(6), 065010.

Bean, J. C. (1993). Techniques for the growth of crystalline films by molecular beam deposition. In O. Auciello and J. Engemann (Eds.), *Multicomponent and Multilayered Thin Films for Advanced Microtechnologies: Techniques, Fundamentals and Devices*, Volume 234 of *NATO ASI Series E: Applied Sciences*, pp. 87 – 107. Dordrecht, The Netherlands: Kluwer Academic Publishers.

Behrisch, R. and W. Eckstein (2007). Introduction and overview. In R. Behrisch and W. Eckstein (Eds.), *Sputtering by Particle Bombardment: Experiments and Computer Calculations from Threshold to MeV Energies*, Volume 110 of *Topics in Applied Physics*, Chapter 1, pp. 1–10. Berlin Heidelberg: Springer Verlag.

Berg, S., H.-O. Blom, T. Larsson, and C. Nender (1987). Modeling of reactive sputtering of compound materials. *Journal of Vacuum Science and Technology A 5*(2), 202–207.

Berg, S., T. Larsson, and H.-O. Blom (1986). The use of nitrogen flow as a deposition rate control in reactive sputtering. *Journal of Vacuum Science and Technology A 4*(3), 594–597.

Berg, S. and T. Nyberg (2005). Fundamental understanding and modeling of reactive sputtering processes. *Thin Solid Films 476*(2), 215–230.

Biersack, J. P. and L. G. Haggmark (1980). A Monte Carlo computer program for the transport of energetic ions in amorphous targets. *Nuclear Instruments and Methods 174*(1–2), 257–269.

Bilek, M. and D. McKenzie (2006). A comprehensive model of stress generation and relief processes in thin films deposited with energetic ions. *Surface and Coatings Technology 200*(14), 4345–4354.

Birkett, M., W. M. Linhart, J. Stoner, L. J. Phillips, K. Durose, J. Alaria, J. D. Major, R. Kudrawiec, and T. D. Veal (2018). Band gap temperature-dependence of close-space sublimation grown Sb_2Se_3 by photo-reflectance. *APL Materials 6*(8), 084901.

Blondeel, A., P. Persoone, and W. De Bosscher (2009). Rotatable magnetron sputter technology for large area glass and web coating. *Vakuum in Forschung und Praxis 21*(3), 6–13.

Bobzin, K., N. Bagcivan, P. Immich, S. Bolz, J. Alami, and R. Cremer (2009). Advantages of nanocomposite coatings deposited by high power pulse magnetron sputtering technology. *Journal of Materials Processing Technology 209*(1), 165–170.

Bogaerts, A., I. Kolev, and G. Buyle (2008). Modeling of the magnetron discharge. In D. Depla and S. Mahieu (Eds.), *Reactive Sputter Deposition*, Chapter 3, pp. 61–130. Berlin Heidelberg: Springer Verlag.

Bogaerts, A., K. A. Temelkov, N. K. Vuchkov, and R. Gijbels (2007). Calculation of rate constants for asymmetric charge transfer, and their effect on relative sensitivity factors in glow discharge mass spectrometry. *Spectrochimica Acta B 62*(4), 325–336.

Bohlmark, J., J. T. Gudmundsson, J. Alami, M. Lattemann, and U. Helmersson (2005). Spatial electron density distribution in a high-power pulsed magnetron discharge. *IEEE Transactions on Plasma Science 33*(2), 346–347.

Bohlmark, J., M. Lattemann, J. T. Gudmundsson, A. P. Ehiasarian, Y. A. Gonzalvo, N. Brenning, and U. Helmersson (2006). The ion energy distributions and ion flux composition from a high power impulse magnetron sputtering discharge. *Thin Solid Films 515*(5), 1522–1526.

Bohm, D., E. H. S. Burhop, and H. S. W. Massey (1949). The use of probes for plasma exploration in strong magnetic fields. In A. Guthrie and R. K. Wakerling (Eds.), *The characteristics of electrical discharges in magnetic fields*, Number I, volume 5 in National

nuclear energy series – Manhattan project technical section, Chapter 2, pp. 13–76. New York: McGraw-Hill.

Bradley, J., H. Bäcker, P. J. Kelly, and R. D. Arnell (2001). Time-resolved Langmuir probe measurements at the substrate position in a pulsed mid-frequency DC magnetron plasma. *Surface and Coatings Technology 135*(2-3), 221–228.

Bradley, J. W., A. Mishra, and P. J. Kelly (2015). The effect of changing the magnetic field strength on HiPIMS deposition rates. *Journal of Physics D: Applied Physics 48*(21), 215202.

Bradley, J. W., S. Thompson, and Y. A. Gonzalvo (2001). Measurement of the plasma potential in a magnetron discharge and the prediction of the electron drift speeds. *Plasma Sources Science and Technology 10*(3), 490–501.

Braun, W. and J. Mannhart (2019). Film deposition by thermal laser evaporation. *AIP Advances 9*(8), 085310.

Brenning, N., I. Axnäs, M. A. Raadu, D. Lundin, and U. Helmerson (2008). A bulk plasma model for dc and HiPIMS magnetrons. *Plasma Sources Science and Technology 17*(4), 045009.

Brenning, N., A. Butler, H. Hajihoseini, M. Rudolph, M. A. Raadu, J. T. Gudmundsson, T. Minea, and D. Lundin (2020). Optimization of HiPIMS discharges: The selection of pulse power, pulse length, gas pressure, and magnetic field strength. *Journal of Vacuum Science and Technology A 38*(3), 033008.

Brenning, N., J. T. Gudmundsson, D. Lundin, T. Minea, M. A. Raadu, and U. Helmersson (2016). The role of Ohmic heating in dc magnetron sputtering. *Plasma Sources Science and Technology 25*(6), 065024.

Brenning, N., J. T. Gudmundsson, M. A. Raadu, T. J. Petty, T. Minea, and D. Lundin (2017). A unified treatment of self-sputtering, process gas recycling, and runaway for high power impulse sputtering magnetrons. *Plasma Sources Science and Technology 26*(12), 125003.

Brenning, N., H. Hajihoseini, M. Rudolph, M. A. Raadu, J. T. Gudmundsson, T. M. Minea, and D. Lundin (2021). HiPIMS optimization by using mixed high-power and low-power pulsing. *Plasma Sources Science and Technology 30*(1), 015015.

Brenning, N., D. Lundin, T. Minea, C. Costin, and C. Vitelaru (2013). Spokes and charged particle transport in HiPIMS magnetrons. *Journal of Physics D: Applied Physics 46*(8), 084005.

Brenning, N., D. Lundin, M. A. Raadu, C. Huo, C. Vitelaru, G. D. Stancu, T. Minea, and U. Helmersson (2012). Understanding deposition rate loss in high power impulse magnetron sputtering: I. Ionization-driven electric fields. *Plasma Sources Science and Technology 21*(2), 025005.

Brenning, N., R. L. Merlino, D. Lundin, M. A. Raadu, and U. Helmersson (2009). Faster-

than-Bohm cross-B electron transport in strongly pulsed plasmas. *Physical Review Letters 103*(22), 225003.

Britun, N., M. Palmucci, S. Konstantinidis, and R. Snyders (2015). Particle visualization in high-power impulse magnetron sputtering. I. 2D density mapping. *Journal of Applied Physics 117*(16), 163302.

Bultinck, E. and A. Bogaerts (2009). Particle-in-cell/Monte Carlo collisions treatment of an Ar/O_2 magnetron discharge used for the reactive sputter deposition of TiO_x films. *New Journal of Physics 11*(10), 103010.

Bundesmann, C. and H. Neumann (2018). The systematics of ion beam sputtering for deposition of thin films with tailored properties. *Journal of Applied Physics 124*(23), 231102.

Butler, A., N. Brenning, M. A. Raadu, J. T. Gudmundsson, T. Minea, and D. Lundin (2018). On three different ways to quantify the degree of ionization in sputtering magnetrons. *Plasma Sources Science and Technology 27*(10), 105005.

Buyle, G., W. De Bosscher, D. Depla, K. Eufinger, J. Haemers, and R. De Gryse (2003). Recapture of secondary electrons by the target in a DC planar magnetron discharge. *Vacuum 70*(1), 29–35.

Čada, M., J. T. Gudmundsson, and D. Lundin (2020). Electron dynamics in high power impulse magnetron sputtering discharges. In D. Lundin, T. Minea, and J. T. Gudmundsson (Eds.), *High Power Impulse Magnetron Sputtering: Fundamentals, Technologies, Challenges and Applications*, pp. 81–110. Amsterdam, The Netherlands: Elsevier.

Cai, X.-M., X.-Q. Su, F. Ye, H. Wang, X.-Q. Tian, D.-P. Zhang, P. Fan, J.-T. Luo, Z.-H. Zheng, G.-X. Liang, and V. A. L. Roy (2015). The n-type conduction of indium-doped Cu_2O thin films fabricated by direct current magnetron co-sputtering. *Applied Physics Letters 107*(8), 083901.

Čapek, J. and S. Kadlec (2017). Return of target material ions leads to a reduced hysteresis in reactive high power impulse magnetron sputtering: Experiment. *Journal of Applied Physics 121*(17), 171911.

Cardoso, F., F. Ferreira, A. Cavaleiro, and A. Ramalho (2021). Performance of diamond-like carbon coatings (produced by the innovative Ne-HiPIMS technology) under different lubrication regimes. *Wear 477*, 203775.

Casiraghi, C., J. Robertson, and A. C. Ferrari (2007). Diamond-like carbon for data and beer storage. *Materials Today 10*(1-2), 44–53.

Changyom, P., K. Leksakul, D. Boonyawan, P. Premphet, and N. Vichiansan (2023). Comparison of properties of multilayer film sputtered on glass and polypropylene substrates with angular DC magnetron co-sputtering system. *Heliyon 9*(11), e22247.

Chapin, J. S. (1974). The planar magnetron. *Research/Development 25*(1), 37 – 40.

Chapman, B. (1980). *Glow Discharge Processes: Sputtering and Plasma Etching*. New York, New York: John Wiley & Sons.

Chen, F. F. and J. P. Chang (2003). *Lecture Notes on Principles of Plasma Processing*. New York, New York: Kluwer Academic Publishers.

Chen, R. T., B. W. Muir, L. Thomsen, A. Tadich, B. C. C. Cowie, G. K. Such, A. Postma, K. M. McLean, and F. Caruso (2011). New insights into the substrate–plasma polymer interface. *The Journal of Physical Chemistry B 115*(20), 6495–6502.

Christie, D. J. (2005). Target material pathways model for high power pulsed magnetron sputtering. *Journal of Vacuum Science and Technology A 23*(2), 330–335.

Christou, C. and Z. H. Barber (2000). Ionization of sputtered material in a planar magnetron discharge. *Journal of Vacuum Science and Technology A 18*(6), 2897–2907.

Constantin, D. G., M. Apreutesei, R. Arvinte, A. Marin, O. C. Andrei, and D. Munteanu (2011). Magnetron sputtering technique used for coating deposition. *Recent 12*(1), 29–33.

Cuomo, J. J., S. M. Rossnagel, and H. R. Kaufman (Eds.) (1989). *Handbook of Ion Beam Processing Technology - Principles, Deposition, Film Modification and Synthesis*. Westwood, New Jersey: Noyes Publications.

de Arruda, A. C. S., S. F. Durrant, R. D. Mansano, N. Ordonez, and R. Ruas (2024). Ag behavior on TiN thin films for decorative coatings. *Coatings 14*(3), 322.

DeKoven, B. M., P. R. Ward, R. E. Weiss, D. J. Christie, R. A. Scholl, W. D. Sproul, F. Tomasel, and A. Anders (2003). Carbon thin film deposition using high power pulsed magnetron sputtering. In *Society of Vacuum Coaters 46th Annual Technical Conference Proceedings, May 3 – 8, 2003, San Francisco, California*, Albuquerque, New Mexico, pp. 158–165. Society of Vacuum Coaters.

Dembowski, J., H. Oechsner, Y. Yamamura, and M. Urbassek (1986). Energy distributions of neutral atoms sputtered from Cu, V and Nb under different bombardment and ejection angles. *Nuclear Instruments and Methods in Physics Research Section B: Beam Interactions with Materials and Atoms 18*(1), 464–470.

Depla, D., X. Y. Li, S. Mahieu, and R. D. Gryse (2008). Determination of the effective electron emission yields of compound materials. *Journal of Physics D: Applied Physics 41*(20), 202003.

Depla, D., S. Mahieu, and R. De Gryse (2008). Depositing aluminium oxide: A case study of reactive magnetron sputtering. In D. Depla and S. Mahieu (Eds.), *Reactive Sputter Deposition*, Chapter 5, pp. 153–197. Berlin Heidelberg: Springer Verlag.

Depla, D., S. Mahieu, and R. De Gryse (2009). Magnetron sputter deposition: Linking discharge voltage with target properties. *Thin Solid Films 517*(9), 2825–2839.

Dixon, A. J., M. F. A. Harrison, and A. C. H. Smith (1973). Ionization of metastable rare gas atoms by electron impact. In B. C. Cobić and M. V. Kurepa (Eds.), *8th International*

Conference on the Physics of Electronic and Atomic Collisions (VIII ICPEAC), Belgrade, Yugoslavia, pp. 405–406. Institute of Physics.

Donnelly, V. M. and A. Kornblit (2013). Plasma etching: Yesterday, today, and tomorrow. *Journal of Vacuum Science and Technology A 31*(5), 050825.

Donnet, C. and A. Erdemir (2008). New horizon in the tribology of diamondlike carbon films. *Surface Engineering 24*(6), 399–401.

Drüsedau, T. P. (2002). Gas heating and throw distance for the sputter deposition of aluminum and tungsten. *Journal of Vacuum Science and Technology A 20*(2), 459–466.

Dubois, T., S. Tsikata, and T. Minea (2022). Dynamic features of the electron drift and electron properties in a HiPIMS discharge. *Plasma Sources Science and Technology 31*(11), 115018.

Eckstein, W. (2007). Sputtering yields. In R. Behrisch and W. Eckstein (Eds.), *Sputtering by Particle Bombardment: Experiments and Computer Calculations from Threshold to MeV Energies*, Volume 110 of *Topics in Applied Physics*, Chapter 3, pp. 33–187. Berlin Heidelberg: Springer Verlag.

Ehiasarian, A., P. Hovsepian, L. Hultman, and U. Helmersson (2004). Comparison of microstructure and mechanical properties of chromium nitride-based coatings deposited by high power impulse magnetron sputtering and by the combined steered cathodic arc/unbalanced magnetron technique. *Thin Solid Films 457*(2), 270–277.

Ehiasarian, A., W.-D. Münz, L. Hultman, U. Helmersson, and I. Petrov (2003). High power pulsed magnetron sputtered CrN_x films. *Surface and Coatings Technology 163-164*, 267–272.

Ehiasarian, A. P., R. New, W.-D. Münz, L. Hultman, U. Helmersson, and V. Kouznetzov (2002). Influence of high power densities on the composition of pulsed magnetron plasmas. *Vacuum 65*(2), 147–154.

Ehiasarian, A. P., A. Vetushka, A. Hecimovic, and S. Konstantinidis (2008). Ion composition produced by high power impulse magnetron sputtering discharges near the substrate. *Journal of Applied Physics 104*(8), 083305.

Ehiasarian, A. P., J. G. Wen, and I. Petrov (2007). Interface microstructure engineering by high power impulse magnetron sputtering for the enhancement of adhesion. *Journal of Applied Physics 101*(5), 054301.

Eliasson, H., M. Rudolph, N. Brenning, H. Hajihoseini, M. Zanáška, M. J. Adriaans, M. A. Raadu, T. M. Minea, J. T. Gudmundsson, and D. Lundin (2021). Modeling of high power impulse magnetron sputtering discharges with graphite target. *Plasma Sources Science and Technology 30*(11), 115017.

Erdemir, A. and C. Donnet (2006). Tribology of diamond-like carbon films: recent progress and future prospects. *Journal of Physics D: Applied Physics 39*(18), R311–R327.

Este, G. and W. D. Westwood (1988). A quasi-direct-current sputtering technique for the deposition of dielectrics at enhanced rates. *Journal of Vacuum Science and Technology A 6*(3), 1845–1848.

Farahani, M., T. Kozák, A. D. Pajdarová, T. Tölg, and J. Čapek (2025). On unipolar and bipolar HiPIMS pulse configurations to enhance energy flux to insulating surfaces. *Plasma Sources Science and Technology 34*(3), 03LT02.

Ferreira, F., A. Cavaleiro, and J. Oliveira (2021). Tribological performance of DLC coatings deposited by DOMS in mixed Ar-Ne discharges. *Materials Letters 285*, 129056.

Ferreira, F., R. Serra, J. C. Oliveira, and A. Cavaleiro (2014). Effect of peak target power on the properties of Cr thin films sputtered by HiPIMS in deep oscillation magnetron sputtering (DOMS) mode. *Surface and Coatings Technology 258*, 249–256.

Fischer, J. (2025). *Understanding and Controlling Metal Ionisation in Non-Reactive and Reactive High-Power Impulse Magnetron Sputtering*. Ph. D. thesis, Linköping University, Linköping Sweden.

Fischer, J., M. Renner, J. T. Gudmundsson, M. Rudolph, H. Hajihoseini, N. Brenning, and D. Lundin (2023). Insights into the copper HiPIMS discharge: Deposition rate and ionised flux fraction. *Plasma Sources Science and Technology 32*(12), 125006.

Fruth, H. F. (1932). Cathode sputtering, A commercial application. *Physics 2*(4), 280–288.

García, J. A., P. J. Rivero, E. Barba, I. Fernández, J. A. Santiago, J. F. Palacio, G. G. Fuente, and R. J. Rodríguez (2020). A comparative study in the tribological behavior of DLC coatings deposited by HiPIMS technology with positive pulses. *Metals 10*(2), 174.

García González, L., J. H. Torres, M. G. G. Romo, L. Z. Peredo, A. M. C. Arias, E. L. Sarabia, and F. J. E. Beltrán (2013). Ti/TiSiNO multilayers fabricated by co-sputtering. *Journal of Materials Engineering and Performance 22*(8), 2377–2381.

Gill, W. D. and E. Kay (1965). Efficient low pressure sputtering in a large inverted magnetron suitable for film synthesis. *Review of Scientific Instruments 36*(3), 277–282.

Glang, R. (1970). Vacuum evaporation. In L. I. Maissel and R. Glang (Eds.), *Handbook of Thin Film Technology*, Chapter 1, pp. 1–3 – 1–30. New York, New York: McGraw-Hill Book Company.

Gnaser, H. (2007). Energy and angular distributions of sputtered species. In R. Behrisch and W. Eckstein (Eds.), *Sputtering by Particle Bombardment: Experiments and Computer Calculations from Threshold to MeV Energies*, Volume 110 of *Topics in Applied Physics*, Chapter 5, pp. 231–328. Berlin Heidelberg: Springer Verlag.

Goranchev, B., V. Orlinov, and V. Popova (1976). D.C. cathode sputtering: influence of the oxygen content in the gas flow on the discharge current. *Thin Solid Films 33*(21), 173–183.

Graper, E. B. (1970). Charged particle flux generated by an electron-beam deposition source. *Journal of Vacuum Science and Technology 7*(1), 282–285.

Graves, D. B., C. B. Labelle, M. J. Kushner, E. S. Aydil, V. M. Donnelly, J. P. Chang, P. Mayer, L. Overzet, S. Shannon, S. Rauf, and D. N. Ruzic (2024). Science challenges and research opportunities for plasma applications in microelectronics. *Journal of Vacuum Science and Technology B 42*(4), 042202.

Greczynski, G., I. Zhirkov, I. Petrov, J. E. Greene, and J. Rosen (2017). Gas rarefaction effects during high power pulsed magnetron sputtering of groups IVb and VIb transition metals in Ar. *Journal of Vacuum Science and Technology A 35*(6), 060601.

Grove, W. R. (1852). On the electro-chemical polarity of gases. *Philosophical Magazine, Series 4 4*(28), 498–514.

Gudmundsson, J. T. (2008). Ionization mechanism in the high power impulse magnetron sputtering (HiPIMS) discharge. *Journal of Physics: Conference Series 100*, 082013.

Gudmundsson, J. T. (2010). The high power impulse magnetron sputtering discharge as an ionized physical vapor deposition tool. *Vacuum 84*(12), 1360–1364.

Gudmundsson, J. T. (2016). On reactive high power impulse magnetron sputtering. *Plasma Physics and Controlled Fusion 58*(1), 014002.

Gudmundsson, J. T. (2020). Physics and technology of magnetron sputtering discharges. *Plasma Sources Science and Technology 29*(11), 113001.

Gudmundsson, J. T., J. Alami, and U. Helmersson (2002). Spatial and temporal behavior of the plasma parameters in a pulsed magnetron discharge. *Surface and Coatings Technology 161*(2-3), 249–256.

Gudmundsson, J. T., A. Anders, and A. von Keudell (2022). Foundations of physical vapor deposition with plasma assistance. *Plasma Sources Science and Technology 31*(8), 083001.

Gudmundsson, J. T., N. Brenning, D. Lundin, and U. Helmersson (2012). The high power impulse magnetron sputtering discharge. *Journal of Vacuum Science and Technology A 30*(3), 030801.

Gudmundsson, J. T., J. Fisher, B. P. Hinriksson, M. Rudolph, and D. Lundin (2022). Ionization region model of a high power impulse magnetron sputtering discharge of copper. *Surface and Coatings Technology 442*, 128189.

Gudmundsson, J. T. and D. Lundin (2020). Introduction to magnetron sputtering. In D. Lundin, T. Minea, and J. T. Gudmundsson (Eds.), *High Power Impulse Mangetron Sputtering: Fundamentals, Technologies, Challenges and Applications*, Chapter 1, pp. 1–48. Amsterdam, The Netherlands: Elsevier.

Gudmundsson, J. T., D. Lundin, N. Brenning, M. A. Raadu, C. Huo, and T. M. Minea (2016). An ionization region model of the reactive Ar/O_2 high power impulse magnetron sputtering discharge. *Plasma Sources Science and Technology 25*(6), 065004.

Gudmundsson, J. T., P. Sigurjonsson, P. Larsson, D. Lundin, and U. Helmersson (2009). On

the electron energy in the high power impulse magnetron sputtering discharge. *Journal of Applied Physics 105*(12), 123302.

Hagstrum, H. D. (1954). Auger ejection of electrons from tungsten by noble gas ions. *Physical Review 96*(2), 325–335.

Hajihoseini, H. (2020). *High Power Impulse Magnetron Sputtering(HiPIMS): The effect of stationary magnetic fieldon the deposition rate and ionized flux fraction*. Ph. D. thesis, University of Iceland.

Hajihoseini, H., N. Brenning, M. Rudolph, M. A. Raadu, D. Lundin, J. Fischer, T. M. Minea, and J. T. Gudmundsson (2022). Target ion and neutral spread in high power impulse magnetron sputtering. *Journal of Vacuum Science and Technology A 41*(1), 013002.

Hajihoseini, H., M. Čada, Z. Hubička, S. Ünaldi, M. A. Raadu, N. Brenning, J. T. Gudmundsson, and D. Lundin (2019). The effect of magnetic field strength and geometry on the deposition rate and ionized flux fraction in the HiPIMS discharge. *Plasma 2*(2), 201–221.

Hajihoseini, H. and J. T. Gudmundsson (2017). Vanadium and vanadium nitride thin films grown by high power impulse magnetron sputtering. *Journal of Physics D: Applied Physics 50*(50), 505302.

Hála, M., J. Čapek, O. Zabeida, J. E. Klemberg-Sapieha, and L. Martinu (2012). Pulse management in high power pulsed magnetron sputtering of niobium. *Surface and Coatings Technology 206*(19-20), 4186–4193.

Hala, M., N. Viau, O. Zabeida, J. E. Klemberg-Sapieha, and L. Martinu (2010). Dynamics of reactive high-power impulse magnetron sputtering discharge studied by time- and space-resolved optical emission spectroscopy and fast imaging. *Journal of Applied Physics 107*(4), 043305.

Hammadi, O. A. and N. E. Naji (2018). Characterization of polycrystalline nickel cobaltite nanostructures prepared by DC plasma magnetron co-sputtering for gas sensing applications. *Photonic Sensors 8*(1), 43–47.

Handoo, A. K. and P. K. Ray (1992). Sputtering yield of chromium by argon and xenon ions with energies from 50 to 500 eV. *Applied Physics A 54*(1), 92–94.

Hannesdottir, H. and J. T. Gudmundsson (2016). The role of the metastable $O_2(b^1\Sigma_g^+)$ and energy-dependent secondary electron emission yields in capacitively coupled oxygen discharges. *Plasma Sources Science and Technology 25*(5), 055002.

Harper, J. M. E. (1978). Ion beam deposition. In J. L. Vossen and J. J. Cuomo (Eds.), *Thin Film Processes*, Chapter II-5, pp. 175–206. Academic Press.

Hasselkamp, D. (1992). Kinetic electron emission from solid surfaces under ion bombardment. In D. Hasselkamp, H. Rothard, K.-O. Groeneveld, J. Kemmler, P. Varga, and H. Winter (Eds.), *Particle induced electron emission II*, Volume 123 of *Springer Tracts in Modern Physics*, pp. 1–95. Berlin - Heidelberg: Springer Verlag.

Hauert, R., K.Thorwarth, and G. Thorwarth (2013). An overview on diamond-like carbon coatings in medical applications. *Surface and Coatings Technology 233*, 119–130.

Hecimovic, A., K. Burcalova, and A. P. Ehiasarian (2008). Origins of ion energy distribution function (IEDF) in high power impulse magnetron sputtering (HIPIMS) plasma discharge. *Journal of Physics D: Applied Physics 41*(9), 095203.

Hecimovic, A. and A. P. Ehiasarian (2011). Temporal evolution of the ion fluxes for various elements in HIPIMS plasma discharge. *IEEE Transactions on Plasma Science 39*(4), 1154–1164.

Hecimovic, A. and A. von Keudell (2018). Spokes in high power impulse magnetron sputtering plasmas. *Journal of Physics D: Applied Physics 51*(45), 453001.

Held, J., P. A. Maaß, V. Schulz-von der Gathen, and A. von Keudell (2020). Electron density, temperature and the potential structure of spokes in HiPIMS. *Plasma Sources Science and Technology 29*(2), 025006.

Helmersson, U., M. Lattemann, J. Bohlmark, A. P. Ehiasarian, and J. T. Gudmundsson (2006). Ionized physical vapor deposition (IPVD): A review of technology and applications. *Thin Solid Films 513*(1-2), 1–24.

Hofer, W. O. (1991). Angular, energy, and mass distribution of sputtered particles. In R. Behrisch and K. Wittmaack (Eds.), *Sputtering by Particle Bombardment III: Characteristics of Sputtered Particles, Technical Applications*, Volume 64 of *Topics in Applied Physics*, Chapter 2, pp. 15–90. Berlin Heidelberg: Springer Verlag.

Hoffman, D. W. (1985). A sputtering wind. *Journal of Vacuum Science and Technology A 3*(3), 561–566.

Hopwood, J. (1998). Ionized physical vapor deposition of integrated circuit interconnects. *Physics of Plasmas 5*(5), 1624–1631.

Hopwood, J. A. (2000a). Plasma physics. In J. A. Hopwood (Ed.), *Ionized Physical Vapor Deposition*, Volume 27 of *Thin Films*, pp. 181–207. San Diego, California: Academic Press.

Hopwood, J. A. (2000b). The role of ionized physical vapor deposition in integrated circuit fabrication. In J. A. Hopwood (Ed.), *Ionized Physical Vapor Deposition*, Volume 27 of *Thin Films*, pp. 1–7. San Diego: Academic Press.

Hosokawa, N., T. Tsukada, and H. Kitahara (1980). Effect of discharge current and sustained self-sputtering. In *Proceedings of the 8th International Vacuum Congress*, September 22-26, Cannes, France, pp. 11–14.

Hubička, Z., J. T. Gudmundsson, P. Larsson, and D. Lundin (2020). Hardware and power management for high power impulse magnetron sputtering. In D. Lundin, T. Minea, and J. T. Gudmundsson (Eds.), *High Power Impulse Magnetron Sputtering: Fundamentals, Tech-*

nologies, Challenges and Applications, Chapter 2, pp. 49–80. Amsterdam, The Netherlands: Elsevier.

Huo, C. (2013). *Modeling and Experimental Studies of High Power Impulse Magnetron Sputtering Discharges*. Ph. D. thesis, KTH Royal Institute of Technology, Stockholm.

Huo, C., D. Lundin, J. T. Gudmundsson, M. A. Raadu, J. W. Bradley, and N. Brenning (2017). Particle-balance models for pulsed sputtering magnetrons. *Journal of Physics D: Applied Physics 50*(35), 354003.

Huo, C., D. Lundin, M. A. Raadu, A. Anders, J. T. Gudmundsson, and N. Brenning (2013). On sheath energization and ohmic heating in sputtering magnetrons. *Plasma Sources Science and Technology 22*(4), 045005.

Huo, C., D. Lundin, M. A. Raadu, A. Anders, J. T. Gudmundsson, and N. Brenning (2014). On the road to self-sputtering in high power impulse magnetron sputtering: particle balance and discharge characteristics. *Plasma Sources Science and Technology 23*(2), 025017.

Huo, C., M. A. Raadu, D. Lundin, J. T. Gudmundsson, A. Anders, and N. Brenning (2012). Gas rarefaction and the time evolution of long high-power impulse magnetron sputtering pulses. *Plasma Sources Science and Technology 21*(4), 045004.

Hurlbatt, A., A. R. Gibson, S. Schröter, J. Bredin, A. P. S. Foote, P. Grondein, D. O'Connell, and T. Gans (2017). Concepts, capabilities, and limitations of global models: A review. *Plasma Processes and Polymers 14*(1–2), 1600138.

Iseki, T. (2009). Target utilization of planar magnetron sputtering using a rotating tilted unbalanced yoke magnet. *Vacuum 84*(2), 339–347.

Iseki, T. (2010). Completely flat erosion magnetron sputtering using a rotating asymmetrical yoke magnet. *Vacuum 84*(12), 1372–1376.

Joung, Y.-H., H. I. Kang, J. H. Kim, H.-S. Lee, J. Lee, and W. S. Choi (2012). SiC formation for a solar cell passivation layer using an RF magnetron co-sputtering system. *Nanoscale Research Letters 7*(1), 22.

Kadlec, S. (2007). Simulation of neutral particle flow during high power magnetron impulse. *Plasma Processes and Polymers 4*(S1), S419–S423.

Kadlec, S., C. Quaeyhaegens, G. Knuyt, and L. M. Stals (1997). Energy distribution of ions in an unbalanced magnetron plasma measured with energy-resolved mass spectrometry. *Surface and Coatings Technology 89*(1–2), 177–184.

Kadlec, S. and J. Čapek (2017). Return of target material ions leads to a reduced hysteresis in reactive high power impulse magnetron sputtering: Model. *Journal of Applied Physics 121*(17), 171910.

Kanitz, A., A. Hecimovic, M. Böke, and J. Winter (2016). Two dimensional spatial argon metastable dynamics in HiPIMS discharges. *Journal of Physics D: Applied Physics 49*(12), 125203.

Karolewski, M. A. (2005). Kalypso: a software package for molecular dynamics simulation of atomic collisions at surfaces. *Nuclear Instruments and Methods in Physics Research Section B: Beam Interactions with Materials and Atoms 230*(1–4), 402–405.

Kay, E. (1963). Magnetic field effects on an abnormal truncated glow discharge and their relation to sputtered thin-film growth. *Journal of Applied Physics 34*(4), 760–768.

Kelly, P. (2011). Continual development keeps reactive sputter deposition at the forefront of surface engineering processes. *Materials Technology 26*(1), 1–2.

Keraudy, J., R. P. B. Viloan, M. A. Raadu, N. Brenning, D. Lundin, and U. Helmersson (2019). Bipolar HiPIMS for tailoring ion energies in thin film deposition. *Surface and Coatings Technology 359*, 433–437.

Kersch, A., W. Morokoff, and C. Werner (1994). Selfconsistent simulation of sputter deposition with the Monte Carlo method. *Journal of Applied Physics 75*(4), 2278–2285.

Kim, J.-H., H.-J. Kil, S. Lee, J. Park, and J.-W. Park (2022). Interfacial delamination at multilayer thin films in semiconductor devices. *ACS Omega 7*(29), 25219–25228.

Kobayashi, T. (2001). Computer simulation of gas rarefaction effects and film deposition characteristics in a magnetron sputtering apparatus. *Applied Surface Science 169–170*, 405–409.

Kolev, I. and A. Bogaerts (2008). Calculation of gas heating in a dc sputter magnetron. *Journal of Applied Physics 104*(9), 093301.

Konstantinidis, S., J. P. Dauchot, M. Ganciu, and M. Hecq (2006). Influence of pulse duration on the plasma characteristics in high-power pulsed magnetron discharges. *Journal of Applied Physics 99*(1), 013307.

Kouznetsov, V., K. Macák, J. M. Schneider, U. Helmersson, and I. Petrov (1999). A novel pulsed magnetron sputter technique utilizing very high target power densities. *Surface and Coatings Technology 122*(2-3), 290–293.

Kozák, T. and J. Lazar (2018). Gas rarefaction in high power impulse magnetron sputtering: comparison of a particle simulation and volume-averaged models. *Plasma Sources Science and Technology 27*(11), 115012.

Kramida, A., Yu. Ralchenko, J. Reader, and and NIST ASD Team (2024). NIST Atomic Spectra Database (ver. 5.12), [Online]. Available: `https://physics.nist.gov/asd` [2025, July 31]. National Institute of Standards and Technology, Gaithersburg, MD.

Krüger, D., K. Köhn, S. Gallian, and R. P. Brinkmann (2018). Reconstruction of the static magnetic field of a magnetron. *Physics of Plasmas 25*(6), 061207.

Kubart, T., M. Čada, D. Lundin, and Z. Hubička (2014). Investigation of ionized metal flux fraction in HiPIMS discharges with Ti and Ni targets. *Surface and Coatings Technology 238*, 152–157.

Laegreid, N. and G. K. Wehner (1961). Sputtering yields of metals for Ar^+ and Ne^+ ions with energies from 50 to 600 eV. *Journal of Applied Physics 32*(3), 365–369.

Lennon, M. A., K. Bell, H. B. Gilbody, J. G. Hughes, A. E. Kingston, M. Murray, and F. J. Smith (1988). Recommended data on the electron impact ionization of atoms and ions: Fluorine to nickel. *Journal of Physical and Chemical Reference Data 17*(3), 1285–1363.

Lettington, A. H. (1998). Applications of diamond-like carbon thin films. *Carbon 36*(5–6), 555–560.

Lieberman, M. A. and R. A. Gottscho (1994). Design of high-density plasma sources for materials processing. In M. Francombe and J. Vossen (Eds.), *Plasma Sources for Thin Film Deposition and Etching*, Volume 18 of *Physics of Thin Films*, pp. 1 – 119. New York: Academic Press.

Lieberman, M. A. and A. J. Lichtenberg (2005). *Principles of Plasma Discharges and Materials Processing* (2 ed.). Hoboken, New Jersey: John Wiley & Sons.

Liebig, B., N. S. J. Braithwaite, P. J. Kelly, R. Chistyakov, B. Abraham, and J. Bradley (2011). Time-resolved plasma characterisation of modulated pulsed power magnetron sputtering of chromium. *Surface and Coatings Technology 205*, S312–S316.

Lin, J., W. D.Sproul, R. Wei, and R. Chistyakov (2014). Diamond like carbon films deposited by HiPIMS using oscillatory voltage pulses. *Surface and Coatings Technology 258*, 1212–1222.

Lockwood Estrin, F., S. K. Karkari, and J. W. Bradley (2017). Triple probe interrogation of spokes in a HiPIMS discharge. *Journal of Physics D: Applied Physics 50*(29), 295201.

Lundin, D., M. Čada, and Z. Hubička (2015). Ionization of sputtered Ti, Al, and C coupled with plasma characterization in HiPIMS. *Plasma Sources Science and Technology 24*(3), 035018.

Lundin, D., A. Hecimovic, T. Minea, A. Anders, N. Brenning, and J. T. Gudmundsson (2020). Physics of high power impulse magnetron sputtering discharges. In D. Lundin, T. Minea, and J. T. Gudmundsson (Eds.), *High Power Impulse Mangetron Sputtering: Fundamentals, Technologies, Challenges and Applications*, Chapter 7, pp. 265–332. Amsterdam, The Netherlands: Elsevier.

Lundin, D., U. Helmersson, S. Kirkpatrick, S. Rohde, and N. Brenning (2008). Anomalous electron transport in high power impulse magnetron sputtering. *Plasma Sources Science and Technology 17*(2), 025007.

Lundin, D., S. A. Sahab, N. Brenning, C. Huo, and U. Helmersson (2011). Internal current measurements in high power impulse magnetron sputtering. *Plasma Sources Science and Technology 20*(4), 045003.

Lundin, D. and K. Sarakinos (2012). An introduction to thin film processing using high power impulse magnetron sputtering. *Journal of Materials Research 27*(5), 780–792.

Lundin, D., C. Vitelaru, L. de Poucques, N. Brenning, and T. Minea (2013). Ti-Ar scattering cross sections by direct comparison of Monte Carlo simulations and laser-induced fluorescence spectroscopy in magnetron discharges. *Journal of Physics D: Applied Physics 46*(17), 175201.

Machura, P. D., A. Hecimovic, S. Gallian, J. Winter, and T. de los Arcos (2014). Simultaneous characterization of static and induced magnetic fields in high power impulse magnetron sputtering discharges. *Plasma Sources Science and Technology 23*(6), 065043.

Magnus, F., T. K. Tryggvason, S. Olafsson, and J. T. Gudmundsson (2012). Current-voltage-time characteristics of the reactive Ar/O_2 high power impulse magnetron sputtering discharge. *Journal of Vacuum Science and Technology A 30*(5), 050601.

Mahne, N., M. Čekada, and M. Panjan (2022). Total and differential sputtering yields explored by SRIM simulations. *Coatings 12*(10), 1541.

Maissel, L. I. (1970). Application of sputtering to the deposition of films. In L. I. Maissel and R. Glang (Eds.), *Handbook of Thin Film Technology*, Chapter 4, pp. 4–1 – 4–44. New York, New York: McGraw-Hill Book Company.

Malherbe, J. B., S. Hofmann, and J. M. Sanz (1986). Preferential sputtering of oxides: A comparison of model predictions with experimental data. *Applied Surface Science 27*(3), 355–365.

Man, K. F., A. C. H. Smith, and M. F. A. Harrison (1987). A measurement of the cross section for ionisation of Cr^+ by electron impact. *Journal of Physics B: Atomic, Molecular and Optical Physics 20*(11), 2571–2578.

Manova, D., J. W. Gerlach, and S. Mändl (2010). Thin film deposition using energetic ions. *Advances in Surface Coatings 3*(8), 4109–4141.

Martines, E., R. Cavazzana, G. Serianni, M. Spolaore, L. Tramontin, M. Zuin, and V. Antoni (2001). Electrostatic fluctuations in a direct current magnetron sputtering plasma. *Physics of Plasmas 8*(6), 3042–3050.

Mason, S. J. (1953). Feedback theory - some properties of signal flow graphs. *Proceedings of the IRE 41*(9), 1144–1156.

Matsunami, N., Y. Yamamura, Y. Itikawa, N. Itoh, Y. Kazumata, S. Miyagawa, K. Morita, R. Shimizu, and H. Tawara (1983). Energy dependence of the yields of ion-induced sputtering of monatomic solids. Technical Report IPPJ-AM-32, Institute of Plasma Physics, Nagoya University.

Matsunami, N., Y. Yamamura, Y. Itikawa, N. Itoh, Y. Kazumata, S. Miyagawa, K. Morita, R. Shimizu, and H. Tawara (1984). Energy dependence of the ion-induced sputtering yields of monatomic solids. *Atomic Data and Nuclear Data Tables 31*(1), 1 – 80.

Mattox, D. (2001). History of vacuum coating - sputter deposition: Early efforts. *Plating and Surface Finishing 88*, 60–63.

Mattox, D. M. (1998). *Handbook of Physical Vapor Deposition (PVD) Processing: Film Formation, Adhesion, Surface Preparation and Contamination Control*. Westwood, New Jersey: Noyes Publications.

Meassick, S., C. Chan, and R. Allen (1992). Thin film deposition techniques utilizing the anodic vacuum arc. *Surface and Coatings Technology 54-55*, 343–348.

Merlo, A. and G. Léonard (2021). Magnetron sputtering vs. electrodeposition for hard chrome coatings: A comparison of environmental and economic performances. *Materials 14*(14), 2823.

Minea, T., T. Kozák, C. Costin, J. T. Gudmundsson, and D. Lundin (2020). Modeling the high power impulse magnetron sputtering discharge. In D. Lundin, T. Minea, and J. T. Gudmundsson (Eds.), *High Power Impulse Mangetron Sputtering: Fundamentals, Technologies, Challenges and Applications*, Chapter 5, pp. 159–221. Amsterdam, The Netherlands: Elsevier.

Mishra, A., P. J. Kelly, and J. W. Bradley (2010). The evolution of the plasma potential in a HiPIMS discharge and its relationship to deposition rate. *Plasma Sources Science and Technology 19*(4), 045014.

Mishra, A., P. J. Kelly, and J. W. Bradley (2011). The 2D plasma potential distribution in a HiPIMS discharge. *Journal of Physics D: Applied Physics 44*(42), 425201.

Moisan, M., J. Barbeau, M.-C. Crevier, J. Pelletier, N. Philip, and B. Saoudi (2002). Plasma sterilization. methods and mechanisms. *Pure and Applied Chemistry 74*(3), 349–358.

Möller, W. and W. Eckstein (1984). TRIDYN - a TRIM simulation code including dynamic composition changes. *Nuclear Instruments and Methods in Physics Research Section B: Beam Interactions with Materials and Atoms 2*(1-3), 814–818.

Möller, W., W. Eckstein, and J. Biersack (1988). TRIDYN - binary collision simulation of atomic collisions and dynamic composition changes in solids. *Computer Physics Communications 51*(3), 355–368.

Munro, J. J. and J. Tennyson (2008). Global plasma simulations using dynamically generated chemical models. *Journal of Vacuum Science and Technology A 26*(4), 865–869.

Musson, J. and H. E. Elsayed-Ali (2024). Commissioning of a modulated pulse-power magnetron sputtering system for depositing niobium thin films. *Vacuum 229*, 113547.

Münz, W.-D., D. Schulze, and F. Hauzer (1992). A new method for hard coatings: ABS^{TM} (arc bond sputtering). *Surface and Coatings Technology 50*(2), 169–178.

Nakano, T., N. Hirukawa, S. Saeki, and S. Baba (2013). Effects of target voltage during pulse-off period in pulsed magnetron sputtering on afterglow plasma and deposited film structure. *Vacuum 87*, 109–113.

Naqi, M., N. Kwon, S. H. Jung, P. Pujar, H. W. Cho, Y. I. Cho, H. K. Cho, B. Lim, and S. Kim

(2021). High-performance non-volatile InGaZnO based flash memory device embedded with a monolayer Au nanoparticles. *Nanomaterials 11*(5), 1101.

National Research Council (1991). *Plasma Processing of Materials: Scientific Opportunities and Technological Challenges*. Washington, DC: The National Academies Press.

Nelson, A. N. (1976). Electron impact ionization cross sections of gold, chromium and iron. Technical Report AFML-TR-75-198, Massachusetts Institute of Technology, Cambridge, Massachusetts.

Nowicki, R. S. (1977). Properties of rf-sputtered Al_2O_3 films deposited by planar magnetron. *Journal of Vacuum Science and Technology 14*(1), 127–133.

Ogugua, S., H. Swart, and O. Ntwaeaborwa (2020). Latest development on pulsed laser deposited thinfilms for advanced luminescence applications. *Coatings 10*(11), 1078.

Oks, E. and A. Anders (2009). Evolution of the plasma composition of a high power impulse magnetron sputtering system studied with a time-of-flight spectrometer. *Journal of Applied Physics 105*(9), 093304.

Oliveira, J. C., A. Vahidi, F. Ferreira, R. Serra, and A. Cavaleiro (2024). Quantification of the sp^3 content in diamond-like carbon films: Effects of Ne plasma addition in deep oscillation magnetron sputtering. *Applied Surface Science 669*, 160565.

Pajdarová, A. D., J. Vlček, P. Kudláček, and J. Lukáš (2009). Electron energy distributions and plasma parameters in high-power pulsed dc magnetron sputtering discharges. *Plasma Sources Science and Technology 18*(2), 025008.

Palmero, A., H. Rudolph, and F. H. P. M. Habraken (2005). Gas heating in plasma-assisted sputter deposition. *Applied Physics Letters 87*(7), 071501.

Palmero, A., H. Rudolph, and F. H. P. M. Habraken (2006). Study of the gas rarefaction phenomenon in a magnetron sputtering system. *Thin Solid Films 515*(2), 631–635.

Palmucci, M., N. Britun, S. Konstantinidis, and R. Snyders (2013). Rarefaction windows in a high-power impulse magnetron sputtering plasma. *Journal of Applied Physics 114*(11), 113302.

Pancheshnyi, S., B. Eismann, G. J. M. Hagelaar, and L. C. Pitchford (2008). ZDPlasKin. *http://www.zdplaskin.laplace.univ-tlse.fr*.

Panjan, M., R. Franz, and A. Anders (2014). Asymmetric particle fluxes from drifting ionization zones in sputtering magnetrons. *Plasma Sources Science and Technology 23*(2), 025007.

Pauling, L. (1960). *The Nature of the Chemical Bond and the Structure of Molecules and Crystals* (3 ed.). Ithaca, New York: Cornell University Press.

Penning, F. M. (1936). Die glimmentladung bei niedrigem druck zwischen koaxialen zylindern in einem axialen magnetfeld. *Physica 3*(9), 873–894.

Penning, F. M. and J. H. A. Moubis (1940). Cathode sputtering in a magnetic field. *Proceedings Koninklijke Nederlandse Akademie van Wetenschappen 43*(1), 41–56.

Petrov, I., I. Ivanov, V. Orlinov, J. Kourtev, and J. Jelev (1990). Deposition of carbon films by bias magnetron sputtering in neon and argon. *Thin Solid Films 185*(2), 247–256.

Phelps, A. V. and Z. L. Petrović (1999). Cold-cathode discharges and breakdown in argon: surface and gas phase production of secondary electrons. *Plasma Sources Science and Technology 8*(3), R21–R44.

Phelps, A. V., L. C. Pitchford, C. Pédoussat, and Z. Donkó (1999). Use of secondary-electron yields determined from breakdown data in cathode-fall models for Ar. *Plasma Sources Science and Technology 8*(4), B1–B2.

Plücker, J. (1858). Ueber die Einwirkung des Magneten auf die elektrischen Entladungen in verdünnten Gasen. *Annalen der Physik und Chemie 103*(1), 88–106.

Pocius, A. V. (2012). *Adhesion And Adhesives Technology: An Introduction* (3 ed.). Munich, Germany: Carl Hanser Verlag.

Poolcharuansin, P. and J. W. Bradley (2010). Short and long-term plasma phenomena in a HiPIMS discharge. *Plasma Sources Science and Technology 19*(2), 025010.

Poolcharuansin, P., B. Liebig, and J. Bradley (2010). Plasma parameters in a pre-ionized HIPIMS discharge operating at low pressure. *IEEE Transactions on Plasma Science 38*(11), 3007–3015.

Raadu, M. A., I. Axnäs, J. T. Gudmundsson, C. Huo, and N. Brenning (2011). An ionization region model for high power impulse magnetron sputtering discharges. *Plasma Sources Science and Technology 20*(6), 065007.

Rauch, A. and A. Anders (2013). Estimating electron drift velocities in magnetron discharges. *Vacuum 89*, 53–56.

Reinhard, C., A. P. Ehiasarian, and P. E. Hovsepian (2007). CrN/NbN superlattice structured coatings with enhanced corrosion resistance achieved by high power impulse magnetron sputtering interface pre-treatment. *Thin Solid Films 515*(7–8), 3685–3692.

Robertson, J. (1994). Diamond-like carbon. *Pure and Applied Chemistry 66*(9), 1789–1796.

Robertson, J. (2002). Diamond-like amorphous carbon. *Materials Science and Engineering: R: Reports 37*(4-6), 129–281.

Rossnagel, S. M. (1988a). Gas density reduction effects in magnetrons. *Journal of Vacuum Science and Technology A 6*(1), 19–24.

Rossnagel, S. M. (1988b). Magnetron plasma diagnostics and processing implications. *Journal of Vacuum Science and Technology A 6*(3), 1821–1826.

Rossnagel, S. M. (1990). Magnetron plasma deposition processes. In S. M. Rossnagel, W. D. Westwood, and J. J. Cuomo (Eds.), *Handbook of Plasma Processing Technology:*

Fundamental, Etching, Deposition and Surface Interactions, Materials Science and Process Technology, Chapter 6, pp. 160–182. Park Ridge, New Jersey: Noyes Publications.

Rossnagel, S. M. (1999). Sputter deposition for semiconductor manufacturing. *IBM Journal of Research and Development 43*(1/2), 163–179.

Rossnagel, S. M. (2008). Physical vapor deposition. In R. Doering and Y. Nishi (Eds.), *Handbook of Semiconductor Manufacturing Technology*, Chapter 15, pp. 15–1–15–27. Boca Raton, Florida: CRC Press.

Rossnagel, S. M. and J. J. Cuomo (1988). Select ion beam deposition, film modification and synthesis. *MRS Bulletin 13*(12), 40–45.

Rossnagel, S. M. and J. Hopwood (1993). Magnetron sputter deposition with high levels of metal ionization. *Applied Physics Letters 63*(24), 3285–3287.

Rossnagel, S. M. and H. R. Kaufman (1987). Charge transport in magnetrons. *Journal of Vacuum Science and Technology A 5*(4), 2276–2279.

Rossnagel, S. M. and H. R. Kaufman (1988). Current-voltage relations in magnetrons. *Journal of Vacuum Science and Technology A 6*(2), 223–229.

Roth, J. R. (1995). *Industrial Plasma Engineering: Principles*, Volume 1. Bristol, United Kingdom: Institute of Physics Publishing.

Rudolph, M., P. Birtel, T. Arnold, A. Prager, S. Naumov, U. Helmstedt, A. Anders, and P. C. With (2023). Low-temperature atmospheric pressure plasma conversion of polydimethylsiloxane and polysilazane precursor layers to oxide thin films. *Plasma Processes and Polymers 20*(5), 2200229.

Rudolph, M., N. Brenning, H. Hajihoseini, M. A. Raadu, T. M. Minea, A. Anders, D. Lundin, and J. T. Gudmundsson (2022). Influence of the magnetic field on the discharge physics of a high power impulse magnetron sputtering discharge. *Journal of Physics D: Applied Physics 55*(1), 015202.

Rudolph, M., N. Brenning, M. A. Raadu, H. Hajihoseini, J. T. Gudmundsson, A. Anders, and D. Lundin (2020). Optimizing the deposition rate and ionized flux fraction by tuning the pulse length in high power impulse magnetron sputtering. *Plasma Sources Science and Technology 29*(5), 05LT01.

Rudolph, M., H. Hajihoseini, M. A. Raadu, J. T. Gudmundsson, N. Brenning, T. M. Minea, A. Anders, and D. Lundin (2021). On how to measure the probabilities of target atom ionization and target ion back-attraction in high-power impulse magnetron sputtering. *Journal of Applied Physics 129*(3), 033303.

Rudolph, M., D. Lundin, E. Foy, M. Debongnie, M.-C. Hugon, and T. Minea (2018). Influence of backscattered neutrals on the grain size of magnetron-sputtered TaN thin films. *Thin Solid Films 658*, 46–53.

Rudolph, M., A. Revel, D. Lundin, H. Hajihoseini, N. Brenning, M. A. Raadu, A. Anders,

T. M. Minea, and J. T. Gudmundsson (2021). On the electron energy distribution function in the high power impulse magnetron sputtering discharge. *Plasma Sources Science and Technology 30*(4), 045011.

Samuelsson, M., D. Lundin, K. Sarakinos, F. Björefors, B. Wälivaara, H. Ljungcrantz, and U. Helmersson (2012). Influence of ionization degree on film properties when using high power impulse magnetron sputtering. *Journal of Vacuum Science and Technology A 30*(3), 031507.

Sarakinos, K., J. Alami, and S. Konstantinidis (2010). High power pulsed magnetron sputtering: Scientific and engineering state of the art. *Surface and Coatings Technology 204*(11), 1661–1684.

Sarakinos, K., A. Braun, C. Zilkens, S. Mráz, J. M. Schneider, H. Zoubos, and P. Patsalas (2012). Exploring the potential of high power impulse magnetron sputtering for growth of diamond-like carbon films. *Surface and Coatings Technology 206*(10), 2706–2710.

Sarakinos, K. and L. Martinu (2020). Synthesis of thin films and coatings by high power impulse magnetron sputtering. In D. Lundin, T. Minea, and J. T. Gudmundsson (Eds.), *High Power Impulse Mangetron Sputtering: Fundamentals, Technologies, Challenges and Applications*, Chapter 8, pp. 333–374. Amsterdam, The Netherlands: Elsevier.

Sauerbrey, G. H. (1959). Verwendung von Schwingquarzen zur Wägung dünner Schichten und zur Mikrowägung. *Zeitschrift für Physik 155*(2), 206–222.

Schelfhout, R., K. Strijckmans, and D. Depla (2020). Sputter yield measurements to evaluate the target state during reactive magnetron sputtering. *Surface and Coatings Technology 399*, 126097.

Scherer, M., J. Schmitt, R. Latz, and M. Schanz (1992). Reactive alternating current magnetron sputtering of dielectric layers. *Journal of Vacuum Science and Technology A 10*(4), 1772–1776.

Schiller, S., K. Goedicke, J. Reschke, V. Kirchhoff, S. Schneider, and F. Milde (1993). Pulsed magnetron sputter technology. *Surface and Coatings Technology 61*(1–3), 331 – 337.

Schmid, M. (2006). A simple sputter yield calculator, IAP/TU Wien surface physics group. `https://www2.iap.tuwien.ac.at/www/surface/sputteryield`.

Schmidt, S., Z. Czigány, G. Greczynski, J. Jensen, and L. Hultman (2013). Influence of inert gases on the reactive high power pulsed magnetron sputtering process of carbon-nitride thin films. *Journal of Vacuum Science and Technology A 31*(1), 011503.

Seah, M. P. (1981). Pure element sputtering yields using 500–1000 eV argon ions. *Thin Solid Films 81*(3), 279–287.

Sellers, J. (1998). Asymmetric bipolar pulsed DC: the enabling technology for reactive PVD. *Surface and Coatings Technology 98*(1–3), 1245 – 1250.

Serikov, V. V., S. Kawamoto, and K. Nanbu (1999). Particle-in-cell plus direct simulation

Monte Carlo (PIC-DSMC) approach for self-consistent plasma-gas simulations. *IEEE Transactions on Plasma Science 27*(5), 1389–1398.

Shimizu, T., M. Zanáška, R. P. Villoan, N. Brenning, U. Helmersson, and D. Lundin (2021). Experimental verification of deposition rate increase, with maintained high ionized flux fraction, by shortening the HiPIMS pulse. *Plasma Sources Science and Technology 30*(4), 045006.

Sigmund, P. (1969). Theory of sputtering. I. Sputtering yield of amorphous and polycrystalline targets. *Physical Review 184*(2), 383–416.

Sigmund, P. and A. Schinner (2020). The bloch correction, key to heavy-ion stopping. *Journal of Applied Physics 128*(10), 100903.

Snyders, R., D. Hegemann, D. Thiry, O. Zabeida, J. Klemberg-Sapieha, and L. Martinu (2023). Foundations of plasma enhanced chemical vapor deposition of functional coatings. *Plasma Sources Science and Technology 32*(7), 074001.

Song, R.-X., D. Wang, Y. Yang, J. He, S. Li, H.-L. Yan, and L. Zuo (2025). A review of grain refinement and texture engineering in aluminum alloy magnetron sputtering targets. *Materials 18*(14), 3235.

Steenbeck, K., E. Steinbeiß, and K.-D. Ufert (1982). The problem of reactive sputtering and cosputtering of elemental targets. *Thin Solid Films 92*(4), 371–380.

Stepanova, M. and S. K. Dew (2001). Estimates of differential sputtering yields for deposition applications. *Journal of Vacuum Science and Technology A 19*(6), 2805–2816.

Stepanova, M. and S. K. Dew (2004). Anisotropic energies of sputtered atoms under oblique ion incidence. *Nuclear Instruments and Methods in Physics Research Section B: Beam Interactions with Materials and Atoms 215*(3–4), 357–365.

Strijckmans, K., R. Schelfhout, and D. Depla (2018). Hysteresis during the reactive magnetron sputtering process. *Journal of Applied Physics 124*(24), 241101.

Stuart, R. V. and G. K. Wehner (1960). Sputtering thresholds and displacement energies. *Physical Review Letters 4*(8), 409–410.

Stuart, R. V., G. K. Wehner, and G. S. Anderson (1969). Energy distribution of atoms sputtered from polycrystalline metals. *Journal of Applied Physics 40*(2), 803–812.

Sun, R., C. Lan, T. Zhang, X. Hu, T. Chen, Z. Zhang, X. Xu, Z. Xia, and S. Wang (2025). Fabrication of catalyst layers of proton exchange membrane fuel cell via magnetron sputtering method. *International Journal of Hydrogen Energy 161*, 150602.

Suni, T., K. Henttinen, I. Suni, and J. Mäkinen (2002). Effects of plasma activation on hydrophilic bonding of Si and SiO_2. *Journal of The Electrochemical Society 149*(6), G348–G351.

Suresh Babu, S., J. Fischer, K. Barynova, M. Rudolph, D. Lundin, and J. T. Gudmundsson

(2024). High power impulse magnetron sputtering of a zirconium target. *Journal of Vacuum Science and Technology A 42*(4), 043007.

Suresh Babu, S., M. Rudolph, D. Lundin, T. Shimizu, J. Fischer, M. A. Raadu, N. Brenning, and J. T. Gudmundsson (2022). Ionization region model of a high power impulse magnetron sputtering of tungsten. *Plasma Sources Science and Technology 31*(6), 065009.

Suresh Babu, S., M. Rudolph, P. J. Ryan, J. Fischer, D. Lundin, J. W. Bradley, , and J. T. Gudmundsson (2023). High power impulse magnetron sputtering of tungsten: A comparison of experimental and modelling results. *Plasma Sources Science and Technology 32*(3), 034003.

Takagi, K., A. Ikeda, T. Fujimura, and Y. Kuroki (2001). Inductively coupled plasma application to the resist ashing. *Thin Solid Films 386*(2), 160–164.

Tejero-del-Caz, A., D. Simoes, T. C. Dias, V. Guerra, M. L. da Silva, L. Marques, N. Pinhao, C. D. Pintassilgo, and L. L. Alves (2014). The LisbOn KInetics LoKI-B+C simulation tool. `https://nprime.tecnico.ulisboa.pt/loki/`.

Thanu, D. P., E. S. Srinadhu, M. Zhao, N. V. Dole, and M. Keswani (2019). Fundamentals and applications of plasma cleaning. In R. Kohli and K. L. Mittal (Eds.), *Developments in Surface Contamination and Cleaning: Applications of Cleaning Techniques*, Volume 11, Chapter 8, pp. 289–353. Amsterdam, Netherlands: Elsevier.

Thomae, R. W. (1998). Plasma-immersion ion implantation. *Nuclear Instruments and Methods in Physics Research Section B: Beam Interactions with Materials and Atoms 139*(1), 37–42.

Thompson, J. B. (1987). The velocity distribution of sputtered atoms. *Nuclear Instruments and Methods in Physics Research Section B: Beam Interactions with Materials and Atoms 18*(1–6), 411–429.

Thompson, M. W. (1968). The energy spectrum of ejected atoms during the high energy sputtering of gold. *Philosophical Magazine 18*(152), 377–414.

Thompson, M. W. (1981). Physical mechanisms of sputtering. *Physics Reports 69*(4), 335–371.

Thornton, J. A. (1978). Magnetron sputtering: basic physics and application to cylindrical magnetrons. *Journal of Vacuum Science and Technology 15*(2), 171–177.

Thornton, J. A. and A. S. Penfold (1978). Cylindrical magnetron sputtering. In J. L. Vossen and W. Kern (Eds.), *Thin Film Processes*, Volume 4, pp. 75–113. New York: Academic Press.

Tonks, L. (1967). The birth of "plasma". *American Journal of Physics 35*(9), 857–858.

Vahidi, A., D. Fonseca, J. Oliveira, A. Cavaleiro, A. Ramalho, and F. Ferreira (2021). Advanced tribological characterization of DLC coatings produced by Ne-HiPIMS for the application on the piston rings of internal combustion engines. *Applied Sciences 11*(21), 10498.

Valluzzi, M. G., L. G. Valluzzi, M. Meyer, M. A. Hernández-Fenollosa, and L. C. Damonte (2018). Optical and electrical properties of TiO_2/Co/TiO_2 multilayer films grown by DC magnetron sputtering. *Advances in Condensed Matter Physics 2018*(1), 1257543.

van Dijk, J., K. Peerenboom, M. Jimenez, D. Mihailova, and J. van der Mullen (2009). The plasma modelling toolkit Plasimo. `https://plasma-matters.nl/applications/complex-mixture/global-models.php`.

Vašina, P., M. Meško, L. de Poucques, J. Bretagne, C. Boisse-Laporte, and M. Touzeau (2008). Study of a fast high power pulsed magnetron discharge: role of plasma deconfinement on the charged particle transport. *Plasma Sources Science and Technology 17*(3), 035007.

Vavassori, D., F. Mirani, F. Gatti, D. Dellasega, and M. Passoni (2023). Role of magnetic field and bias configuration on HiPIMS deposition of W films. *Surface and Coatings Technology 458*, 129343.

Vetushka, A. and A. P. Ehiasarian (2008). Plasma dynamic in chromium and titanium HIPIMS discharges. *Journal of Physics D: Applied Physics 41*(1), 015204.

Vickerman, J. C. and I. Gilmore (Eds.) (2009). *Surface Analysis – The Principal Techniques* (2 ed.). Chichester, United Kingdom: John Wiley & Sons.

Vitelaru, C., A. Aijaz, A. C. Parau, A. E. Kiss, A. Sobetkii, and T. Kubart (2018). Discharge runaway in high power impulse magnetron sputtering of carbon: the effect of gas pressure, composition and target peak voltage. *Journal of Physics D: Applied Physics 51*(16), 165201.

Vlček, J. and K. Burcalová (2010). A phenomenological equilibrium model applicable to high-power pulsed magnetron sputtering. *Plasma Sources Science and Technology 19*(6), 065010.

Vlček, J., P. Kudláček, K. Burcalová, and J. Musil (2007). High-power pulsed sputtering using a magnetron with enhanced plasma confinement. *Journal of Vacuum Science and Technology A 25*(1), 42–47.

Vossen, J. L. and J. J. Cuomo (1978). Glow discharge sputter deposition. In J. L. Vossen and W. Kern (Eds.), *Thin Film Processes*, Volume 4, Chapter II-1, pp. 11–73. New York, New York: Academic Press.

Waits, R. K. (1978a). Planar magnetron sputtering. In J. L. Vossen and W. Kern (Eds.), *Thin Film Processes*, Volume 4, Chapter II-4, pp. 131–173. New York, New York: Academic Press.

Waits, R. K. (1978b). Planar magnetron sputtering. *Journal of Vacuum Science and Technology 15*(2), 179 – 187.

Wallin, E. and U. Helmersson (2008). Hysteresis-free reactive high power impulse magnetron sputtering. *Thin Solid Films 516*(18), 6398–6401.

Wehner, G. K. (1975). The aspects of sputtering in surface analysis methods. In A. W.

Czanderna (Ed.), *Methods of Surface Analysis*, Chapter 1, pp. 5–37. Amsterdam, The Netherlands: Elsevier.

Window, B. and N. Savvides (1986). Charged particle fluxes from planar magnetron sputtering sources. *Journal of Vacuum Science and Technology A 4*(2), 196–202.

Winter, H., F. Aumayr, and G. Lakits (1991). Recent advances in understanding particle-induced electron emission from metal surfaces. *Nuclear Instruments and Methods in Physics Research Section B: Beam Interactions with Materials and Atoms 58*(3), 301–308.

Wright, A. W. (1877a). On a new process for the electrical deposition of metals, and for constructing metal-covered glass specula. *American Journal of Science and Arts 14*(81), 169–178.

Wright, A. W. (1877b). On the production of transparent metallic films by the electrical discharge in exhausted tubes. *American Journal of Science and Arts 14*(73), 49–55.

Yamamura, Y., N. Matsunami, and N. Itoh (1983). Theoretical studies on an empirical formula for sputtering yield at normal incidence. *Radiation Effects 71*(1–2), 65–86.

Yamamura, Y. and H. Tawara (1996). Energy dependence of ion-induced sputtering yields from monoatomic solids at normal incidence. *Atomic Data and Nuclear Data Tables 62*(2), 149–253.

Yamashita, M. (1989). Fundamental characteristics of built-in high-frequency coil-type sputtering apparatus. *Journal of Vacuum Science and Technology A 7*(2), 151–158.

Yang, Y., X. Zhou, J. X. Liu, and A. Anders (2016). Evidence for breathing modes in direct current, pulsed, and high power impulse magnetron sputtering plasmas. *Applied Physics Letters 108*(3), 034101.

Yoshida, Y. (1992). Low-gas-pressure sputtering by means of microwave-enhanced magnetron plasma excited by electron cyclotron resonance. *Applied Physics Letters 61*(14), 1733–1734.

Yushkov, G. Y. and A. Anders (2010). Origin of the delayed current onset in high power impulse magnetron sputtering. *IEEE Transactions on Plasma Science 38*(11), 3028–3034.

Ziegler, J. F., J. P. Biersack, and M. D. Ziegler (2008). *SRIM–The Stopping and Range of Ions in Matter*. Chester, Maryland: SRIM Co.

Ziegler, J. F., M. D. Ziegler, and J. P. Biersack (2010). SRIM – the stopping and range of ions in matter (2010). *Nuclear Instruments and Methods in Physics Research Section B: Beam Interactions with Materials and Atoms 268*(11-12), 1818–1823.